University of Southampton

FACULTY OF ENGINEERING AND PHYSICAL SCIENCES

Chemistry

Electrochemically Controlled Deposition of Nanomaterials

by

Nabil A.N. Mohamed

Thesis for the degree of Doctor of Philosophy

January 2024

Abstract

The modification of ammonium-based surfactants used for preparing mesoporous silica films by the electrochemically assisted surfactant assembly (EASA) were investigated by varying either the surfactant chain length (as described in Chapter 3) or by increasing the size of the surfactant head group (as described in Chapter 4). The silica films are formed by using an applied potential to organise the cationic surfactants and the resultant current drives silica condensation in the sol electrolyte. They contain a hexagonal array of pores in vertical orientation, i.e. perpendicular to the substrate surface.

Grazing incidence small-angle X-ray scattering revealed that extending the alkyl chain length from C_{14} to C_{24} resulted in the pore diameter measured by ellipsometric porosimetry shifting from 2.82 nm to 4.40 nm. Increasing the surfactant chain length to from C_{22} to C_{24} saw a collapse in hexagonal ordering, however, vertical pore orientation remained. Following surfactant removal, this work showed that mass transport was faster in the films obtained using larger surfactants.

Mesoporous silicas were prepared from sols containing surfactants with increasing head sizes, specifically using $[C_{18}H_{37}NMe_{3-x}Et_x]Br$, $[C_{20}H_{41}NMe_{3-x}Et_x]Br$ and $[C_{22}H_{45}NMe_{3-x}Et_x]Br$ surfactants. Grazing incidence small-angle X-ray scattering data showed a significant drop in peak intensity, indicating the effect of the larger surfactants on the film's porosity. Electron microscopy revealed uniform and crack free films along with a gradual reduction in hexagonal pore structure as one, two or three methyl substituents were replaced with less hydrophilic ethyl groups in the head group of the surfactant. The CVs showed no faradaic current for films templated by $[C_{18}H_{37}NMe_{3-1}Et_2]Br$ and $[C_{18}H_{37}NMe_{3-0}Et_3]Br$. The charge transfer resistance was influenced by the ordering of pores as the film formed using $[C_{18}H_{37}NMe_{3-2}Et_1]Br$ showed an increase in charge transfer resistance (830.2 Ω) relative to those formed using the $[C_{18}H_{37}NMe_{3-3}Et_0]Br$ surfactant (416.6 Ω). Ellipsometric porosimetry showed that the pore diameter of the silica films increased with increasing head group sizes.

The effect of a surfactant on electrodeposition of nickel was also examined. Electroplating from $NiCl_2.6H_20$ in an acidified aqueous electrolyte containing $[C_{16}H_{33}NMe_{3-3}Et_0]Br$ and boric acid is described in Chapter 5. EDX and SEM analysis indicated the presence of elemental nickel and existence of pores within the CTAB-templated films. The electrochemical surface area was larger for the CTAB-templated nickel (6.0×10^{-4} cm^2) than that of non-templated nickel (3.9×10^{-4} cm^2). The specific capacitance determined from CV studies of CTAB-templated nickel (1565 F g^{-1}) was also higher than non-templated nickel (822 F g^{-1}) at 5 mV s^{-1}.

Table of Contents

Table of Contents

List of Tables

List of Figures

List of Figures

List of Figures

Research Thesis: Declaration of Authorship

Print name: Nabil A.N. Mohamed

Title of thesis: Electrochemically controlled deposition of nanomaterials

I declare that this thesis and the work presented in it are my own and has been generated by me as the result of my own original research.

I confirm that:

1. This work was done wholly or mainly while in candidature for a research degree at this University;
2. Where any part of this thesis has previously been submitted for a degree or any other qualification at this University or any other institution, this has been clearly stated;
3. Where I have consulted the published work of others, this is always clearly attributed;
4. Where I have quoted from the work of others, the source is always given. With the exception of such quotations, this thesis is entirely my own work;
5. I have acknowledged all main sources of help;
6. Where the thesis is based on work done by myself jointly with others, I have made clear exactly what was done by others and what I have contributed myself;
7. Part of this work has been published as:
    1. Increasing the diameter of vertically aligned, hexagonally ordered pores in mesoporous silica thin films
       Mohamed, N. A. N.; Han, Y.; Hector, A. L.; Houghton, A. R.; Hunter-Sellars, E.; Reid, G.; Williams, D. R.; Zhang, W. Increasing the Diameter of Vertically Aligned, Hexagonally Ordered Pores in Mesoporous Silica Thin Films. *Langmuir* **2022**, *38* (7), 2257–2266. https://doi.org/10.1021/acs.langmuir.1c02854.
    2. Effects of surfactant head group modification on vertically oriented mesoporous silica produced by the electrochemically assisted surfactant assembly method
       N. A. N. Mohamed, Y. Han, S. Harcourt-Vernon, A. L. Hector, A. R. Houghton, G. Reid, D. R. Williams and W. Zhang, Effects of surfactant head group modification on vertically oriented mesoporous silica produced by the electrochemically assisted surfactant assembly method, *Nanoscale Adv.*, 2023, 3316–3325.

Signature: ..... Date:.....

Acknowledgements

Firstly, I wish to state my sincere appreciation and gratitude to my PhD thesis supervisors Professor Andrew L. Hector and Professor Gillian Reid for their guidance, inspiration, and support throughout my academic journey at the University of Southampton. I would also like to thank the Hector, Reid, electrochemistry, and ADEPT groups for their constant support. I would also like to acknowledge Dr. Wenjian Zhang, Dr. Andy Lodge, Dr. Tauqir Nasir, and Dr. Li Shao for their contributions to my research study. Moreover, I am very grateful to Anthony Houghton, Ziyou Zhang, Dr. Yisong Han, Julie Herniman and Dr. Gilles Möhl from Imperial College London, University of Warwick, and the University of Southampton for their support with ellipsometic porosimetry, TEM, mass spectrometry and GISAXS analysis. Furthermore, I would like to thank the EPSRC for the financial assistance throughout my PhD study. Finally, I would like to thank my entire family for their love and always supporting me in times of need. I thank you all.

Definitions and Abbreviations

C_{16}TAB	Hexadecyltrimethylammonium bromide
C_{16}TEAB	Hexadecyltriethylammonium bromide
C_{18}TAB	Octadecyltrimethylammonium bromide
C_{18}DMEAB	Octadecyldimethylethylammonium bromide
C_{18}DEMAB	Octadecyldiethylmethylammonium bromide
C_{18}TEAB	Octadecyltriethylammonium bromide
C_{20}TAB	Eicosyltrimethylammonium bromide
C_{20}DMEAB	Eicosyldimethylethylammonium bromide
C_{20}DEMAB	Eicosyldiethylmethylammonium bromide
C_{20}TEAB	Eicosyltriethylammonium bromide
C_{22}TAB	Docosyltrimethylammonium bromide
C_{22}DMEAB	Docosyldimethylethylammonium bromide
C_{22}DEMAB	Docosyldiethylmethylammonium bromide
C_{22}TEAB	Docosyltriethylammonium bromide
C_{24}TAB	Tetracosyltrimethylammonium bromide
CPB	Hexadecylpyridinium bromide
HFCPB	11,11,12,12,13,13,14,14,15,15,16,16,16-tridecafluorocetyl pyridinium bromide
HFOPC	3,3,4,4,5,5,6,6,7,7,8,8,8-tridecafluorooctyl pyridinium chloride
TMB	1,3,5-trimethylbenzene
TIPB	1,3,5-triisopropylbenzene
TEB	1,3,5-triethylbenzene
APTES	Aminopropyltriethoxysilane

MTES	Methyltriethoxysilane
STEM	Scanning transmission electron microscopy
XRD	X-ray diffraction
SAXS	Small-angle X-ray scattering
GISAXS	Grazing incidence small-angle X-ray scattering
NMR	Nuclear magnetic resonance spectroscopy
SEM	Scanning electron microscopy
TEM	Transmission electron microscopy
EP	Ellipsometric porosimetry
CV	Cyclic voltammetry
EIS	Electrochemical impedance spectroscopy
BJH	Barrett-Joyner-Halenda
PSD	Pore size distribution
CMC	Critical micelle concentration
LCT	Liquid crystal templating
IUPAC	International Union of Pure and Applied Chemistry
AAO	Anodic aluminium oxide
EISA	Evaporation induced self-assembly
EASA	Electrochemically assisted surfactant assembly

Chapter 1 Introduction

1.1 Porous materials

Porous materials are variously categorised based on their pore size, structure, shape, and accessibility. These concepts related to classifications of porous materials will be discussed below.

Pores can be grouped based on their accessibility to the active surface as described in Fig. 1.1. Pores which remain open can be accessible to a variety of molecules or ionic species in some cases, the pores can be referred to as open pores through one end or pores that open at both the interior and exterior ends.[1] The porous system can collapse if heat treatment is applied above the material's threshold temperature, preventing access to the surface. For porous materials, the inability of a helium molecule to permeate through the pores at around 30 °C is referred to as closed pores by Ruike et al.[2] On the contrary, if a molecule or ion is larger than the pore diameter, the porous system is stated to have closed pores.

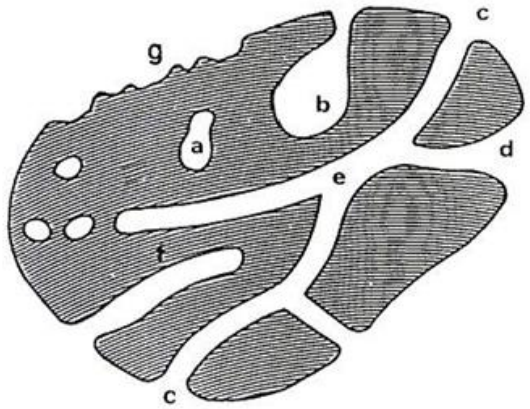

Figure 1.1 Pore classification diagram based on their availability to the active surface, (a) blocked pores, (b), (f) open pores at one side (c), (d), (g) accessible pores and (e) open pores at two sides.[3]

Another classification of pores is based on the geometric shape of the pores as described by the International Union of Pure and Applied Chemistry (IUPAC) and Kaneko et al.[3,4] Figure 1.2. shows the pore classification corresponding to Kaneko which is split up into different geometric shapes of cylinders, slit-shape, cone, and inkbottle. The classification of pores organised by Kaneko is virtually in agreement with IUPAC but diverges slightly in that the cone-shape is replaced with a funnel-based geometry.

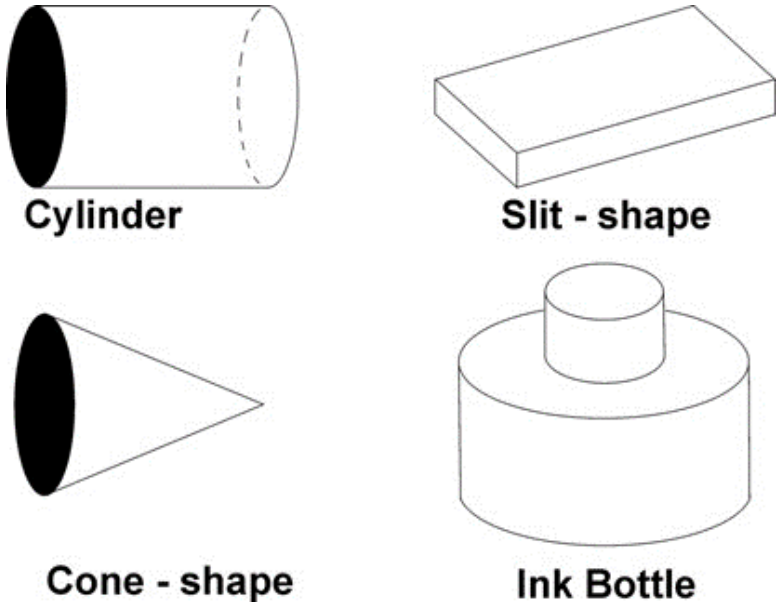

Figure 1.2 The classification of pores based on their geometry as organised by Kaneko.[4]

The pore diameter has important implications with regards to its applicability in industrial settings. As previously mentioned, the geometry of pores is a means to define the pores. The classification of pores that is adopted by IUPAC is based on Everett[5], Sing[6] and later revised by Dubinin[7] et al. The pores were grouped according to their different sizes. Microporous materials are categorised as having pore diameters ranging from 0.2 –2 nm, whereas mesoporous materials contain pores in the region of 2 – 50 nm and macropores range from 50 – 1000 nm. There are a range of materials that act as templates for example, anodic aluminium oxide[8], aluminophosphates[9], metal organic frameworks[10], track etched polymer membranes[8], zeolites[11], and silica[12]. Anodic aluminium oxide (AAO), track etched polymer membranes and mesoporous silica are used as hard templates.[8]

1.2 Mesoporous silica

Zeolites are often regarded as ideal porous materials due to their molecular sieving properties and tuneable pore diameter. However, despite the many marketable applications of zeolites where ordered microporous systems are needed, there has been a constant demand for a range of mesoporous materials in a variety of applications.[11]

In 1990, Yanagisawa et al.[13] explored the synthesis of mesoporous materials that had similar properties to that of MCM-41. The process involved the intercalation of the silicate kanemite with an organic molecule which was later termed a structure-directing agent or surfactant. High temperature treatment was required to remove the organic molecule to produce a three-

dimensional network of SiO_2 layers exhibiting mesopores. It was also shown that increasing the alkyl chain length in the trimethylammonium halide resulted in the pores expanding.

In 1992, Kresge[14] and co-workers at Mobil cooperation discovered the family of mesoporous materials based on silicates and aluminosilicates termed M41S. The synthesis of these materials is based on the liquid crystal templating (LCT) mechanism where the template support is a surfactant as opposed to metal ions or hydrated molecules but rather associated with the self-organisation of micelles in solution. This family of materials have shown to have three distinct phases i.e., MCM-41 (hexagonal), MCM-48 (cubic) and MCM-50 (lamellar or layered) (Fig 1.3).[15] The porous materials have found their way into many applications such as catalysis,[16] adsorption media[17] and for the separation of chemicals,[18] as the pores are uniformly packed with larger pore diameters (2 – 50 nm) in relation to crystalline materials of zeolites. Moreover, it is also apparent that a lot more studies have been carried out using MCM-41 compared to other silica-based materials of the same family due to thermal instabilities.[19]

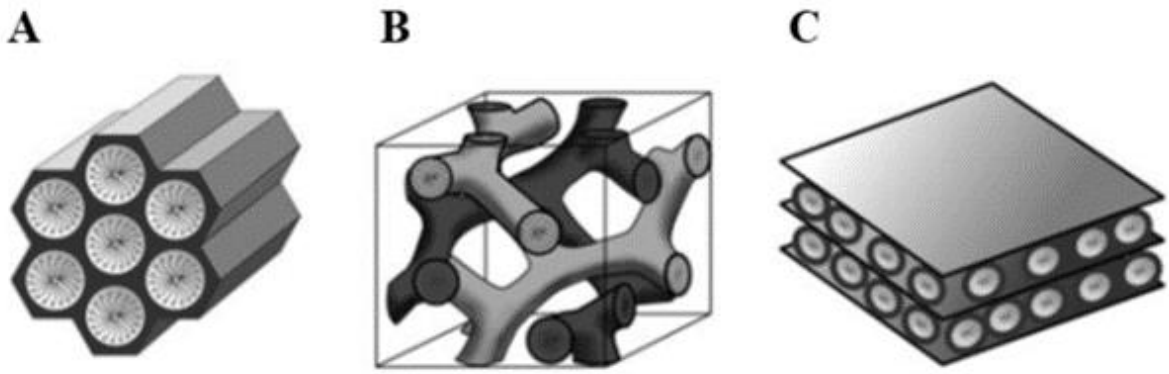

Figure 1.3 Mesoporous (M41S) silica materials of (a) MCM-41, (b) MCM-48 and (c) MCM-50.[15]

The synthesis of MCM-41 is based on the LCT mechanism which involves the interaction between the positively charged quaternary ammonium head group of surfactants and negatively charged silica species as the sol precursors. The surfactants (e.g., alkyltrimethylammonium bromide) act as a template for the formation of micelles in solution. The cationic or non-ionic surfactants and the silica species self-assemble to form hexagonal arrays, layered or cubic structures under high pH levels and temperatures around 150 °C. The hexagonally arranged mesopores are formed by the condensation of silicate species (i.e. a sol-gel process) around the micelles or by the silicate species adsorbing on the exterior side of the rod-shaped micelle through electrostatic interactions. The MCM-41 silica material possesses pore diameters between 1.5 to 10 nm and a surface area of 1000 $m^2\ g^{-1}$.[14,20]

The advancements of zeolite materials intrigued further development of mesoporous materials, as they possessed high surface areas, high pore accessibility and ordered porosity. The expansion of pores could be achieved and the functional properties could be modified by varying the type of surfactant, silica reagent, and in some cases the use of swelling agents. The MCM-41 material is an extremely good adsorbent. However, porous silicates and aluminosilicates reported by Kresge et al.[14] included shortcomings such as low thermal, hydrothermal and mechanical stability in comparison to zeolites due to their thin pore walls.[20,21] The narrow pore diameters could also impact the grafting process of a variety of functional organic groups. Yet, the ability to optimise the porous materials at the nanometre scale has overcome many of these issues over the years.[22]

In the late 1990s, a novel class of well-defined mesoporous silica materials was produced by scientists at Santa Barbara. The synthesis of the silica materials involves the addition of a template and tetraethylorthosilicate (TEOS) as the silica precursor to an acid/water mix. Generally, block copolymers containing ethylene oxide or propylene oxide linkers are used as non-ionic surfactants.[23] The sol is aged overnight at high temperatures and filtration is used to recover the amorphous solid followed by washing and drying under atmospheric pressure. The product undergoes calcination at high temperatures to remove the surfactant therefore, SBA-15 (SBA = Santa Barbara Amorphous) which has a *P*6*mm* hexagonal pore structure with pore diameters reaching as high as 30 nm with the support of swelling agents.[23] The expansion in pore diameters relative to MCM family of materials is possible as the longer chained triblock copolymer consisting of P123 {$[CH_2CH_2O]_{20}[CH(CH_3)\ CH_2O]_{70}\ [CH_2CH_2O]_{20}$, $EO_{20}PO_{70}EO_{20}$} results in larger micelles in solution when compared to smaller ionic based surfactants used previously. Initially, it was assumed that MCM-41 was analogous to that of SBA-15 but with smaller pore apertures. Nevertheless, it was later known that unlike MCM-41, SBA-15 exhibits microporous domains within the mesoporous framework which is caused by permeation of the silica matrix by the flexible and long chained polymer surfactants. Such interlayered meso-micro porosity results in an increase in pore wall thickness and hence improves the thermal and hydrothermal stability in comparison to MCM-41.[24] As time passed, other block copolymers such as $EO_{106}PO_{70}EO_{106}$ (F127) were discovered, with this an example of a surfactant that was effective for confined cubic based structures. The SBA family of materials with a diversity of structures include SBA -12 (3D-hexagonal, *P6mm*), SBA-14 (layered structure), SBA-15 (2D-hexagonal, *P6mm*) and SBA-16 (body centred cubic, *Im2m*).[25] The differences in descriptor properties between MCM-41 and their counterparts are tabulated in Table 1.1.

Table 1.1 Descriptor properties of MCM and SBA silica materials.[26]

Descriptor properties	**SBA-15**	**SBA-16**	**MCM-41**	**MCM-48**	**HMS**
Name	Santa Barbara Amorphous type 15	Santa Barbara Amorphous type 16	Mobil Composition of Matter no. 41	Mobil Composition of Matter no. 48	Hexagonal (H) Mesoporous Silica
Surfactant	Pluronic P123	Pluronic F127	CTAB	CTAB	Amines
Sol electrolyte	pH ~1	pH ~1	pH ~11-13	pH ~11-13	pH ~9
Structure	2D (H) mesopores *P6mm* laue group	3D cubic mesopores *Im3m* laue group	1D (H) mesopores *P6mm* laue group	3D cubic mesopores *Ia3d* laue group	Wormhole mesoporous structures
Pore diameter	4-30 nm uniform pores	4-30 nm non-uniform pores	1.5-10 nm slow ion transport	2-3 nm slow ion transport	2-10 nm smaller than SBA-15
Surface area	~ 1000 m^2g^{-1}	~ 1000 m^2g^{-1}	~ 800 m^2g^{-1}	~ 1100 m^2g^{-1}	800-1000 m^2g^{-1}
Stability	Wall thickness up to 9 nm with good thermal stability	Wall thickness similar to SBA-15 with good thermal stability	Thin walls of 0.9 nm with poor hydrothermal stability	Same as MCM-41	Less ordered but similar stability to MCM materials

1.3 Mesoporous silica thin films

Mesoporous silica thin films are generally prepared through a surfactant templating mechanism with uniform pore diameters ranging in the region of 2-30 nm. In 1994 Ogawa and co-workers[27] prepared porous silica films at the solid-liquid interface. It was not until later that coating techniques were developed for the self-assembly of mesoporous silica. Three main types of coating techniques have been discussed in the literature, these are dip coating, spin coating, and spray coating.[8] The latter is often used to produce thin films of greater thickness. These processes have been widely used today and are collectively referred to as evaporation induced self-assembly.

1.3.1 The evaporation induced self-assembly method

The most common approach to prepare mesoporous silica films is by evaporation induced self-assembly (EISA).[12,28] This method involves the preparation of an aqueous ethanol solution containing a surfactant and silica precursors to produce a homogenous solution of stable species. The initial surfactant concentration (C_o) of the prepared solution is significantly lower in comparison to the critical micelle concentration ($C_o << CMC$). Once the films have been deposited in solution by either dip or spin coating, the ethanol solvent evaporates from the deposited film resulting in the surfactant concentration increasing which in turn triggers the self-assembly process and micelle formation, producing well-organized porous structures in the liquid crystalline phase before condensing the silica species. The EISA film can be calcined to clear the surfactant and any residual solvent from the pores in addition to hardening the silica framework. Where linear pores are present, such as in the *P*6*mm* hexagonal system pictured in Fig. 1.4, EISA tends to produce ordered silica films with the pores horizontal to the substrate surface.

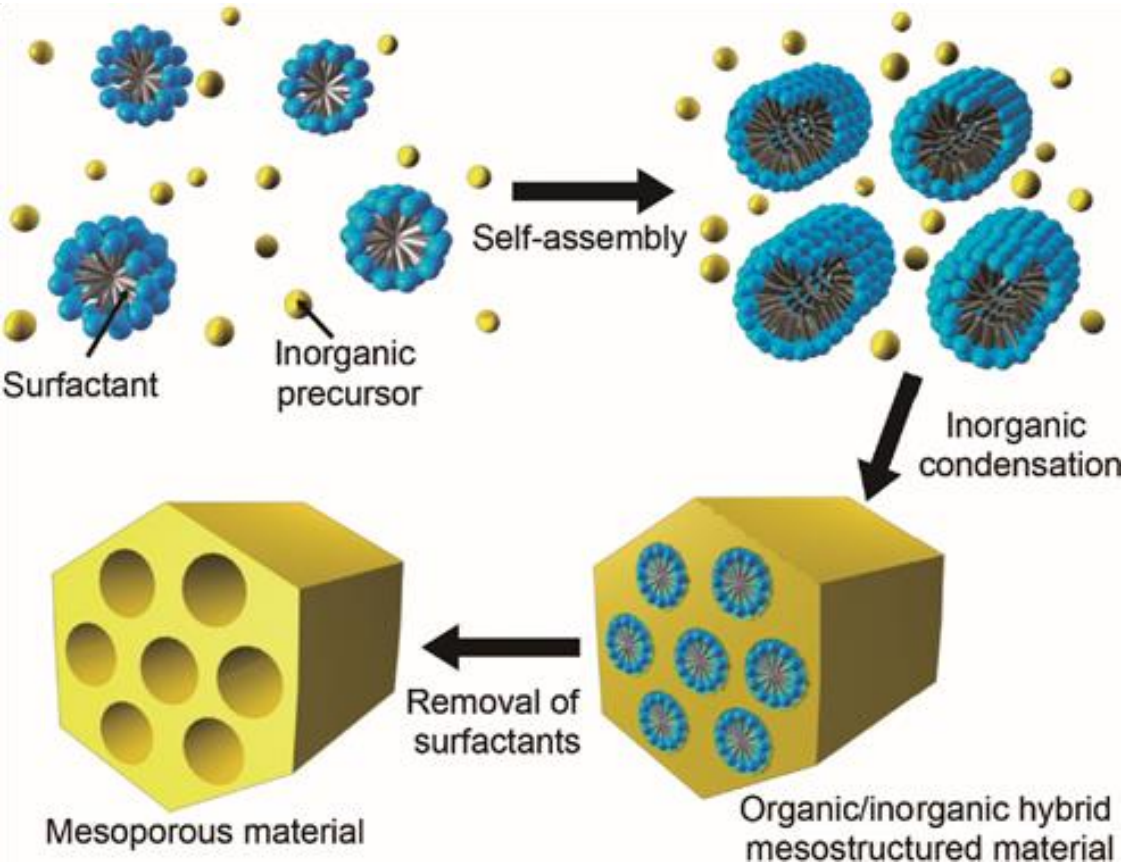

Figure 1.4 The mechanism of mesoporous silica films produced by EISA.[29]

1.3.2 The Stöber – solution growth method

Research into the growth of vertically aligned porous silica films has been reported by Teng et al.[30] They initially deposited films from solutions containing cetyltrimethylammonium bromide (CTAB), a silica precursor, ethanol and ammonia at high temperatures using conductive substrates namely indium-tin oxide. Stöber-solution growth is based on the formation of hemispherical micelles of a cationic surfactant on a negatively charged substrate, and interactions with silica oligomers encouraging vertical growth of those micelles. This process can be used to prepare silica films with continuous film coverage, low defect concentration, high thermal stability, uniform film thickness and good mechanical stability. In contrary to the EISA method, the mesopores tend to be vertical, i.e. perpendicular to the substrate, due to the way in which the formed silicate species interact with the micelles at the solution-film interface.[30] Pizzoccaro-Zilamy et al.[31] prepared mesoporous silica membranes by the conventional Stöber-solution method. They discovered that extending the growth process of porous silica from 15 to 62 hours led to an increase in the film thickness from 25 to 50 nm. Furthermore, the presence of silica spheres on the film's surface did not disrupt the water accessibility performance which was three times greater than that prepared using EISA.

Other methods for the preparation of oriented films include magnetic field of high strength,[32] epitaxial growth,[33] and radio sputtering[34]. However, these methods suffer from high cost for formulation, increased pore disorder, limited substrate compatibility and long preparation times to make very thin films. Figure 1.5 shows a schematic diagram of the formation of silica on a conductive substrate and the elimination of surfactant by calcination to produce films with open pores.

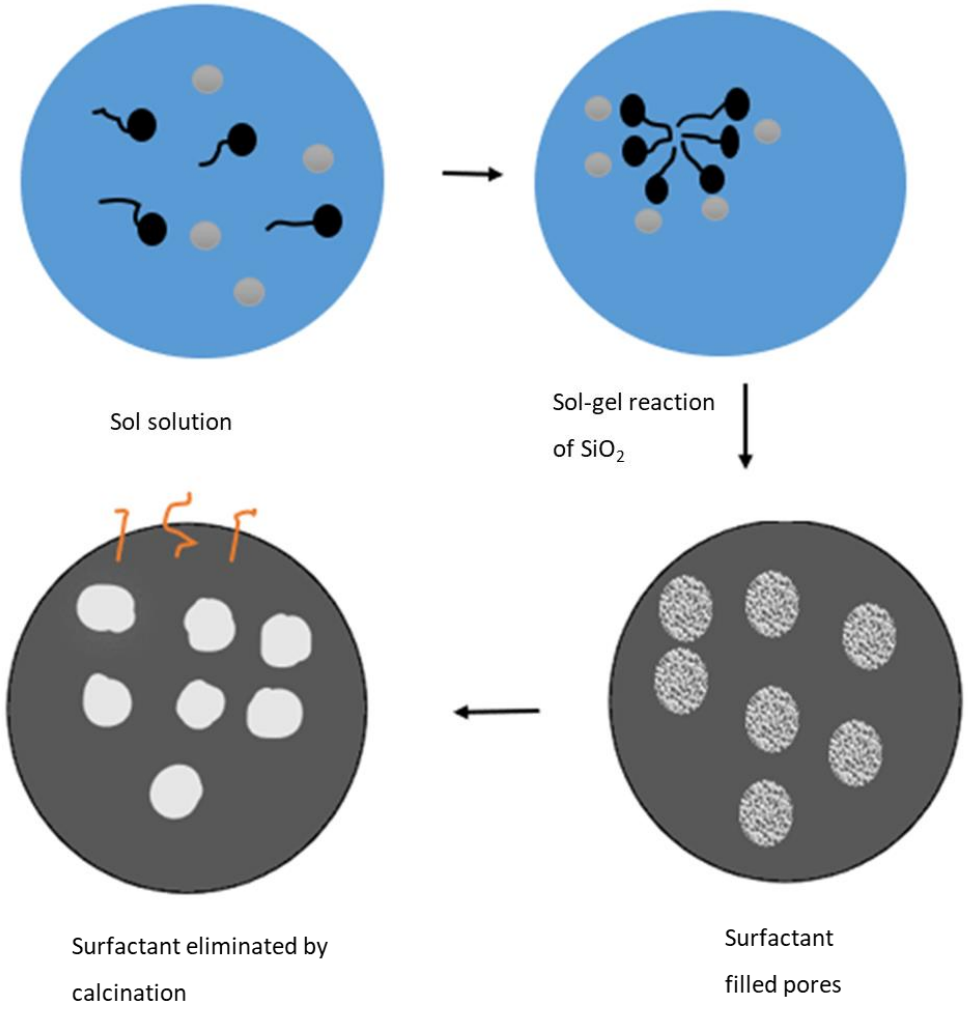

Figure 1.5 The formation of vertical oriented mesoporous silica films by the Stöber-solution method.

1.3.3 The electrochemically assisted surfactant assembly method

The electrochemically assisted surfactant assembly method (EASA) was discovered by Walcarius et al.[35] in 2007 and revealed that the preparation of vertically oriented mesoporous silica films was possible under electrochemical control. The mechanism for porous silica formation involves applying a negative potential to the substrate to be coated, while it sits in a solution containing the surfactant and silica precursors dissolved in an ethanol/water mixture. This results in the

generation of hydroxide ions in solution, and the pH swings from acidic to alkaline at the electrode surface. The electric field is thought to play a pivotal role in the self-organization of the cationic surfactant into hemi-micelles and the pH change catalyzes the polycondensation of the sol, leading to mesoporous silica films with perpendicular (vertical) pore channels (2-3 nm) and uniform film thickness (150-200 nm). Mesoporous silica films can be obtained by the EASA method within as little as 20 seconds. The prolonged deposition of porous silica (> 20 seconds) leads to the overgrowth of silica randomly scattered on the surface with similar hexagonal structures to the underlying film. These are randomly oriented, so diffraction rings are observed in grazing incidence small-angle X-ray scattering (GISAXS) experiments. The EASA method is flexible in that parameters of surfactant, temperature, silica reagent and pH can be regulated to fit specific applications. The deposition potential and time are important parameters in controlling film thickness and pore order. Additionally, the versatility of this method has seen several different substrates used for deposition of porous silicas and include ITO, copper, gold, platinum, glassy carbon and titanium nitride.[35,36,44] EASA films can also be prepared with zinc-doped indium oxide substrates, organically improved ITO substrates and phosphorus doped silicon materials as reported by Cheng et al.[37]

An in-depth study by Goux et al.[36] looks into more detail at the parameters that control the EASA process for example, it was revealed that adjusting the surfactant: silica ratio from 0.16 to 0.64 resulted in the preparation of an amorphous nonporous framework, followed by a disordered porous film, then ordered hexagonal structures, thus reiterating the careful parameter control for the effective growth of ordered silica films with hexagonal pore structures. Figure 1.6 a demonstrates that micelles can form on conductive surfaces at various arrangements such as spherical, bilayers and cylindrical micelles as determined by the deposition potential and the surfactant concentration. Figure 1.6 b shows a graphic of the EASA process used to produce mesoporous silica films with vertical mesopores.

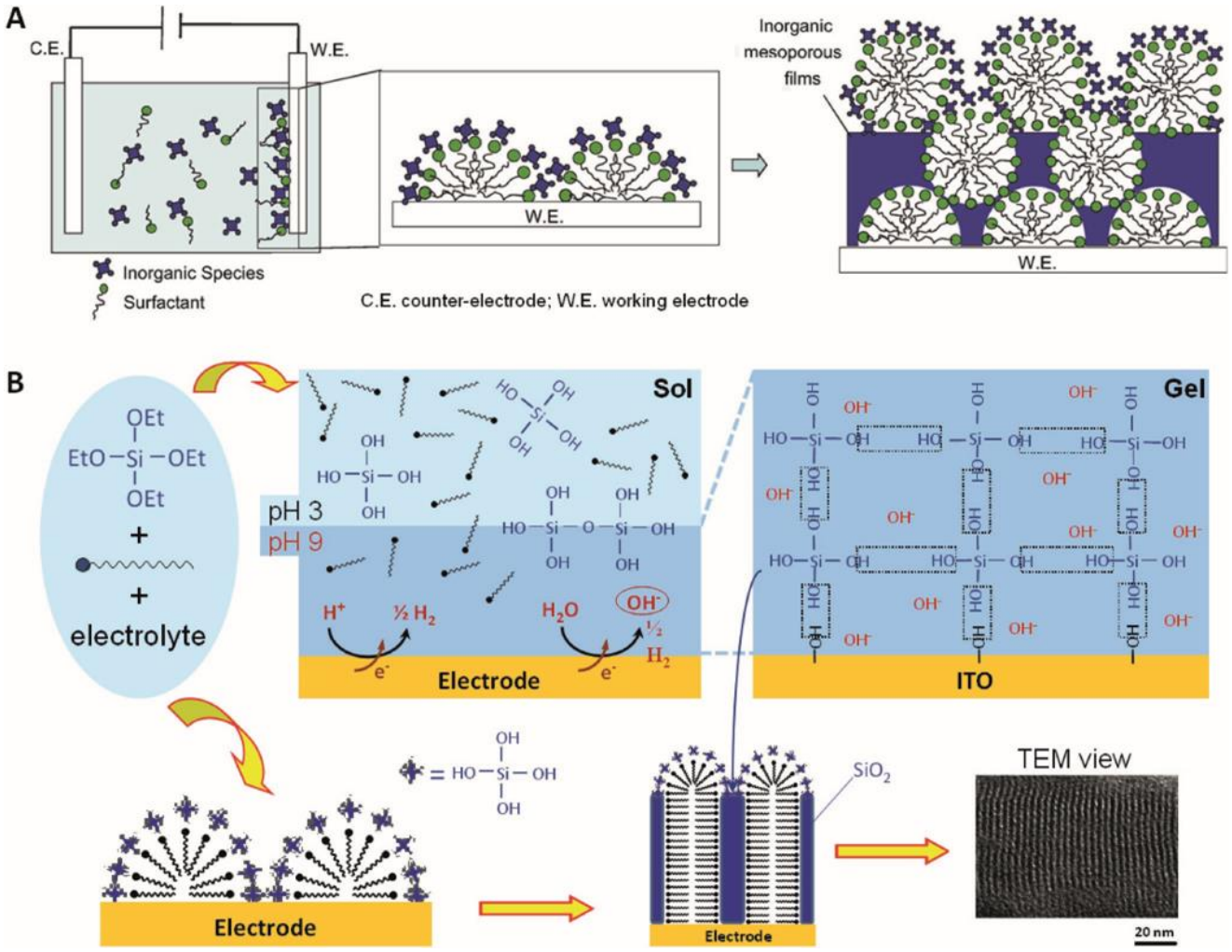

Figure 1.6 The proposed mechanism of vertically aligned mesoporous silica films by EASA.[38]

1.4 The components for sol-gel synthesis

1.4.1 Surfactants

Surfactants have been an important component in the synthesis of mesostructured silica materials as mentioned earlier. The choice of surfactant is crucial in the control of pore diameters, wall thickness and symmetry of pore materials. The main type of surfactants typically employed for porous systems are non-ionics and cationics. The largest group of surfactants are the anionics, however they are used less frequently for the preparation of mesoporous silicas. Furthermore, zwitterionic surfactants have not been used at all for preparation of porous silicas.

As previously stated, Kresge et al. synthesised MCM-41 silica materials using the well-known cationic CTAB surfactant and TEOS as the silica supply through a LCT mechanism.[14] Hao et al.[39] explored the possibility to prepare mesoporous silica nanomaterials using a mixture of cationic and anionic surfactants through an ammonium catalysed sol gel process. They revealed that

mesostructured silica of different shapes of films, platelets, spheres, and rods can be attained with accessible mesopores. In porous silica films the pores could be directed normal to the substrate by manipulating the CTAB and tetrabutylammonium iodide surfactant concentrations. Tanev et al.[40] demonstrated the synthesis of MCM-41 using a neutral amine surfactant (e.g. dodecylamine) of different chain lengths and a neutral silica precursor. The templating method is based on hydrogen bonding between the surfactant-silica components in turn giving rise to porous silica materials with improved ordering. The increase in pore wall thickness improves both thermal and hydrothermal stability of the porous system. An advantage of this neutral pathway is that the surfactant can be recycled from the pores by solvent removal techniques.[41] In contrary, the MCM-41 produced by the conventional method results in difficulty in surfactant recycling due to charged sol precursors. It is also possible to synthesise mesoporous silicas with modified surfactants to produce larger pores for instance, by increasing the surfactant head size, increasing the alkyl tail length of surfactants or by using dimeric structures of Gemini surfactants where two hydrophilic heads and two hydrophobic tails are connected by a spacer close to the head group.[42]

Vila et al.[43] reported the synthesis of vertically aligned EASA films using CTAB and octadecyltrimethylammonium bromide (OTAB) as the organic templates. It was uncovered that the pore diameter could be increased from 2.0 to 2.9 nm when switching from CTAB to OTAB and this resulted in a retention in hexagonal structure and pore alignment. These outcomes suggest that the EASA process is open to the modification of surfactants. Robertson et al.[44] reported the electrochemically assisted deposition of silica using a surfactant with a bulky head group, cetylpyridinium bromide (CPB) as opposed to CTAB. It was determined from GISAXS that a reduction in hexagonal ordering was noticed however, there was a significant increase in pore spacing compared to CTAB and that was linked to an increase in pore size. Gosh et al.[45] reported the preparation and synthesis of mesoporous silica thin films using fluorinated surfactants of different chain lengths of 11,11,12,12,13,13,14,14,15,15,16,16,16-tridecafluorocetyl pyridinium bromide (HFCPB) and 3,3,4,4,5,5,6,6,7,7,8,8,8-tridecafluorooctyl pyridinium chloride (HFOPC) which were compared with CPB using the EISA dip coating method. The authors realised that the presence of CO_2 uptake (172 bar at 25 ℃) for the fluorinated films led to a significant increase in pore diameter for HFCPB (5.19 nm) and HFOPC (2.76 nm) examined from transmission electron microscopy (TEM). Furthermore, the silica films with fluorinated surfactants were successfully synthesised on low energy modified glass substrates whereas silica films with CPB were not possible to synthesise using these substrates. Figure 1.7 illustrates a range of modified cationic surfactants used to produce porous silica materials.

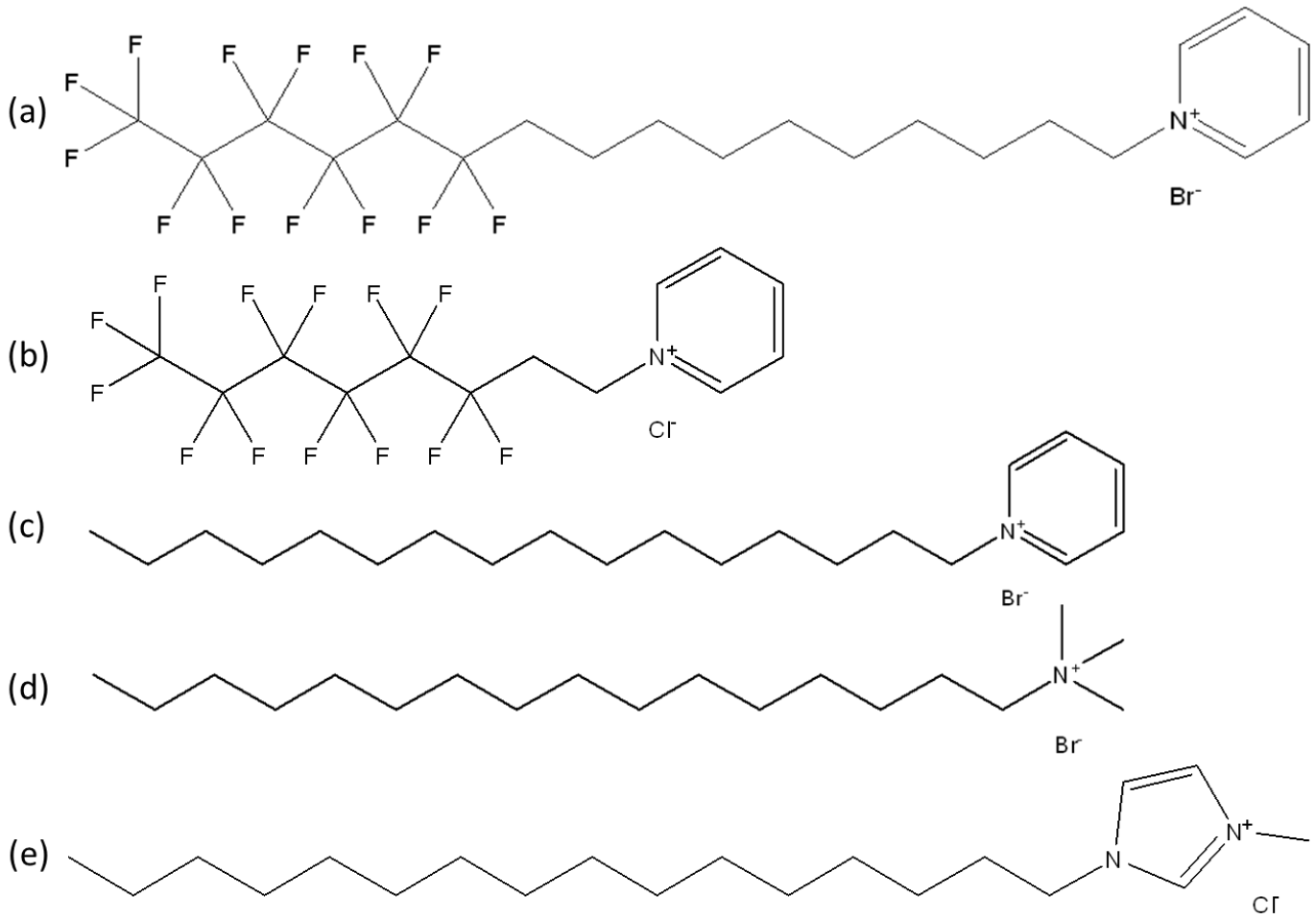

Figure 1.7 Cationic surfactants (a) 11,11,12,12,13,13,14,14,15,15,16,16,16-tridecafluorocetyl pyridinium bromide (HFCPB), (b) 3,3,4,4,5,5,6,6,7,7,8,8,8-tridecafluorooctyl pyridinium chloride (HFOPC), (c) cetylpyridinium bromide (CPB), (d) hexadecyltrimethylammonium bromide and (e) 1-hexadecyl-3-methylimidazolium chloride.

Dunphy and co-workers[46] demonstrated an increase in pore size for F127 templated-mesoporous silica films produced by EISA. They discovered that the diameter of 8 nm pores could be pushed to around 15 nm, as determined by N_2 adsorption-desorption analysis. This was achieved by altering the parameters of surfactant/silica ratio in the EISA process.

Vavra et al.[47] reported the synthesis of vertically oriented mesoporous silica films by EASA. The authors found that replacing CTAB with 1-hexadecyl-3-methylimidazolium chloride (C_{16}MIMCl) maintained the hexagonal structure and alignment along with a distinct pore size of 2.5 nm, as estimated by TEM.

For the preparation of EASA films, the surfactants that are most frequently used are cationics such as CTAB. Moreover, EASA films can also be synthesised by using cationic surfactants of increasing alkyl chain lengths or substituting the halide counter ion. Whereas anionics, neutral and zwitterionic surfactants have not been used for producing EASA films.

1.4.2 Swelling agents

A well-known method for enhancing pore size is the use of swelling agents. The method involves organic molecules passing into the hydrophobic region of the micellar structure resulting in its expansion. The most frequently used swelling agents for mesoporous silicas are benzenes with alkyl substituents such as 1,3,5-trialkylbenzenes, xylene, ethylbenzene, and toluene. Namba et al.[48] prepared silica materials through a hydrothermal process using 1,3,5-trimethylbenzene (TMB) or 1,3,5-triisopropylbenzene (TIPB). The introduction of TMB resulted in the Barrett-Joyner-Halenda (BJH) pore size of MCM-41 expanding to 12 nm. However, the silica material showed a degradation in hexagonal pore ordering and a lowering in thermal and hydrothermal stabilities. On the contrary, the synthesis of MCM-41 with TIPB led to increases in pore order and higher levels of thermal and hydrothermal stabilities but the BJH pore size did not exceed 4 nm. Cao et al.[23] prepared Pluronic P123 templated SBA-15 materials with larger pore diameters using cyclohexane, 1,3,5-triethylbenzene (TEB) and TIPB as the swelling agents. It was concluded that the presence of TIPB gave rise to a BJH pore diameter around 34 nm with good retention in the 2D hexagonal pore structure. The swelling agents of cyclohexane and TEB were also used to expand the SBA-15 mesopores. The former was found to be effective in pushing the pore diameter to around 15 nm whereas TEB led to a significant lessening in the pore ordering as determined by small-angle x-ray scattering (SAXS). Figure 1.8 displays a series of swelling agents used to push the pores to greater diameters in mesoporous silica materials.

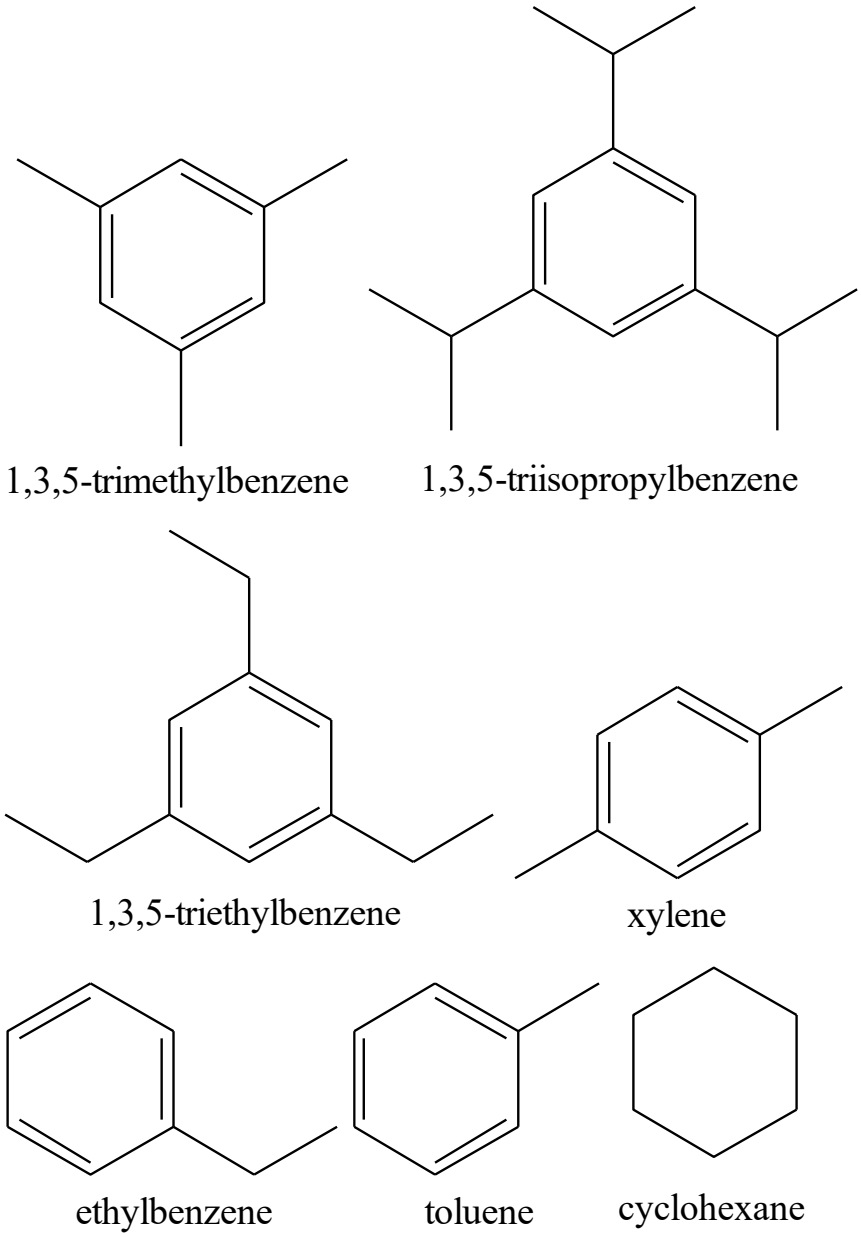

Figure 1.8 A list of swelling agents used for pore size expansion in mesoporous silicas.

Swelling agents have also been incorporated in EASA films for pore expansion. For example, Guillemin [49] et al. used TMB to increase the pore diameter of CTAB templated silica film while maintaining a reasonable and regular pore structure. They determined from electron microscopy and cyclic voltammetry studies that larger pore diameters were obtained when using specific amounts of TMB in the sol electrolyte. Even though the pore diameter increased, this was compromised by poor hexagonal ordering of the silica film when using TMB. On the other hand, Robertson et al.[44] synthesised EASA films with CTAB on titanium nitride electrodes. They determined that additions of TMB to the sol at specific ratios afforded increases in pore diameter determined by electron microscopy to be 2.4 nm from 1.6 nm with the hexagonal structure intact.

1.5 The functionalisation of mesoporous silica materials

Changes to the surface chemistry of mesoporous silica has attracted many researchers from across the world. The modification of the porous silica material with organic reagents manipulates the physicochemical properties of the materials. This ability has brought great importance to many applications of adsorption, sensing, ecology, and nanotechnology.[50] The incorporation of organic reagents in the porous material favours the fine tuning of properties including hydrophilicity, hydrophobicity, acidity and basicity, shielding the silica surface from any unwanted chemical reactions and the modification of the silica surface while simultaneously showing excellent stability towards sol-gel reactions.[51] Another advantage of introducing functional groups in the pore channels is the possibility of expanding the pore diameter as well as the surface properties which could either increase or decrease the rate of mass transport of various ionic species depending on the hydrophobic or hydrophilic nature of the pore walls along with the size of active species. However, it is essential that select functional groups are applied to stop the functionalised film from acting as barring gates to select ions in solution when undergoing pore transit measurements.

These functionalised materials are generally synthesised through two methods. The first one consists of two steps; the synthesis of porous silica followed by the grafting of the silica surface by organosilanes. The benefit for modifying porous silica is that the incorporation of organic molecules does not significantly reduce the pore ordering and alignment of the material. Additionally, the selective functionalisation of porous silica is achieved by bonding the functional group to silanol groups (Si-OH) on the walls by continual grafting methods as shown in Fig 1.9. The most used approach for surface manipulation is by silylation.[51] Dioum et al[52] modified porous SBA-15 silica materials through grafting of aminopropyltriethoxysilane (APTES) or N-(trimethoxysilylpropyl)-N,N,N-trimethylammonium chloride (TMTMAC) to determine whether silica modification improves the adsorption of nitrate ions in water. The results show that TMTMAC functionalised SBA-15 displays good adsorption capacity of NO_3^- (62.5 mg g^{-1}) at 25 °C. Vila and co-workers[53] evaluated the multi-step grafting of azide and ferrocene groups using the classic reaction based on click chemistry involving the Huisgen cycloaddition. Upon assessing the electrochemical performance, they discovered that the peak currents were significantly influenced by the concentration of supporting electrolyte. A detailed study by Fukuda et al.[54] reported the synthesis of porous silicas of MCM-41, SBA-15, and HUS-6. It was found that the material could be modified with the addition of a titanium source ($Ti(acac)_4$) to the silica surface for enhanced catalytic behaviour for epoxidation. This shows that the synthetic grafting of materials is not limited to organosilane reagents, but that transition metals can also be incorporated whilst retaining porosity.

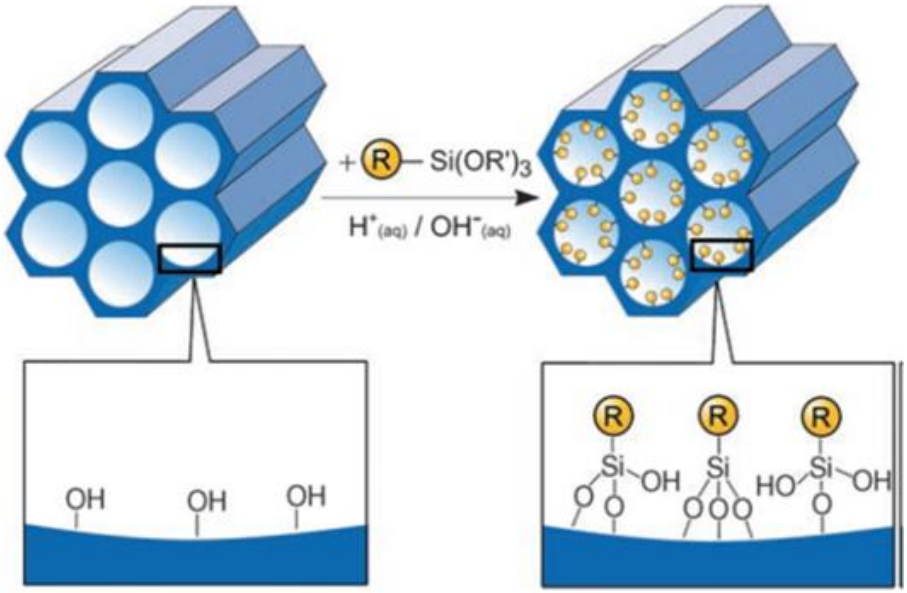

Figure 1.9 The post synthesis grafting of silica pore walls with organic reagents.[15]

Another route to the functionalisation of the silica surface with organic groups is by the co-condensation method as shown in Fig 1.10. Unlike the grafting method, the organosilane reagent is added in the sol electrolyte mixture containing the surfactant and silica precursors. Griselda Castruita-de León successfully produced functionalised MCM-48 through co-condensation using APTES.[55] The XRD data of porous MCM-48 showed high structural ordering after the anchoring of APTES on the pore walls. Furthermore, the fine tuning of reaction time and concentration of APTES were important in controlling the amount of amino functional groups on the walls. The preparation of organically modified mesoporous silica films using EASA has been studied by Guillemin and co-workers.[56] They revealed that the co-condensation of two silica precursors of methyltriethoxysilane (MTES) and TEOS resulted in the chemical modification of the silica surface and more importantly, the pore ordering and orientation remained constant despite the film containing MTES at a molar ratio of 60 %.

Nevertheless, the two-step functionalisation of silica materials is often structurally more stable and unreactive towards hydrolysis than the one-step co-condensation process. Another advantage of the grafting approach is that the surfactant template can be extracted by calcination prior to the grafting of functional groups to the walls. However, an uneven distribution of organic reagents to the active sites is most frequently seen with the grafting method. On the other hand, the one-step synthesis has the advantage of high loading of organic groups in both the inner and outer pore channels than post synthetic functionalisation by grafting, uniform distribution of functional groups on the silica surface and faster preparation times. For example, Robertson et al.

investigated the post synthetic grafting of organosilane reagents in EASA films templated by CTAB. It was discovered that larger functional groups attached to the silane molecule would only react at the necks of the small pores produced by EASA as opposed to smaller organosilane grafting molecules, as indicated by ^{29}Si nuclear magnetic resonance (NMR) spectroscopy. Furthermore, the co-condensation process has its drawbacks for instance, greater care is needed to remove the surfactant template used to produce the silica film. The calcination process is not used as it would have a negative effect on the functionalised pore walls. Although, Soxhlet extraction is commonly used to remove the surfactant from the mesopores, an incomplete removal of surfactant is mostly spotted.[15]

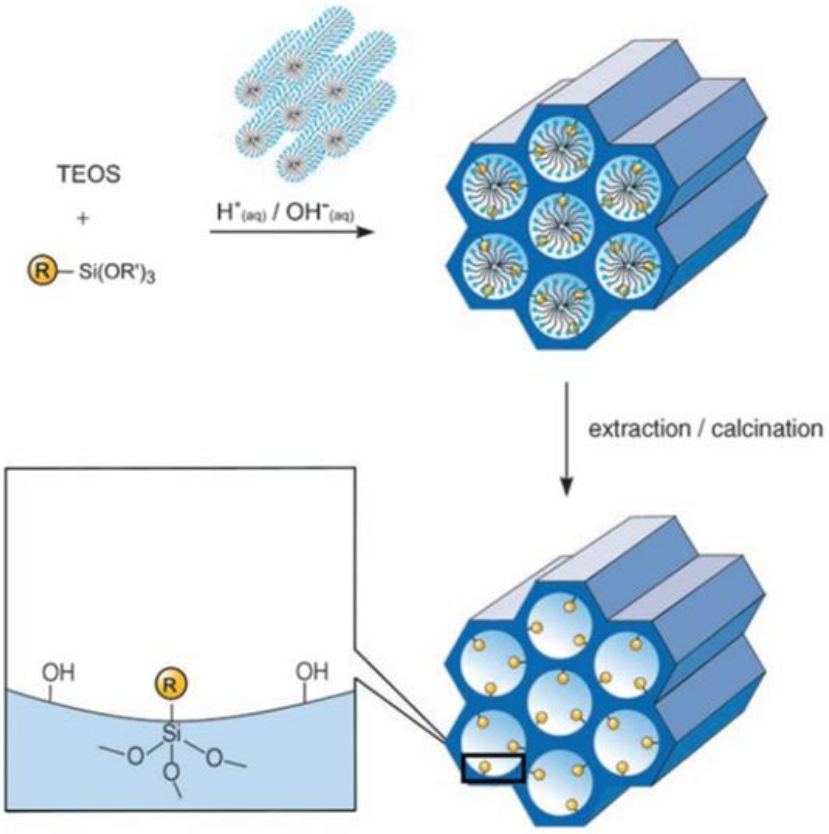

Figure 1.10 The one step co-condensation method to functionalise the silica pore walls with organic reagents.[15]

1.6 Mesoporous metals and metal oxides synthesised by hard and soft templates

The soft templating approach consists of two methods namely the ligand-assisted method and by EISA. Soft templating uses molecular species which includes organic surfactants and block copolymers or a liquid crystal to form the template. The process between the molecular species and metal ions is directed by weak van der waals forces, electrostatic interactions and hydrogen bonding.[59] In the ligand-assisted approach a metallic precursor is covalently bonded to the surfactant head group before hydrolysis[58]. Even though mesoporous silica materials can be functionalised with transition metal cations, it was not until 1995 when Antonelli et al.[57] reported the first synthesised mesoporous transition metal oxide using linear chained surfactants of alkyl amines. The ligand-assisted approach was also useful in the preparation of mesoporous Ta_2O_5 and Nb_2O_5.[58,59] These templated materials have well-ordered mesoporous structures and amorphous walls. The need for mesoporous materials with larger pore diameters and higher surface areas for several applications led to the exploration of non-ionic surfactants. For instance, the commercially available poly (ethylene oxide)- b- poly (propylene oxide)-b-poly(ethylene oxide) (PEO-PPO-PEO) block co-polymers are found as Pluronic P123 and Pluronic F127 or other in house copolymers as surfactant templates have been successfully utilized in alcoholic solutions.[60,59]

The idea of using hard templates has created new opportunities for producing novel mesoporous materials. The term “nanocasting” has been used interchangeably with the hard templating approach and was first designed using the Al_2O_3 porous membrane as hard template.[61] These porous Al_2O_3 templates have been used to synthesise metals, metal oxides and metal sulphide mesoporous structures by chemical vapour deposition and electrodeposition.[59] The pore diameters obtained from these materials are typically larger than 15 nm with highly disorganised porous systems. Well-ordered mesoporous silicates may serve as viable alternatives to porous Al_2O_3 membranes. Mesoporous silicas were first used as a hard templates for preparing CMK-1 and 3D mesoporous carbon.[62] Even though the method was initially used for synthesising mesoporous carbons, it was later used for metal oxides. A range of functionalised or non-functionalised mesoporous silicas or mesoporous carbons have been employed as hard templates which include SBA-15, MCM-48, KIT-6, SBA-16, FDU-12, and CMK-3.[59] Nasir et al. prepared mesoporous silica thin films through EASA and was used as the hard template for the synthesis of Au in the form of nanowire arrays.[8] Bartlett et al. used AAO membranes as hard templates for producing Sn nanowires with feature sizes as low as 7 nm. However, the deposition of Sn nanowires in vertically aligned mesoporous silica films with 1.5 nm pores did not lead to wires that could be observed by TEM, possibly due to tin being very mobile at this scale.[63] Goux et al.[64]

demonstrated the electrodeposition of Prussian blue nanowires in porous silicas produced by EASA but found that the deposition process suffered from molecular sieving properties of the template.

The advantages of soft templates are that surfactants can be cheap; the synthesis is straightforward and easy compared to hard templates. Additionally, materials can be synthesised at relatively low temperature levels. The primary disadvantage to this approach is that products obtained from soft templates usually have amorphous or semi-crystalline walls and poor thermal stability which is similar to silica materials synthesised under similar conditions and so limiting their usage in a variety of applications.[65,59]

There are numerous advantages to the hard template approach for example, metal oxides with highly crystalline pore walls are possible using hard templates of mesoporous silicas as they prevent the material from damaging under high temperature conditions. The incorporation of lithium into mesoporous materials of transition metal oxides can significantly widen the array of mesoporous materials produced as well as providing a better outlook to potential applications. Nevertheless, the hard template approach also has its shortcomings. For instance, the stability of the mesoporous metal oxides is heavily reliant on solutions used to remove the silica template and so HF and NaOH might pose problems in this regard. Therefore mesoporous CMK-3 carbon is used as an alternative for the preparation of mesoporous ZnO, Al_2O_3 and MgO, as the porous carbon template can be removed by calcination.[59] Figure 1.11 a shows a schematic representation of SBA-15 which is used as the hard template. Whereas Figure 1.11 b and c presents MCM-48 as the template used to synthesise 3D mesoporous carbon and a network of porous platinum.

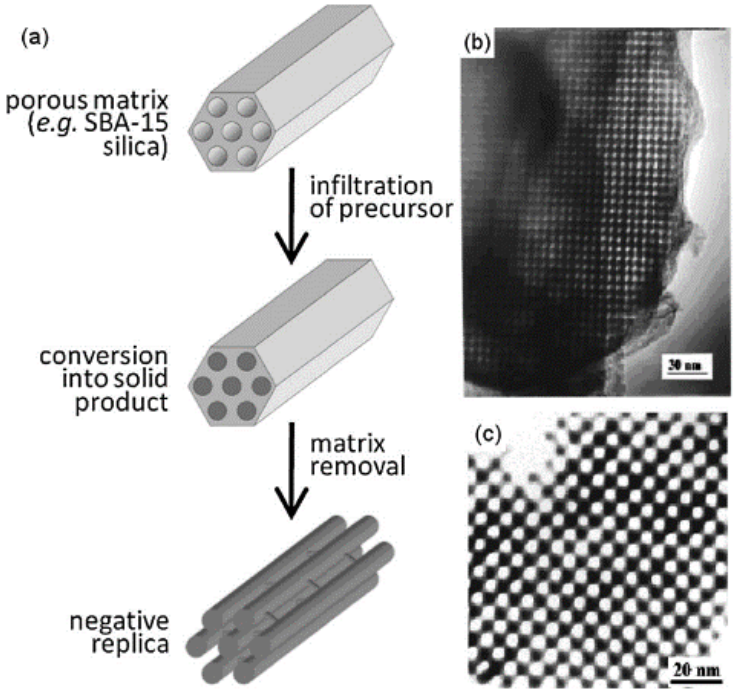

Figure 1.11 (a) A schematic of the hard templating process and top view TEM micrographs of (b) mesoporous carbon (CMK-117) and (c) a network of platinum atoms using MCM-48 as hard template.[59,66]

1.6.1 Applications of mesoporous metals and metal oxides

Mesoporous platinum films can be prepared by electrodeposition from a lyotropic liquid crystal (LLC) templating electrolyte. Attard et al.[67] used non-ionic surfactants of octaethyleneglycol monohexadecyl ether ($C_{16}EO_8$) as the template to produce metallic platinum films with well-defined network of pores. Such materials have potential as electrode materials in supercapacitors, batteries, and fuel cells. Metallic nickel films have been successfully electrodeposited in LLC medium with $C_{16}H_{33}(\text{-}OCH_2\text{-}CH_2)_{10}OH$ (Brij 56) and $HO\text{-}[C_2H_4O]_{19}\text{-}(CH_2)\text{ -}(CH_2)\text{-}O\text{-}CH_2\text{-}CH_2\text{-}[CH_2]_{15}\text{-}CH_3$ (Brij 78) as the surfactant templates. The ordered mesoporous nickel films have pore spacings between 5 and 8 nm with the surface estimated to be 100 times larger than the nonporous nickel films.[68] It is also possible to synthesise mesoporous nickel oxide (NiO) films by heat treatment of the mesoporous nickel films mentioned earlier under atmospheric conditions at a range of temperatures. The specific capacitance of 590 F g^{-1} was observed for the mesoporous NiO films after annealing at temperatures above 200 ℃ for a duration of 1.5 h.[69] Attard and co-workers[70] developed mesoporous platinum-ruthenium alloys from LLC electrolytes containing non-ionic polymeric surfactants. Electron microscopy studies showed the hexagonal array of pores with an estimated pore diameter of 37 Å. Such materials have shown potential as porous catalysts.

1.7 Aims and objectives

The electrochemically assisted surfactant assembly is a method for preparing aligned thin films with vertical mesopores. To-date, this method has not produced mesoporous silica films with pore diameters exceeding 2-3 nm. While it has been shown previously that it is possible to electrodeposit nanowires into porous silica templates,[63] the stability of very small nanowires of some materials is poor in pores with diameters below 2 nm. Hence, producing EASA films with larger vertical pores is the focus of this thesis. The aim of this thesis is therefore to expand the range of surfactants, by varying the chain length or the size of the head group and explore their application in EASA for the expansion of pore -diameters beyond the current 2-3 nm limit.

In detail, the surfactants will be modified by extending the single straight alkyl chain with a fixed trimethylammonium head group. A second approach to surfactant modification is to increase the surfactant head size whilst simultaneously increasing the alkyl chain length. Such changes to the surfactant functionality are used to produce EASA films and characterised by GISAXS, CV, EIS, TEM, SEM, and ellipsometric porosimetry to determine whether the hexagonal pore structure and vertical pore orientation are maintained whilst increasing the pore spacings, mass transport properties, and hence pore diameter. Additionally, the effect of surfactant on the electrodeposition of nickel in acidified aqueous solutions will be examined. Subsequently, the electrochemical performance of these films will be studied to determine their potential as electrodes in supercapacitors.

1.8 References

1 B. D. Zdravkov, J. J. Čermák, M. Šefara and J. Janků, Pore classification in the characterization of porous materials: A perspective, *Cent. Eur. J. Chem.*, 2007, **5**, 385–395.

2 M. Ruike, T. Kasu, N. Setoyama, T. Suzuki and K. Kaneko, Inaccessible Pore Characterization of Less-Crystalline Microporous Solids, *J. Phys. Chem*, 1994, **98**, 9594–9600.

3 J. Rouquerol, D. Avnir, C.W. Fairbridge, D.H. Everett, J.H. Haynes, N. Pernicone, J.D.F. Ramsay, K.S.W Sing and K.K. Unger, IUPAC-Recommendations For The Characterization Of Porous Solids, *Pure Appl. Chem.,* 1994, **66**, 1739–1758.

4 K. Kaneko, Determination of pore size and pore size distribution. 1. Adsorbents and catalysts, *J. Memb. Sci.*, 1994, **96**, 59–89.

5 D. H. Everett, Manual of symbols and terminology for physicochemical quantities and units, *Pure Appl. Chem.*, 1972, **31**, 577–638.

6 K.S.W. Sing, D.H. Everett, R.A.W. Haul, L. Moscou, R.A. Pierotti, J. Rouquerol and T. Siemieniewska, Reporting Physisorption Data For Gas/Solid Systems With Special Reference To The Determination Of Surface Area And Porosity, *Pure Appl. Chem.*, 1985, **57**, 603–619.

7 M. M. Dubinin, The Potential Theory Of Adsorption Of Gases And Vapors For Adsorbents With Energetically Nonuniform Surfaces, *Chem. Rev.,* 1959, **60**, 235–241.

8 T. Nasir, L. Shao, Y. Han, R. Beanland, P. N. Bartlett and A. L. Hector, Mesoporous silica films as hard templates for electrodeposition of nanostructured gold, *Nanoscale Adv.*, 2022, **4**, 4798–4808.

9 A. Sayari, I. Moudrakovski, J. S. Reddy, C. Gk, C. I. Ratcliffe, J. A. Ripmeester and K. F. Preston, Synthesis of Mesostructured Lamellar Aluminophosphates Using Supramolecular Templates, *Chem. Mater.,* 1996, **8**, 2080–2088.

10 N. Zhao, K. Cai and H. He, The synthesis of metal–organic frameworks with template strategies, *Dalt. Trans.,* 2020, **49**, 11467–11479.

11 J. Zhu, X. Meng and F. Xiao, Mesoporous zeolites as efficient catalysts for oil refining and natural gas conversion, *Chem. Sci. Eng.,* 2013, **7**, 233–248.

12 C. J. Brinker, Evaporation-induced self-assembly: Functional nanostructures made easy, *MRS Bull.*, 2004, **29**, 631–640.

13 T. Yanagisawa, T. Shimizu, K. Kuroda and C. Kato, The Preparation of Alkyltrimethylammonium-Kanemite Complexes and Their Conversion to Microporous Materials, *Bull. Chem. Soc. Jpn.,1990, **63,** 988-992*.

14 C. T. Kresge, M. E. Leonowicz, W. J. Roth, J. C. Vartuli and J. S. Beckt, Ordered mesoporous molecular sieves synthesized by a liquid- crystal template mechanism, *Nature*, 1992, **359**, 710–712.

15 A. Erigoni and U. Diaz, Porous Silica - Based Organic - Inorganic Hybrid Catalysts : A Review, *Catalysts*, 2021, **11**, 1–41.

16 A. Corma, A. Martinez, V. Martinez-Soria, and J.B. Montón, Hydrocracking of Vacuum Gasoil on the Novel Mesoporous MCM-41 Aluminosilicate Catalyst, *J. Catal.*, 1995, **153**, 25–31.

17 J. Rathousky and A. Zukal, Adsorption on MCM-41 Mesoporous Molecular Sieves, *J. Chem. Soc. Faraday Trans.,* 1994, **90**, 2821–2826.

18 J. M. Thomas, The chemistry of crystalline sponges, *Nature*, 1994, **368**, 289–290.

19 J.C. Vartuli, K.D. Schmitt, C.T. Kresge, W.J. Roth, M.E. Leonowicz, S.B. McCullen, S.D. Hellring, J.S. Beck, J.L. Schlenker, D.H. Olson and E.W. Sheppard, Effect of Surfactant / Silica Molar Ratios on the Formation of Mesoporous Molecular Sieves : Inorganic Mimicry of Surfactant Liquid-Crystal Phases and Mechanistic Implications, *Chem. Mater.*, 1994, **6**, 2317–2326.

20 J. S. Beck, J. C. Vartuli, W. J. Roth, M. E. Leonowicz, C. T. Kresge, K. D. Schmitt, C. T. W. Chu, D. H. Olson, E. W. Sheppard, S. B. McCullen, J. B. Higgins and J. L. Schlenker, A New Family of Mesoporous Molecular Sieves Prepared with Liquid Crystal Templates, *J. Am. Chem. Soc.*, 1992, **114**, 10834–10843.

21 B. A. Stein, B. J. Melde and R. C. Schroden, Hybrid Inorganic-Organic Mesoporous Silicates-Nanoscopic Reactors Coming of Age, *Adv. Mater.*, 2000, **12**, 1403–1419.

22 D. Park, N. Nishiyama, Y. Egashira and K. Ueyama, Enhancement of Hydrothermal Stability and Hydrophobicity of a Silica MCM-48 Membrane by Silylation, *Ind. Eng. Chem. Res.*, 2001, **40**, 6105–6110.

23 L. Cao, T. Man and M. Kruk, Synthesis of Ultra-Large-Pore SBA-15 Silica with Two-Dimensional Hexagonal Structure Using Triisopropylbenzene As Micelle Expander, *Chem. Mater.*, 2009, **21**, 1144–1153.

24 A.Y. Khodakov, V.L. Zholobenko, R. Bechara, and D. Durand, Impact of aqueous impregnation on the long-range ordering and mesoporous structure of cobalt containing MCM-41 and SBA-15 materials, *Microporous Mesoporous Mater.*, 2005, **79**, 29–39.

25 C. Lin, Y. Pang, M. Chao, B. Chen, H. Lin, C. Tang and C. Lin, Synthesis of SBA-16 and SBA-15 mesoporous silica crystals templated with neutral block copolymer surfactants, *J. Phys. Chem. Solids*, 2008, **69**, 415–419.

26 P. Verma, Y. Kuwahara, K. Mori, R. Raja and H. Yamashita, Functionalized mesoporous SBA-15 silica: recent trends and catalytic applications, *Nanoscale*, 2020, **12**, 11333–11363.

27 M. Ogawa, Formation of Novel Oriented Transparent Films of Layered Silica-Surfactant Nanocomposites, *J. Am. Chem. Soc*, 1994, **116**, 7941–7942.

28 Y. Yan, S. C. King, M. Li, T. Galy, M. Marszewski, J. S. Kang, L. Pilon, Y. Hu and S. H. Tolbert, Exploring the Effect of Porous Structure on Thermal Conductivity in Templated Mesoporous Silica Films, *J. Phys. Chem. C*, 2019, **123**, 21721–21730.

29 V. Malgras, Q. Ji, Y. Kamachi, T. Mori, F. K. Shieh, K. C. W. Wu, K. Ariga and Y. Yamauchi, Templated synthesis for nanoarchitectured porous materials, *Bull. Chem. Soc. Jpn.*, 2015, **88**, 1171–1200.

30 Z. Teng, G. Zheng, Y. Dou, W. Li, C. Y. Mou, X. Zhang, A. M. Asiri and D. Zhao, Highly ordered mesoporous silica films with perpendicular mesochannels by a simple stöber-solution growth approach, *Angew. Chemie - Int. Ed.*, 2012, **51**, 2173–2177.

31 M. A. Pizzoccaro-Zilamy, C. Huiskes, E. G. Keim, S. N. Sluijter, H. Van Veen, A. Nijmeijer, L. Winnubst and M. W. J. Luiten-Olieman, New Generation of Mesoporous Silica Membranes Prepared by a Stöber-Solution Pore-Growth Approach, *ACS Appl. Mater. Interfaces*, 2019, **11**, 18528–18539.

32 Y. Yamauchi, Field-Induced alignment controls of one-dimensional mesochannels in mesoporous materials, J. Ceram. Soc. Japan., 2013, **121**, 831-840.

33 E. K. Richman, T. Brezesinski and S. H. Tolbert, Vertically oriented hexagonal mesoporous films formed through nanometre-scale epitaxy, *Nat. Mater.*, 2008, **7**, 712–717.

34 J. Otomo, S. Wang, H. Takahashi and H. Nagamoto, Microstructure development of mesoporous silica thin films with pore channels aligned perpendicularly to electrode surfaces and application to proton conducting composite electrolyte membranes, *J. Memb. Sci.*, 2006, **279**, 256–265.

35 A. Walcarius, E. Sibottier, M. Etienne and J. Ghanbaja, Electrochemically assisted self-assembly of mesoporous silica thin films, *Nat. Mater.*, 2007, **6**, 602–608.

36 A. Goux, M. Etienne, E. Aubert, C. Lecomte, J. Ghanbaja and A. Walcarius, Oriented mesoporous silica films obtained by electro-assisted self-assembly (EASA), *Chem. Mater.*, 2009, **21**, 731–741.

37 J. Cheng, S.J. Rathi, P. Stradins, G.L. Frey, R.T. Collins, and S.K.R. Williams, Free Standing Silica Thin Films with Highly Ordered Perpendicular Nanopores, *RSC Adv.*, 2014, **4**, 7627–7633.

38 A. Walcarius, Mesoporous Materials-Based Electrochemical Sensors, *Electroanalysis*, 2015, **27**, 1303–1340.

39 N. Hao, X. Chen, K. W. Jayawardana, B.Wu, M. Sundhoro, and M. Yan, Shape Control of Mesoporous Silica Nanomaterials Templated with Dual Cationic Surfactants and Their Antibacterial Activities, *Biomater Sci.*, 2015, **4**, 87–91.

40 P. T. Tanev and T. J. Pinnavaia, A neutral templating route to mesoporous molecular sieves, Amer. Assoc. Adv. Sci., 1995, **267**, 865–867.

41 L. Mercier and T. J. Pinnavaia, Direct synthesis of hybrid organic-inorganic nanoporous silica by a neutral amine assembly route: Structure-function control by stoichiometric incorporation of organosiloxane molecules, *Chem. Mater.*, 2000, **12**, 188–196.

42 C. Ma, L. Han, Z. Jiang, Z. Huang, J. Feng, Y. Yao and S. Che, Growth of mesoporous silica film with vertical channels on substrate using gemini surfactants, *Chem. Mater.*, 2011, **23**, 3583–3586.

43 N. Vilà, E. André, R. Ciganda, J. Ruiz, D. Astruc and A. Walcarius, Molecular Sieving with Vertically Aligned Mesoporous Silica Films and Electronic Wiring through Isolating Nanochannels, *Chem. Mater.*, 2016, **28**, 2511–2514.

44 C. Robertson, R. Beanland, S. A. Boden, A. L. Hector, R. J. Kashtiban, J. Sloan, D. C. Smith and A. Walcarius, Ordered mesoporous silica films with pores oriented perpendicular to a titanium nitride substrate, *Phys. Chem. Chem. Phys.*, 2015, **17**, 4763–4770.

45 K. Ghosh, H. J. Lehmler, S. E. Rankin and B. L. Knutson, Supercritical carbon dioxide swelling of fluorinated and hydrocarbon surfactant templates in mesoporous silica thin films, *J. Colloid Interface Sci.*, 2012, **367**, 183–192.

46 D. R. Dunphy, P. H. Sheth, F. L. Garcia and C. Je, Enlarged Pore Size in Mesoporous Silica Films Templated by Pluronic F127: Use of Poloxamer Mixtures and Increased Template/SiO2 Ratios in Materials Synthesized by Evaporation-Induced Self-Assembly, *Chem. Mater*, 2015, **27**, 75–84.

47 S. Vavra, N. Vilà, A. Lotsari, A. Walcarius and A. Martinelli, An imidazolium ionic liquid as effective structure-directing agent for the fabrication of silica thin films with vertically aligned nanochannels, *Microporous Mesoporous Mater.*, 2020, 1-9.

48 S. Namba and A. Mochizuki, Effect of auxiliary chemicals on preparation of silica MCM-41, *Res. Chem. Intermed.*, 1998, **24**, 561–570.

49 Y. Guillemin, J. Ghanbaja, E. Aubert, M. Etienne and A. Walcarius, Electro-assisted self-assembly of cetyltrimethylammonium-templated silica films in aqueous media: Critical effect of counteranions on the morphology and mesostructure type, *Chem. Mater.*, 2014, **26**, 1848–1858.

50 A. Vinu, K. Hossain, and K. Ariga, Recent Advances in Functionalization of Mesoporous Silica., *J. Nanosci. Nanotechnol.*, 2005, **5**, 347–371.

51 S. Bhattacharyya, G. Lelong and M. L. Saboungi, Recent progress in the synthesis and selected applications of MCM-41: A short review, *J. Exp. Nanosci.*, 2006, **1**, 375–395.

52 A. Dioum and S. Hamoudi, Mono- and quaternary-ammonium functionalized mesoporous silica materials for nitrate adsorptive removal from water and wastewaters, *J. Porous Mater.*, 2014, **21**, 685–690.

53 N. Vilà and A. Walcarius, Electrochemical response of vertically-aligned, ferrocene-functionalized mesoporous silica films: Effect of the supporting electrolyte, *Electrochim. Acta*, 2015, **179**, 304–314.

54 M. Fukuda, N. Tsunoji, Y. Yagenji, Y. Ide, S. Hayakawa, M. Sadakane and T. Sano, Highly actIVe and selectIVe Ti-incorporated porous silica catalysts derIVed from grafting of titanium(IV)acetylacetonate, *J. Mater. Chem. A*, 2015, **3**, 15280–15291.

55 G. Castruita-De León, Y. A. Perera-Mercado, L. A. García-Cerda, J. A. Mercado-Silva, H. I. Meléndez-Ortiz, Y. Olivares-Maldonado and L. Alvarez-Contreras, Synthesis of amino-functionalized MCM-48 silica via direct co-condensation at room temperature, *Microporous Mesoporous Mater.*, 2015, **204**, 156–162.

56 Y. Guillemin, M. Etienne, E. Aubert and A. Walcarius, Electrogeneration of highly methylated mesoporous silica thin films with vertically-aligned mesochannels and electrochemical monitoring of mass transport issues, *J. Mater. Chem.*, 2010, **20**, 6799–6807.

57 D.M. Antonelli and J.Y. Ying, Synthesis of Hexagonally Packed Mesopores TiO_2 by a Modified Sol-Gel Method, *Angew. Chemie Int. Ed. English*, 1995, **34**, 2014–2017.

58 J.Y. Ying, C.P. Mehnert, and M.S. Wong, Synthesis and Applications of Supramolecular-Templated Mesoporous Materials., *Angew. Chemie - Int. Ed.*, 1999, **38**, 56–77.

59 Y. Ren, Z. Ma and P. G. Bruce, Ordered mesoporous metal oxides: Synthesis and applications, *Chem. Soc. Rev.*, 2012, **41**, 4909–4927.

60 P. Yang, D. Zhao, D.I. Margolese, B.F. Chmelka and G.D. Stucky, Generalized syntheses of large-pore mesoporous metal oxides with semicrystalline frameworks, *Nature*, 1998, **396**, 6–9.

61 M. E. Martin, R. M. Narske and K. J. Klabunde, Mesoporous metal oxides formed by aggregation of nanocrystals. Behavior of aluminum oxide and mixtures with magnesium oxide in destructive adsorption of the chemical warfare surrogate 2-chloroethylethyl sulfide, *Microporous Mesoporous Mater.*, 2005, **83**, 47–50.

62 R. Ryoo, S. H. Joo and S. Jun, Synthesis of highly ordered carbon molecular sieves via template-mediated structural transformation, *J. Phys. Chem. B*, 1999, **103**, 7743–7746.

63 P. N. Bartlett, R. Beanland, J. Burt, M. M. Hasan, A. L. Hector, R. J. Kashtiban, W. Levason, A. W. Lodge, S. Marks, J. Naik, A. Rind, G. Reid, P. W. Richardson, J. Sloan and D. C. Smith, Exploration of the Smallest Diameter Tin Nanowires Achievable with Electrodeposition: Sub 7 nm Sn Nanowires Produced by Electrodeposition from a Supercritical Fluid, *Nano Lett.*, 2018, **18**, 941–947.

64 A. Goux, J. Ghanbaja and A. Walcarius, Prussian Blue electrodeposition within an oriented mesoporous silica film: Preliminary observations, *J. Mater. Sci.*, 2009, **44**, 6601–6607.

65 F. Jiao, A. Harrison, J. Jumas, A. V Chadwick, W. Kockelmann and P. G. Bruce, Ordered mesoporous Fe_2O_3 with crystalline walls, *J. Am. Chem. Soc*, 2006 128, **16,** 5468–5474.

66 H. J. Shin, R. Ryoo, Z. Liu and O. Terasaki, Template synthesis of asymmetrically mesostructured platinum networks, *J. Am. Chem. Soc.*, 2001, **123**, 1246–1247.

67 G. S. Attard, P. N. Bartlett, N. R. B. Coleman, J. M. Elliott, J. R. Owen and J. H. Wang, Mesoporous Platinum Films from Lyotropic Liquid Crystalline Phases, Amer. Assoc. Adv. Sci., 1997, **278**, 838–840.

68 P. A. Nelson, J. M. Elliott, G. S. Attard and J. R. Owen, Mesoporous nickel/nickel oxide - A nanoarchitectured electrode, *Chem. Mater.*, 2002, **14**, 524–529.

69 D. D. Zhao, M. W. Xu, W. J. Zhou, J. Zhang and H. L. Li, Preparation of ordered mesoporous nickel oxide film electrodes via lyotropic liquid crystal templated electrodeposition route, *Electrochim. Acta*, 2008, **53**, 2699–2705.

70 G. S. Attard, S. A. A. Leclerc, S. Maniguet, A. E. Russell, I. Nandhakumar and P. N. Bartlett, Mesoporous Pt/Ru alloy from the hexagonal lyotropic liquid crystalline phase of a nonionic surfactant, *Chem. Mater.*, 2001, **13**, 1444–1446.

Chapter 2 Experimental methods

This chapter reviews the basic principles of a variety of instrumentation used in this thesis. It begins with details on materials characterisation methods to determine the content of surfactants, pore orientation and structure, surface topography and composition of mesoporous silica films using NMR, mass spectrometry in the positive ion electrospray ionization mode, GISAXS, scanning electron microscopy (SEM) and TEM. Furthermore, this chapter describes the gas adsorption methods for quantifying pore size distributions of a range of mesoporous silica films. Finally, this chapter concludes with a discussion of electrochemical techniques used for pore accessibility measurements of a range of silica films using cyclic voltammetry (CV) and electrochemical impedance spectroscopy (EIS).

2.1 Nuclear magnetic resonance spectroscopy and mass spectrometry

In this study, ^{1}H and $^{13}C\{^{1}H\}$ NMR data for the surfactants in D-chloroform and D-methanol were collected with a Bruker AVII400 spectrometer at 25 °C. Solutions for mass spectrometry were prepared by dissolving 50 μg of the surfactant in 1 ml of methanol. The surfactants were analyzed using ultrahigh performance liquid chromatography (UHPLC) system coupled to a TQD mass tandem quadrupole mass spectrometer (Waters) with a TUV detector at 254 nm. The chromatography analysis was carried out on a Waters BEH C18 column (50 mm x 2.1 mm, 1.7 μm) with a flow rate of 0.6 ml/min. The mobile phase was made up of 0.2 % formic acid in an aqueous solution and 0.2 % formic acid in acetonitrile. This was followed by the recording of the mass spectrum in the positive ion electrospray ionisation mode.

2.2 X-ray diffraction

In X-ray diffraction, we have an X-ray tube, a sample holder, and an X-ray detector (Fig.2.1). The source emits monochromatic X-rays towards the sample then, the X-rays are scattered by electrons in the atoms within the sample which is then recorded and processed by the detector. Copper and molybdenum are the most normally used target materials which have X-ray wavelengths of 154.18 pm and 71.07 pm respectively. Interference between the scattered X-rays can be constructive in certain directions, where the difference in path length between scattered X-rays by different crystal lattice planes equates to an integral number of wavelengths, and this phenomenon is referred to as diffraction. This is described by Braggs law (shown in equation (Eq.) 2.1) where λ is the X-ray wavelength, n is an integer, d is the real space dimension between the

planes of atoms in a known object and θ is the angle between the planes of atoms and incident X-rays.[1]

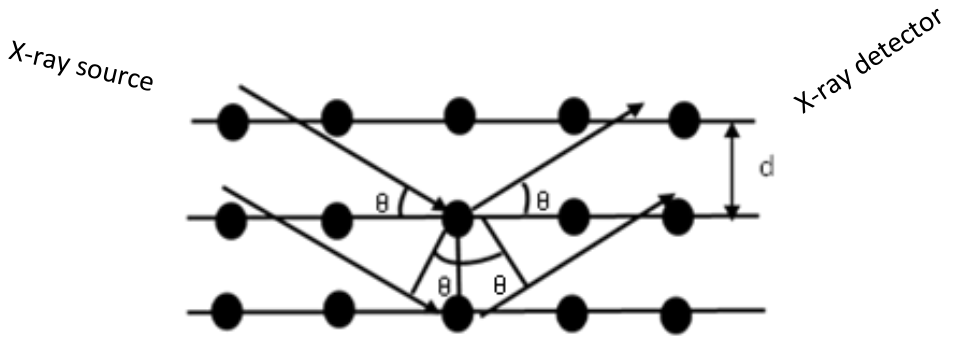

Figure 2.1 A schematic of a 2D lattice structure with grid lines representing sets of planes. In phase diffraction is produced when X-radiation falls onto the sample at an angle defined by the Bragg equation (Eq. 2.1).

$$2d \sin \theta = n\lambda \qquad \text{Eq. 2.1}$$

2.2.1 Small angle X-ray scattering

SAXS is a technique whereby X-rays are elastically scattered by the sample at very low angles, most often between 0.1-10°. SAXS provides information on ordered and non-ordered systems including pore size distributions and nanosized objects generally in the range of 0.5 and 100 nm.[2] For ordered assemblies, Braggs reflection is seen just like with X-ray diffraction, but with larger d-spacings and hence smaller diffraction angles. However, non-ordered systems still have features associated with shorter-range correlations that can also be used to gain structural understanding. Palaniappan et al.[3] demonstrated the synthesis of mesoporous silica films using sol gel chemistry together with a calcination technique involving argon plasma. It was understood that upon elimination of CTAB from the pores, mesoporous silica was obtained, then analysed by SAXS confirming the disorganised porous structure.

2.2.2 Grazing-incidence small-angle X-ray scattering

Grazing-incidence small-angle X-ray scattering (GISAXS) is a technique whereby the scattering of X-rays by electrons within a sample surface is used to quantify interfaces of micro- and nano-structured systems, thin films, and coatings, amongst others. This research study has shown that GISAXS is a useful technique for the determination of pore orientation and structure of ordered mesoporous silica films. The in-plane and out-of-plane modes relay important information on the mesopore direction of ordered systems. The combination of instrumentation of GISAXS and TEM provides further clarity on structure by relating 2D GISAXS and TEM images, providing detailed observations on porous networks, Laue group and any variations to the mesophase, for example pore disorder. The GISAXS experimental geometry is shown in Fig.2.2, where an incident beam penetrates the sample surface at a small angle α and the beam scattered by the sample is recorded with built in 2D detector with respect to the exit angle a_f and the scattering angle φ. The scattering path is denoted as q_z and q_y and the incident beam angle is close to the critical angle of the substrate, the angle responsible for the total external reflection of X-rays.[4] GISAXS can also provide parameters of pore spacing a_o (Eq. 2.2) which is directly linked to d-spacing.

$$a_0 = d_{10}/\cos 30 \qquad \text{Eq. 2.2}$$

In this research study, a Rigaku Smartlab X-ray diffractometer with a Hypix-3000 2D detector was used for GISAXS experiments. The incidence angle for all silica and nickel samples were 0.25° and 0.4° with measurements collected as 2D images or as 1D scans collected in-plane with 0.5° incident and 0.228° exit Soller slits and an angle range of 1-10° and 20-100° 2θ.

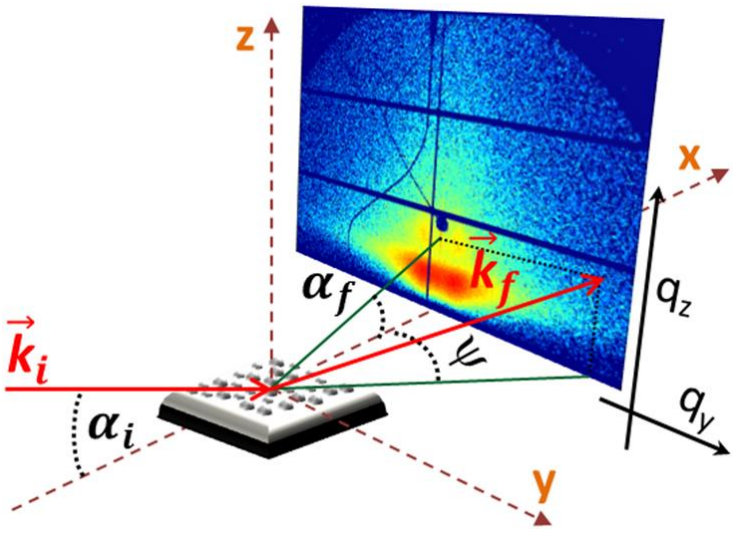

Figure 2.2 A schematic diagram of a GISAXS experimental set up consisting of an incident beam angle (αi), exit (α_f), and scattering angles (Ψ) with the scattering path denoted as q_z and q_y.[4]

2.3 Scanning electron microscopy

Scanning electron microscopy (SEM) works by generating monochromatic electrons of high energy at potentials ranging from 1 to 40 kV. A beam of these electrons is rastered across the sample surface as shown in Fig. 2.3. The kinetic energy of the beam creates ionized electrons within the sample, producing a range of signals of secondary electrons, photons, and electromagnetic waves e.g., visible light. The detector gathers the electrons and provides information that is processed by the computer to produce an image. The electrons required for the creation of a sample image are backscattered and secondary electrons. The secondary electrons are important for the determination of the sample topography, while backscattered electrons display contrasts in the sample composition. The interaction between the primary electrons and the specimen within a three-dimensional zone is referred to as the interaction volume. Unlike TEM, large and thick silica samples can be investigated using SEM.[5]

Scanning electron microscopy (SEM) used in this thesis was a Jeol JSM-6500F, JSM-7200F and Zeiss Sigma 500 with a field emission gun and built in energy dispersive X-ray spectrometer (EDX) operating at an accelerating voltage of 5 kV. The samples used were non-conducting porous silica films. The SEM images were often distorted by charging, the build up of static charge density on the sample surface. To overcome charging, the porous silica films were coated with a thin layer of gold to improve the conductivity of the material before obtaining top view and cross-sectional scanning electron micrographs.

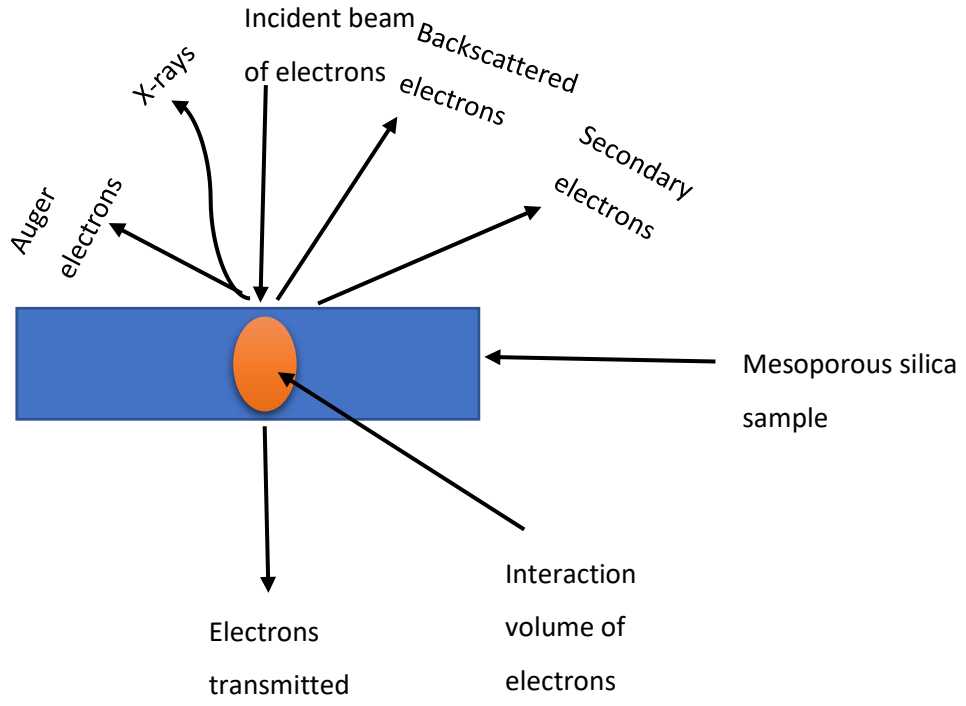

Figure 2.3 Electrons released from the sample surface when high energy electrons from the SEM hit the sample.

2.4 Transmission electron microscopy

TEM is based on the emission of electrons from an electron gun, the electrons are typically accelerated at a voltage range of 60-300 keV. The resolution is about 1 Å due to the position from the optical lens centre, also referred to a spherical aberration. In the past twenty years, the development of the spherical aberration has seen significant improvements in the TEM resolution.[6] TEM requires a high quality vacuum (usually $< 10^{-5}$ mbar) to alleviate the scattering of electrons in all directions. The electrons are then focussed using the magnetic lenses which allows the electrons to be directed towards the sample surface which in turn is detected electronically using a detector as presented in Fig. 2.4. The sample thickness is required to be very thin at the nanometre regime therefore, making it easier for electrons to interact with the sample surface.[7,8]

Scanning transmission electron microscopy (STEM) micrographs of the mesoporous silica films used in this thesis were recorded by Yisong Han (University of Warwick), using a JEOL ARM200f double-corrected TEM performed at 200 kV. STEM is different from TEM, as in STEM the focused electron beam is scanned on specific points on the sample, whereas in TEM a parallel electron beam is focused over large areas of the sample.[6] TEM samples were prepared by removing a flake of silica from the film with a scalpel and attaching it on a TEM grid.

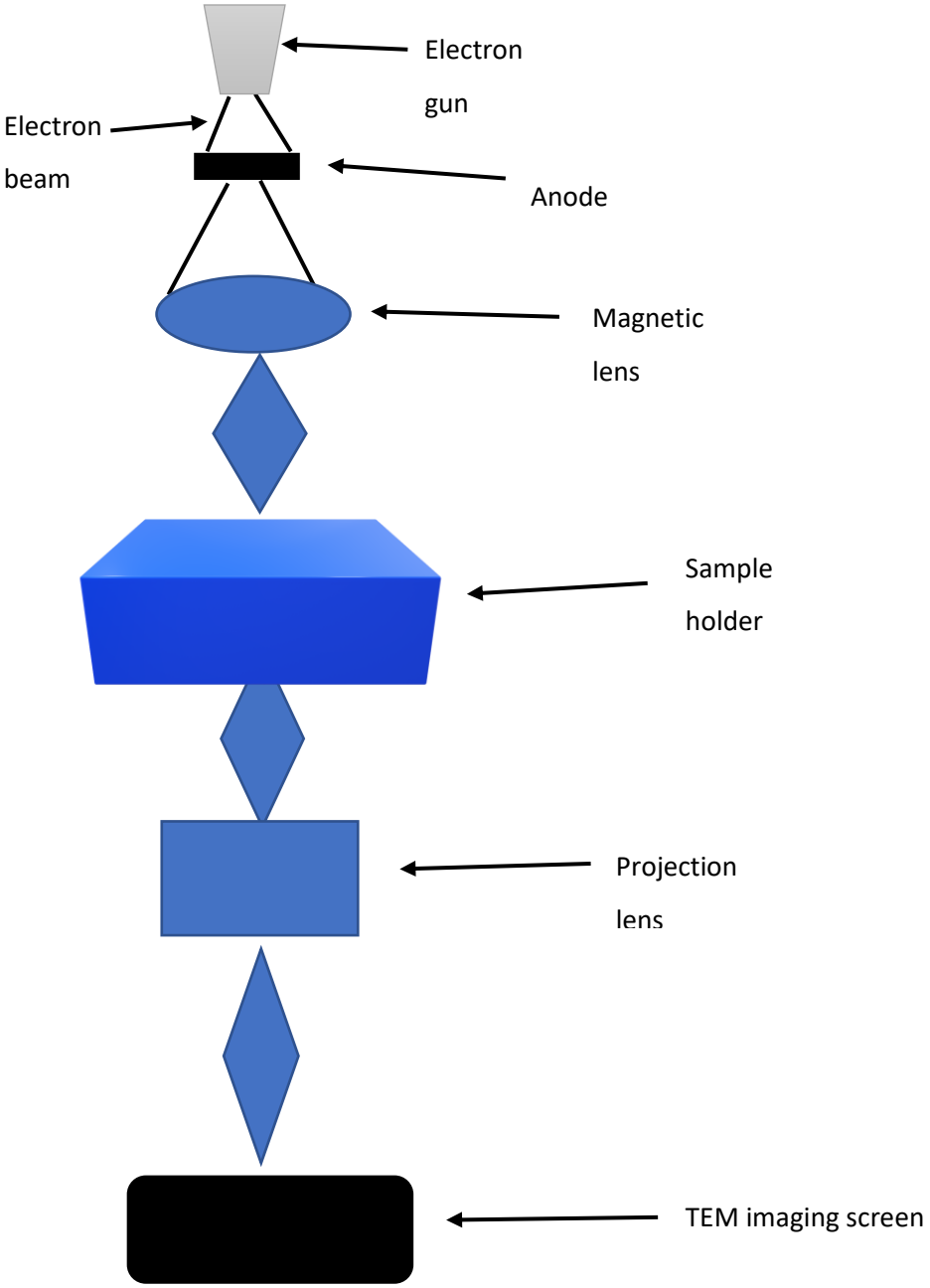

Figure 2.4 A schematic of the principles of TEM.

2.5 N_2 sorption analysis

Porous materials can also be classified based on their adsorption properties. The adsorption of gases inside porous materials is expressed by an adsorption isotherm, whereby the amount of gas adsorbed is measured at constant temperature as a function of partial pressure. There are six different types of isotherms described by IUPAC[9] which relate to pore structures of different shapes and sizes (shown in Fig 2.5). Microporous materials typically generate type I isotherms. These examples include zeolites with molecular sieving properties, porous oxides, and carbons. In type I, a large amount of gas fills the micropore region at lower partial pressure (p/p^o). Type II

isotherms relate to nonporous or microporous materials. Type III plots associate with microporous materials and type IV and V sorption plots show information on materials characteristics of silicas, carbons, and alumina. It is to be noted that a hysteresis loop is observed owing to condensation in the pores and formation of a meniscus which means that the liquid is more difficult to evaporate hence, it is removed at lower partial pressure than when it condensed. The stepwise plot for type VI isotherm constitutes to several adsorption layers for materials of carbon black and graphitic samples. In the isotherms of type II and IV (shown in Fig 2.5), the point B signifies the completion of monolayer coverage and the initiation of multilayer adsorption.[10]

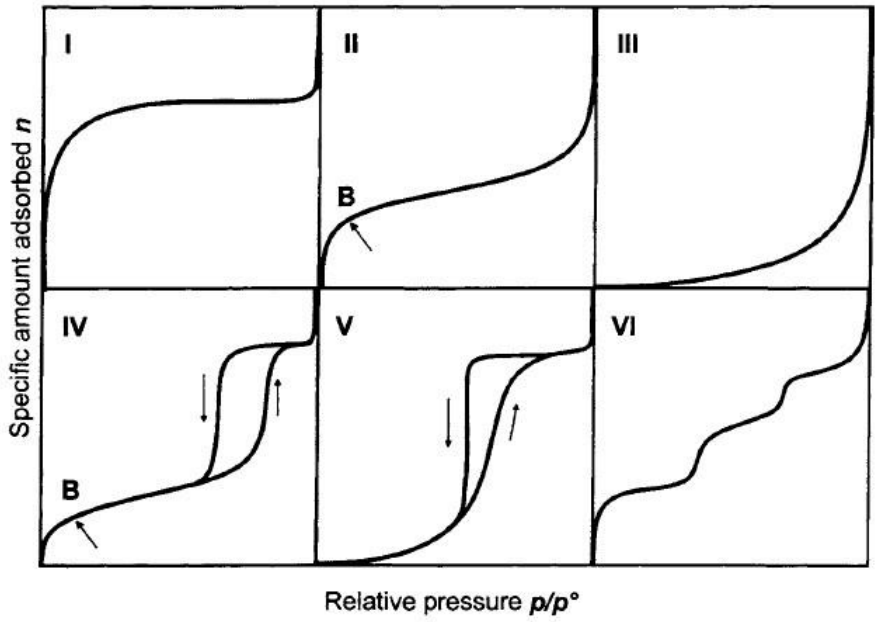

Figure 2.5 A categorisation of adsorption isotherms according to IUPAC with hysteresis loops in type IV and V isotherms.[11]

Hysteresis loops were initially classified according to De Boer[12] and later revised by IUPAC. Fig. 2.6 shows the hysteresis classification based on IUPAC, type H1 is most often seen for porous materials with cylindrical pores or clusters of homogeneous spheres. Type H2 is attributed to disordered porous materials and when the shape and size of pores are not well defined. H3 hysteresis is ascribed to pores having slit shaped features, while type H4 hysteresis loops are accredited to porous systems with tapered pores.[10] The hysteresis loop of H5 has a characteristic form which is related to mesopore structures with a combination of open and partially closed pores. A common example of this phenomenon is noticed in hexagonally ordered templated mesoporous silicas.[13]

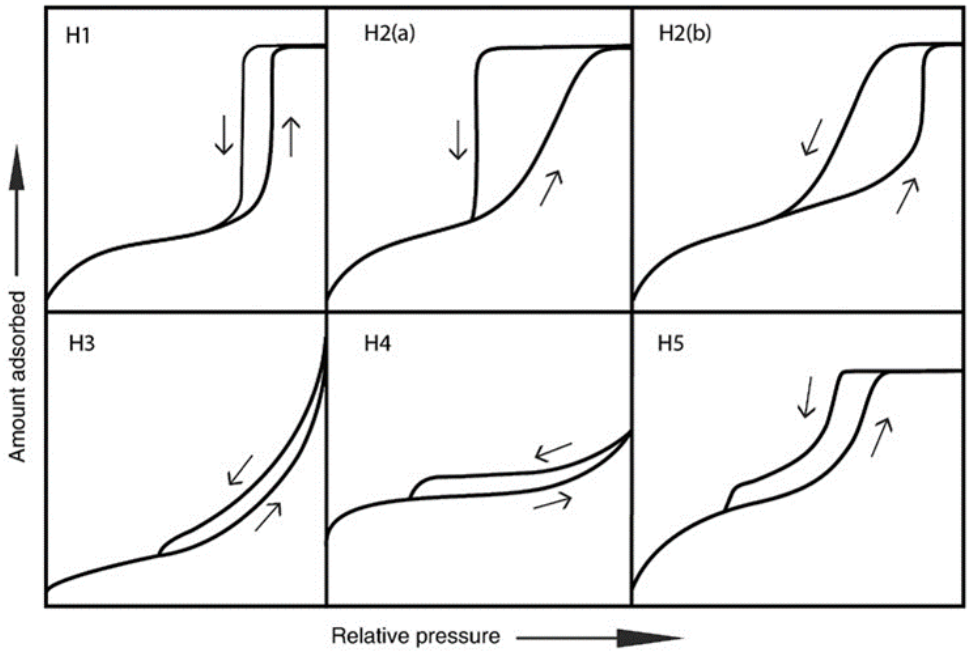

Figure 2.6 The correlation between pore size and shape and adsorption isotherm.[13]

The Kelvin equation (Eq. 2.3) describes the filling of pores through multilayer adsorption from the nitrogen gas phase where, γ is the surface tension, V_1 is the molar volume, p/p^o is the comparative pressure and r_m is the measured radius of droplets.[14] However, the method produced by BJH in 1951 is still applied today for the calculation of pore size distribution from a suitable nitrogen sorption isotherm.[15]

$$\ln (p/p_o) = \gamma V1/rmRT \qquad \text{Eq. 2.3}$$

2.5.1 Ellipsometric porosimetry

Ellipsometric porosimetry (EP) measures the variance in polarisation as radiation is emitted from the sample and is very good for characterising sample surfaces and thin films. This technique has the capacity to measure pore size distributions to the nanometre scale and does not need sample preparation or scratching of the sample surface. It is also capable of measuring multilayer thin films with different compositions with consistency. The EP technique is utilised by monitoring the optical properties of the porous system during capillary condensation to determine the amount of solvent condensed or adsorbed in the pore channels. The technique consists of an organic solvent (e.g., toluene) and a vacuum pump. Before carrying out the experiment the vacuum system is cleaned of any residue before the organic adsorptive can enter the system. The porous materials

are usually heated to very high temperatures to remove water from the pores. Once the gaseous solvent vapours enter the vacuum, this provides a means to the study of pore size distribution.[16]

A Dynamic Vapour Sorption instrument together with a FS-1 multi-wavelength ellipsometer (Film Sense, USA) was used to acquire EP data. The measurements were performed in an environmental chamber at constant conditions of ambient temperature, at atmospheric pressure and a partial pressure range of 0-95 % P/P_o. A mass flow controller and a sound sensor were used to sustain and observe the partial pressure throughout experimental analysis. The experiments were performed at an incidence angle of 65 ° using four wavelengths of 465, 525, 595 and 635 nm to generate high signals in the detector. Changes in refractive index values were measured continuously during the experiment, which allowed for the volume of toluene present within the pore surface to be calculated using the Lorentz-Lorenz effective medium approximation.[16]

2.5.2 Cyclic voltammetry

In cyclic voltammetry (CV), the potential at the working electrode is ramped at a constant rate from one value to another while the current is measured, then the direction of the potential is ramped back to the original value. The current or current density is plotted vs. applied potential. CV was used to determine the accessibility of the pores in the mesoporous silica films on ITO electrodes using a range of redox probes. The aqueous probe solution was made up of 0.5 mmol dm^{-3} ferrocenemethanol, $C_{11}H_{12}FeO$ (FcMeOH), 5 mmol dm^{-3} ($[Ru(NH_3)_6]Cl_3$), or 0.5 mmol dm^{-3} each of ($K_3[Fe(CN)_6]$) and ($K_4[Fe(CN)_6]\cdot 3H_2O$), in all cases with 0.1 mol dm^{-3} $NaNO_3$ supporting electrolyte. The advantage of neutral transition metal ions is it's ability to diffuse through the anionic silica surface without the probes experiencing electrostatic interactions with the silanol groups connected to the pore walls. However, positively charged transition metal ions demonstrate an accumulation effect due to electrostatic interactions with the silica surface. This is observed through changes in the current from CVs.[17] The $NaNO_3$ supporting electrolyte was used to improve the conductivity in solution, whereas water provides an accessible potential window from -1 V to 1 V in order to undergo electrochemical measurements. The working electrode was the ITO coated with mesoporous silica, a platinum gauze was used as the counter electrode and the reference electrode contained Ag/AgCl in 4 mol dm^{-3} KCl solution. The potentiostat used was a Biologic SP150.

2.5.3 Electrochemical impedance spectroscopy

An electrochemical cell is used to generate an electrical current from reactions involving redox species, which is influenced by the concentration of redox active species, charge transfer and mass transfer from the electrolyte towards the electrode, as well electrolyte resistance.

Therefore, EIS is useful in the investigation of diffusion processes, charge transfer and mass transfer. The impedance is different from resistance, as it does not directly follow Ohm's law, but is involved in multiplex electrical systems. The impedance of a particular system follows Eq. 2.4, where Z is the impedance, E is the voltage, I is the current, ω is the frequency, and ϕ is the phase shift. The terms of magnitude (Z_o) and ϕ are used to represent impedance.[18]

$$Z = E/I = Z_o \exp(i\phi) = Z_o (\cos\phi + i\sin\phi) \qquad \text{Eq. 2.4}$$

The EIS plot of imaginary part (Zimag) as a function of real part (Zreal), a "Nyquist graph" is produced. On the x-axis, low frequency impedance is seen at the right side of the graph, while the left side comprises of the high frequency region.

By applying a negative potential to a conductive electrode and monitoring the current, it is possible to measure the impedance. An EIS experiment was first reported in 1975 where the variation in sinusoidal potential and current was recorded. The Nyquist graphs (shown in Fig 2.7) display information on an electrochemical process related to the reversible transfer of electrons at the solution-electrode interface and is simulated using a simple Randles equivalent circuit where R_s, R_{ct}, C_{dl} and Z_w are the electrolyte resistance, charge transfer resistance, double layer capacitance and Warburg impedance. The diffusional processes that take place at the solution-electrode interface is defined by the Warburg impedance which can be obtained from the sloped line at 45 °. The Nyquist graph is highly reliant on the working electrode component and the electrochemical signal from the electrodes surface or in the electrolyte. Therefore, a range of Nyquist graphs could be produced, for instance, one semicircle, two semicircles or a half × 2 semi circles are possible for certain electrochemical systems.[18]

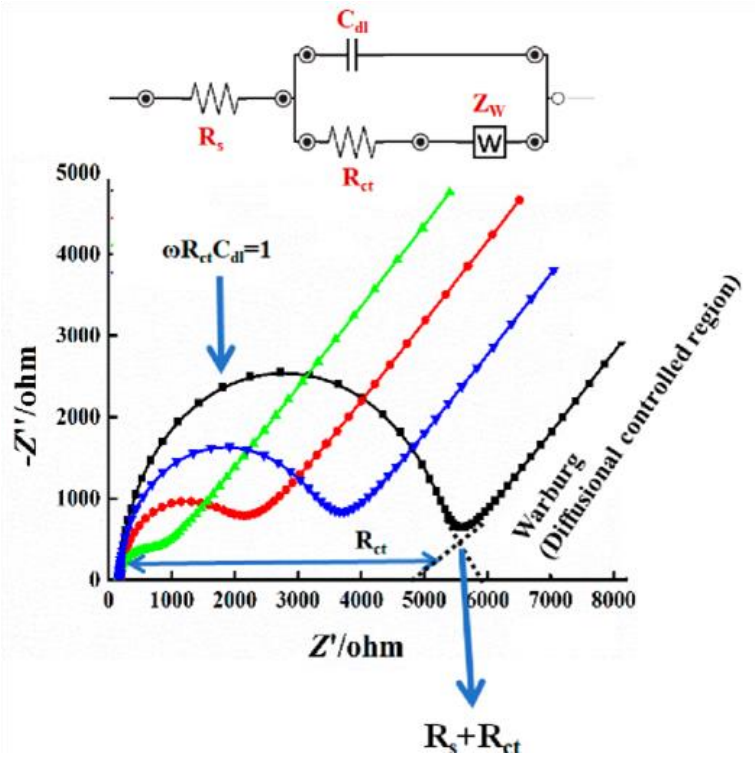

Figure 2.7 A typical Nyquist plot of both experimental and simulated data for an electrochemical system. A simple Randle's equivalent circuit was used to obtain R_s, R_{ct} and W from the x-axis which represents Z_{real}. An AC potential of 5 mV was used with an applied frequency range of 10,000 to 0.1 Hz using 1 mmol dm^{-3} ($K_3[Fe(CN)_6]$) as the redox active species.[18] An increase in R_{ct} is noticed from green to black Nyquist plots.

In this thesis, EIS data for the films with $[C_{18}H_{37}NMe_{3\text{-}3}Et_0]Br$, C_{18}TAB and $[C_{18}H_{37}NMe_{3\text{-}2}Et_1]Br$, C_{18}DMEAB were recorded with a frequency range from 250 kHz to 100 mHz whereas EIS data for the films with $[C_{18}H_{37}NMe_{3\text{-}1}Et_2]Br$, C_{18}DEMAB and $[C_{18}H_{37}NMe_{3\text{-}0}Et_3]Br$, C_{18}TEAB were recorded with a frequency range from 500 kHz to 100 mHz. A perturbation amplitude of 10 mV was applied in both cases, using an aqueous solution of 0.5 mmol dm^{-3} ($K_3[Fe(CN)_6]$) with 0.1 mol dm^{-3} $NaNO_3$ as the supporting electrolyte. The working electrode was a silica/ITO coated film, the counter electrode was a platinum gauze, and the reference was Ag/AgCl in 4 mol dm^{-3} KCl solution.

2.6 References

1 A. A. Bunaciu, E. G. Udriştioiu and H. Y. Aboul-Enein, X-Ray Diffraction: Instrumentation and Applications, *Crit. Rev. Anal. Chem.*, 2015, **45**, 289–299.

2 J. Feng, M. Kriechbaum and L. E. Liu, In situ capabilities of Small Angle X-ray Scattering, *Nanotechnol. Rev.*, 2019, **8**, 352–369.

3 A. Palaniappan, J. Zhang, X. Su and F. E. H. Tay, Preparation of mesoporous silica films using sol-gel process and argon plasma treatment, *Chem. Phys. Lett.*, 2004, **395**, 70–74.

4 G. Santoro and S. Yu, *Grazing Incidence Small Angle X-Ray Scattering as a Tool for In- Situ Time-Resolved Studies*, IntechOpen, 2017, 30-60.

5 K. Akhtar, S. A. Khan, S. B. Khan, and A. M. Asiri, *Scanning Electron Microscopy: Principle and Applications in Nanomaterials Characterization*, 2018, 113-147.

6 X. Zhou and G. E. Thompson, *Electron and Photon Based Spatially Resolved Techniques*, Elsevier Ltd., 2017.

7 T. Kogure, *Electron Microscopy*, Elsevier Ltd., 2nd edn., 2013, vol. 5.

8 V. Stolojan, *Nanometrology Using the Transmission Electron Microscope*, Morgan & Claypool publishers, IOP Concis., 2015.

9 M. D. Donohue and G. L. Aranovich, Classification of Gibbs adsorption isotherms, *Adv. Colloid Interface Sci.*, 1998, **76**, 137–152.

10 Z. A. Alothman, A review: Fundamental Aspects of Silicate Mesoporous Materials, *Materials (Basel).*, 2012, **5**, 2874–2902.

11 M. Alhamami, H. Doan and C. H. Cheng, A review on breathing behaviors of metal-organic-frameworks (MOFs) for gas adsorption, *Materials (Basel).*, 2014, **7**, 3198–3250.

12 K. S. W. Sing and R. T. Williams, Physisorption hysteresis loops and the characterization of nanoporous materials, *Adsorpt. Sci. Technol.*, 2004, **22**, 773–782.

13 M. Thommes, K. Kaneko, A. V. Neimark, J. P. Olivier, F. Rodriguez-Reinoso, J. Rouquerol and K. S. W. Sing, Physisorption of gases, with special reference to the evaluation of surface area and pore size distribution (IUPAC Technical Report), *Pure Appl. Chem.*, 2015, **87**, 1051–1069.

14 P. Löbmann, Characterization of sol – gel thin films by ellipsometric porosimetry, *J Sol-Gel Sci Technol*, 2017, **84**, 2–15.

15 K. Sing, The use of nitrogen adsorption for the characterisation of porous materials, *Colloids Surfaces A Physicochem. Eng. Asp.*, 2001, **188**, 3–9.

16 M. R. Baklanov, K. P. Mogilnikov, V. G. Polovinkin and F. N. Dultsev, Determination of pore size distribution in thin films by ellipsometric porosimetry, *J. Vac. Sci. Technol. B Microelectron. Nanom. Struct.*, 2000, **18**, 1385.

17 A. Walcarius, Mesoporous materials and electrochemistry, *Chem. Soc. Rev.*, 2013, **42**, 4098–4140.

18 H. S. Magar, R. Y. A. Hassan and A. Mulchandani, Electrochemical Impedance Spectroscopy (EIS): Principles, Construction, and Biosensing Applications, *Sensors*, 2021, **21**, 1–21.

Chapter 3 Increasing the diameter of vertically aligned, hexagonally ordered pores in mesoporous silica films

This chapter focuses on the variation in pore size in mesoporous silica films produced by electrochemically assisted surfactant assembly (EASA) as a function of surfactant chain length. The cationic surfactants of C_{20}TAB, C_{22}TAB and C_{24}TAB were synthesised by reaction of the appropriate alkyl bromide and trimethylamine under reflux. GISAXS revealed that extending the alkyl chain length from C_{14} to C_{24} resulted in an increase in diameter from C_{14} to C_{22}, followed by the collapse in the hexagonal pore order for C_{24}, however, vertical pores remain present within the silica film from the latter, as shown by TEM. The pore spacings started to plateau for C_{20}, C_{22} and C_{24} surfactants, suggesting a limit for micelle expansion. The diffusion coefficients of neutral, cationic, and anionic redox molecules increased with larger surfactants. Ellipsometric porosimetry measurements showed a sizable increase in pore diameter from 2 to 5 nm using C_{16} to C_{22} surfactants.

Part of this work has been published in *Langmuir*, 2022, **38**, 2257–2266.

3.1 Acknowledgement

I would like to thank Anthony Houghton and Ziyou Zhang for undertaking the porosimetry measurements, as well as Richard Beanland and Yisong Han for their support in TEM analysis.

3.2 Introduction

Oriented mesoporous silica films are potential hard templates for the electrodeposition of nanowire-based devices[1], with possible applications in Li-ion batteries[2,3], thermoelectrics[4] and supercapacitors.[5] In order for the electrode surface to remain accessible to the electrolyte it is necessary to arrange the pores perpendicular to the substrate surface, often referred to as the vertical orientation. Whilst the growth of platinum nanowires in silica with horizontal pores occurred readily, Kanno *et al* showed that the electrodeposition of Au nanowires was much easier in perpendicular pores.[6,7] Whilst the literature on electrodeposition in very small pore templates is limited, there are some examples, e.g. of 3 nm tin nanowires[8] or 5 to 8 nm bismuth nanowires,[9] produced in this way.

Pore orientation, pore diameter and organo-functionalisation[10,11] are important factors in the rate of ion diffusion through porous films. Etienne and co-workers reported TiO_2 with the anatase structure in an open porous network, in which positively charged species were more mobile than negatively charged ones.[12] The fine tuning of parameters has also made silica films attractive materials for biosensing and electrochemical sensing applications,[13,14] for example, Nasir *et al*[15] developed an electrochemical pathway for detecting cationic paraquat salts in oriented mesoporous silica films.

The most common approach to prepare mesoporous silica films is by EISA.[16,17,18] This method tends to produce ordered silica films with the pores either horizontal to the substrate surface or randomly oriented. Glazneva et al.[19] demonstrated the synthesis of mesoporous silica films using cetyltrimethylammonium bromide (CTAB) on oxidised titanium electrodes by EISA. The authors showed that the mesoporous structure could be adjusted from hexagonal to cubic by modifying the surfactant/silica ratio. The surfactant template was removed from the film by steady heating until reaching 250 ℃ under vacuum, which resulted in a surface area of 1080 $m^2 g^{-1}$ with a calculated pore diameter of 2.8 nm determined by the Brunauer-Emmett-Teller method. Keilbach et al.[20] replicated a composite templated material of P123-mesoporous silica/AAO membranes using the EISA process. The hexagonally arranged mesopores inside the AAO membrane was filled by metallic nanowires of Cu, Ag and Te using electrochemical deposition. The nanowire diameters of copper and silver were estimated by TEM imaging and found to be in the region of 10 nm.

Several strategies have been devised to produce orientated silica films, including through application of a magnetic field,[21] epitaxial growth,[22] and radio sputtering.[23] For example, Yamauchi *et al.* used an external magnetic field to control pore alignment from an EISA process either vertically or horizontally to the substrate surface.[24] Otomo *et al*.[25] synthesised aligned mesoporous silica films by a radiofrequency sputter deposition of Co-Si-O films where the surface

morphology was influenced by the argon gas pressure applied (15 mTorr) producing vertical Co arrays , followed by wet chemical etching to remove the Co from the films.

Stöber-solution growth is based on formation of hemispherical micelles of a cationic surfactant on a negatively charged substrate, and interactions with silica oligomers encouraging vertical growth of those micelles.[26] This method can take days to grow very thin aligned films.

Walcarius and co-workers[27] revealed that the preparation of vertically oriented mesoporous silica films was possible under electrochemical control, which resulted in perpendicular (vertical) pore channels (diameter = 2-3 nm) and uniform film thickness (150-200 nm). Mesoporous films can be obtained by the EASA method within as little as 20 seconds. EASA was developed with a $[Me_3NC_{16}H_{33}]Br$ (CTAB or $C_{16}TAB$) surfactant, and this leads to pores with a diameter of around 2 nm diameter depending on conditions and substrate.[28] Vavra and co-workers[29] reported the production of mesoporous silica films with hexagonally arranged pores by EASA. They discovered that the substitution of CTAB with alkyl-methylimidazolium chloride ionic liquid cations in the sol electrolyte (where the alkyl chain extended from C_{12} to C_{16}), influenced the lattice parameters and hence pore diameter, evidenced from GISAXS measurements. The C_{14} and C_{16} methylimidazolium chloride cations maintained the hexagonal pattern, but with C_{12}, a significant reduction in pore order was noticed.

Robertson *et al*[30] showed that mesitylene can be used as a swelling agent for CTAB-templated EASA films on titanium nitride, causing the pore diameter to increase from 1.6 nm to 2.4 nm. However, higher amounts of mesitylene resulted in a reduction in the ordering of the porosity.

Larger and vertically aligned pores may prove beneficial as hard templates for nanowire electrodeposition and increase the range of sensing applications. Ullah et al. recently showed that polyaniline nanowires with different widths could be produced in EASA silica films formed using $C_{16}TAB$ or $C_{18}TAB$.[31] Therefore, expanding the pore size whilst maintaining pore alignment and structure is pivotal when investigating at what size deposition of nanomaterials into the pores becomes feasible.

In this chapter, it is demonstrated that systematic increases in the pore diameter beyond 2 nm while maintaining vertical ordering and hence pore access are achievable by EASA when utilising surfactants created by further extending the single straight alkyl chain.

3.3 Experimental summary

3.3.1 General experimental methods

Tetradecyltrimethylammonium bromide (C_{14}TAB, 99%), hexadecyltrimethylammonium bromide (C_{16}TAB, 98%) and octadecyltrimethylammonium bromide (C_{18}TAB, 98%) were purchased from Sigma-Aldrich.

3.3.2 Surfactant preparation and characterisation of mesoporous silica films

The synthesis of longer chain alkyltrimethylammonium bromide surfactants (Scheme 3.1) was carried out according to Scheraga et al.[32] The synthesis used alkyl bromides $C_nH_{2n+1}Br$ where n = 20 (5.0001 g, 13.83 mmol ≥ 97 %, Sigma Aldrich), 22 (5.0001 g, 12.84 mmol, 96 %, Santa Cruz Biotechnology) or 24 (0.8915 g, 2.14 mmol, synthesised as described below). The alkyl bromide was dissolved in ethanol (25 cm^3) and 30% trimethylamine in an ethanol solution (7.6000 g, 128.6 mmol for C_{20} and C_{22}, or 1.3000 g, 22.0 mmol for C_{24}, Sigma Aldrich) was added dropwise into this solution. The mixture was refluxed at 100 °C for 8 h with stirring under a dry ice condenser. The solution was then filtered and stored overnight in a freezer to precipitate the product. The crude product was filtered, and the resulting solid was recovered using a rotary evaporator then recrystallised three times from ethanol. Final yields were 4.50 g, 10.7 mmol eicosyltrimethylammonium bromide (C_{20}TAB, 90%, off white solid), 4.22 g, 9.4 mmol docosyltrimethylammonium bromide (C_{22}TAB, 84%, white solid) and 0.78 g, 1.6 mmol tetracosyltrimethylammonium bromide (C_{24}TAB, 88%, white solid).

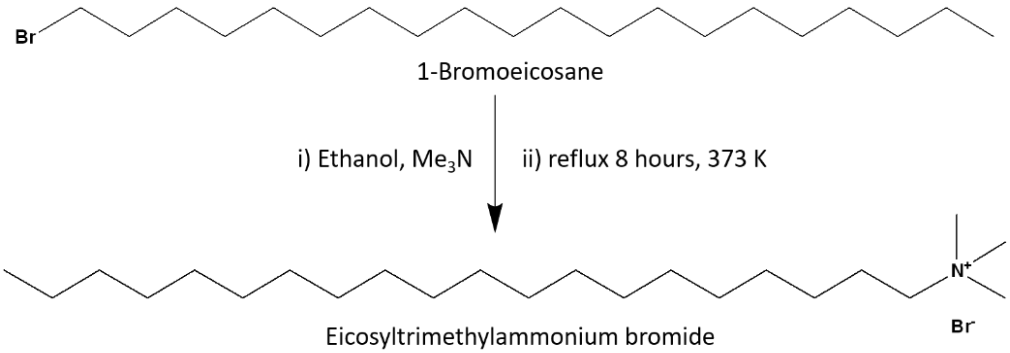

Scheme 3.1 Reaction of 1-bromoeicosane with trimethylamine to form the quaternary ammonium salt, C_{20}TAB. The same general method was used for C_{22}TAB and C_{24}TAB surfactants.

The synthesis of 1-bromotetracosane ($C_{24}H_{49}Br$) was based on the procedure reported by Al-Dulayymi *et al.*[33] The method involved dissolving triphenylphosphine (0.800 g, 3.05 mmol, 99%, Avocado Research Chemicals Ltd), tetracosan-1-ol (1.000 g, 2.82 mmol, > 98 %, Tokyo Chemical

Industry UK Ltd) and N-bromosuccinimide (1.500 g, 8.43 mmol, 99%, Sigma Aldrich) in dry dichloromethane (50 cm^3). The reaction mixture was stirred at ambient temperature for 5 hours and then quenched with water (200 cm^3), extracted into dichloromethane and dried using a rotary evaporator to give a red solid. The product was then refluxed in petroleum ether (500 cm^3) and ethyl acetate (5 cm^3), filtered, and the filtrate taken to dryness using a rotary evaporator to give $C_{24}H_{49}Br$ (0.892 g, 2.14 mmol, 89.2 % yield). This material was used directly for the preparation of the C_{24}TAB surfactant. NMR spectroscopic and positive ion ESI MS data are given below for each surfactant.

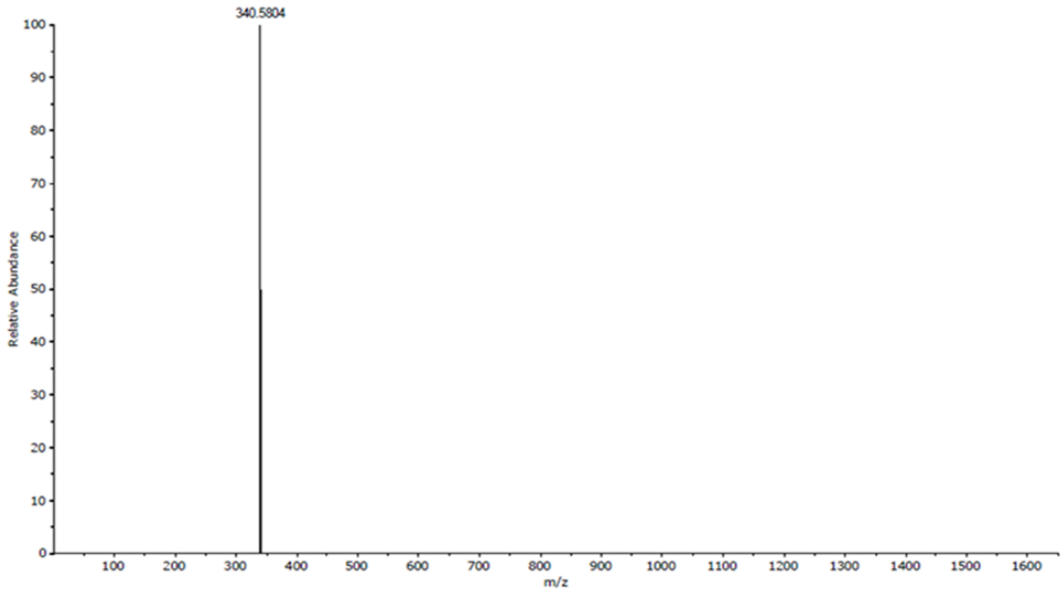

Figure 3.1 Positive ion mass spectrum of C_{20}TAB (calculated 340.58 m/z value) in methanol at 25 ℃.

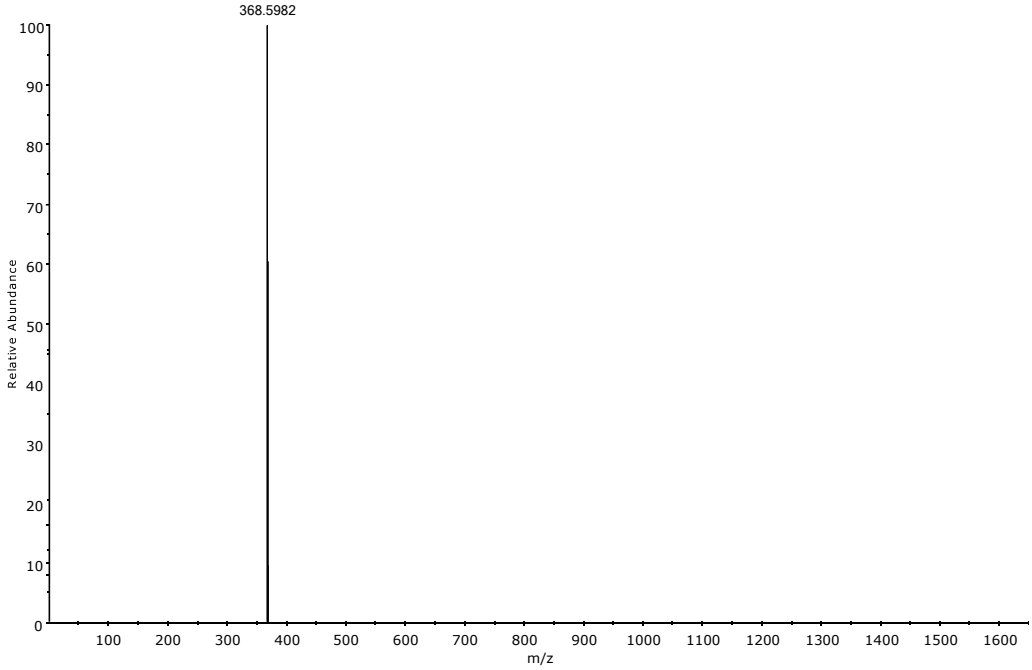

Figure 3.2 Positive ion mass spectrum of C_{22}TAB (calculated 368.60 m/z value) in methanol at 25 ℃.

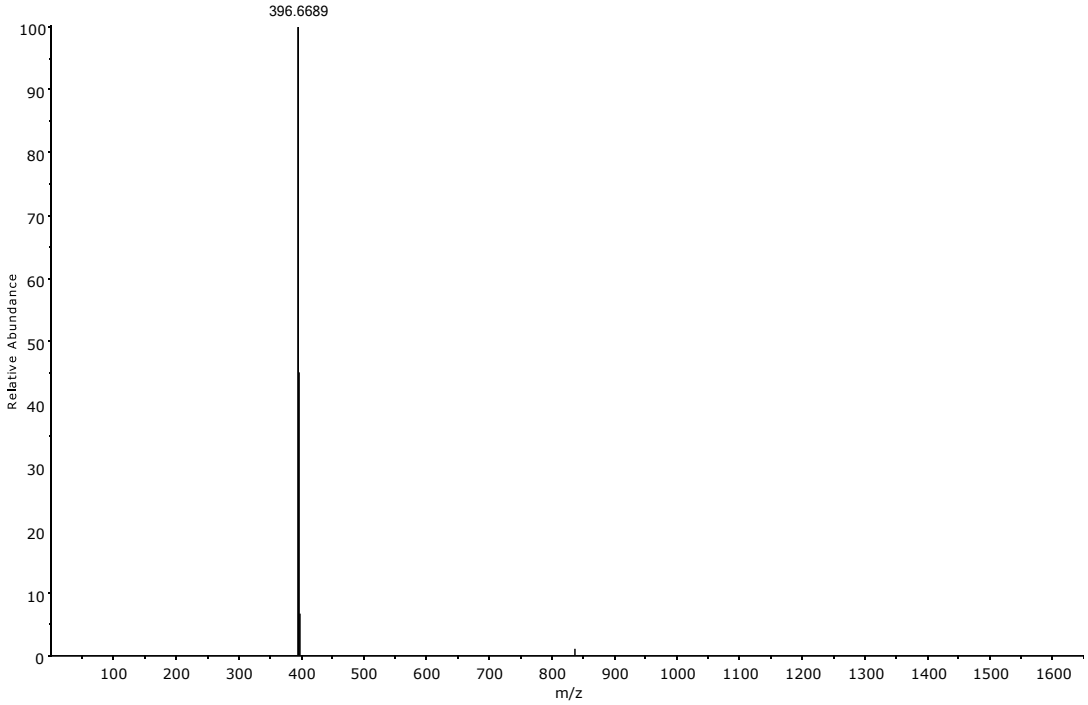

Figure 3.3 Positive ion mass spectrum of C_{24}TAB (calculated 396.67 m/z value) in methanol at 25 ℃.

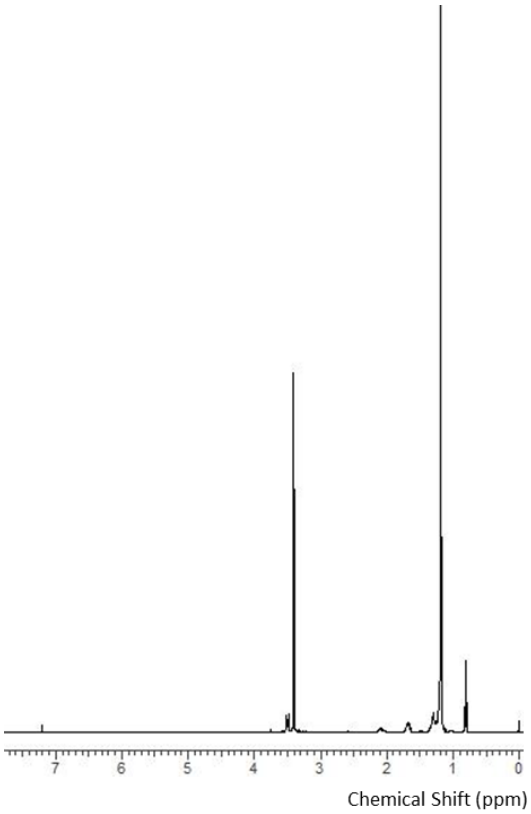

Figure 3.4 ^{1}H NMR spectrum of C_{20}TAB in $CDCl_3$ (7.3 ppm) at 25 °C.

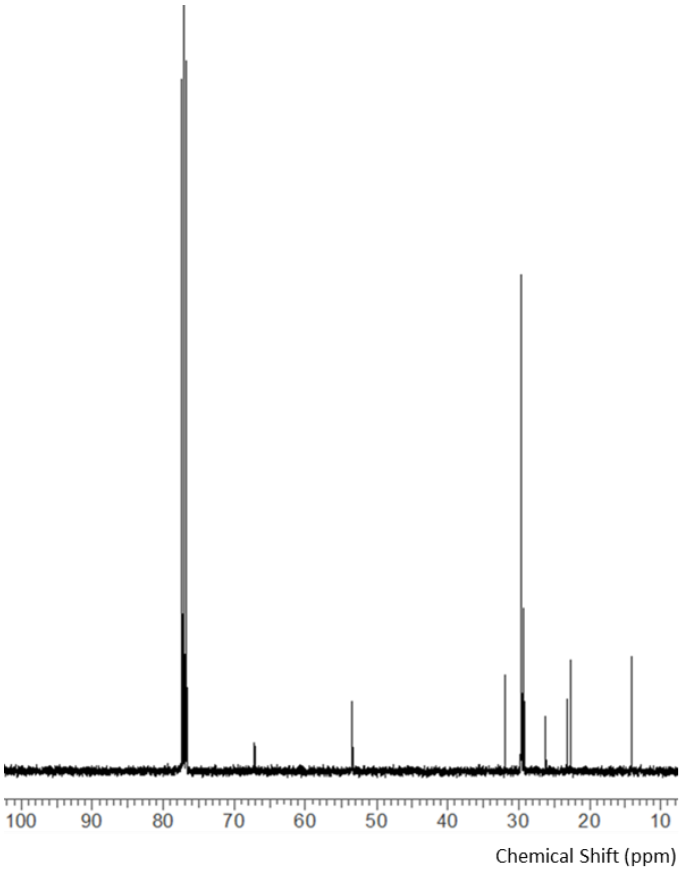

Figure 3.5 $^{13}C\{^{1}H\}$ NMR spectrum of $C_{20}TAB$ in $CDCl_3$ (77.2 ppm) at 25 ℃.

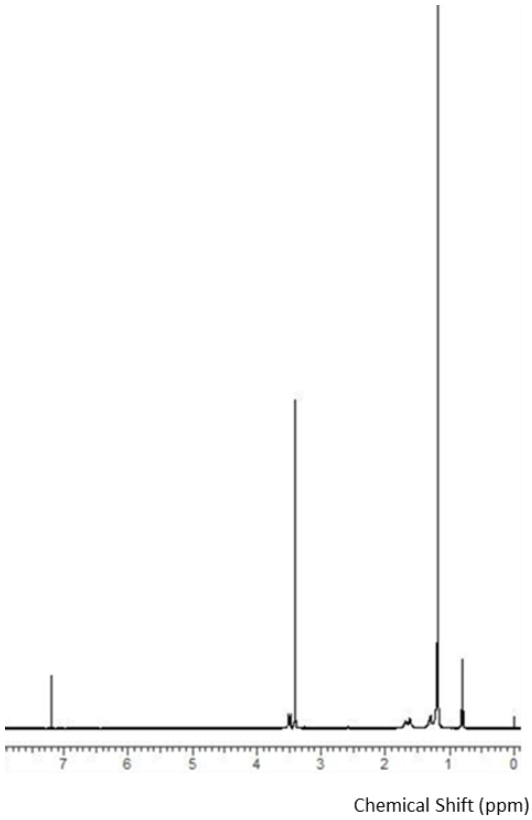

Figure 3.6 ^{1}H NMR spectrum of $C_{22}TAB$ in $CDCl_3$ (7.3 ppm) at 25 °C.

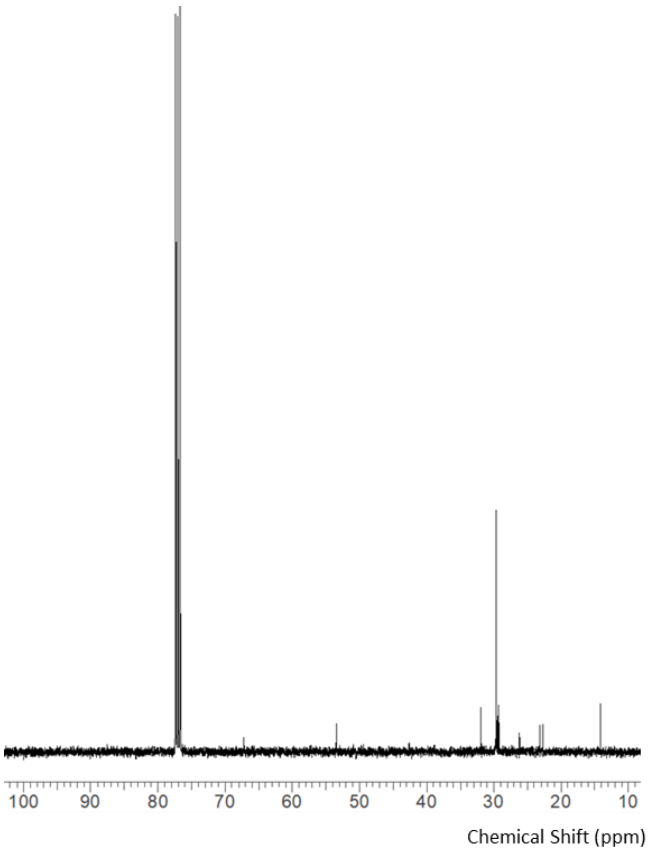

Figure 3.7 $^{13}C\{^{1}H\}$ NMR spectrum of C_{22}TAB in $CDCl_3$ (77.2 ppm) at 25 °C.

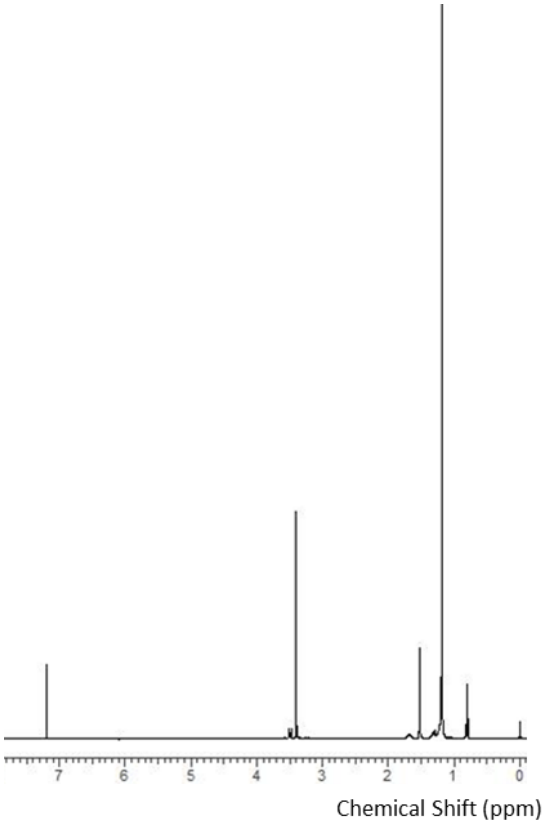

Figure 3.8 ^{1}H NMR spectrum of C_{24}TAB in $CDCl_3$ (7.3 ppm) at 25 °C.

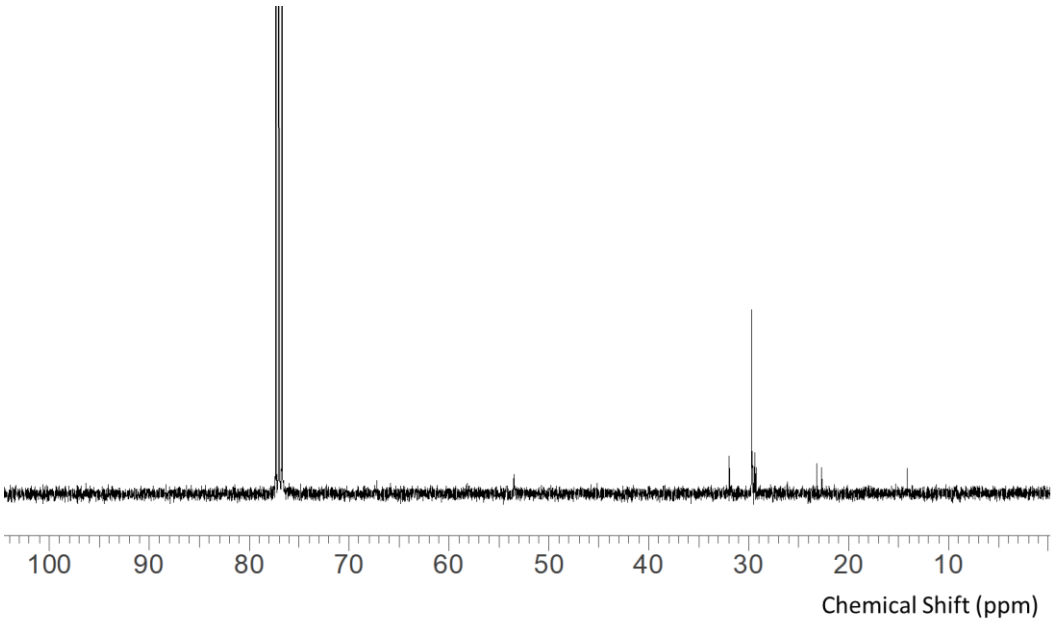

Figure 3.9 $^{13}C\{^{1}H\}$ NMR spectrum of C_{24}TAB in $CDCl_3$ (77.2 ppm) at 25 °C.

C_{20}TAB. ^{1}H NMR ($CDCl_3$): δ/ppm 0.83 (t, CH_3, [3H]), 1.17 (br s, CH_2, [32H]), 1.26-1.37 (m, CH_2, [2H]), 1.63-1.77 (m, CH_2, [2H]), 3.41 (s, CH_3, [9H]), 3.47-3.56 (m, CH_2, [2H]). $^{13}C\{^{1}H\}$ NMR ($CDCl_3$): δ/ppm 14.12, 22.70, 23.23, 26.19, 26.22, 29.23, 29.32, 29.36, 29.47, 29.54, 29.59, 29.63, 29.66, 29.68, 29.70, 29.71, 31.92, 53.41, 58.43, 67.12. MS (ESI^+ in CH_3OH): found *m/z* = 340.58; required for $\{C_{23}H_{50}N^+\}$: m/z = 340.

C_{22}TAB. ^{1}H NMR ($CDCl_3$): δ/ppm 0.82 (t, CH_3, [3H]), 1.19 (br s, CH_2, [36H]), 1.29-1.37 (m, CH_2, [2H]), 1.61-1.65 (m, CH_2, [2H]), 3.41 (s, CH_3, [9H]), 3.47-3.53 (m, CH_2, [2H]). $^{13}C\{^{1}H\}$ NMR ($CDCl_3$): δ/ppm 14.10, 22.72, 23.21, 26.17, 29.22, 29.27, 29.32, 29.35, 29.36, 29.46, 29.59, 29.65, 29.66, 29.69, 29.71, 31.89, 31.91, 31.93, 42.63, 53.45, 67.18, 67.21. MS (ESI^+ in CH_3OH): found *m/z* = 368.60; required for $\{C_{25}H_{54}N^+\}$: m/z = 368.

C_{24}TAB. ^{1}H NMR ($CDCl_3$) δ/ppm 0.82 (t, CH_3, [3H]), 1.18 (s, CH_2, [40H]), 1.22-1.33 (m, CH_2, [42H]), 1.63-1.72 (m, CH_2, [2H]), 3.40 (s, CH_3, [9H]), 3.46-3.54 (m, CH_2, [2H]). $^{13}C\{^{1}H\}$ NMR ($CDCl_3$): δ/ppm 14.12, 22.70, 23.25, 25.32, 25.33, 26.18, 29.20, 29.29, 29.33, 29.37, 29.44, 29.55, 29.58, 29.65, 29.67, 29.69, 29.71, 31.94, 43.65, 53.46, 53.51, 53.54, 53.59, 53.60. MS (ESI^+ in CH_3OH): found *m/z* = 396.70; required for $\{C_{27}H_{58}N^+\}$: m/z = 396.

3.3.3 Mesoporous silica growth

(i) $C_{14}TAB$ – $C_{18}TAB$

The synthesis of vertically ordered silica films under electrochemical control used the method previously reported by Goux *et al.*[34] The electrolyte was prepared by mixing $C_{14}TAB$ (0.4801 g, 1.43 mmol), $C_{16}TAB$ (0.4801 g, 1.32 mmol) or $C_{18}TAB$ (0.4801 g, 1.22 mmol) into 0.1 mol dm^{-3} $NaNO_3$ in 20 cm^3 deionised water and 20 cm^3 ethanol, then TEOS, 98%, Sigma Aldrich), 905 μL, 4.08 mmol) was added to the solution. The sol was adjusted close to pH 3 using 0.2 mol dm^{-3} HCl, then allowed to hydrolyse for 2.5 hours. The ratio of the surfactant: silica precursors was kept constant at around 0.3 with each experiment containing a newly prepared sol electrolyte.

(ii) $C_{20}TAB$-$C_{24}TAB$

The sol preparation was altered slightly when using $C_{20}TAB$ (0.3000 g, 0.71 mmol), $C_{22}TAB$ (0.3000 g, 0.67 mmol) and $C_{24}TAB$ (0.3000 g, 0.63 mmol) due to surfactant solubility problems with the standard method described above. The electrolytes were prepared by mixing 0.1 mol dm^{-3} $NaNO_3$ in water (20 cm^3) with isopropyl alcohol (20 cm^3), adding TEOS (905 μL, 4.08 mmol) and adjusting the sol pH to between 3 and 3.5 using 0.2 M HCl. The sol was then stirred for 90 minutes. The surfactants were added to the sol and allowed to stir for a further 60 minutes. The $C_{22}TAB$ and $C_{24}TAB$ surfactants did not dissolve in the solution at 25 °C, so the temperature was raised to 35 °C, which caused dissolution. The solutions were then allowed to hydrolyse for 2.5 hours. The surfactant: silica ratio was kept constant at around 0.17:1 with each experiment using a fresh sol electrolyte.

(iii) Electrochemically assisted silica deposition

The electrodeposition of porous silica was carried out in a Teflon cell with 2 × 1 cm indium tin oxide-coated glass (ITO; surface resistivity 8-12 Ω Sigma Aldrich) used as the working electrode. Prior to deposition, the electrodes were washed with water and ethanol and dried under N_2 gas. The working electrode was submerged vertically into the sol electrolyte, a stainless-steel cone was used as the counter electrode and a silver rod as the reference electrode. A Biologic SP150 potentiostat was used to apply a constant potential of -1.25 V (vs. Ag/Ag^+) for a duration of 20 seconds. After each experiment the silica films (1 × 1 cm) were quickly rinsed with water and ethanol, then dried in an oven at 130 °C for 16 hours. To remove the surfactants from the pore channels, the films were then immersed in a solution of 0.2 mol dm^{-3} HCl (Fisher Scientific) in ethanol for 15 minutes under gentle stirring.

3.4 Results and Discussion

3.4.1 The structure and characterisation of mesoporous silica films on ITO electrodes

The EASA method was originally devised by Walcarius[27] and has been shown to be a versatile method to produce highly ordered silica films with pores vertical to the substrate. The preliminary experimental model was established by Walcarius whereby a Teflon cell with an 8 mm O-ring placed at the bottom of the cell was used for the deposition process. A stainless-steel cone was used as the auxiliary electrode, a silver rod as the reference electrode and the working electrode was an ITO (surface resistivity 8-12 Ω) transparent electrode.

In the present study, the deposition of silica films using a series of cationic surfactants with different alkyl chain lengths, C_{14}-C_{24}, was undertaken with the aim of investigating the range of pore sizes that can be produced in a vertical orientation.[28,35] Deposition potentials above -1.2 V (vs. Ag/Ag^+) result in no film formation, whereas below -1.3 V (vs. Ag/Ag^+) the ITO electrode is damaged by the reduction of indium oxide. Depositions were therefore carried out at -1.25 V, over time periods of between 10-20 seconds, producing thickness values of 40-150 nm.[27,36] The longer alkyl chain lengths increase the hydrophobicity of the surfactant, so the sol composition and temperature had to be varied to achieve surfactant solubility and produce highly ordered porous silica films, including switching the ethanol component of the sol to isopropyl alcohol. The resulting films were rinsed and then dried, and the surfactant removed by solvent extraction as described above.

The deposition of mesoporous silica was followed by in-plane GISAXS measurements to determine the pore ordering and alignment. The 1D in-plane scattering pattern for the EASA film grown with C_{18}TAB is shown in Fig. 3.10 and contains the typical peaks for mesoporous materials with a hexagonal arrangement of cylindrical pores in *P6mm* symmetry, namely the SBA-15[37,38] and MCM[39,40] families of materials. The incident beam angle found to provide the most intense diffraction features was 0.25 °, at which an intense diffraction peak was observed at 2.13 ° which relates to the 10 reflection. Three more peaks were observed at 3.71 °, 4.35 ° and 5.71 °, which correspond to the 11, 20 and 21 reflections, respectively. The 10 peak position corresponds to a d-spacing of 4.15 nm and the resulting pore spacing, a_0 is 4.79 nm for the silica film with C_{18}TAB. As expected, the d-spacing and pore spacing values were greater than for silica films with C_{16}TAB (see Table 3.1), indicating a possible increase in the pore diameter.

The 2D GISAXS image of the EASA film templated with C_{18}TAB is presented in the insets to Fig. 3.10. The four in-plane spots in the horizontal plane relate to the 10, 11 and 20 reflections discussed in the previous paragraph. The positions of these spots in the horizontal plane shows

that the pores are oriented vertically, i.e., perpendicular to the plane of the substrate. An important observation is that no out-of-plane rings were present in the pattern which suggests a reduction in the silica surface overgrowth.

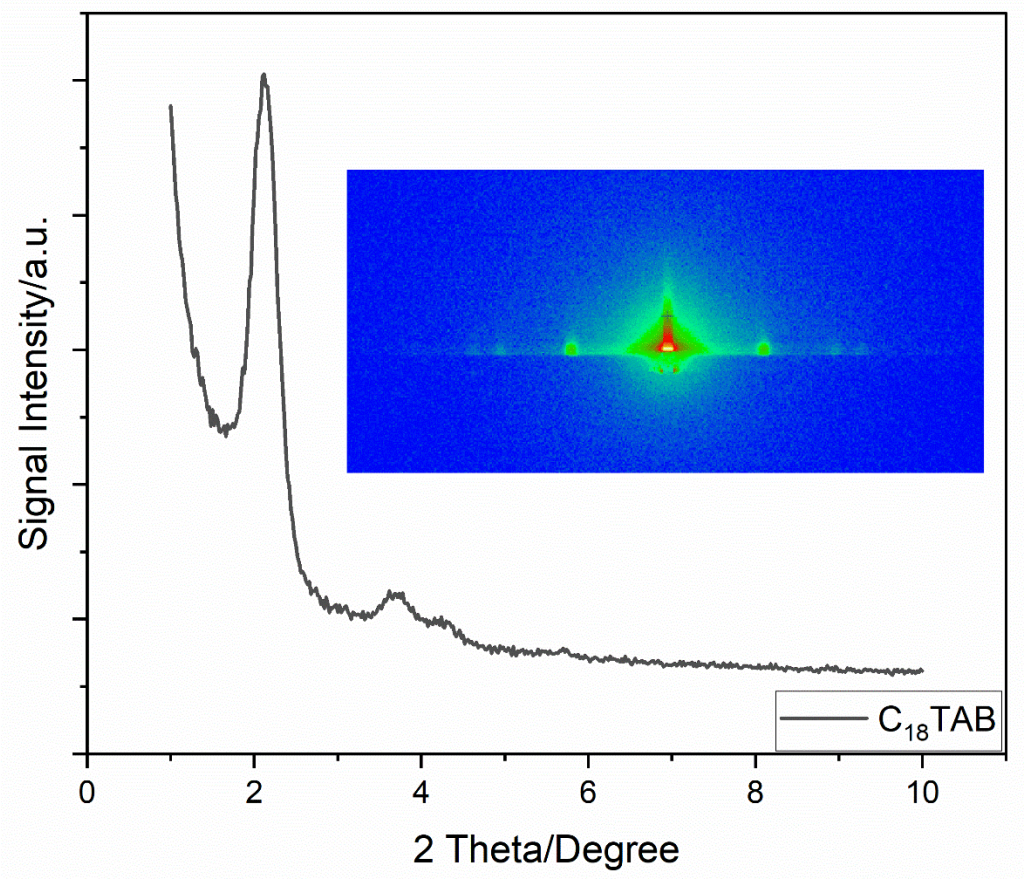

Figure 3.10 1D in-plane GISAXS pattern of an EASA film with C_{18}TAB deposited at a potential of -1.25 V (vs. Ag/Ag^+) for 20 s on an ITO electrode. Inset: 2D in-plane GISAXS pattern of C_{18}TAB templated EASA film.

The surfactant with an alkyl chain length of 20 carbons was synthesised according to Scheraga et al.[32] and is referred to as C_{20}TAB. In this study, GISAXS measurements were carried out to determine whether increasing the alkyl chain length would result in changes to the lattice parameters. The 1D in-plane scattering pattern (Fig. 3.11) shows a similar hexagonal pattern to that of C_{18}TAB however, the 2θ values of 1.97 °, 3.44 °, 3.97 ° and 5.23 ° for the peaks relating to 10, 11, 20 and 21, are more pronounced and intense, indicating an increase in the hexagonal pore order. Furthermore, the peak positions are seen to shift to lower angle, leading to d-spacing and pore spacing values of 4.48 nm and 5.18 nm respectively. For C_{20}TAB, the changes in lattice spacings in relation to C_{18}TAB suggest larger micelles as the carbon chain length of surfactant increases.

The pore orientation in a mesoporous silica film with C_{20}TAB deposited on an ITO electrode was characterised by 2D GISAXS. The image in Fig 3.11 inset shows four Bragg spots on the horizontal

plane, these are not observed for the C_{18}TAB film. These spots arise from the 10, 11, 20 and 21 planes and are indicative of high levels of hexagonal pore ordering and vertical mesopore orientation over a wide area. Additionally, it is to be noted that the Bragg spots are more concentrated and defined for the C_{20}TAB film and the presence of the weak 21 reflection, indicates improved hexagonal order when compared to the C_{18}TAB film. The formation of low intensity rings is noticed in the 2D GISAXS image, a feature that provides information on the pore structure. In this case, this could indicate either pore disorder or as mentioned earlier, a silica layer formed on the film surface.

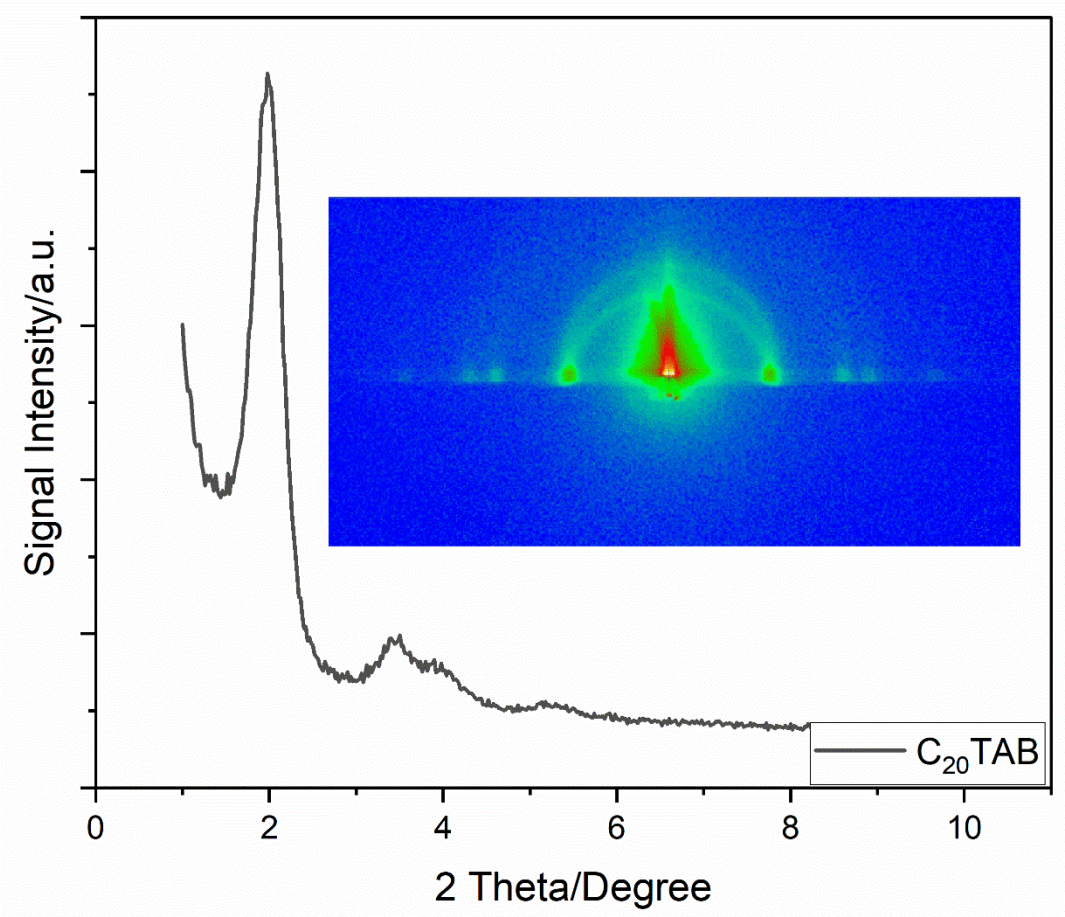

Figure 3.11 1D in-plane GISAXS pattern of an EASA film with C_{20}TAB deposited at a potential of -1.25 V (vs. Ag/Ag^+) for 20 s on an ITO electrode. Inset: 2D in-plane GISAXS pattern of C_{20}TAB templated EASA film.

The surfactant chain length was further increased to 22 carbons with the sol process adjusted for effective surfactant (C_{22}TAB) dissolution as previously stated. GISAXS was used to study the crystallinity after surfactant extraction. According to the 1D GISAXS data for the silica film with C_{22}TAB (Fig. 3.12), a large diffraction peak at 2.00 ° followed by three less intense peaks at 3.43 °, 3.96 ° and 5.22 °, relating to the 10, 11, 20 and 21 hexagonal lattice planes, are observed. The d-spacing and pore spacing values for the 10 reflection were 4.42 nm and 5.10 nm (calculated from Eq. 2.1 and 2.2), respectively. As expected, the same set of peaks is seen for C_{18}TAB and

C_{20}TAB films, indicating improved structural pore order within the film. Ryoo et al.[41] synthesised MCM-41 silica materials with trimethylammonium bromide surfactants where the alkyl chain length extended from C_{12} to C_{22}. It was understood that lamellar mesoporous structures were most attainable with C_{22}TAB whereas, hexagonal mesophases were favoured with C_{12} and C_{14}. This is contrary for EASA, as significant pore disorder is obtained for films with C_{12}TAB,[34] and an ordered hexagonal array of pores is present when the sol electrolyte mixture contains C_{22}TAB.

For the 2D GISAXS image (Fig 3.12 inset), intense diffraction spots are observed for the silica film with C_{22}TAB, suggesting that the hexagonal pore arrangement and vertical orientation are maintained when increasing the surfactant size. The four diffraction spots along the parallel plane are associated with the 10, 11 and 20 reflections. Rings situated around the spots are observed at similar d-spacings to the in-plane spots, and these features increase in intensity with longer deposition times (experimentally observed). Goux *et al*[34] reported similar GISAXS features for C_{16}TAB-generated EASA films.

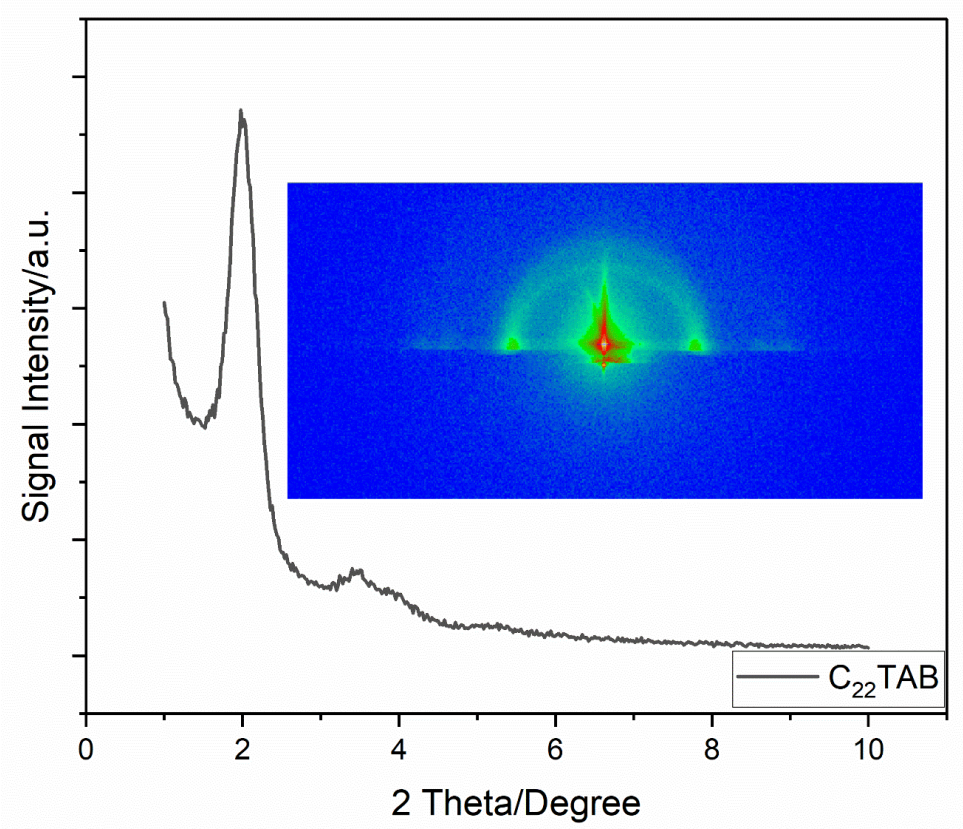

Figure 3.12 1D in-plane GISAXS pattern of an EASA film with C_{22}TAB deposited at a potential of -1.25 V (vs. Ag/Ag^+) for 20 s on an ITO electrode. Inset: 2D in-plane GISAXS pattern of C_{22}TAB templated EASA film.

In contrast to the C_{22}TAB templated silica film, the addition of C_{24}TAB to the sol electrolyte resulted in a disordered sol-gel film as indicated by the 1D in-plane GISAXS data shown in Fig. 3.13. A clear reduction in the intensity of the broad 10 diffraction peak and a total loss of the 11

and 20 diffraction peaks was observed, indicating a significant loss of the hexagonal order. However, the GISAXS data indicates that the silica film does retain porosity as shown previously.

The inset of Fig. 3.13 illustrates the 2D GISAXS data obtained for the EASA film containing C_{24}TAB after surfactant removal. The position of the 10 diffraction spots in the horizontal plane shows this film also has vertically aligned pores, but the hexagonal domains have very little longer-range order, which also accounts for the low intensity of the 1D GISAXS pattern.

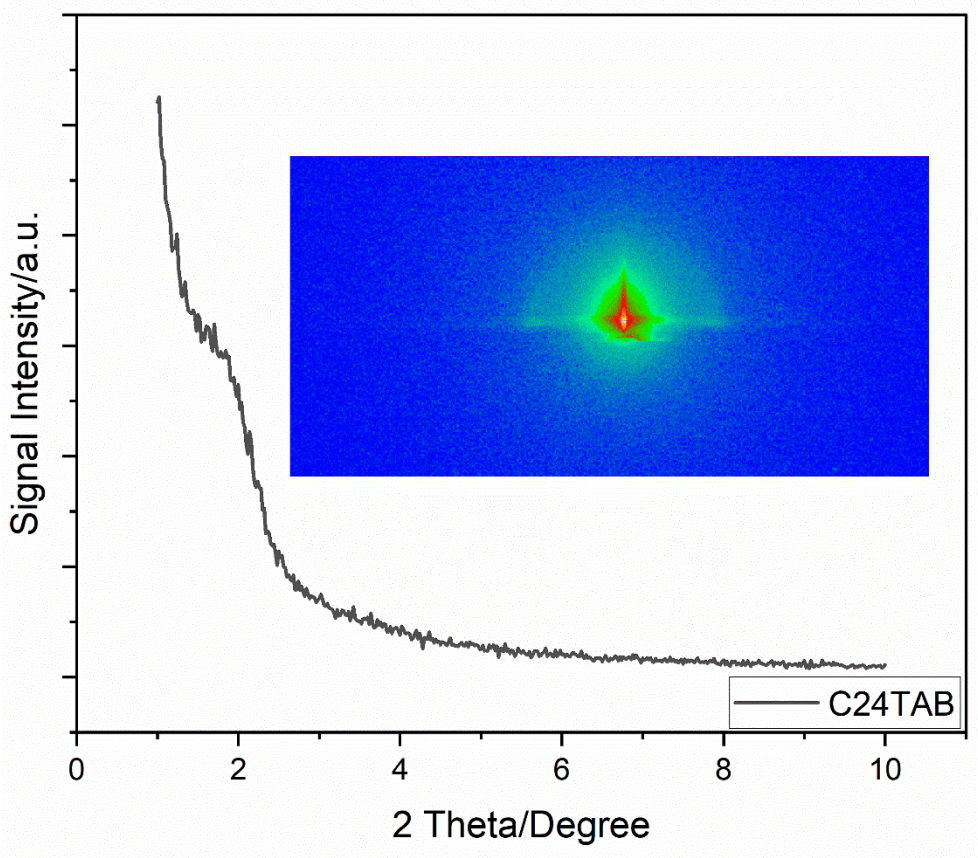

Figure 3.13 1D in-plane GISAXS pattern of an EASA film with C_{24}TAB deposited at a potential of -1.25 V (vs. Ag/Ag^+) for 20 s on an ITO electrode. Inset: 2D in-plane GISAXS pattern of C_{24}TAB templated EASA film.

3.4.2 The effect of varying the lipophilic tail of surfactants

The effects of increasing alkyl chain length of six surfactants were investigated. The surfactants included were C_{14}TAB, C_{16}TAB, C_{18}TAB, C_{20}TAB, C_{22}TAB and C_{24}TAB. A stack plot of 1D GISAXS patterns from a range of EASA films generated by surfactants of increasing chain length is shown in Fig. 3.14. The incorporation of C_{14}TAB in the sol electrolyte resulted in a shift in the 10 peak to higher angle (2.62 °) which equates to a d-spacing of 3.46 nm (Fig. 3.14). When switching the surfactant to C_{16}TAB in the sol, the peak positions shift noticeably to smaller angle, whereby the 10 peak is situated at 2.34 ° which corresponds to a higher d-spacing compared to C_{14}TAB.

Furthermore, the diffraction peaks appear more intense and sharper (Fig. 3.14), suggesting an improvement in the hexagonal pore ordering.

In general, as the surfactant chain length increases, a shift in peak positions to lower 2θ angle is clearly noticed for films with C_{14}-C_{22} surfactants as shown in Table 3.1. It is to be noted that the peak intensities increase upon gradually extending the surfactant chain length from C_{14}-C_{22}, implying that the steady increase in pore spacings is accompanied by an increase in hexagonal pore order. This cannot be achieved with other methods using the same surfactants. The C_{24}TAB generated film did not follow this trend, evidenced by the significant drop off in peak intensity (shown in Fig. 3.14).

Overall, the XRD data suggest an increase in the pore diameter upon increasing the surfactant size from C_{14}-C_{22}, with good retention in ordering. Nevertheless, this is not certain as the pore spacings do not provide definitive information on pore expansion, as this could also be explained by an increase in the pore wall thickness, rather than in the size of the pores. Hence, the pore spacing only provides an indirect indication of a change in pore size.

The pore diameter or spacings vs. surfactant chain length (C_{14}, C_{16}, C_{18}, C_{20} and C_{22}) for a range of EASA films are also shown in Fig. 3.15, confirming an increase in the pore spacing values upon increasing the surfactant chain length. The pore spacing values start to plateau at longer chain lengths, suggesting that increasing the surfactant's carbon chain unit will have less influence on the pore spacings and hence pore growth from these porous silica films.

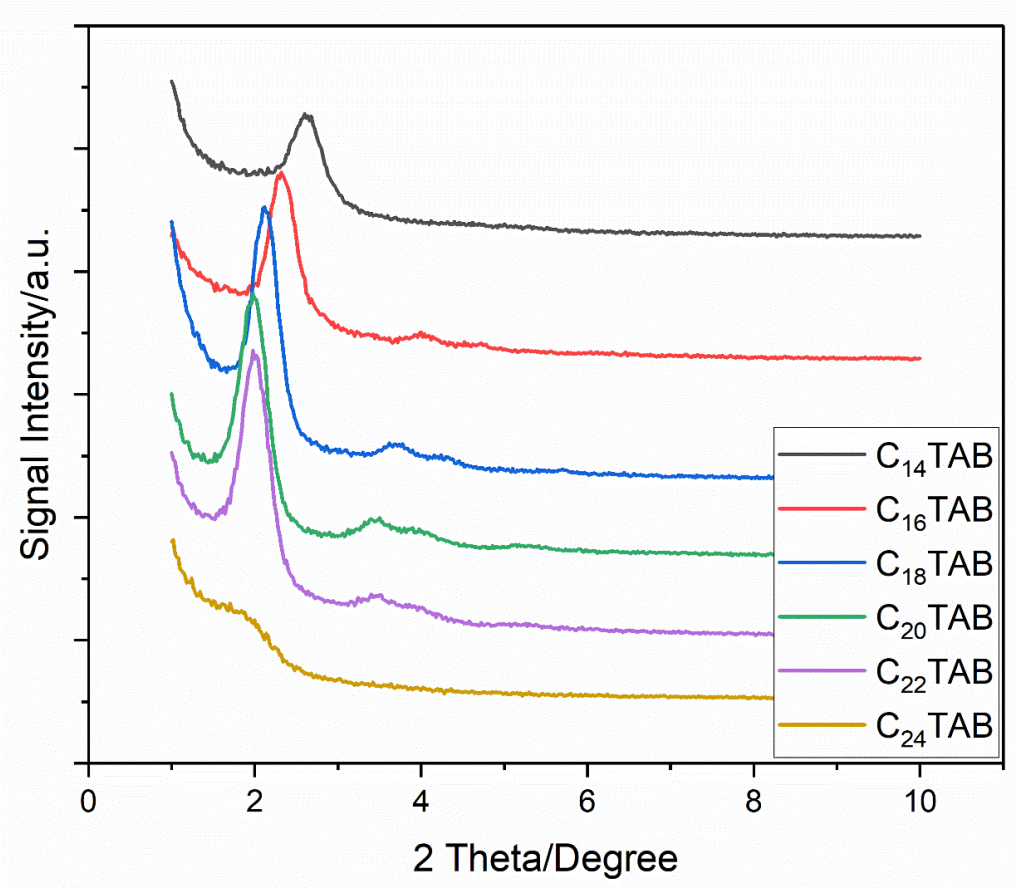

Figure 3.14 1D in-plane GISAXS patterns of EASA films with C_{14}TAB, C_{16}TAB, C_{18}TAB, C_{20}TAB, C_{22}TAB and C_{24}TAB deposited at a potential of -1.25 V (vs. Ag/Ag^{+}) for 20 s on ITO electrodes.

Table 3.1 shows the extrapolated data from the XRD patterns for a range of EASA films on ITO electrodes.

Surfactant	Symmetry	Peak Location (2Θ) 10	Peak Location (2Θ) 11	Peak Location (2Θ) 20	Peak Location (2Θ) 21	d_{10} (nm)	a_0 (nm)
C_{14}TAB	Hexagonal	2.62	4.40	/	/	3.46	3.99
C_{16}TAB	Hexagonal	2.34	4.02	4.68	/	3.77	4.36
C_{18}TAB	Hexagonal	2.13	3.71	4.35	5.71	4.15	4.79
C_{20}TAB	Hexagonal	1.97	3.44	3.97	5.23	4.48	5.18
C_{22}TAB	Hexagonal	2.00	3.43	3.96	5.22	4.42	5.10

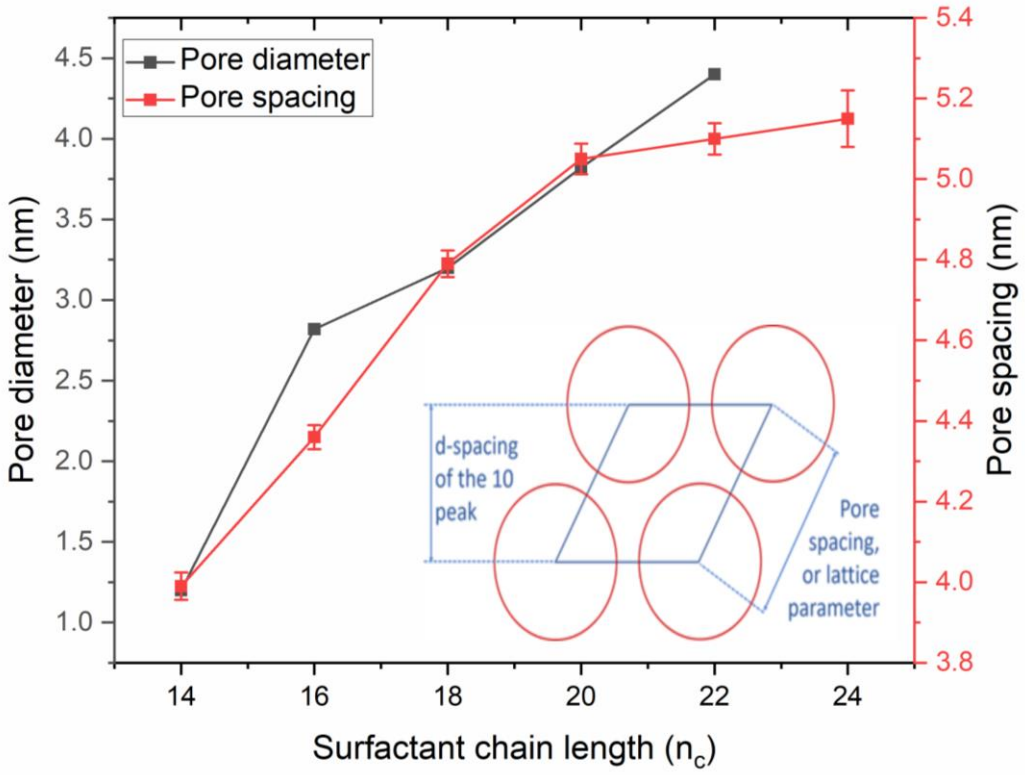

Figure 3.15 A plot of pore spacing (nm) of the 10 reflection and pore diameter (nm) determined by ellipsometric porosimetry as a function of surfactant chain lengths of EASA films grown with $C_{14}TAB$[35], $C_{16}TAB$, $C_{18}TAB$, $C_{20}TAB$, $C_{22}TAB$ and $C_{24}TAB$.

3.4.3 The effect of deposition time on the intensity of rings

Materials that possess ordered structures will result in well-defined scattering features such as rings or spots on the GISAXS image. The reason as to why the rings appear for a particular material, is the focus of this particular aspect of this work. Previously, the rings have been suggested to be due to Stöber growth in the bulk solution. Therefore, we investigated the effect of deposition time on the ring intensity for mesoporous silica films templated by $C_{22}TAB$, which were deposited for 10, 15 and 20 seconds, as characterised by GISAXS (Fig. 3.16). Deposition for the shortest time (10 s) led to no out-of-plane rings in the 2D diffraction pattern (Fig. 3.16 a). On the other hand, the films deposited for longer periods (15 s and 20 s) led to additional out-of-plane rings on the horizontal plane (Fig.3.16 b and c).

To gauge a further understanding on the occurrence of these rings, the same films were characterised by field emission gun scanning electron microscopy (FEG-SEM) to determine the link between rings and silica aggregates on the film's surface, with the data presented in Fig. 3.17. It is evident that the quantity of silica aggregates on the surface reduces as the deposition time drops from 20 s to 10 s. Previous reports have stated that the presence of the silica aggregates on the electrode surface arises from the diffusion of hydroxide ions from the electrode-electrolyte

interface and into the neighbouring bulk solution.[42] The diffusion layer thickness, calculated by $\sqrt{\pi DT}$ (where D is the diffusion coefficient of OH^- that equals 4×10^{-5} cm^2 s^{-1} and t is the time taken for the deposition process), is notably larger (500 μm) than the thickness of the aligned porous silica films. In this diffusion layer, silica continues to condense in the bulk solution, resulting in a layer of silica sphere aggregates on the film surface produced through a conventional Stöber process,[26,42] also visible in Fig. 3.17. This silica overgrowth can be removed with sticky tape[27], or reduced by either optimising the sol composition, or adjusting the deposition potential and time. The "Scotch tape test"[27] can also be used to test film adhesion on the ITO surface, and when the tape is attached directly onto the surface and peeled off, the silica remains intact.

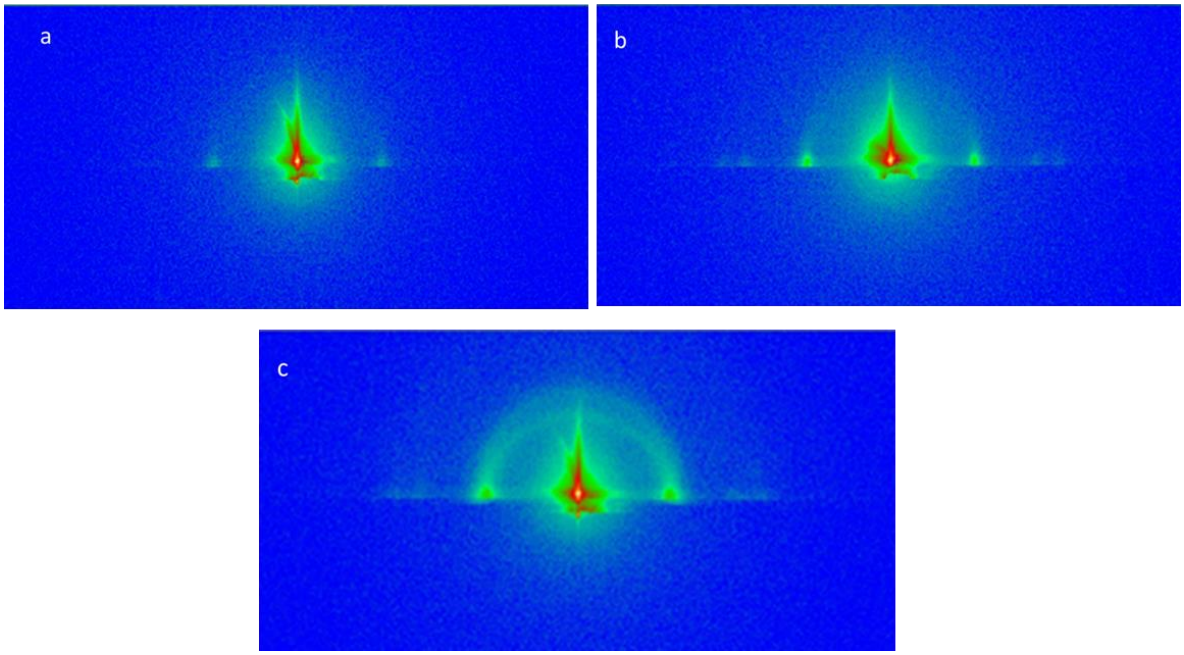

Figure 3.16 2D in-plane GISAXS patterns of EASA films with C_{22}TAB deposited at a potential of -1.25 V (vs. Ag/Ag^+) for 10 s (a), 15 s (b) and 20 s (c) on ITO electrodes.

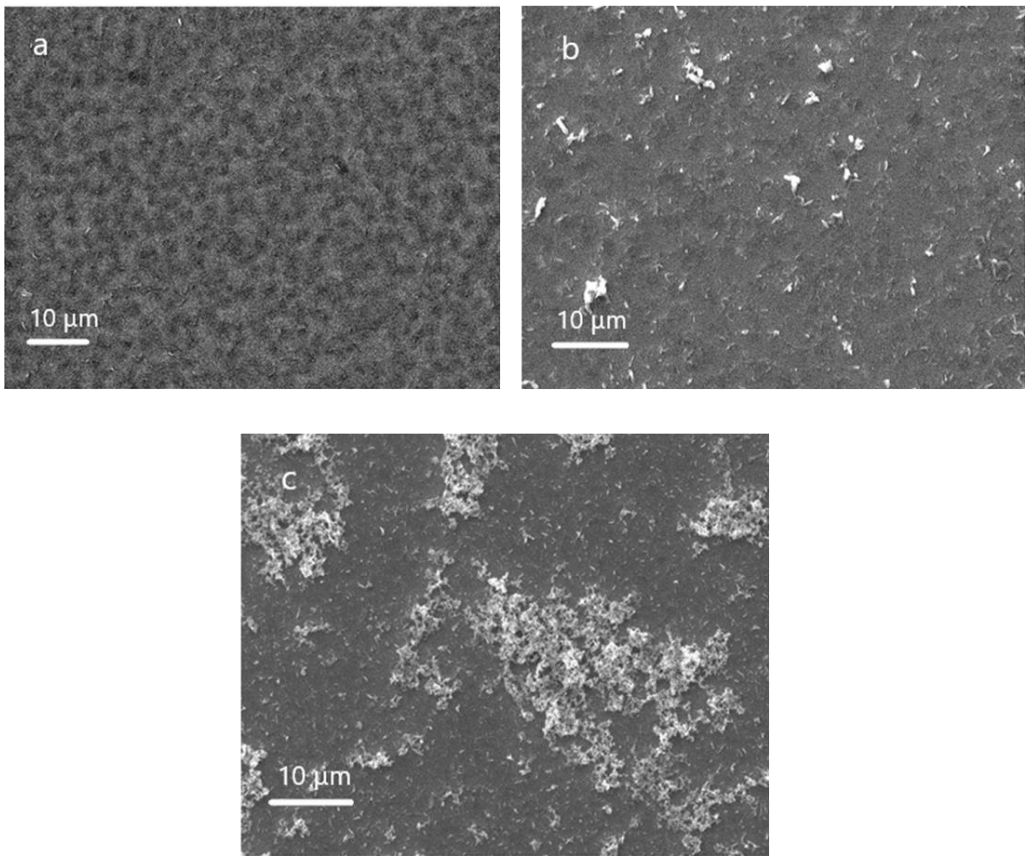

Figure 3.17 Top view SEM images of C_{22}TAB-templated silica films deposited at an applied potential of -1.25 V (Ag/Ag^+) for 10 s (a), 15 s (b) and 20 s (c) on ITO electrodes.

The silica films were soaked in a solution containing 0.2 mol dm^{-3} HCl in ethanol to remove the surfactant from the films. Top view SEM images (Fig. 3.18) provided evidence that the films were free of microcracks, pinholes or flaky areas. The coating thickness of mesoporous silica was found (through cross-sectional imaging) to be in the range of 100-150 nm, similar to films produced with C_{16}TAB under similar conditions.[27]

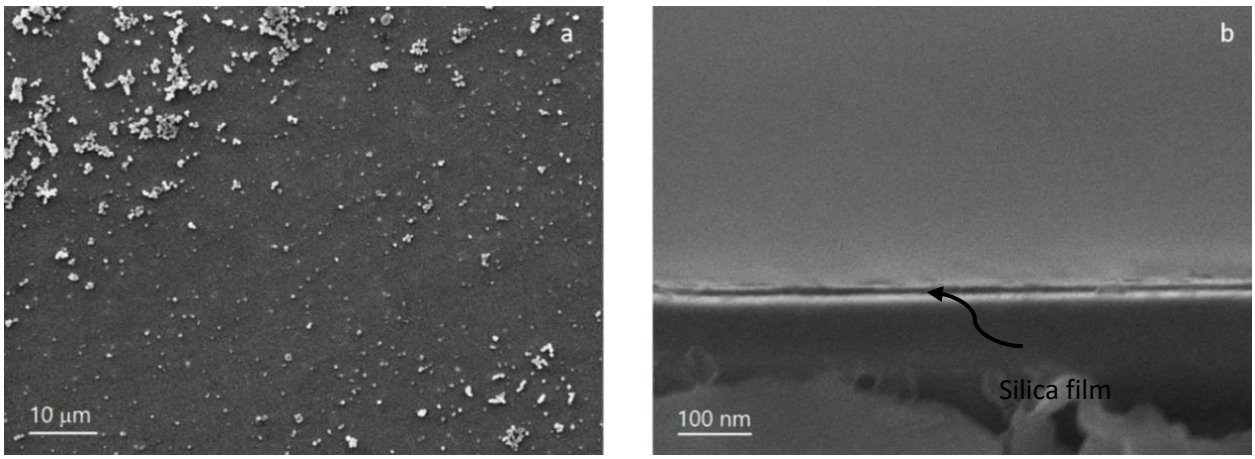

Figure 3.18 (a) Top view and (b) cross-sectional SEM image of a C_{18}TAB-templated film deposited at an applied potential of -1.25 V (Ag/Ag^+) for 20 s on an ITO electrode.

To further investigate the porous silica structure, TEM samples were prepared from C_{20}TAB, C_{22}TAB and C_{24}TAB. The GISAXS data (Fig. 3.14) had suggested the strong hexagonal order found with C_{16}TAB could be maintained up to C_{22}TAB, but that with C_{24}TAB loss of order had occurred. The images in Fig. 3.19 support this finding. Since the mesopores in the C_{20}TAB and C_{22}TAB derived silica films have vertical orientation with large hexagonal domains across the film. In contrast, the TEM samples of silica films prepared with C_{24}TAB retain the mesoporosity, but have only very small regions of hexagonal order in the pore structure. This image was taken from a flake of silica removed from the film with a scalpel which sits flat on the TEM grid, and the pores are clearly still vertical, consistent with the GISAXS data.

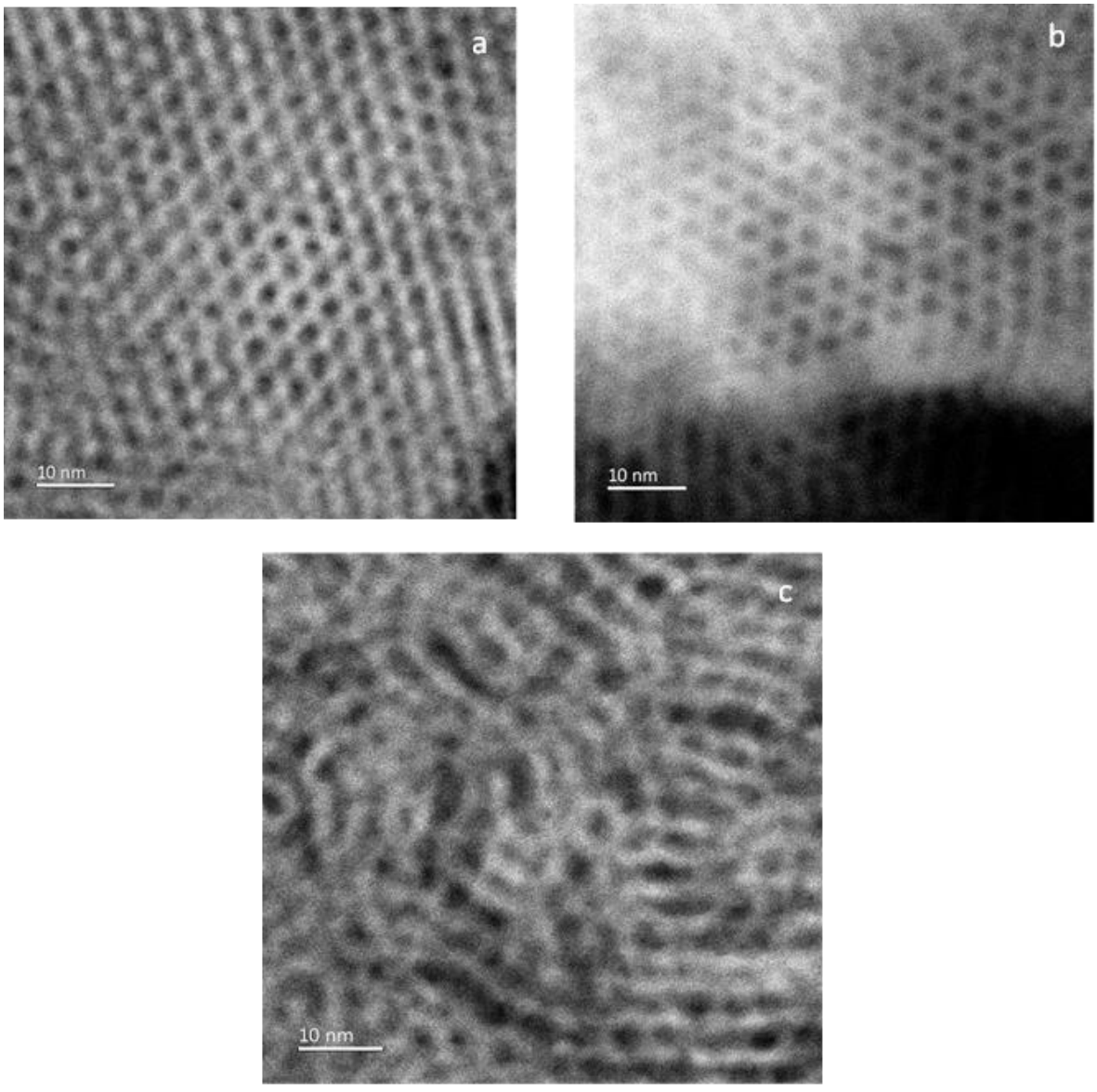

Figure 3.19 TEM images of mesoporous silica films produced with (a) C_{20}TAB, (b) C_{22}TAB and (c) C_{24}TAB deposited at -1.25 V (vs. Ag/Ag^+) for 20 s on ITO electrodes.

3.4.4 Ellipsometric porosimetry analysis of mesoporous silica films

Ellipsometric porosimetry (EP) was used to examine the silica surface of EASA films grown with different sized surfactants. EP can provide detailed information about the porosity, sorption isotherms and pore size distribution. Toluene was chosen as the probe molecule as it primarily interacts with surfaces through non-polar dispersion forces.[43,44] Changes in the refractive index values were measured during the experiment, which allowed for the volume of toluene present within the pores to be calculated using the Lorentz-Lorenz effective medium approximation.[43]

Robertson et al.[45] reported porosity measurements of mesoporous silica films produced by EASA using water, toluene, isopropyl alcohol, and methanol as the absorptive. It was understood that toluene condenses/adsorbs in the mesopores with considerable ease at low partial pressures. However, protic solvents and water suffer from hysteresis in the isotherm curves, which is caused by hydrogen bonding interactions with the silanol groups attached to the silica pore channels, therefore making toluene the solvent of choice for porosity measurements of EASA films. According to IUPAC, the adsorption isotherm is determined by the pore width and surface features of the material.[46] There are six different types of IUPAC isotherms which relate to porous materials of different shapes and sizes (see chapter 2 section 2.5).

Toluene condensed easily in the pores due to its high boiling point, enabling a drop in the partial pressure sufficient for the solvent to undergo capillary condensation, thus filling the pore channels and producing an isotherm characteristic of type I (b) and type IV (b)[47] for the silica film containing C_{16}TAB (Fig. 3.20). On the contrary, the isotherm shape does not level off at around 0.17 P/P_0 therefore, most resembling a type II isotherm as opposed to the typical type I (b) and type IV (b) isotherm shapes. This indicates the possibility of micropores present within the mesoporous network which explains the upward bend of the isotherm. Low levels of hysteresis are present throughout the adsorption-desorption branches due to the lack of hydrogen bonding between the solvent molecules and the internal pore walls or that the size of the mesopores being below the critical diameter for the completion of the capillary condensation process.

The silica films produced using C_{18}TAB showed an isotherm similar to C_{16}TAB. A similar partial pressure was required to level off the arc of the isotherm for film produced with C_{16}TAB, albeit slightly broader, which can be attributed to a greater degree of micropore and mesopore filling for the films with C_{18}TAB. Fig. 3.21 also shows minimal hysteresis present in the low partial pressure region which again suggests minimal interactions between the solvent and high silanol density within the silica pore walls, similar to that of C_{16}TAB. Solvent trapping may also be present within the silica material as the solvent fraction does not return to its origin after desorption. The reasoning behind this could be due to micropores or narrow pores found within the porous

framework having similar widths to the kinetic diameter of toluene (0.585 nm)[48] which makes diffusion through the pores challenging at these smaller sizes. In sol-gel derived materials micropores are common due to the development of the polymer network in solution.[49]

The silica film grown with C_{20}TAB (Fig. 3.22) displayed similar isotherms to those using C_{16}TAB and C_{18}TAB, however, a sudden increase in the isotherm was noticed in the minor partial pressure region and this is closely associated with type IV isotherms, which are commonly produced by mesoporous materials. The isotherm is completely reversible in the relative pressure region of 0.18-0.95 P/P_0 and there was no hysteresis present toward the higher partial pressure region in the isotherm, again indicating that any mesopores present within the silica-based material are below the critical diameter. Calleja et al[50] reported a similar isotherm curve for the MCM-41 material, albeit under nitrogen vapour sorption, with no hysteresis present in the higher partial pressure range.

For the silica film produced using C_{22}TAB (Fig 3.23.), the isotherm shape closely resembles that of a type IV (a), which is common for mesoporous materials. For this isotherm hysteresis is present, a feature which is not observed previously for films with C_{16}TAB, C_{18}TAB and C_{20}TAB, indicating that the mesopore diameter goes beyond the critical diameter therefore, mesopore filling occurs by capillary condensation. Such factors are a result of an increase in pore size beyond 4 nm. The hysteresis loop is similar to the H4 and H5 type, which is found with mesoporous zeolites, micro-mesoporous carbons, and templated silica materials.[47]

Fig. 3.20-3.23 shows the pore size distribution (PSD) curves for the silica films with increasing chain lengths, C_{16}-C_{22}, which were calculated according to the modified Kelvin equation where the pores are assumed to have cylindrical symmetry.[37] These plots display peak pore sizes in the region of 2.82, 3.24, 3.82 and 4.40 nm for the surfactants of C_{16}-C_{22}, respectively, which were all obtained from the desorption branch of the isotherms. The sharp peaks observed in the PSD plots are indicative of a high level of homogenous pore size and porosity in the ordered mesoporous silica materials. Interestingly, it is also noticed that the pore diameter increases steadily upon increasing the carbon units in the surfactant chain. This compared well with the GISAXS derived pore spacing in Fig. 3.15 and shows a fairly consistent trend.

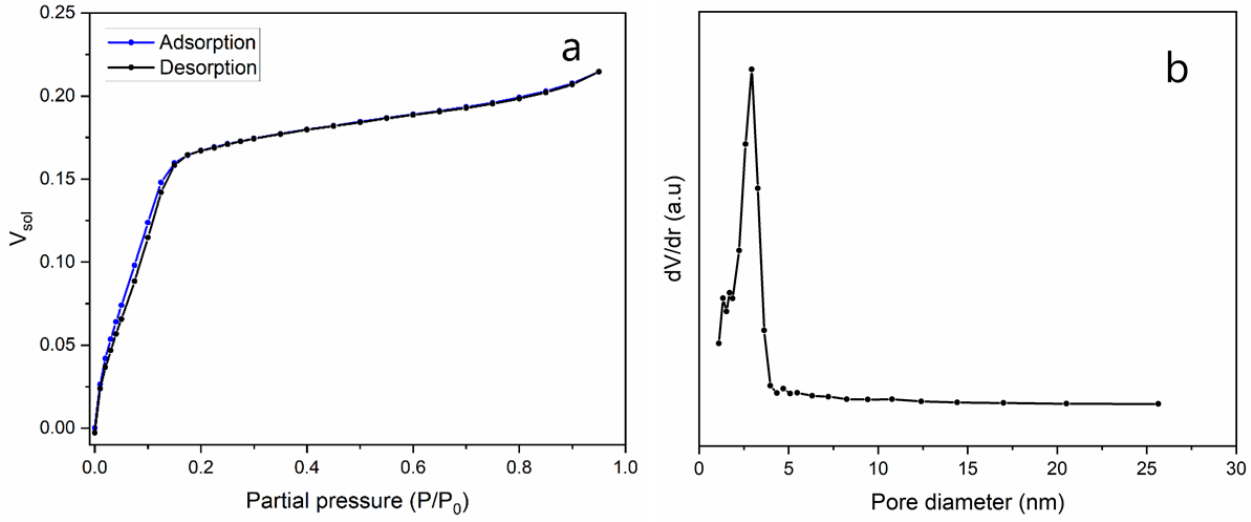

Figure 3.20 shows (a) the corresponding adsorption/desorption isotherms of the porous silica film templated with C_{16}TAB and (b) the pore size distribution of an EASA film grown with C_{16}TAB surfactant using toluene.

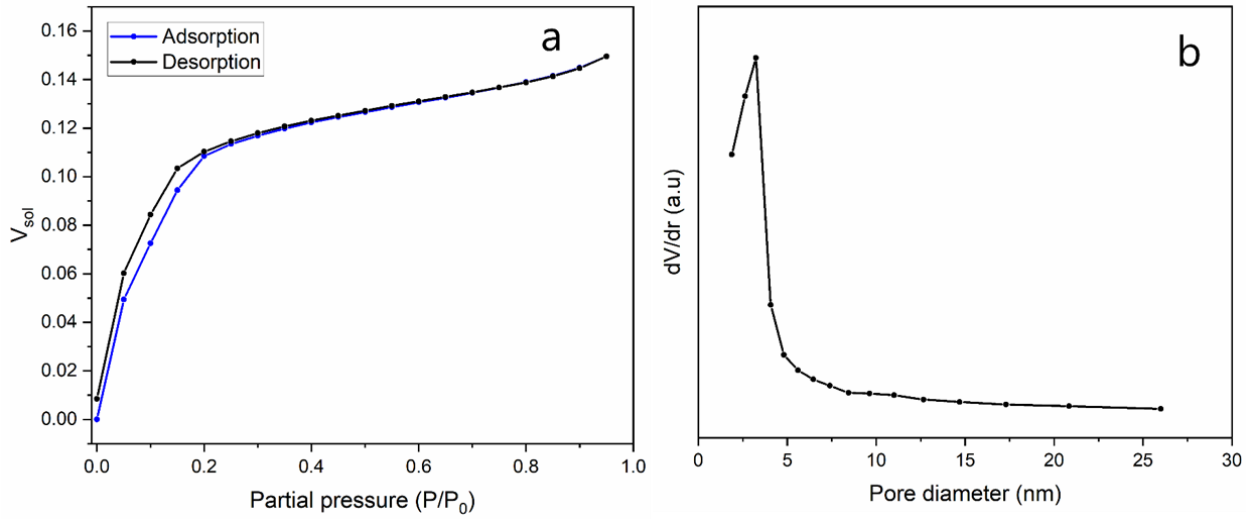

Figure 3.21 shows (a) the corresponding adsorption/desorption isotherms of the porous silica film templated with C_{18}TAB and (b) the pore size distribution of an EASA film grown with C_{18}TAB surfactant using toluene.

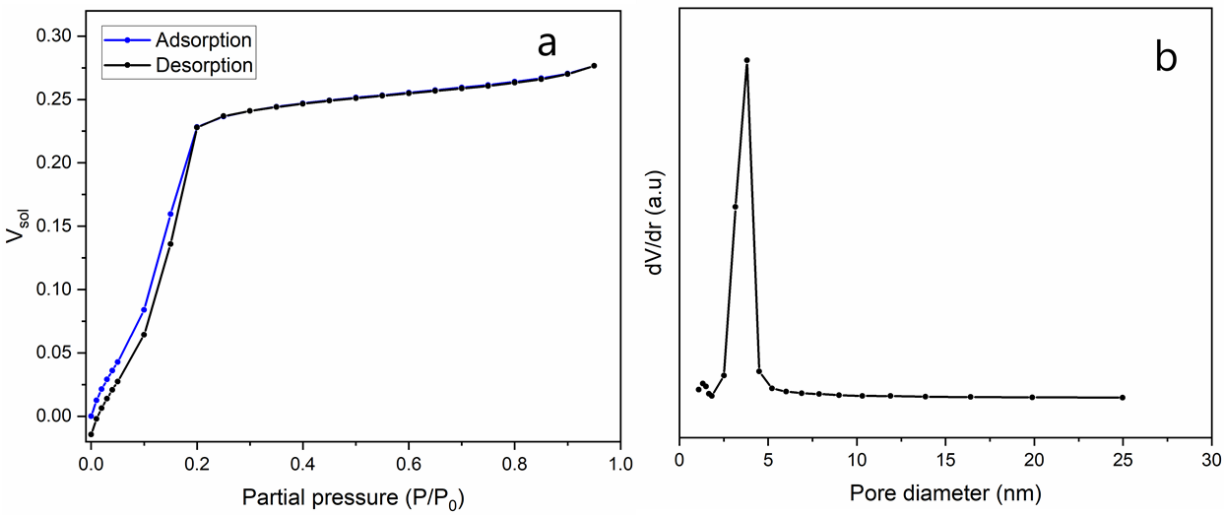

Figure 3.22 shows (a) the corresponding adsorption/desorption isotherms of the porous silica film templated with C_{20}TAB and (b) the pore size distribution of an EASA film grown with C_{20}TAB surfactant using toluene.

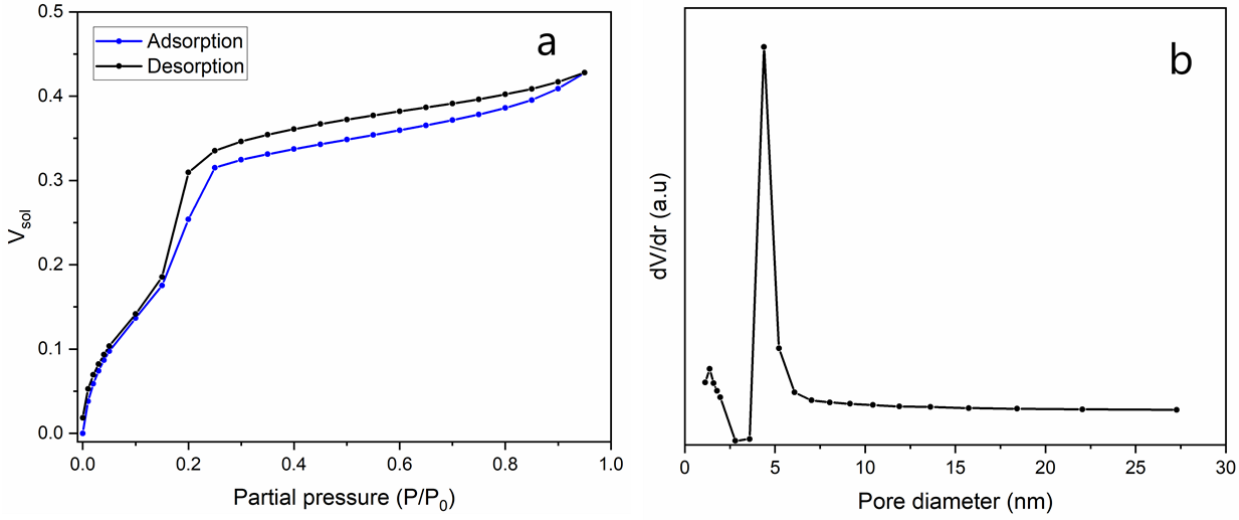

Figure 3.23 shows (a) the corresponding adsorption/desorption isotherms of the porous silica film templated with C_{22}TAB and (b) the pore size distribution of an EASA film grown with C_{22}TAB surfactant using toluene.

3.4.5 Electrochemical characterisation of the films before and after surfactant elimination

In general, porous silica films have been shown to be resistive towards charged ions in aqueous solution, and this is highly dependent on the type of mesoporous structure (i.e., hexagonal, cubic and orthorhombic) and the pore alignment. It is noted that faster electron transfer processes occur when the pore channels are directed perpendicular to the plane of the electrode rather than parallel to the electrode. The rate of charge transport is also reliant on the pore width, as larger pores tend to result in higher diffusivity of ions in comparison to films with smaller pore

sizes. Also, factors such as size, charge and concentration of redox active probes plays a pivotal role in the rate of ion transport through the film. It is to be noted that the pore transient characteristics can be modified by the addition of organic reagents to the internal silica pore walls to form new active sites, changes in the pH, surfactant size, swelling agents and fine tuning the ionic concentration of the supporting electrolyte.[51]

The isoelectric point of the silica surface is known to be in the region of 2-3 at low pH levels, to which negative ions are present on the surface. This is expected to have an adverse effect in the permeation ability of ionic probes, whereby cationic molecules ($[Ru(NH_3)_6]^{3+/2+}$) can diffuse through the mesopores, but anionic molecules ($[Fe(CN)_6]^{3-/4-}$) tend to be restricted due to unfavourable electrostatic interactions (Donnan exclusion).[52]

To that end, we investigated the pore accessibilities of mesoporous silica films templated by C_{18}TAB on ITO electrodes using 0.5 mmol dm^{-3} and 5 mmol dm^{-3} solutions of a range of redox active probes, including [FcMeOH], $[Ru(NH_3)_6]^{3+/2+}$ or $[Fe(CN)_6]^{3-/4-}$, containing 0.1 mol dm^{-3} $NaNO_3$ as the supporting electrolyte using cyclic voltammetry at a scan rate of 20 mV s^{-1}. This approach has been used previously to demonstrate pore accessibility in EASA-derived silica films,[27,53] with similar results to those shown for the films made with C_{20}TAB and C_{22}TAB (Figs. 3.25 and 3.26). To avoid potential charging effects, we chose FcMeOH as the active species because it is a neutral molecule, readily undergoing a one-electron oxidation to form the corresponding cation, as presented in equation (Eq.) 3.1.

$$[FcMeOH] \underset{+e^-}{\overset{-e^-}{\rightleftharpoons}} [FcMeOH]^+ \qquad \text{Eq 3.1}$$

Figure 3.24 compares the voltammograms of the deposited silica films before and after template extraction. As can be seen (Fig. 3.24 a), before surfactant removal (red curve), an anodic peak comes into view at + 0.73 V (vs. Ag/AgCl) which relates to formation of the ferrocenium cation, $[FcMeOH]^+$, whereas a small cathodic peak appears at approximately + 0.49 V (vs. Ag/AgCl) which correspond to reduction back to [FcMeOH]. This probe experienced difficulty in its ability to diffuse through the surfactant-blocked pores, which was deduced from the large peak potential separation (ΔE_P = 240 mV) compared to that of bare ITO (ΔE_P = 90 mV). The peak separation value of bare ITO (black curve) was closer to the theoretical Nernstian value (ΔE_P = 59 mV), resulting in the [FcMeOH] redox couple being quasi-reversible. This indicates that electron transfer kinetics for the neutral probe is slow and cannot sustain the concentrations of both oxidation and reduction processes as stated by the Nernst equation. It appears that when scanning towards more positive potentials an oxidation peak is clearly shown, however, a small reduction peak is

evident in the return scan. It was suggested that the [FcMeOH] species has the ability to dissolve in the surfactant's liquid crystalline phase therefore, enabling the active species to diffuse through the film to undergo oxidation and reduction at the electrode surface, which is similar to the electrochemical signal observed by Walcarius et al.[27] It was also apparent that prior to surfactant removal both the anodic and cathodic peak potentials were shifted towards the positive direction. Reasons for the shift in potentials could be that the reduced FcMeOH species is stabilised in the surfactant phase while the ferrocenium cation is unstable. It is also possible that electrostatic interactions between the cationic species $[FcMeOH]^+$ and surfactant cation of $C_{18}TAB$ $[C_{18}TA]^+$ also contribute to the shift in peak positions and also provide a driving force in the significant drop in the cathodic peak intensity.[54] This electrochemical phenomenon is comparable to $C_{20}TAB$ and $C_{22}TAB$ silica films (Figs. 3.25 a and 3.26 a) and EASA films reported in the literature.[27] Additionally, the shift in potential for the active species was noticed for ferrocene analogues dissolved in alcoholic solutions containing $C_{16}TAB$.[55]

After surfactant removal (blue curve), by solvent extraction in this instance, a dramatic increase in the current was observed. This can be seen by the well-defined oxidation at + 0.36 V (vs. Ag/AgCl) and reduction + 0.25 V (vs. Ag/AgCl) peaks from the CV plot which corresponds to the $[FcMeOH]^+$ and [FcMeOH] species. The peak potential separation for the surfactant removed films (ΔE_P = 110 mV) was similar to bare ITO, suggesting faster electron transfer kinetics for the redox reaction taking place at the electrode surface.

We also evaluated the accessibility of pores using the cationic $[Ru(NH_3)_6]^{3+/2+}$ redox species, whereby the reversible redox reaction of the ruthenium cation is shown below (Eq. 3.2). In Fig. 3.24 b, it was found that no faradaic current was observed before extracting the surfactant (red curve). A typical oxidation and reduction peak was noticed after extracting the surfactant (blue curve), which was seen previously for the [FcMeOH] active species (Fig. 3.24 a) The peak separation potential (ΔE_P = 260 mV) was similar to that for bare ITO (black curve) (ΔE_P = 194 mV). Furthermore, the peak current of bare ITO was slightly smaller than the mesoporous silica coated ITO electrode, owing to the cations having the propensity to build up and concentrate at the electrode surface.[27]

$$[Ru(NH_3)_6]^{2+} \underset{+e^-}{\overset{-e^-}{\rightleftharpoons}} [Ru(NH_3)_6]^{3+} \qquad \text{Eq 3.2}$$

This study also included the anionic ferricyanide redox species (electrochemical equation for ferricyanide is shown in Eq. 3.3) to compare between the current intensities from the CV profiles on either bare or mesoporous silica coated ITO electrodes. It was apparent that a reduction in the

current signals occurred (Fig. 3.24 c and d) for films before surfactant extraction (red curve), which implies that the surfactant molecules are acting as preventative gates and thus limiting the active species from diffusing through the pore channels towards the ITO surface. Interestingly, the current from the CV profiles was suppressed, which suggests that the film contains no microcracks and so confirming the films to be of high quality. The reduction in current was similar to that for the ruthenium active species discussed above.

Upon removing the surfactant template (blue curve), Figs. 3.24 c and d, reveal a reduction in the peak intensity for the anionic species. This is attributed to the permselective nature of the mesochannels to attract opposite ions and to resist like-for-like ions to balance the surface charges. A further drop in the current intensity is often seen for anionic species at lower concentrations of supporting electrolyte.[51] The drop in current could be associated with the Gibbs-Donnan effect[53] which is also seen for charged ions in the region of semi-permeable membranes.[56] In Fig 3.24 c (blue curve) an anodic oxidation peak is observed at + 0.35 V (vs. Ag/AgCl) which associates with the $[Fe(CN)_6]^{4-}$ species, whereas a cathodic reduction peak is seen at + 0.19 V (vs. Ag/AgCl), which relates to the $[Fe(CN)_6]^{3-}$ species. The process is indicative of slow electron transfer kinetics between the silica coated ITO electrode and the analyte, as the peak potential separation (ΔE_P = 160 mV) is significantly larger than for bare ITO (ΔE_P = 90 mV).

$$[Fe(CN)_6]^{4-} \underset{+e^-}{\overset{-e^-}{\rightleftharpoons}} [Fe(CN)_6]^{3-} \qquad \text{Eq 3.3}$$

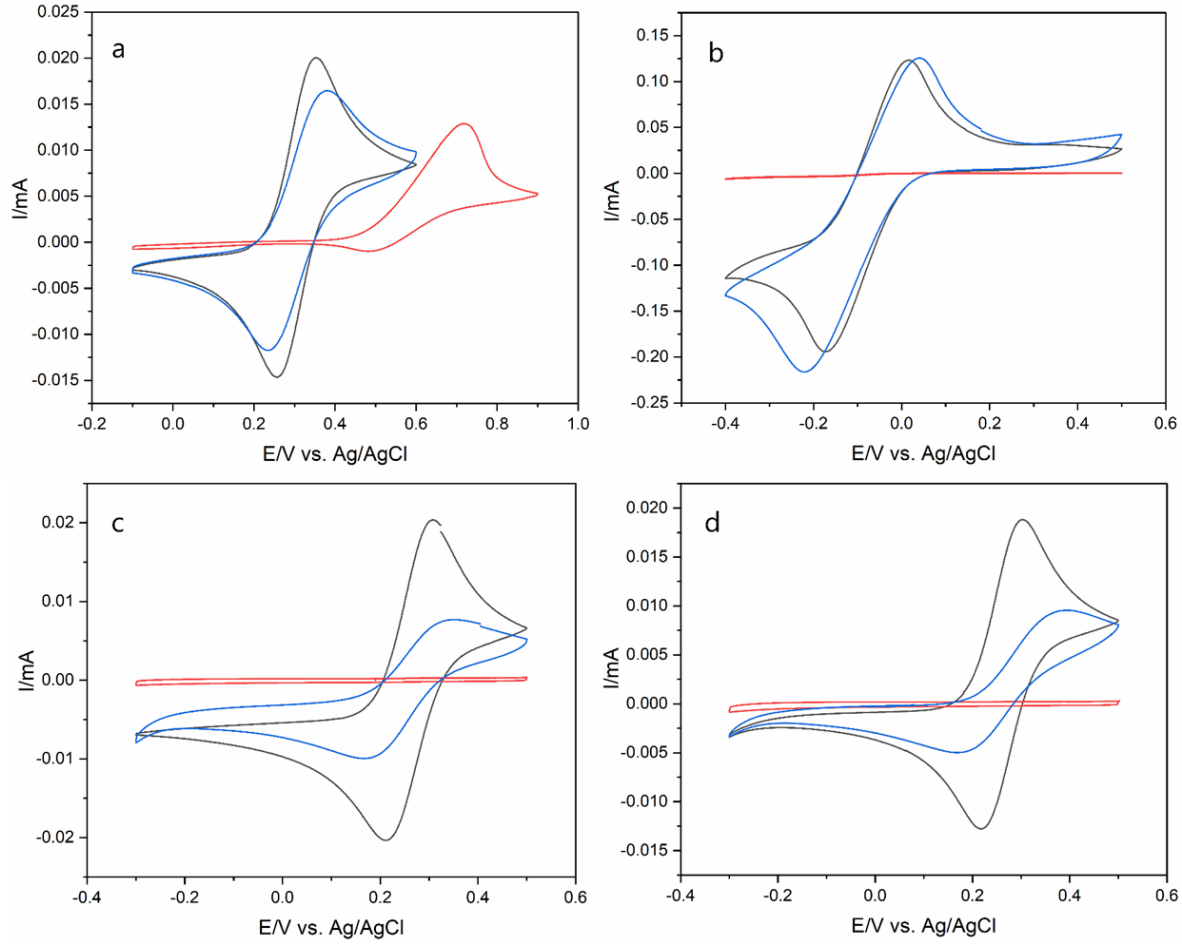

Figure 3.24 Cyclic Voltammograms (20 mV s^{-1} sweep rate) of (a) 0.5 mmol dm^{-3} [FcMeOH], (b) 5 mmol dm^{-3} $[Ru(NH_3)_6]^{3+/2+}$ and (c), (d) 0.5 mmol dm^{-3} $[Fe(CN)_6]^{3-/4-}$ in 0.1 mol dm^{-3} $NaNO_{3(aq)}$ on bare ITO electrode (black line), and with a silica film before surfactant removal (red line) and after surfactant removal (blue line). The generated mesoporous silica film using C_{18}TAB as the surfactant was deposited at -1.25 V (vs. Ag/AgCl) for 20 s on an ITO electrode.

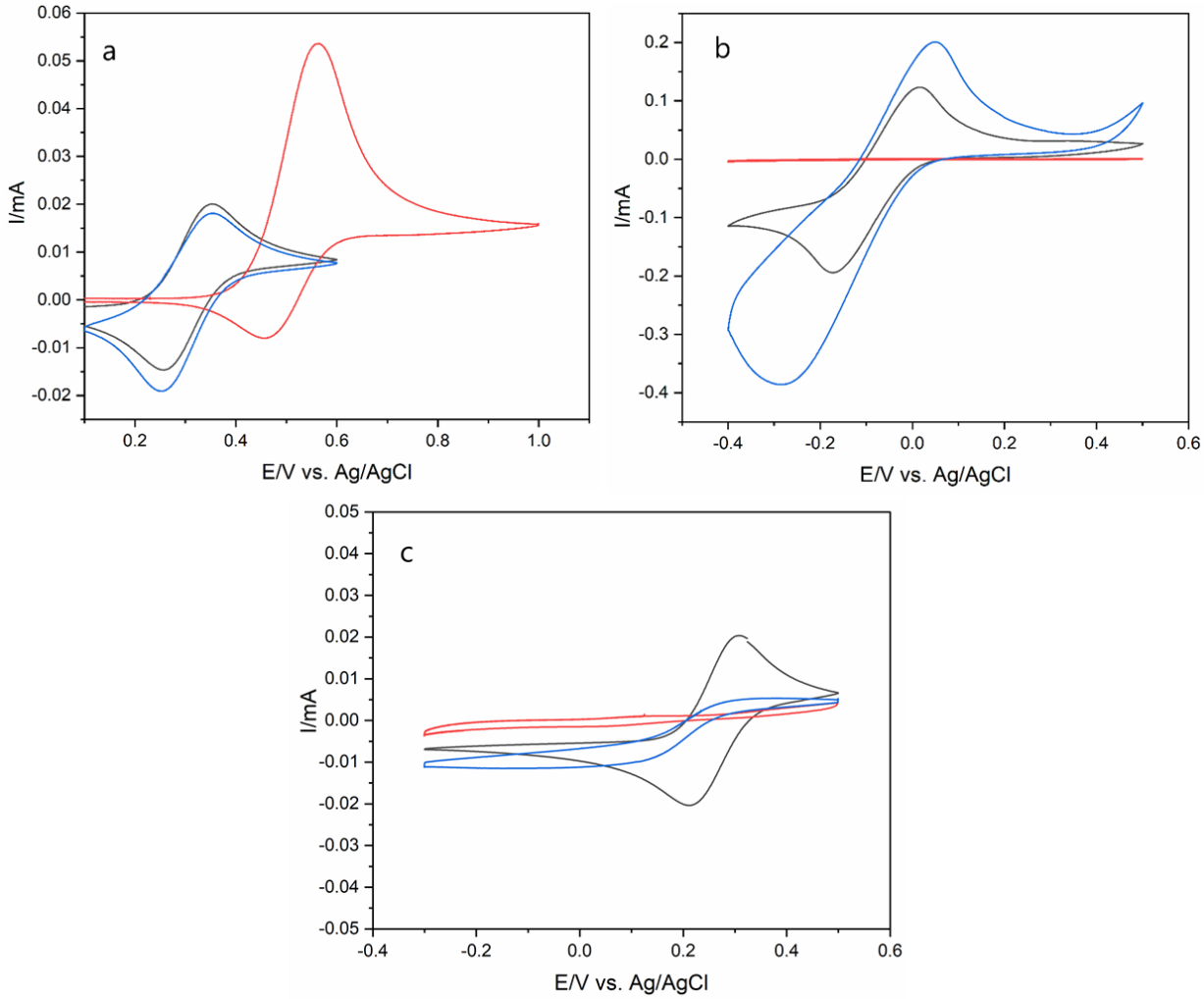

Figure 3.25 Cyclic Voltammograms (20 mV s^{-1} sweep rate) of (a) 0.5 mmol dm^{-3} [FcMeOH], (b) 5 mmol dm^{-3} $[Ru(NH_3)_6]^{3+/2+}$ and (c) 0.5 mmol dm^{-3} $[Fe(CN)_6]^{3-/4-}$ in 0.1 mol dm^{-3} $NaNO_3$(aq) on bare ITO electrode (black line), before surfactant removal (red line) and after surfactant removal (blue line). The generated mesoporous silica film using C_{20}TAB as the surfactant was deposited at -1.25 V (vs. Ag/AgCl) for 20 s on an ITO electrode.

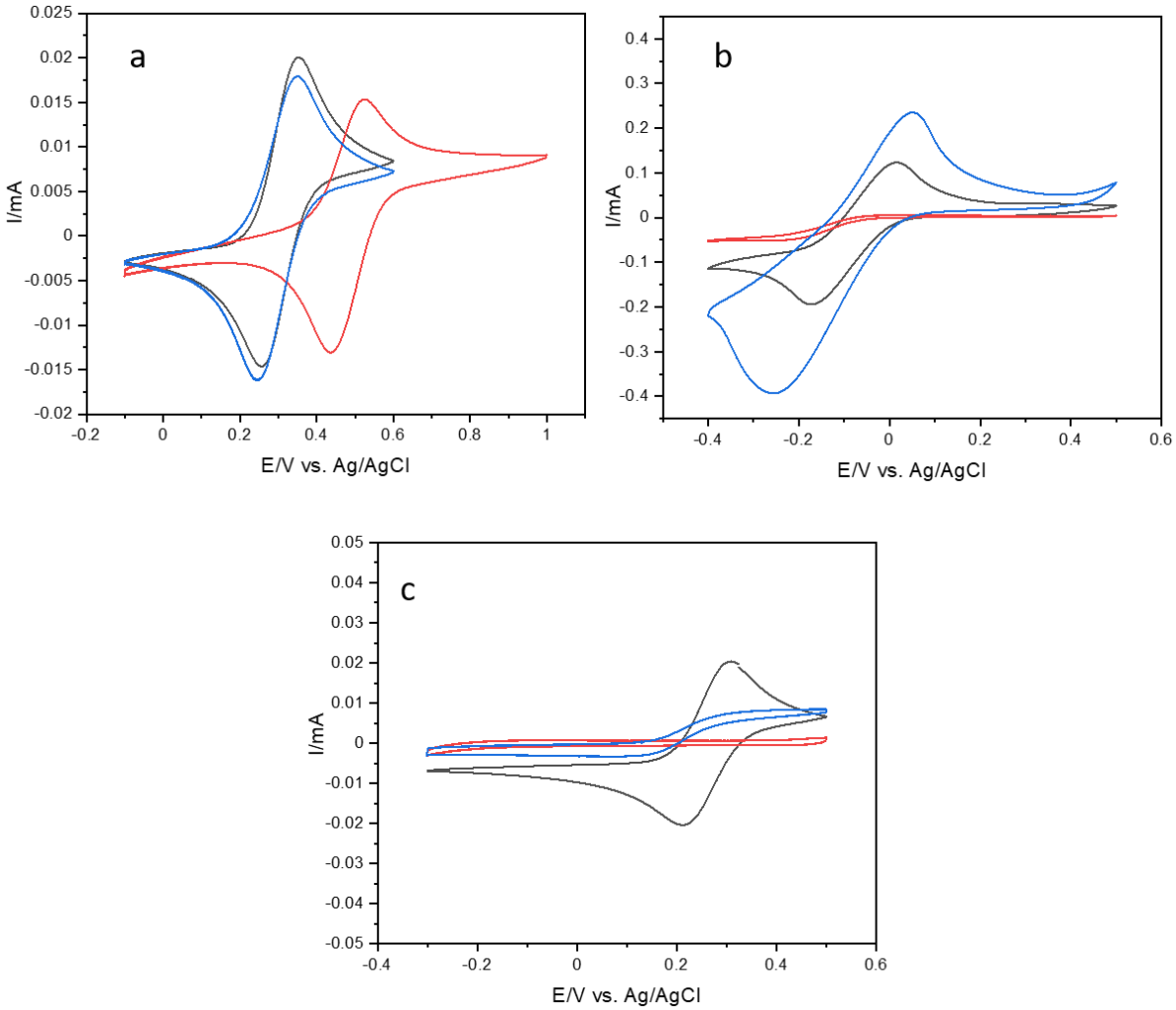

Figure 3.26 Cyclic Voltammograms (20 mV s^{-1} sweep rate) of (a) 0.5 mmol dm^{-3} [FcMeOH], (b) 5 mmol dm^{-3} $[Ru(NH_3)_6]^{3+/2+}$ and (c) 0.5 mmol dm^{-3} $[Fe(CN)_6]^{3-/4-}$ in 0.1 mol dm^{-3} $NaNO_3$(aq) on bare ITO electrode (black line), before surfactant removal (red line) and after surfactant removal (blue line). The generated mesoporous silica film using C_{22}TAB as the surfactant was deposited at -1.25 V (vs. Ag/AgCl) for 20 s on an ITO electrode.

Mesoporous silica films with larger pore diameters and good hexagonal ordering could improve ionic diffusion rates and charge selectivity of redox active species. For instance, Walcarius' group studied porosity measurements of EASA films grown with C_{12}TAB to C_{18}TAB using FcMeOH as the redox probe. It was concluded that the increase in current from the CV plots was associated with increases to the lipophilic surfactant chain.[34]

As demonstrated in the CVs presented in Figure 3.27 a-c (Fig. 3.28-3.31), extending the alkyl chain length of surfactants (C_{14}, C_{16}, C_{18}, C_{20} and C_{22}) affects the rate of diffusion of the active species into the porous silica medium. The CVs were recorded at increasing scan rates between 2 and 100 mV s^{-1} for [FcMeOH] and $[Ru(NH_3)_6]^{3+/2+}$ and between 2 and 20 mV s^{-1} for $[Fe(CN)_6]^{4-/3-}$, as the CV profiles became distorted at faster scan rates for the latter. The peak potential (i_p) as the function of the square root of scan rate ($v^{1/2}$) is shown in Fig. 3.27 d-f., for 0.5 mmol dm^{-3} and 5 mmol dm^{-3} solutions of [FcMeOH], $[Fe(CN)_6]^{4-/3}$ and $[Ru(NH_3)_6]^{3+/2+}$ in an aqueous solution containing 0.1 mol dm^{-3} $NaNO_3$. A linear trend is observed for the Ip vs. $v^{1/2}$ scan rate, indicating that mass transport is governed by diffusion. For electron transfer reactions of diffusion processes in solution it is possible to use the Randles- Sevcik (RS) equation to determine the diffusion coefficients of redox active species through the porous silica medium.

The RS equation (Eq. 3.4) describes how the current increases with the square root of scan rate. I_p is the peak current, n is the number of electrons transferred in the oxidation and reduction reaction, A is the electrode area, D is the diffusion coefficient, T is the temperature and C is the concentration of the bulk solution. In the CV plots, the peak potential separations are greater than 59 mV for the various redox active species, indicating effects due to IR drop and possible quasi reversible behaviour. The RS equation applies to electrochemically reversible systems, so the calculated diffusion coefficients will be affected by resistance effects. The shift in peak current position with scan rate is likely due to IR drop. In Fig. 3.27 b, the increase in concentration of the ruthenium species results in a dramatic increase in current in comparison to the lower concentration of FcMeOH and $[Fe(CN)_6]^{4-/3-}$, indicating a greater IR drop.

$$i_p = (2.69 \times 10^5)\, n^{3/2} A C D^{1/2} v^{1/2} \qquad \text{Eq 3.4}$$

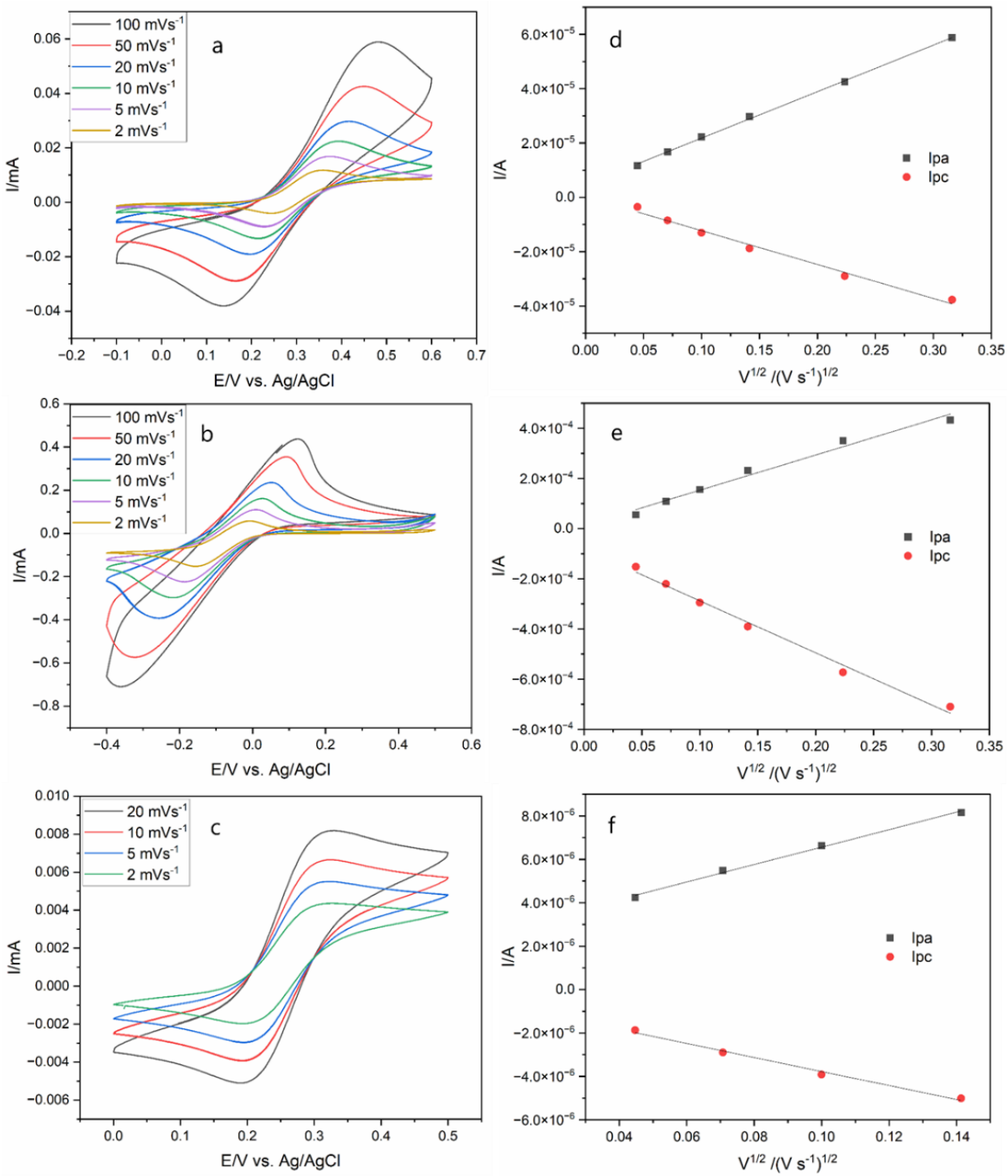

Figure 3.27 The CVs of (a) 0.5 mmol dm^{-3} [FcMeOH], (b) 5 mmol dm^{-3} $[Ru(NH_3)_6]^{3+/2+}$ and (c) 0.5 mmol dm^{-3} $[Fe(CN)_6]^{4-/3-}$ in 0.1 mol dm^{-3} $NaNO_3$ at various scan rates (2, 5, 10, 20, 50 and 100 mV s^{-1} for the [FcMeOH] and $[Ru(NH_3)_6]^{3+/2+}$ redox species and 2, 5, 10 and 20 mV s^{-1} for the $[Fe(CN)_6]^{4-/3-}$ redox couple); reliance of peak current as a function of square root of scan rates for the film containing C_{22}TAB deposited at -1.25 V (vs. Ag/AgCl) for 20 s on an ITO electrode. All experiments were carried out after surfactant removal: (d) [FcMeOH], (e) $[Ru(NH_3)_6]^{3+/2+}$ and (f) $[Fe(CN)_6]^{4-/3-}$.

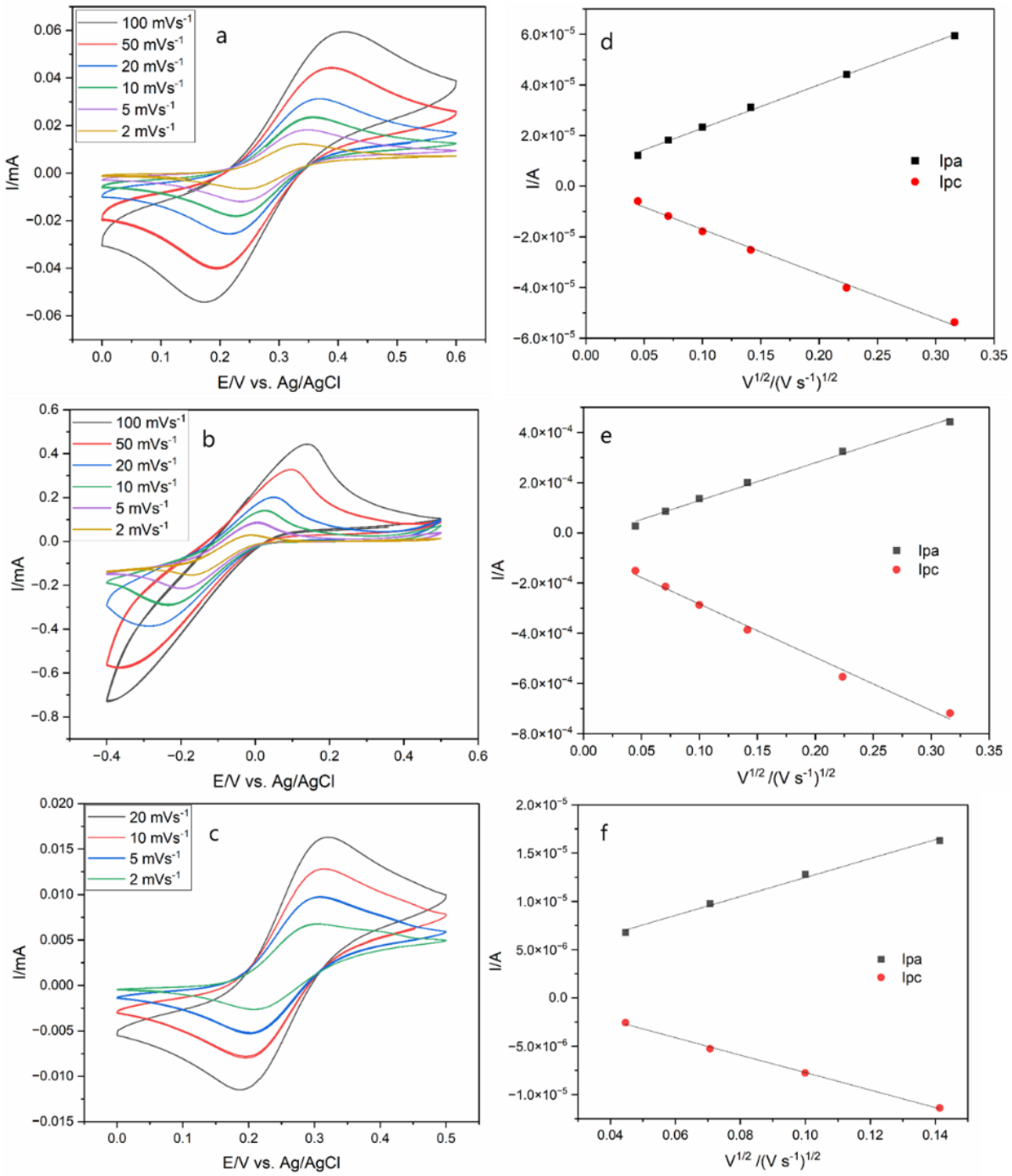

Figure 3.28 The CVs of (a) 0.5 mmol dm^{-3} [FcMeOH], (b) 5 mmol dm^{-3} $[Ru(NH_3)_6]^{3+/2+}$ and (c) 0.5 mmol dm^{-3} $[Fe(CN)_6]^{4-/3-}$ at various scan rates (2, 5, 10, 20, 50 and 100 mV s^{-1} for [FcMeOH] and $[Ru(NH_3)_6]^{3+/2+}$ redox species and 2, 5, 10 and 20 mV s^{-1} for $[Fe(CN)_6]^{4-/3-}$ redox couple); reliance of peak current as a function of square root of scan rates for the film containing C_{20}TAB deposited at -1.25 V (vs. Ag/AgCl) for 20 s on an ITO electrode. All experiments were carried out after surfactant removal: (d) [FcMeOH], (e) $[Ru(NH_3)_6]^{3+/2+}$ and (f) $[Fe(CN)_6]^{4-/3-}$.

The RS equation may be modified to take account of the proportion of the surface that is accessible to the electrolyte by including a porosity parameter as shown in Eq. 3.5.[57] Porosity (φ) values calculated from the pore spacing and pore diameter measurements were in the range between 0.1 and 0.7 (as shown in Table 3.2). The apparent diffusion coefficients calculated from the gradient of the linear plots, and assuming that the concentrations of the redox species in the film are the same as those in the bulk solution, are given in Table 3.3 together with the surfactants and the active species. The apparent diffusion coefficient increases with the size of surfactant used to produce the film, providing further evidence of pore expansion and easier electrochemical access through the pores with surfactant chain length. However, it is noted that the silica film will change the concentration of the active species in the pores relative to the bulk solution to some extent. For example, the D values for $[Fe(CN)_6]^{4-/3-}$ species are smaller than for the [FcMeOH] and $[Ru(NH_3)_6]^{3+/2+}$ species due to the Gibbs-Donnan effect mentioned earlier.

Similar D values were obtained for an EASA film templated by C_{16}TAB using FcEtOH as the redox probe molecule (9×10^{-8} cm^2 s^{-1}), as reported by Goux et al.[34] Such small D values were also observed for porous silicas prepared by EISA and non-porous silica films at $\sim 1 \times 10^{-8}$ cm^2 s^{-1} and $< 1 \times 10^{-9}$ cm^2 s^{-1} respectively.

$$i_p = (2.69 \times 10^5)\, n^{3/2}\, \varphi A C D^{1/2}\, v^{1/2} \qquad \text{Eq 3.5}$$

Table 3.2 The porosity values (φ) determined from the pore diameter and pore spacing measurements.

Surfactants	Pore diameter / nm	Pore area / nm^2	Spacing/ nm	Unit cell area / nm^2	Porosity (fraction)
C_{14}	1.3	1.3	4.0	13.8	0.1
C_{16}	2.8	6.2	4.4	16.5	0.4
C_{18}	3.2	8.2	4.8	19.9	0.4
C_{20}	3.8	11.5	5.1	22.1	0.5
C_{22}	4.4	15.2	5.1	22.5	0.7

Table 3.3 Apparent diffusion coefficients of EASA films with surfactants of increasing chain length using a range of redox active probes.

Surfactant	$D_{[FcMeOH]}$	$D_{[Ru(NH3)6]3+/2+}$	$D_{[Fe(CN)6]4-/3-}$
C_{14}TAB	7.4×10^{-7} cm^2 s^{-1}	6.8×10^{-7} cm^2 s^{-1}	1.4×10^{-7} cm^2 s^{-1}
C_{16}TAB	8.9×10^{-7} cm^2 s^{-1}	8.2×10^{-7} cm^2 s^{-1}	2.8×10^{-7} cm^2 s^{-1}
C_{18}TAB	9.4×10^{-7} cm^2 s^{-1}	1.1×10^{-6} cm^2 s^{-1}	3.8×10^{-7} cm^2 s^{-1}
C_{20}TAB	2.3×10^{-6} cm^2 s^{-1}	2.2×10^{-6} cm^2 s^{-1}	5.2×10^{-7} cm^2 s^{-1}
C_{22}TAB	4.6×10^{-6} cm^2 s^{-1}	3.5×10^{-6} cm^2 s^{-1}	8.6×10^{-7} cm^2 s^{-1}

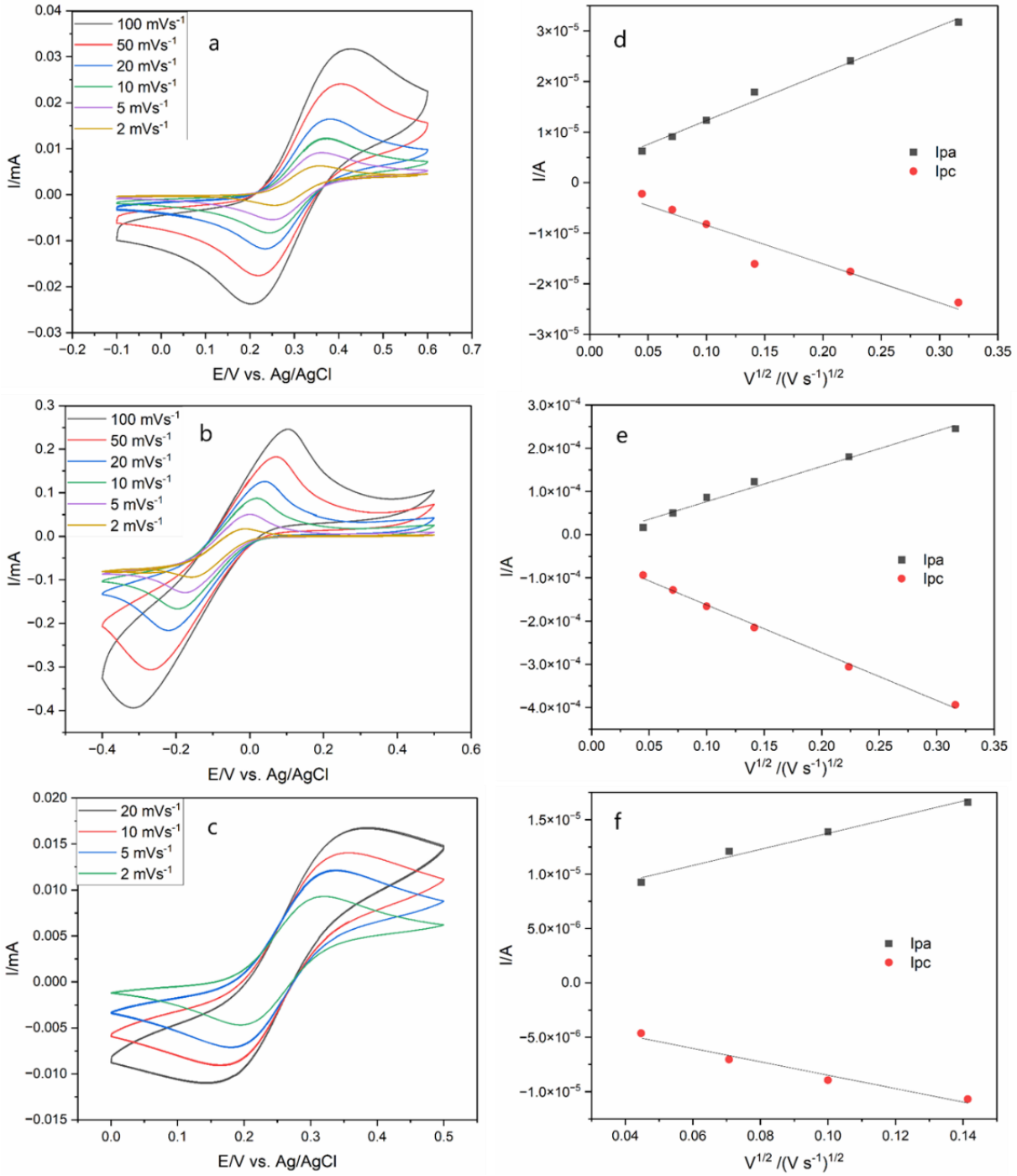

Figure 3.29 The CVs of (a) 0.5 mmol dm^{-3} [FcMeOH], (b) 5 mmol dm^{-3} $[Ru(NH_3)_6]^{3+/2+}$ and (c) 0.5 mmol dm^{-3} $[Fe(CN)_6]^{4-/3-}$ at various scan rates (2, 5, 10, 20, 50 and 100 mV s^{-1} for [FcMeOH] and $[Ru(NH_3)_6]^{3+/2+}$ redox species and 2, 5, 10 and 20 mV s^{-1} for $[Fe(CN)_6]^{4-/3-}$ redox couple); reliance of peak current as a function of square root of scan rates for the film containing C_{18}TAB deposited at -1.25 V (vs. Ag/AgCl) for 20 s on an ITO electrode. All experiments were carried out after surfactant removal: (d) [FcMeOH], (e) $[Ru(NH_3)_6]^{3+/2+}$ and (f) $[Fe(CN)_6]^{4-/3-}$.

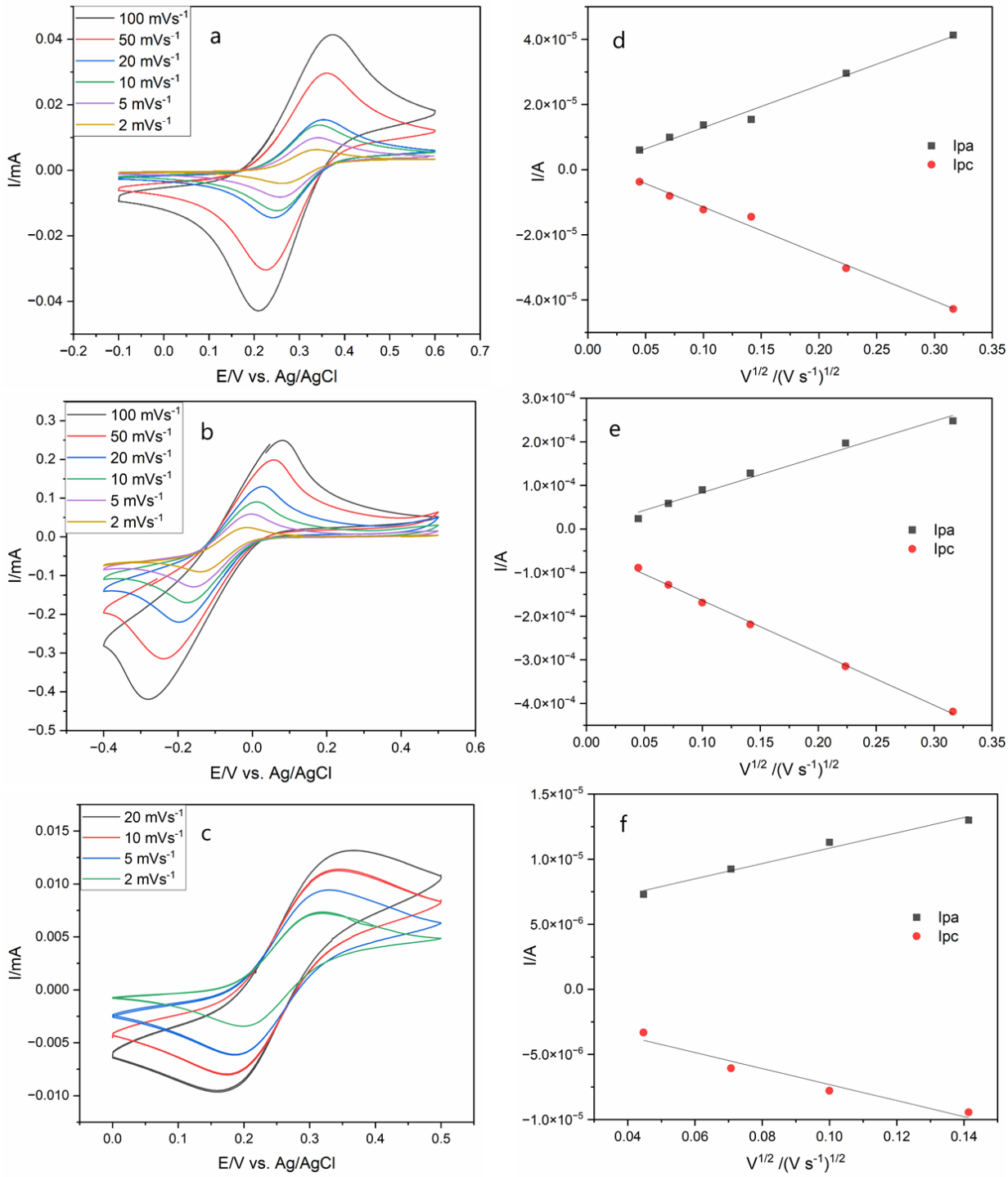

Figure 3.30 The CVs of (a) 0.5 mmol dm^{-3} [FcMeOH], (b) 5 mmol dm^{-3} $[Ru(NH_3)_6]^{3+/2+}$ and (c) 0.5 mmol dm^{-3} $[Fe(CN)_6]^{4-/3-}$ at various scan rates (2, 5, 10, 20, 50 and 100 mV s^{-1} for [FcMeOH] and $[Ru(NH_3)_6]^{3+/2+}$ redox species and 2, 5, 10 and 20 mV s^{-1} for $[Fe(CN)_6]^{4-/3-}$ redox couple); reliance of peak current as a function of square root of scan rates for the film containing C_{16}TAB deposited at -1.25 V (vs. Ag/AgCl) for 20 s on an ITO electrode. All experiments were carried out after surfactant removal: (d) [FcMeOH], (e) $[Ru(NH_3)_6]^{3+/2+}$ and (f) $[Fe(CN)_6]^{4-/3-}$.

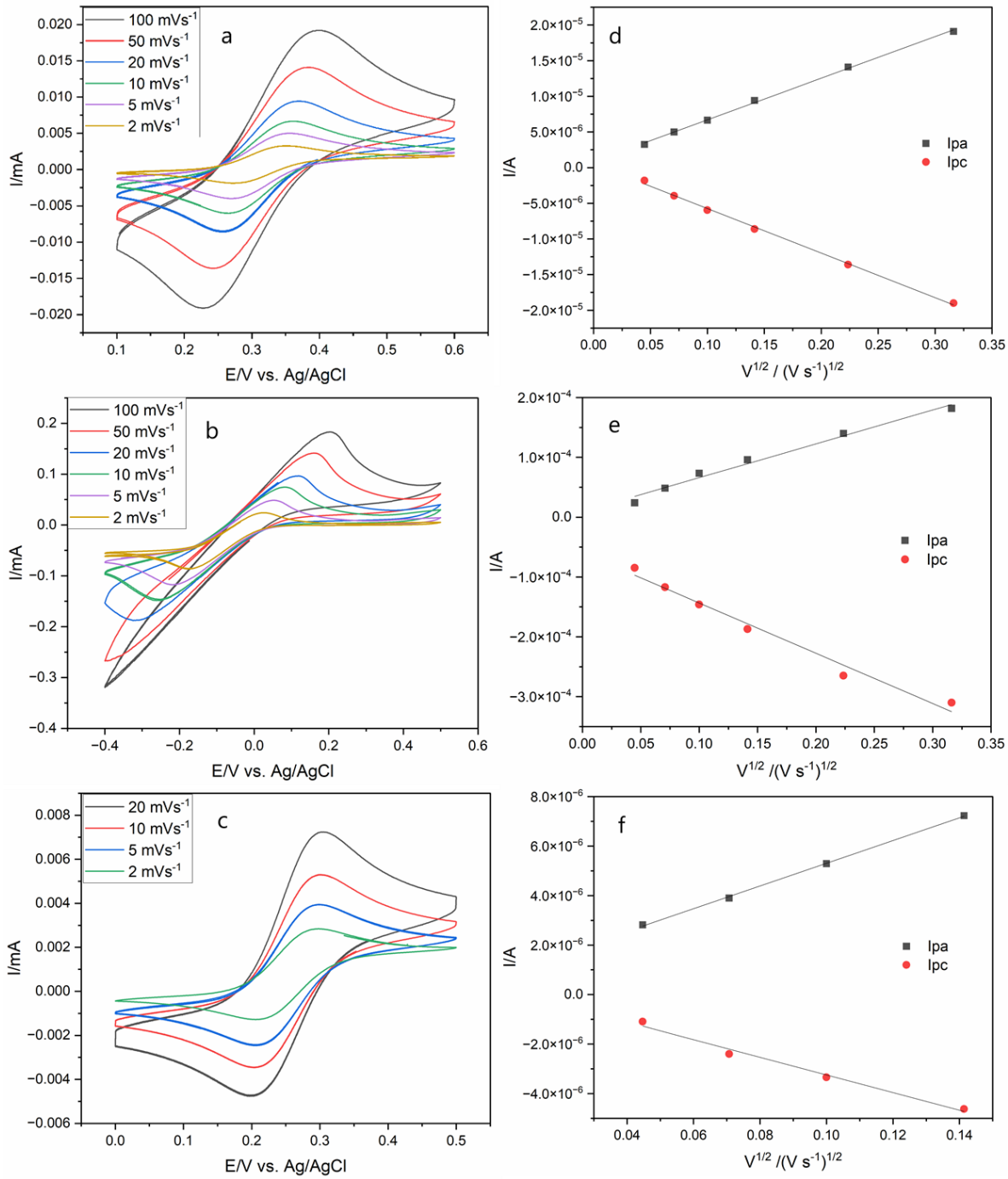

Figure 3.31 The CVs of (a) 0.5 mmol dm^{-3} [FcMeOH], (b) 5 mmol dm^{-3} $[Ru(NH_3)_6]^{3+/2+}$ and (c) 0.5 mmol dm^{-3} $[Fe(CN)_6]^{4-/3-}$ at various scan rates (2, 5, 10, 20, 50 and 100 mV s^{-1} for [FcMeOH] and $[Ru(NH_3)_6]^{3+/2+}$ redox species and 2, 5, 10 and 20 mV s^{-1} for $[Fe(CN)_6]^{4-/3-}$ redox couple); reliance of peak current as a function of square root of scan rates for the film containing C_{14}TAB deposited at -1.25 V (vs. Ag/AgCl) for 20 s on an ITO electrode. All experiments were carried out after surfactant removal: (d) [FcMeOH], (e) $[Ru(NH_3)_6]^{3+/2+}$ and (f) $[Fe(CN)_6]^{4-/3-}$.

3.4.6 Conclusions

Ordered mesoporous silica films with vertically aligned nanopores were produced by an electrochemically driven sol-gel method (EASA). To date, CTAB has been a widely chosen surfactant for the synthesis of mesoporous silica films. However, the system experiences molecular sieving properties (i.e. narrow pore width). Increasing the pore diameter was the main objective of this study. This was achieved by extending the alkyl chain length in the $[Me_3NR]Br$ surfactant from 16 to 22 carbons, which resulted in larger pore diameters while retaining the ordering. Conversely, the film structure started to degrade when using $C_{24}TAB$ in the sol electrolyte, indicating a constraint in response to micelle expansion using linear chained surfactants. The ion diffusion rates using redox active probes were found to increase with surfactant size. Additional features of this work focussed on porosity measurements which increased from 2.8 nm using $C_{16}TAB$ to 4.4 nm using $C_{22}TAB$. The expanded pores in these vertically aligned mesoporous silica films may make them more amenable as templates for electrochemical deposition of nanowires, and change their behaviour in sensing applications, e.g., for electrochemical sensors.

3.4.7 References

(1) Li, C.; Iqbal, M.; Lin, J.; Luo, X.; Jiang, B.; Malgras, V.; Wu, K. C. W.; Kim, J.; Yamauchi, Y. Electrochemical Deposition: An Advanced Approach for Templated Synthesis of Nanoporous Metal Architectures. *Acc. Chem. Res.* **2018**, *51* (8), 1764–1773.

(2) Hao, J.; Yang, Y.; Zhao, J.; Liu, X.; Endres, F.; Chi, C.; Wang, B.; Liu, X.; Li, Y. Ionic Liquid Electrodeposition of Strain-Released Germanium Nanowires as Stable Anodes for Lithium Ion Batteries. *Nanoscale* **2017**, *9* (24), 8481–8488.

(3) Kim, H.; Cho, J. Hard Templating Synthesis of Mesoporous and Nanowire SnO2 Lithium Battery Anode Materials. *J. Mater. Chem.* **2008**, *18* (7), 771–775.

(4) Tan, M.; Hao, Y.; Deng, Y.; Yan, D.; Wu, Z. Tilt-Structure and High-Performance of Hierarchical Bi1.5Sb0.5Te3 Nanopillar Arrays. *Sci. Rep.* **2018**, *8* (1), 1–9.

(5) Xu, Y.; Ding, Q.; Li, L.; Xie, Z.; Jiang, G. Facile Fabrication of Porous Co3O4 Nanowires for High Performance Supercapacitors. *New J. Chem.* **2018**, *42* (24), 20069–20073.

(6) Kanno, Y.; Suzuki, T.; Yamauchi, Y.; Kuroda, K. Preparation of Au Nanowire Films by Electrodeposition Using Mesoporous Silica Films as a Template: Vital Effect of Vertically Oriented Mesopores on a Substrate. *J. Phys. Chem. C* **2012**, *116* (46), 24672–24680.

(7) Wu, C. W.; Yamauchi, Y.; Ohsuna, T.; Kuroda, K. Structural Study of Highly Ordered Mesoporous Silica Thin Films and Replicated Pt Nanowires by High-Resolution Scanning Electron Microscopy (HRSEM). *J. Mater. Chem.* **2006**, *16* (30), 3091–3098.

(8) Bartlett, P. N.; Beanland, R.; Burt, J.; Hasan, M. M.; Hector, A. L.; Kashtiban, R. J.; Levason, W.; Lodge, A. W.; Marks, S.; Naik, J.; Rind, A.; Reid, G.; Richardson, P. W.; Sloan, J.; Smith, D. C. Exploration of the Smallest Diameter Tin Nanowires Achievable with Electrodeposition: Sub 7 Nm Sn Nanowires Produced by Electrodeposition from a Supercritical Fluid. *Nano Lett.* **2018**, *18* (2), 941–947.

(9) Xu, J.; Zhang, W.; Morris, M. A.; Holmes, J. D. The Formation of Ordered Bismuth Nanowire Arrays within Mesoporous Silica Templates. *Mater. Chem. Phys.* **2007**, *104* (1), 50–55.

(10) Nasir, T.; Zhang, L.; Vilà, N.; Herzog, G.; Walcarius, A. Electrografting of 3-Aminopropyltriethoxysilane on a Glassy Carbon Electrode for the Improved Adhesion of Vertically Oriented Mesoporous Silica Thin Films. *Langmuir* **2016**, *32* (17), 4323–4332.

(11) Rohlfing, D. F.; Rathouský, J.; Rohlfing, Y.; Bartels, O.; Wark, M. Functionalized Mesoporous Silica Films as a Matrix for Anchoring Electrochemically Active Guests. *Langmuir* **2005**, *21* (24), 11320–11329.

(12) Etienne, M.; Grosso, D.; Boissière, C.; Sanchez, C.; Walcarius, A. Electrochemical Evidences of Morphological Transformation in Ordered Mesoporous Titanium Oxide Thin Films. *Chem. Commun.* **2005**, No. 36, 4566–4568.

(13) Sun, Q.; Yan, F.; Yao, L.; Su, B. Anti-Biofouling Isoporous Silica-Micelle Membrane Enabling Drug Detection in Human Whole Blood. *Anal. Chem.* **2016**, *88* (17), 8364–8368.

(14) Yan, F.; Zheng, W.; Yao, L.; Su, B. Direct Electrochemical Analysis in Complex Samples Using ITO Electrodes Modified with Permselective Membranes Consisting of Vertically Ordered Silica Mesochannels and Micelles. *Chem. Commun.* **2015**, *51* (100), 17736–17739.

(15) Nasir, T.; Herzog, G.; Hébrant, M.; Despas, C.; Liu, L.; Walcarius, A. Mesoporous Silica Thin Films for Improved Electrochemical Detection of Paraquat. *ACS Sensors* **2018**, *3* (2), 484–493.

(16) Brinker, C. J. Evaporation-Induced Self-Assembly: Functional Nanostructures Made Easy. *MRS Bull.* **2004**, *29* (9), 631–640.

(17) Yan, Y.; King, S. C.; Li, M.; Galy, T.; Marszewski, M.; Kang, J. S.; Pilon, L.; Hu, Y.; Tolbert, S. H. Exploring the Effect of Porous Structure on Thermal Conductivity in Templated Mesoporous Silica Films. *J. Phys. Chem. C* **2019**, *123* (35), 21721–21730.

(18) Miyata, H.; Takahashi, M. Lithographically Formed Fine Wavy Surface Morphology for Universal Alignment Control of Mesochannels in Mesostructured Silica Films. *Langmuir* **2021**, *37* (6), 2179–2186.

(19) Glazneva, T. S.; Rebrov, E. V.; Schouten, J. C.; Paukshtis, E. A.; Ismagilov, Z. R. Synthesis and Characterization of Mesoporous Silica Thin Films as a Catalyst Support on a Titanium Substrate. *Thin Solid Films* **2007**, *515* (16 SPEC. ISS.), 6391–6394.

(20) Keilbach, A.; Moses, J.; Köhn, R.; Döblinger, M.; Bein, T. Electrodeposition of Copper and Silver Nanowires in Hierarchical Mesoporous Silica/Anodic Alumina Nanostructures. *Chem. Mater.* **2010**, *22* (19), 5430–5436.

(21) Yamauchi, Y. Field-Induced Alignment Controls of One-Dimensional Mesochannels in Mesoporous Materials. *Nippon Seramikkusu Kyokai Gakujutsu Ronbunshi/Journal Ceram. Soc. Japan* **2013**, *121* (1417), 831–840.

(22) Richman, E. K.; Brezesinski, T.; Tolbert, S. H. Vertically Oriented Hexagonal Mesoporousfilms Formed through Nanometre-Scaleepitaxy. *Nat. Mater.* **2008**, *7* (9), 712–717.

(23) Otomo, J.; Wang, S.; Takahashi, H.; Nagamoto, H. Microstructure Development of Mesoporous Silica Thin Films with Pore Channels Aligned Perpendicularly to Electrode Surfaces and Application to Proton Conducting Composite Electrolyte Membranes. *J. Memb. Sci.* **2006**, *279* (1–2), 256–265.

(24) Yamauchi, Y.; Sawada, M.; Sugiyama, A.; Osaka, T.; Sakka, Y.; Kuroda, K. Magnetically Induced Orientation of Mesochannels in 2D-Hexagonal Mesoporous Silica Films. *J. Mater. Chem.* **2006**, *16* (37), 3693–3700.

(25) Otomo, J.; Kurokawa, R.; Takahashi, H.; Nagamoto, H. Kinetic Process of Phase Separation in Co-SiO2 Thin Films and Preparation of Mesoporous SiO_2 Thin Films with Mesopore Channels Aligned Perpendicularly to Substrate Surfaces. *Vacuum* **2007**, *81* (8), 1003–1011.

(26) Teng, Z.; Zheng, G.; Dou, Y.; Li, W.; Mou, C. Y.; Zhang, X.; Asiri, A. M.; Zhao, D. Highly Ordered Mesoporous Silica Films with Perpendicular Mesochannels by a Simple Stöber-Solution Growth Approach. *Angew. Chemie - Int. Ed.* **2012**, *51* (9), 2173–2177.

(27) Walcarius, A.; Sibottier, E.; Etienne, M.; Ghanbaja, J. Electrochemically Assisted Self-Assembly of Mesoporous Silica Thin Films. *Nat. Mater.* **2007**, *6* (8), 602–608.

(28) Vilà, N.; André, E.; Ciganda, R.; Ruiz, J.; Astruc, D.; Walcarius, A. Molecular Sieving with Vertically Aligned Mesoporous Silica Films and Electronic Wiring through Isolating Nanochannels. *Chem. Mater.* **2016**, *28* (8), 2511–2514.

(29) Vavra, S.; Vilà, N.; Lotsari, A.; Walcarius, A.; Martinelli, A. An Imidazolium Ionic Liquid as Effective Structure-Directing Agent for the Fabrication of Silica Thin Films with Vertically Aligned Nanochannels. *Microporous Mesoporous Mater.* **2020**, No. March.

(30) Robertson, C.; Beanland, R.; Boden, S. A.; Hector, A. L.; Kashtiban, R. J.; Sloan, J.; Smith, D. C.; Walcarius, A. Ordered Mesoporous Silica Films with Pores Oriented Perpendicular to a Titanium Nitride Substrate. *Phys. Chem. Chem. Phys.* **2015**, *17* (6), 4763–4770.

(31) Ullah, W.; Herzog, G.; Vila, N.; Walcarius, A. Polyaniline Nanowire Arrays Generated through Oriented Mesoporous Silica Films: Effect of Pore Size and Spectroelectrochemical Response. *Faraday Discuss.* **2021**, 1–14.

(32) Scheraga, H. A.; Backus, J. K. Flow Birefringence in Solutions of N-Hexadecyltrimethylammonium Bromide. *J. Am. Chem. Soc.* **1951**, *73* (11), 5108–5112.

(33) Al Dulayymi, J. R.; Baird, M. S.; Roberts, E. The Synthesis of a Single Enantiomer of a Major α-Mycolic Acid of M. Tuberculosis. *Tetrahedron* **2005**, *61* (50), 11939–11951.

(34) Goux, A.; Etienne, M.; Aubert, E.; Lecomte, C.; Ghanbaja, J.; Walcarius, A. Oriented Mesoporous Silica Films Obtained by Electro-Assisted Self-Assembly (EASA). *Chem. Mater.* **2009**, *21* (4), 731–741.

(35) Etienne, M.; Guillemin, Y.; Grosso, D.; Walcarius, A. Electrochemical Approaches for the Fabrication and/or Characterization of Pure and Hybrid Templated Mesoporous Oxide Thin Films: A Review. *Anal. Bioanal. Chem.* **2013**, *405* (5), 1497–1512.

(36) Ding, L.; Su, B. An Electrochemistry Assisted Approach for Fast, Low-Cost and Gram-Scale Synthesis of Mesoporous Silica Nanoparticles. *RSC Adv.* **2015**, *5* (81), 65922–65926.

(37) Kruk, M.; Jaroniec, M.; Ko, C. H.; Ryoo, R. Characterization of the Porous Structure of SBA-15. *Chem. Mater.* **2000**, *12* (7), 1961–1968.

(38) Wang, Z.; Chen, B.; Quan, G.; Li, F.; Wu, Q.; Dian, L.; Dong, Y.; Li, G.; Wu, C. Increasing the Oral Bioavailability of Poorly Water-Soluble Carbamazepine Using Immediate-Release Pellets Supported on SBA-15 Mesoporous Silica. *Int. J. Nanomedicine* **2012**, *7* (November), 5807–5818.

(39) Beck, J. S.; Vartuli, J. C.; Roth, W. J.; Leonowicz, M. E.; Kresge, C. T.; Schmitt, K. D.; Chu, C. T. W.; Olson, D. H.; Sheppard, E. W.; McCullen, S. B.; Higgins, J. B.; Schlenker, J. L. A New Family of Mesoporous Molecular Sieves Prepared with Liquid Crystal Templates. *J. Am. Chem. Soc.* **1992**, *114* (27), 10834–10843.

(40) Kruk, M.; Jaroniec, M.; Kim, J. M.; Ryoo, R. Characterization of Highly Ordered MCM-41 Silicas Using X-Ray Diffraction and Nitrogen Adsorption. *Langmuir* **1999**, *15* (16), 5279–5284.

(41) Ryoo, R.; Ko, C. H.; Park, I. Synthesis of Highly Ordered MCM-41 by Micelle-Packing Control with Mixed Surfactants. *Chem. Commun.* **1999**, 1413–1414.

(42) A. J. Bard and L. R. Faulkner. *Electrochemical Methods: Fundamentals and Applications*; Wiley: New York, 1980.

(43) Baklanov, M. R.; Mogilnikov, K. P.; Polovinkin, V. G.; Dultsev, F. N. Determination of Pore Size Distribution in Thin Films by Ellipsometric Porosimetry. *J. Vac. Sci. Technol. B Microelectron. Nanom. Struct.* **2000**, *18* (3), 1385.

(44) Baklanov, M. R.; Mogilnikov, K. P. Non-Destructive Characterisation of Porous Low-k Dielectric Films. *Microelectron. Eng.* **2002**, *64* (1–4), 335–349.

(45) Robertson, C.; Lodge, A. W.; Basa, P.; Carravetta, M.; Hector, A. L.; Kashtiban, R. J.; Sloan, J.; Smith, D. C.; Spencer, J.; Walcarius, A. Surface Modification and Porosimetry of Vertically Aligned Hexagonal Mesoporous Silica Films. *RSC Adv.* **2016**, *6* (114), 113432–113441.

(46) Donohue, M. D. and Aranovich, G. L. Classification of Gibbs Adsorption Isotherms Classification of Gibbs Adsorption Isotherms. *Elsevier, Adv. Colloid Interface Sci.* **1998**, *76–77* (October), 137–152.

(47) Thommes, M.; Kaneko, K.; Neimark, A. V.; Olivier, J. P.; Rodriguez-Reinoso, F.; Rouquerol, J.; Sing, K. S. W. Physisorption of Gases, with Special Reference to the Evaluation of Surface Area and Pore Size Distribution (IUPAC Technical Report). *Pure Appl. Chem.* **2015**, *87* (9–10), 1051–1069.

(48) Jahandar Lashaki, M.; Fayaz, M.; Niknaddaf, S.; Hashisho, Z. Effect of the Adsorbate Kinetic Diameter on the Accuracy of the Dubinin-Radushkevich Equation for Modeling Adsorption of Organic Vapors on Activated Carbon. *J. Hazard. Mater.* **2012**, *241–242*, 154–163.

(49) Shimizu, W.; Hokka, J.; Sato, T.; Usami, H.; Murakami, Y. Microstructure Investigation on Micropore Formation in Microporous Silica Materials Prepared via a Catalytic Sol-Gel Process by Small Angle X-Ray Scattering. *J. Phys. Chem. B* **2011**, *115* (30), 9369–9378.

(50) Calleja, G. .; Serrano, D. P. .; Botas, J. A. .; Gutierrez, F. J. . Adsorption Properties of MCM-41 Materials for the VOCs Abatement. *Stud. Surf. Sci. Catal.* **2002**, *142*, 1671–1678.

(51) Walcarius, A. Mesoporous Materials and Electrochemistry. *Chem. Soc. Rev.* **2013**, *42* (9), 4098–4140.

(52) Yan, F.; Lin, X.; Su, B. Electrochemistry and Analytical Applications. *RSC Anal.* **2016**, *141*, 3482–3495.

(53) Karman, C.; Vilà, N.; Walcarius, A. Amplified Charge Transfer for Anionic Redox Probes through Oriented Mesoporous Silica Thin Films. *ChemElectroChem* **2016**, *3* (12), 2130–2137.

(54) Etienne, M.; Cortot, J.; Walcarius, A. Preconcentration Electroanalysis at Surfactant-Templated Thiol-Functionalized Silica Thin Films. *Electroanalysis* **2007**, *19* (2–3), 129–138.

(55) Ryabov, A. D.; Amon, A.; Gorbatova, R. K.; Ryabova, E. S.; Gnedenko, B. B. Mechanism of a “Jumping off” Ferricenium in Glucose Oxidase-D-Glucose-Ferrocene Micellar Electrochemical Systems. *J. Phys. Chem.* **1995**, *99* (38), 14072–14077.

(56) Sarkar, S.; Sengupta, A. K.; Prakash, P. The Donnan Membrane Principle: Opportunities for Sustainable Engineered Processes and Materials. *Environ. Sci. Technol.* **2010**, *44* (4), 1161–1166.

(57) Platt, M.; Dryfe, R. A. W.; Roberts, E. P. L. Voltammetry with Liquid/Liquid Microarrays: Characterization of Membrane Materials. *Langmuir* **2003**, *19* (19), 8019–8025.

Chapter 4 Effects of surfactant head group modification on vertically oriented mesoporous silica produced by electrochemically assisted surfactant assembly

This chapter describes generation of porous silica films from cationic surfactants with differing head sizes. These films were prepared using the electrochemically assisted surfactant assembly (EASA) method with the sol electrolyte tetraalkylammonium head group containing a hydrophobic chain of 18, 20 and 22 carbons, and a mixture of zero, one, two or three ethyl groups, with methyl groups making up the remainder, $[C_{18}H_{37}NMe_{3-x}Et_x]Br$, $[C_{20}H_{41}NMe_{3-x}Et_x]Br$, $[C_{22}H_{45}NMe_{3-x}Et_x]Br$ with x = 0, 1, 2 or 3.The assessment of the resulting films was based on the effect of increasing the surfactant head size on micelle organisation and expansion. The GISAXS data revealed a reduction in pore order in the films as the hydrophilic head group increased in size. Electron microscopy indicated the presence of silica aggregates for select silica films and the gradual decrease in the hexagonal pore structure as ethyl substituents replaced methyl in the hydrophilic head. The peak shapes from CVs and charge transfer resistance found in EIS data were influenced by the ordering of mesopores. The ellipsometric porosimetry analysis indicated an increase in peak pores sizes for the head group-modified C_{18}-based surfactants compared to $C_{18}TAB$.

Part of this work has been published in *Nanoscale Adv*., 2023, **5**, 3316

4.1 Acknowledgement

I would like to thank Anthony Houghton and Ziyou Zhang (Imperial College London) for their analysis of the silica films using ellipsometric porosimetry, and Richard Beanland and Yisong Han (University of Warwick) for examining the samples with TEM.

4.2 Introduction

Since the development of MCM-41, a range of cationic surfactants has been used to produce porous silica materials with different preparation methods, pore structures, pore sizes and other characteristics. Lin et al.[1] investigated the influence of surfactants with modified head groups while maintaining a surfactant chain length of 16 carbon atoms for the formation of MCM-41 silica powders. After hydrothermal treatment, it was found that the addition of an ethyl or benzyl group to the conventional C_{16}TAB surfactant brought about a decline in pore order and a shrinkage in pore size from 4.0 nm (C_{16}TAB) to 3.6 nm (cetyldimethylethylammonium bromide) surfactants. Ryoo et al.[2] reported the post-synthesis heat treatment of MCM-41 materials with C_nTAB and alkyltriethylammonium bromide surfactants, with a carbon chain length from C_{12} to C_{22}. They found that mixing these surfactants together in selected ratios between 0 and 1, could significantly impact pore ordering of MCM-41 silica powders.

Zhao et al.[3] studied the influence of cationic surfactants such as cetyltriethylammonium bromide (C_{16}TEAB) and Gemini surfactants $C_{18}H_{37}N(CH_3)_2(CH_2)_3N(CH_3)_3Br_2$ ($C_{18\text{-}3\text{-}1}$) in the formation of mesoporous silica films, produced by a dip-coating method in an aqueous and a non-aqueous solution. It was demonstrated that silica films containing C_{16}TEAB tend to produce 3D cubic pore structures in aqueous conditions, whereas under highly acidic conditions, 2D-hexagonal pores are favoured using the same surfactant. Under aqueous and non-aqueous environments, silica films with Gemini surfactant, $C_{18\text{-}3\text{-}1}$, produce either 3D-hexagonal or 2D-hexagonal structures, where the pores are oriented parallel to the surface. Vertical pore orientation is rather more difficult in comparison to horizontal orientation using the EISA method. Vertically-oriented mesopores can be achieved by the Stöber process,[4] whereby the silica gel formation is aided by C_{16}TAB, a silica precursor, ethanol and ammonia or an induced co-assembly approach via the addition of an oil (decane) to the sol bath.[5]

However, these methods suffer from long preparation times to make very thin films. An alternative method is electrochemically assisted surfactant assembly (EASA) using a cationic surfactant, usually C_{16}TAB, and a silica precursor.[6,7] This method generally produces ordered silica films with the application of an electrical current. The surfactant is removed from the mesopores by an acidic alcohol solution or calcining for 30 minutes to generate mesoporous silica films with vertical pore channels. Faster ion diffusion rates were observed from a variety of redox probe molecules for films with increasing surfactant chain lengths in Chapter 3, linked to increases in pore size. Robertson et al.[8] previously evaluated the influence of switching the head group of the surfactant to a bulkier cetylpyridinium bromide (CPB) on the lattice parameters and pore ordering. It was concluded that the film became less well-organised, but an increase in the lattice

spacings was noticed. EASA most commonly uses C_{16}TAB, resulting in small diameter pores of 2-3 nm. Post-synthesis grafting may facilitate better electrolyte access to the substrate surface during electrodeposition.[9] Furthermore, increasing the surfactant chain length[2,10] and the use of swelling agents such as mesitylene[11,8] are other avenues to films with larger pores.

In this work, the porosity, structural pore order and pore size are evaluated for porous silicas produced using cationic surfactants with a tetraalkylammonium head group containing a hydrophobic chain of 18, 20 or 22 carbons, and a mixture of zero, one, two or three ethyl groups, with methyl groups making up the remainder, $[C_{18}H_{37}NMe_{3-x}Et_x]Br$, $[C_{20}H_{41}NMe_{3-x}Et_x]Br$, $[C_{22}H_{45}NMe_{3-x}Et_x]Br$ with x = 0, 1, 2 or 3.

4.3 Experimental summary

4.3.1 Synthesis and characterisation of surfactants

Octadecyltrimethylammonium bromide (C_{18}TAB, 98%) was purchased from Sigma Aldrich. The octadecylalkylammonium bromide, eicosylalkylammonium bromide and docosylalkylammonium bromide surfactants were prepared by the reaction of the alkylamine with 1-bromooctadecane, 1-bromoeicosane or 1-bromodocosane in ethanol according to Scheraga et al.[12] The synthesis used 1-bromooctadecane (5.0001 g, ≥ 97 %, Sigma Aldrich), 1-bromoeicosane (5.0001 g, ≥ 97 %, Sigma Aldrich) and 1-bromodocosane (5.0001 g, 96%, Santa Cruz Biotechnology), which was dissolved in ethanol (25 cm^3) and dimethylethylamine (10 x mol eq, ≥ 99 %, Sigma Aldrich), diethylmethylamine (10 x mol eq, 97 %, Sigma Aldrich) or triethylamine (10 x mol eq, ≥ 99.5 %, Sigma Aldrich) was added into the solution. The mixture was refluxed for 8 h under stirring at 100 ℃ using a dry ice condenser. The solution was then filtered to remove particulates, and the filtrate was placed in the freezer to induce precipitation. The crude product was collected by filtration and a rotary evaporator was used to reduce the ethanol solvent significantly to recover the remaining solid from the filtrate. Recrystallisation of the combined 2 crops of product from ethanol produced a final yield of 4.98 g of octadecyldimethylethylammonium bromide, (C_{18}DMEAB, yield = 99 % after drying, white solid), 4.80 g of octadecyldiethylmethylammonium bromide (C_{18}DEMAB, yield = 96 % after drying, off-white solid), 4.76 g of octadecyltriethylammonium bromide (C_{18}TEAB, yield = 95 % after drying, off-white solid), 4.71 g of eicosyldimethylethylammonium bromide (C_{20}DMEAB, yield = 94 % after drying, off white solid), 4.73 g eicosyldiethylmethylammonium bromide (C_{20}DEMAB, yield = 94 % after drying, white solid), 4.87 g of eicosyltriethylammonium bromide (C_{20}TEAB, yield = 97 % after drying, off-white solid), 4.98 g docosyldimethylethylammonium bromide (C_{22}DMEAB, yield = 99 % after drying, white solid), 4.89 g of docosyldiethylmethylammonium bromide (C_{22}DEMAB, yield = 97.8 % after

drying, off-white solid) and 4.87 g of docosyltriethylammonium bromide (C_{22}TEAB, yield = 97 % after drying, off-white solid). ^{1}H and ^{13}C{^{1}H} NMR spectra and positive ion ESI MS in methanol are shown below.

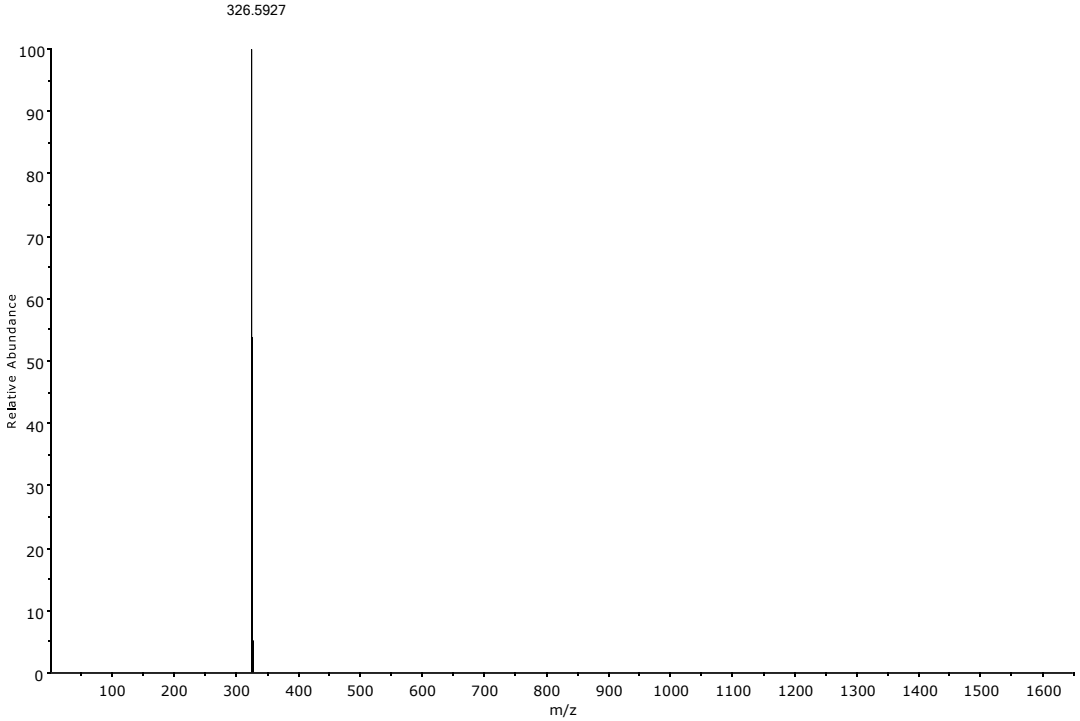

Figure 4.1 Positive ion electrospray mass spectrum of C_{18}DMEAB (calculated 326.60 m/z value) in methanol at 25 ℃.

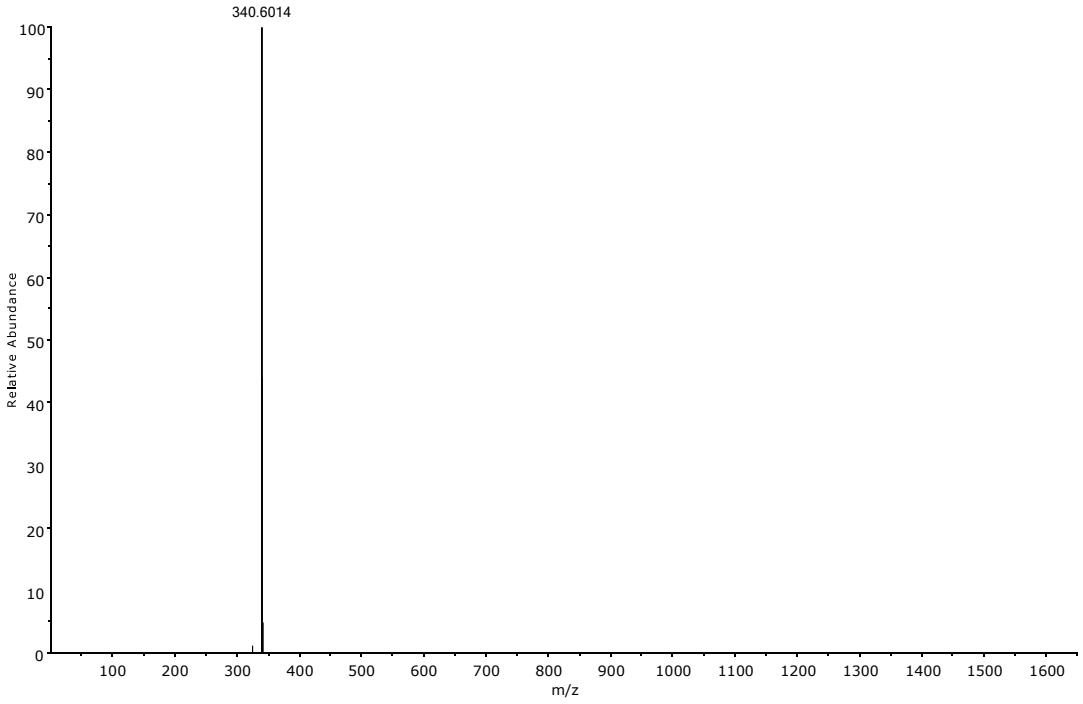

Figure 4.2 Positive ion electrospray mass spectrum of C_{18}DEMAB (calculated 340.60 m/z value) in methanol at 25 ℃.

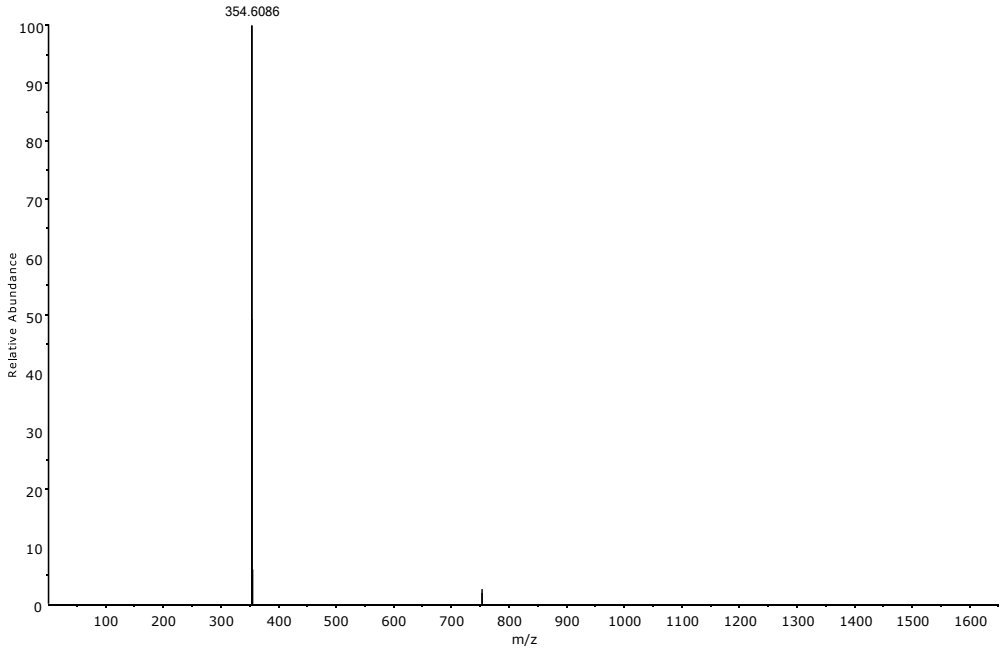

Figure 4.3 Positive ion electrospray mass spectrum of C_{18}TEAB (calculated 354.60 m/z value) in methanol at 25 ℃.

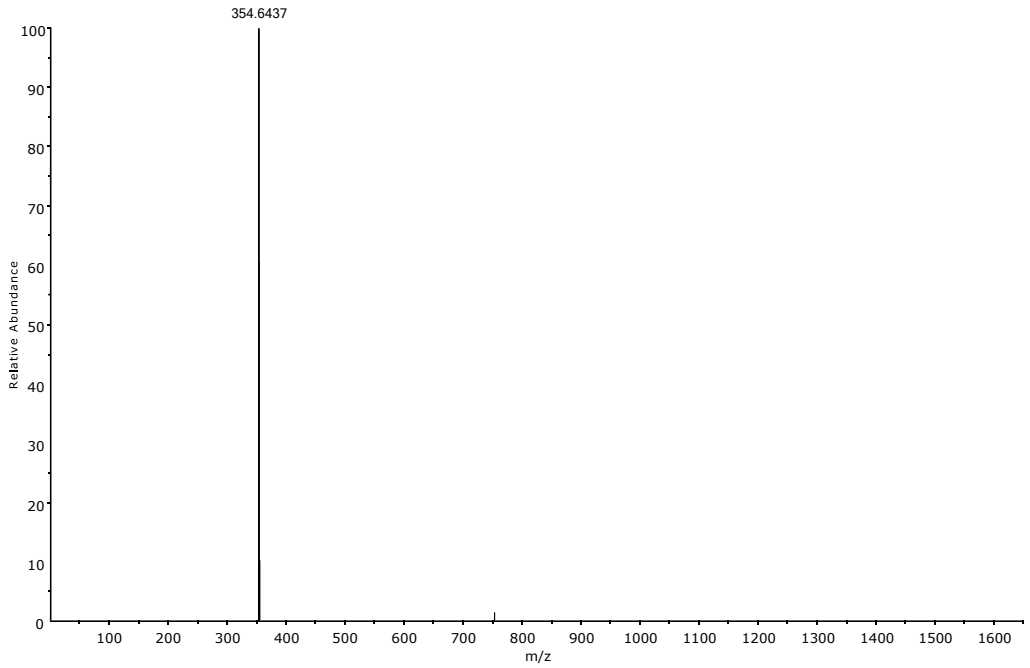

Figure 4.4 Positive ion electrospray mass spectrum of C_{20}DMEAB (calculated 354.64 m/z value) in methanol at 25 ℃.

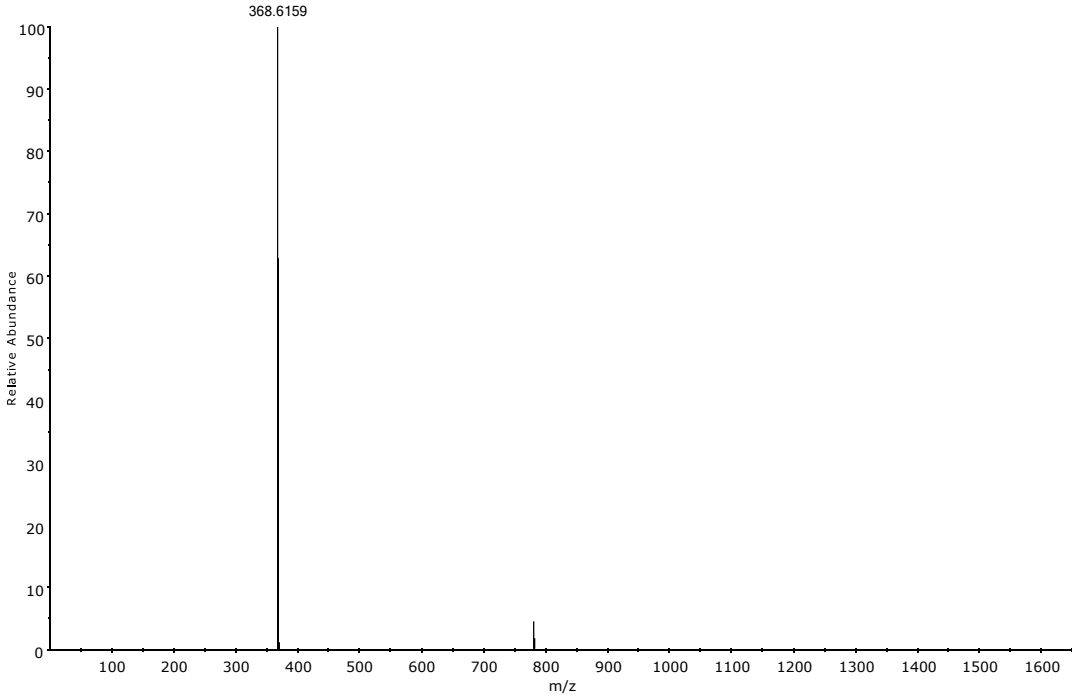

Figure 4.5 Positive ion electrospray mass spectrum of C_{20}DEMAB (calculated 368.62 m/z value) in methanol at 25 ℃.

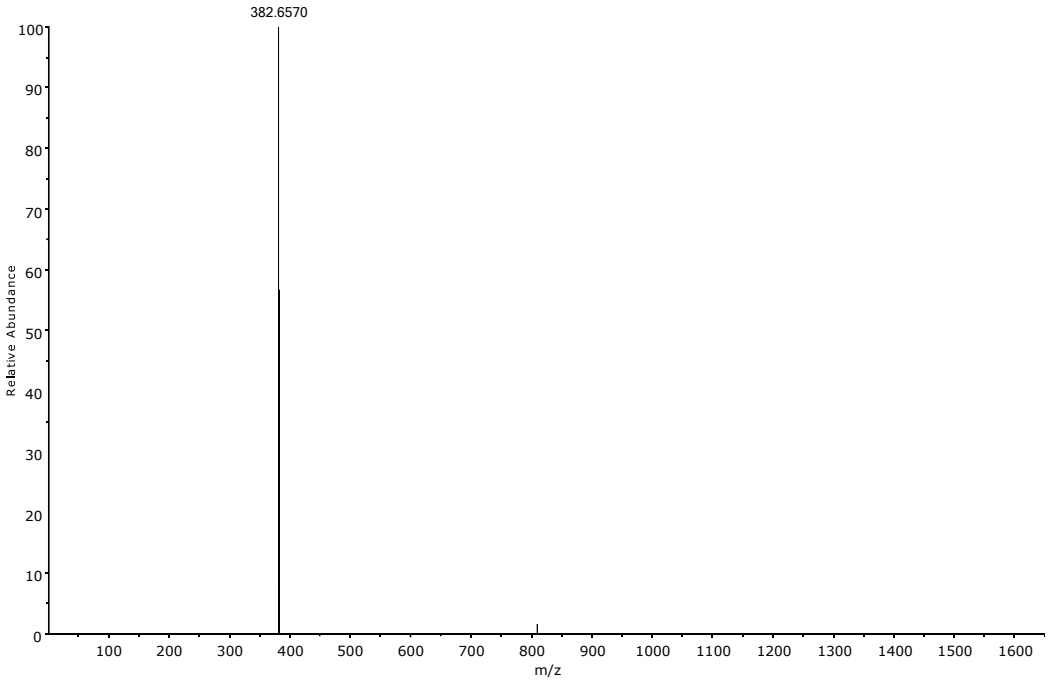

Figure 4.6 Positive ion electrospray mass spectrum of C_{20}TEAB (calculated 382.66 m/z value) in methanol at 25 ℃.

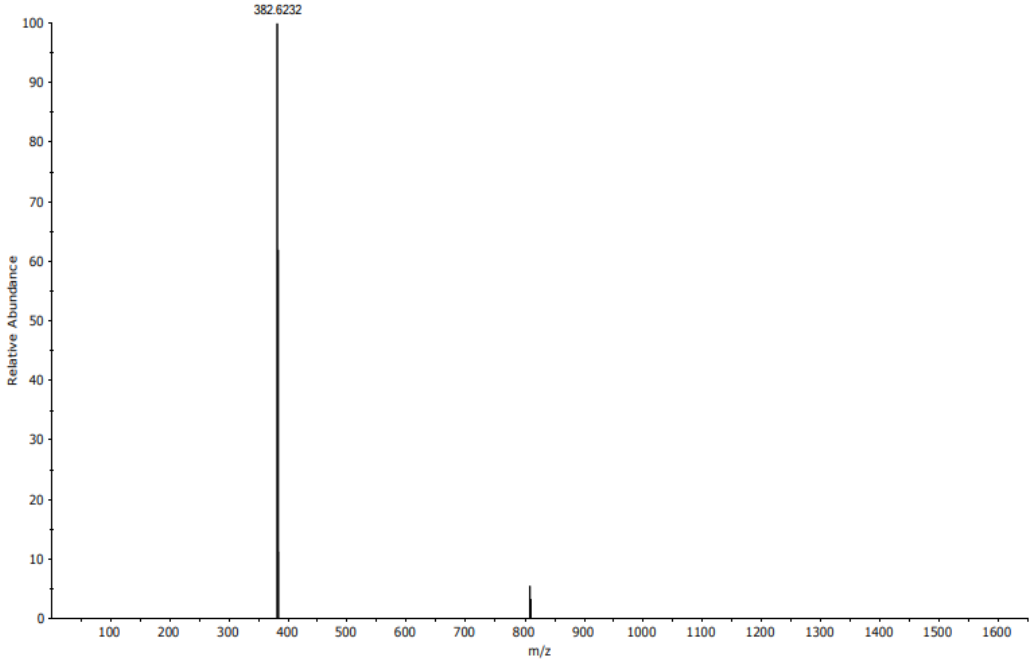

Figure 4.7 Positive ion electrospray mass spectrum of C_{22}DMEAB (calculated 382.62 m/z value) in methanol at 25 ℃.

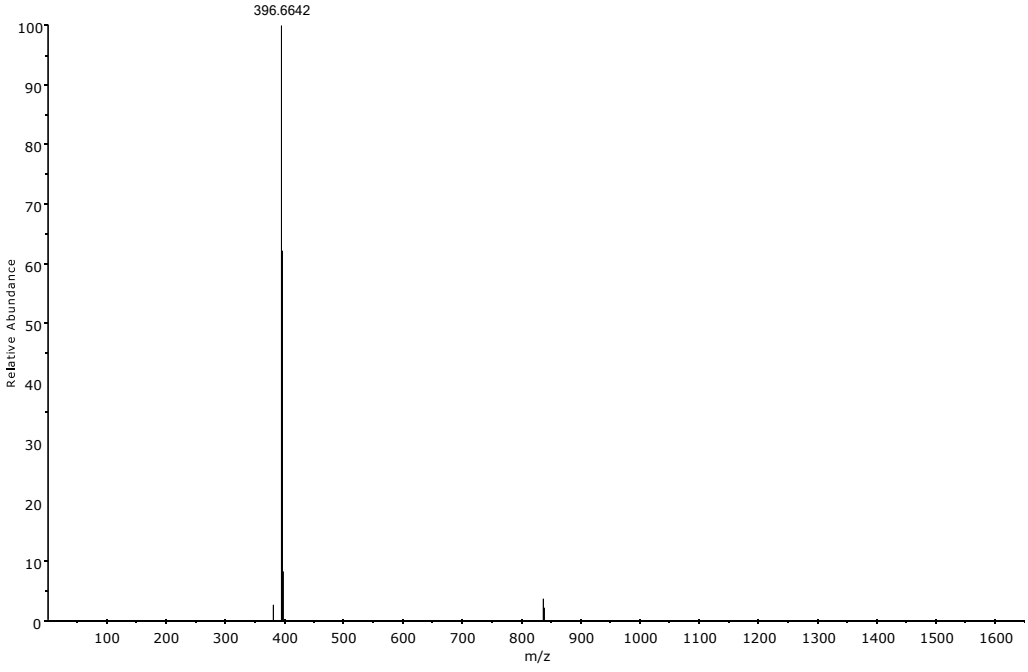

Figure 4.8 Positive ion electrospray mass spectrum of C_{22}DEMAB (calculated 396.66 m/z value) in methanol at 25 ℃.

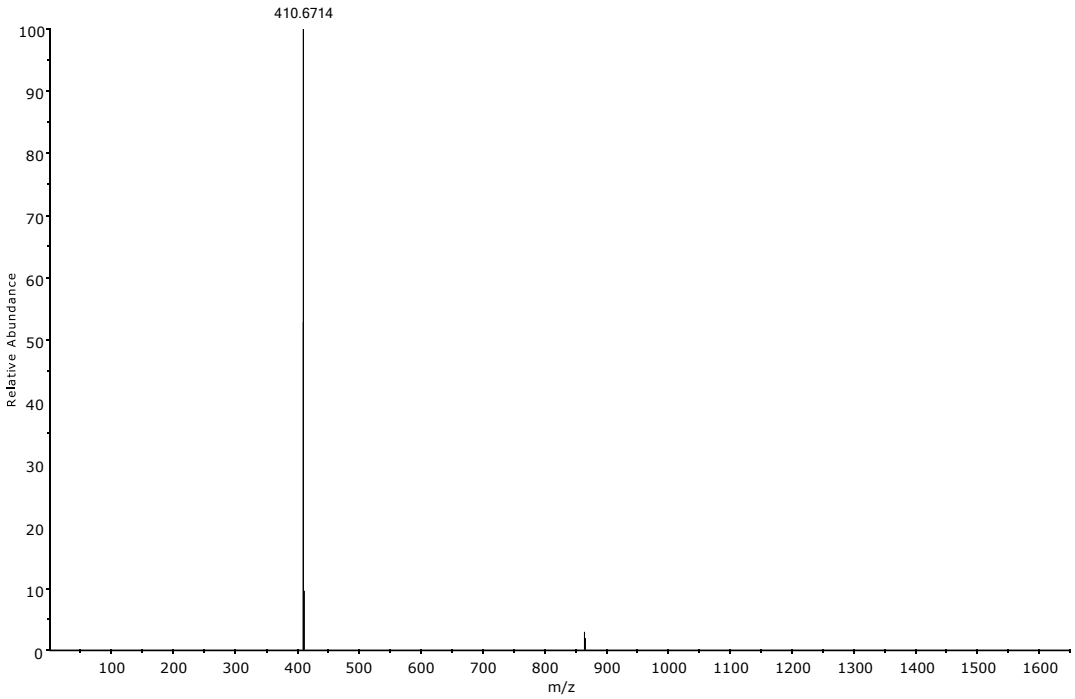

Figure 4.9 Positive ion electrospray mass spectrum of C_{22}TEAB (calculated 410.67 m/z value) in methanol at 25 ℃.

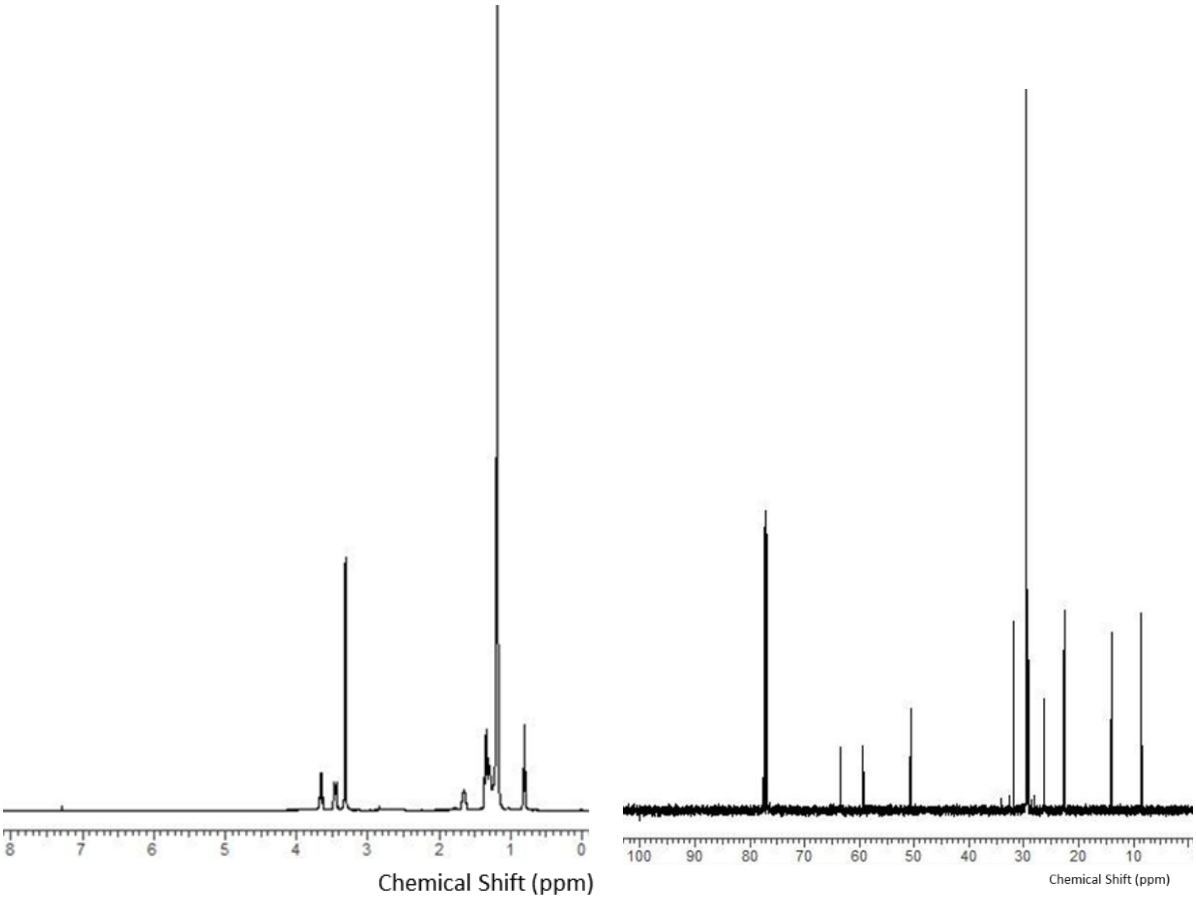

Figure 4.10 ^{1}H and $^{13}C\{^{1}H\}$ NMR spectrums of C_{18}DMEAB in $CDCl_3$ (7.3 ppm and 77.2 ppm) at 25 °C.

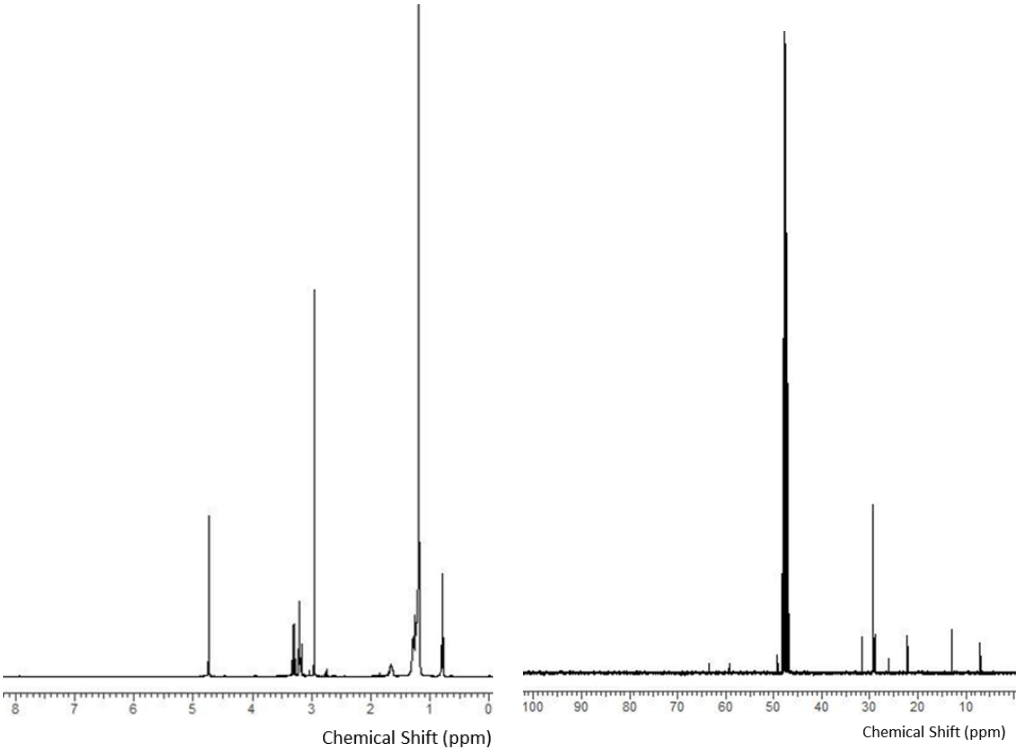

Figure 4.11 ^{1}H and $^{13}C\{^{1}H\}$ NMR spectrums of C_{18}DEMAB in D-methanol (4.8 ppm and 49.3 ppm) at 25 °C.

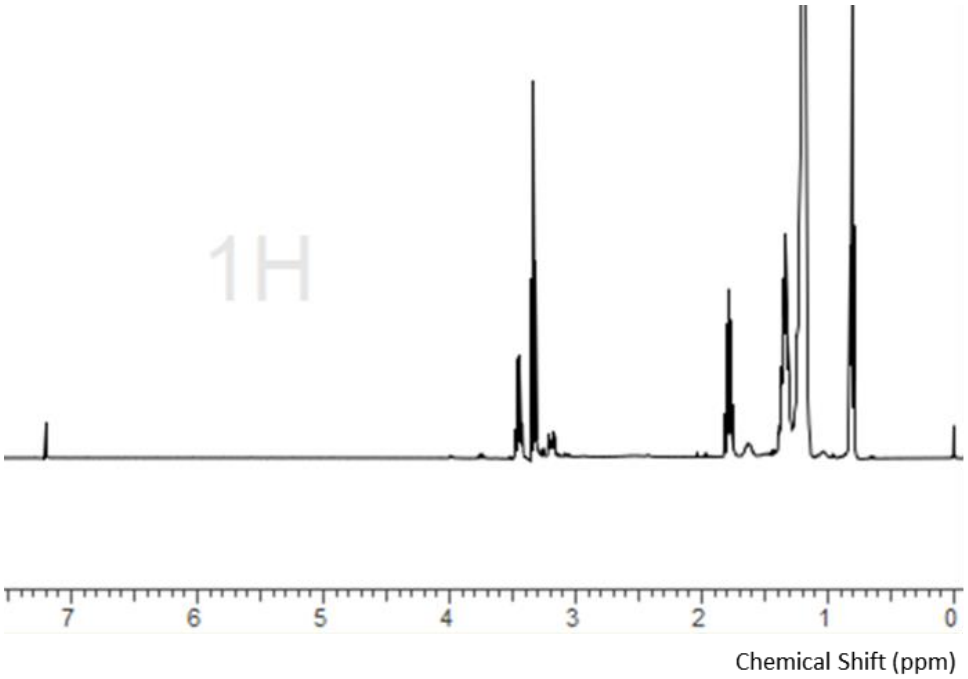

Figure 4.12 ^{1}H NMR spectrum of C_{18}TEAB in $CDCl_3$ (7.3 ppm) at 25 °C.

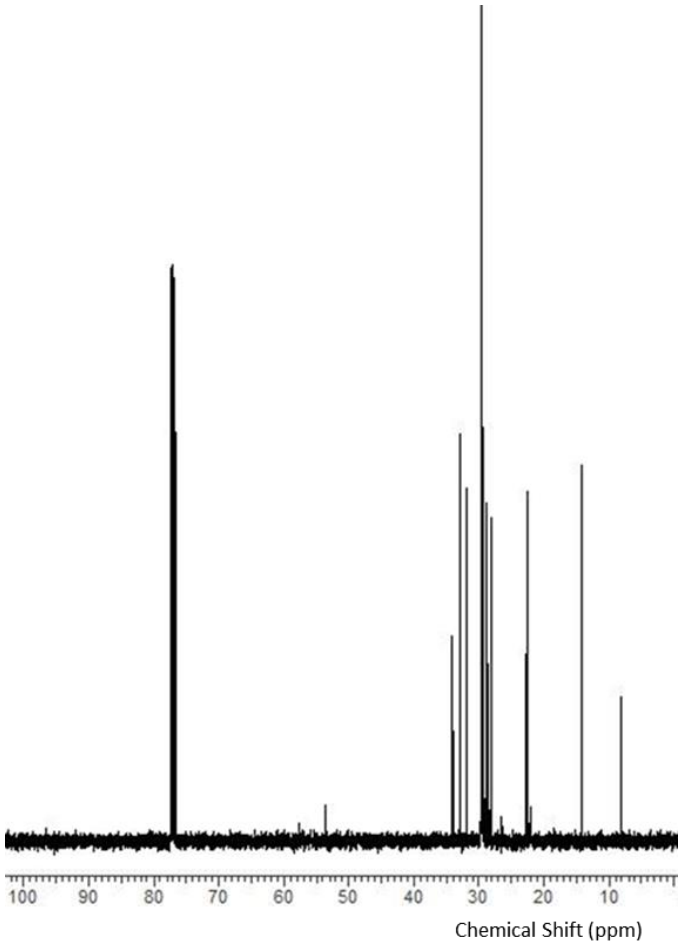

Figure 4.13 $^{13}C\{^{1}H\}$ NMR of C_{18}TEAB in $CDCl_3$ (77.2 ppm) at 25 ℃.

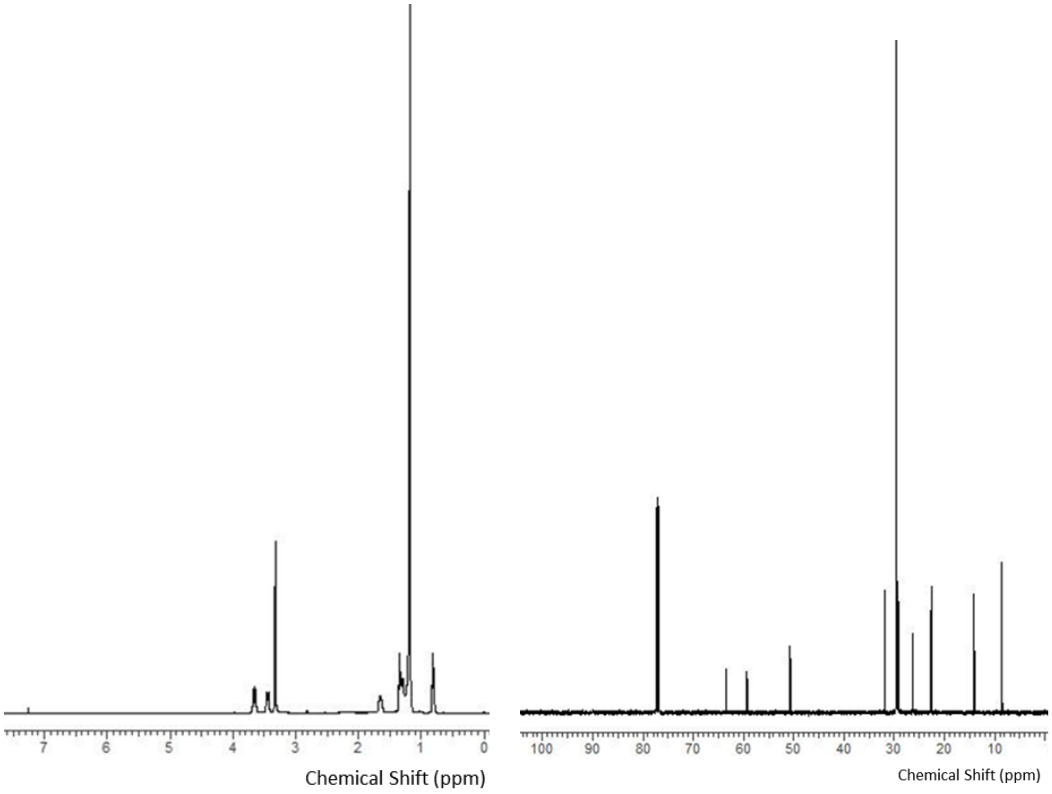

Figure 4.14 ^{1}H and $^{13}C\{^{1}H\}$ NMR spectrums of C_{20}DMEAB in $CDCl_3$ (7.3 ppm and 77.2 ppm) at 25 ℃.

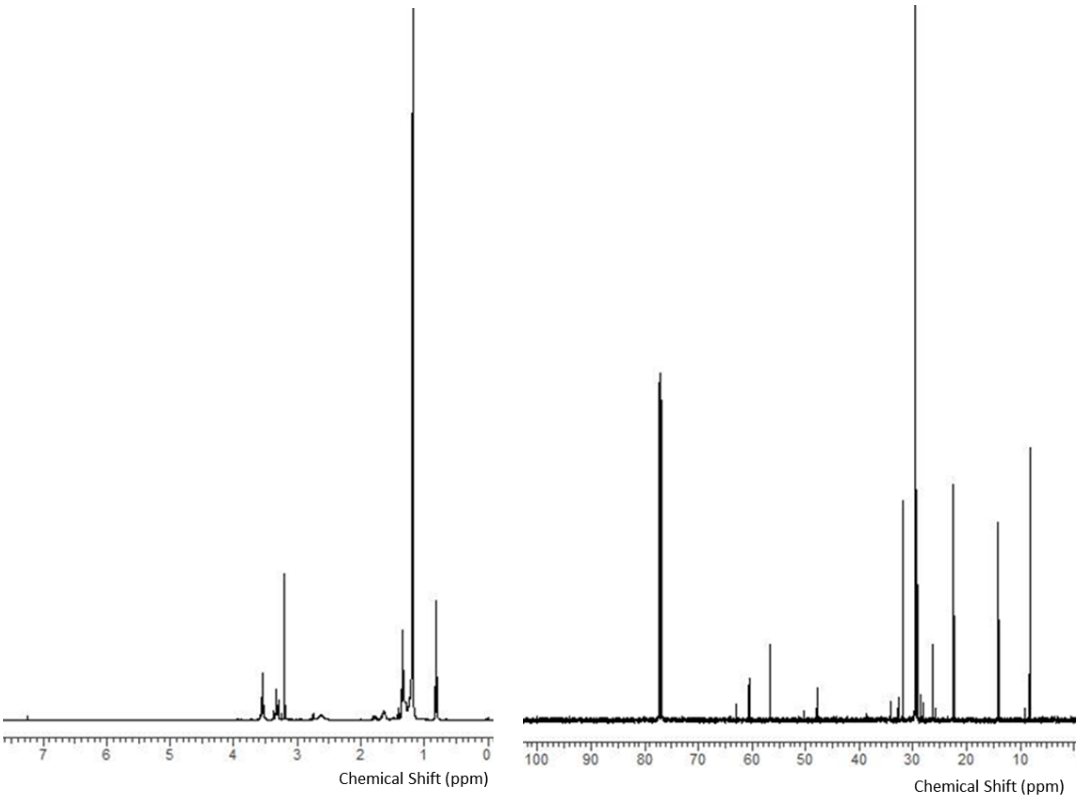

Figure 4.15 ^{1}H and $^{13}C\{^{1}H\}$ NMR spectrums of C_{20}DEMAB in $CDCl_3$ (7.3 ppm and 77.2 ppm) at 25 °C.

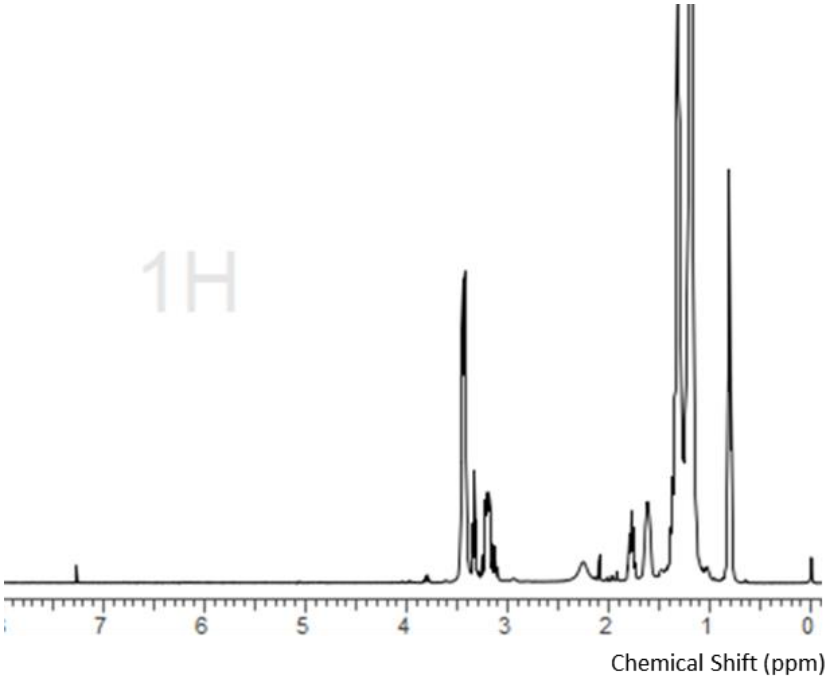

Figure 4.16 ^{1}H NMR spectrum of C_{20}TEAB in $CDCl_3$ (7.3 ppm) at 25 °C.

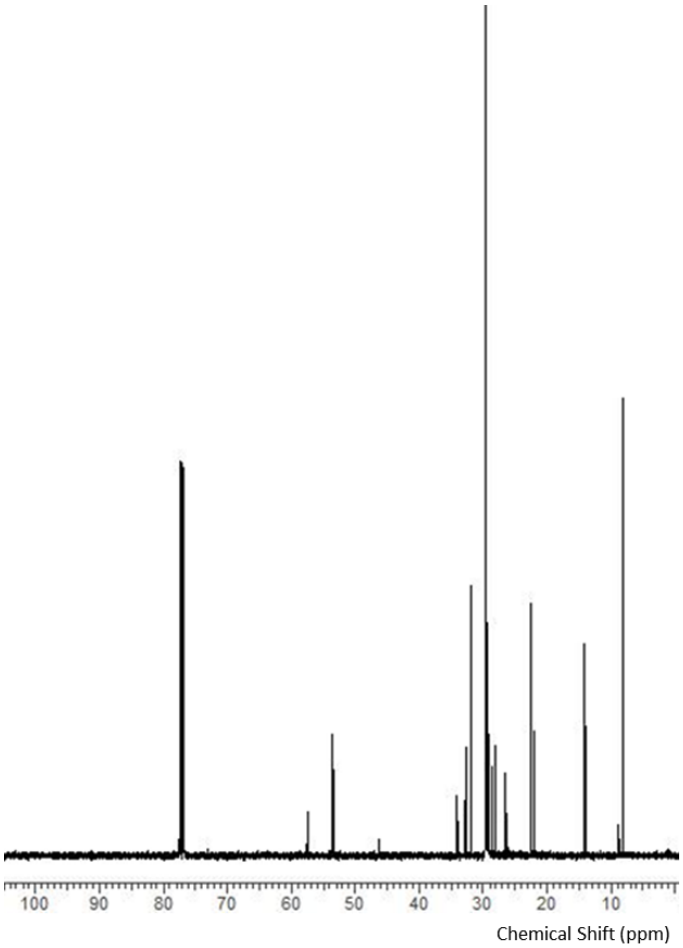

Figure 4.17 $^{13}C\{^{1}H\}$ NMR of C_{20}TEAB in $CDCl_3$ (77.2 ppm) at 25 ℃.

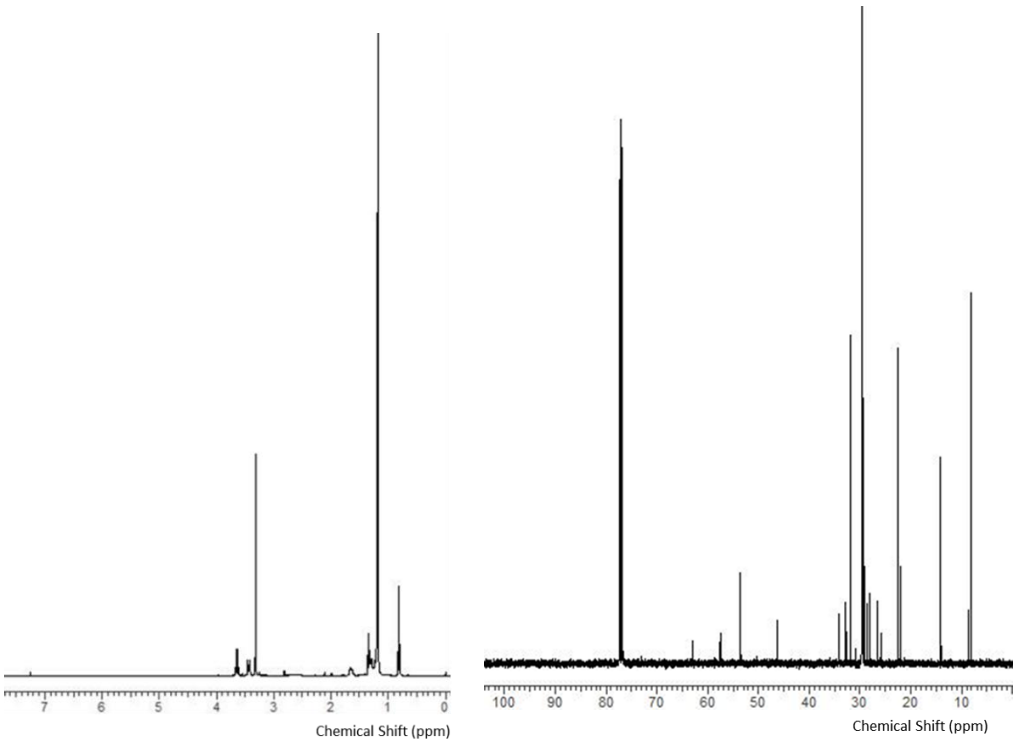

Figure 4.18 ^{1}H and $^{13}C\{^{1}H\}$ NMR spectrums of C_{22}DMEAB in $CDCl_3$ (7.3 ppm and 77.2 ppm) at 25 ℃.

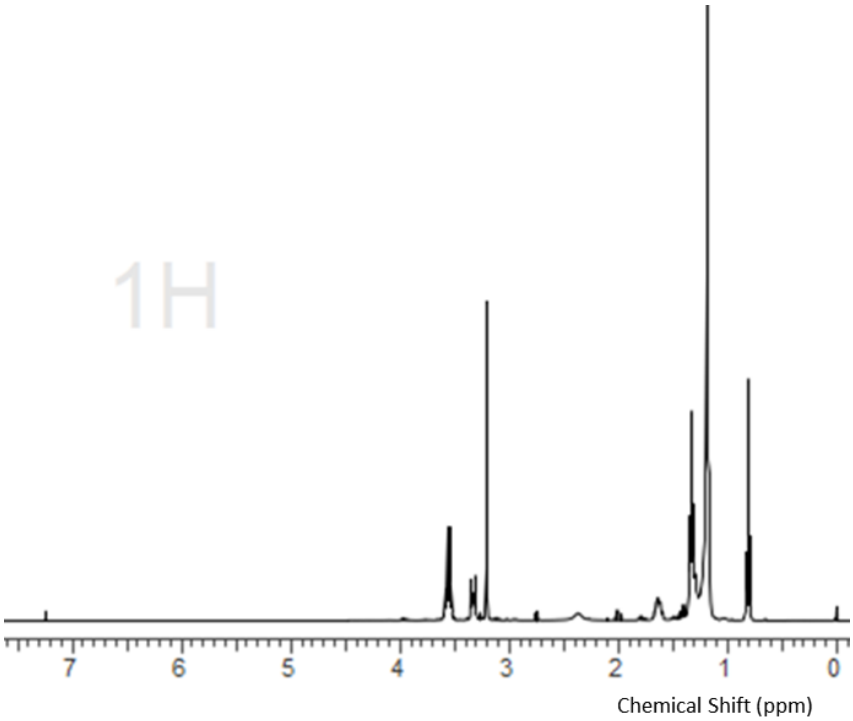

Figure 4.19 ^{1}H NMR spectrum of C_{22}DEMAB in $CDCl_3$ (7.3 ppm) at 25 °C.

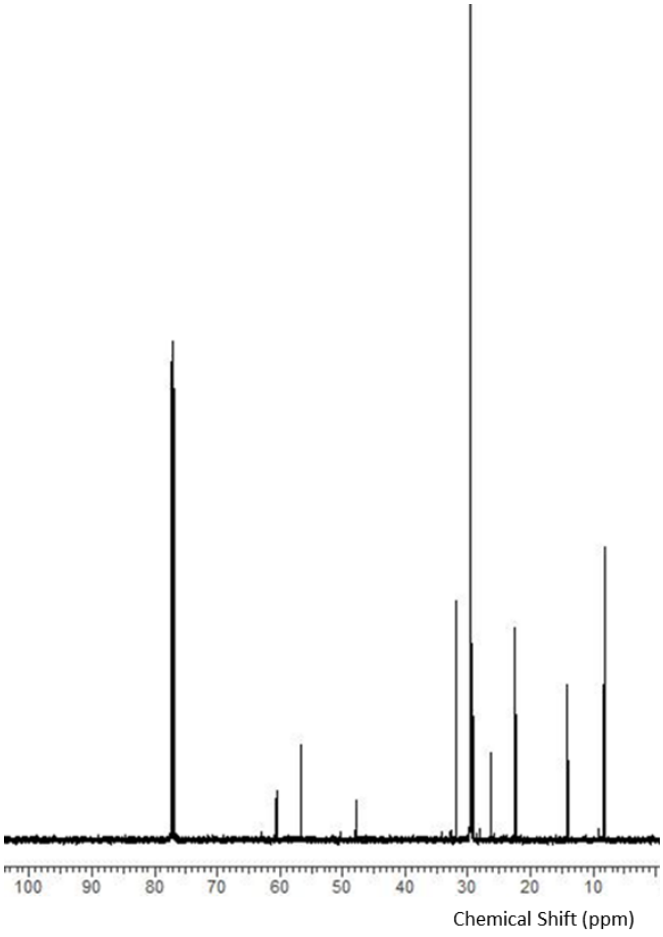

Figure 4.20 $^{13}C\{^{1}H\}$ NMR of C_{22}DEMAB in $CDCl_3$ (77.2 ppm) at 25 °C.

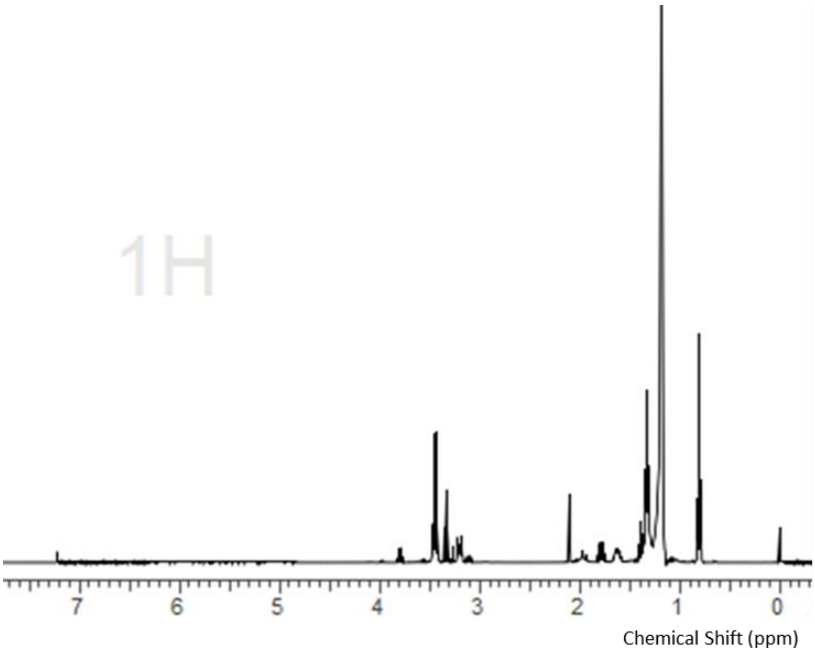

Figure 4.21 ^{1}H NMR spectrum of C_{22}TEAB in $CDCl_3$ (7.3 ppm) at 25 °C.

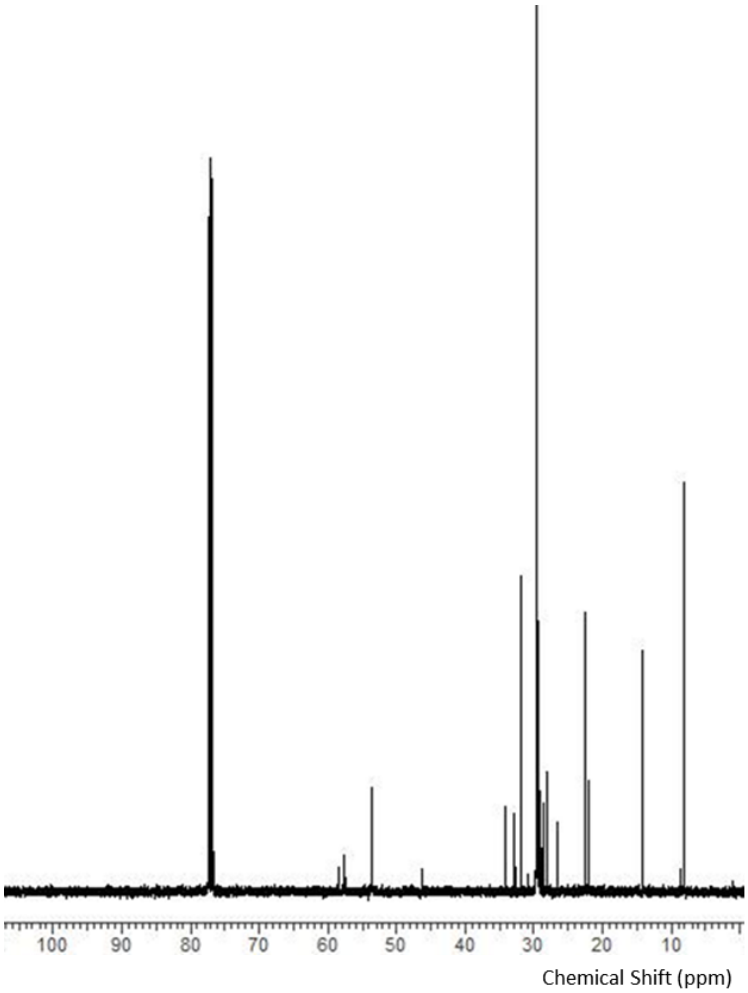

Figure 4.22 $^{13}C\{^{1}H\}$ NMR of C_{22}TEAB in $CDCl_3$ (77.2 ppm) at 25 °C.

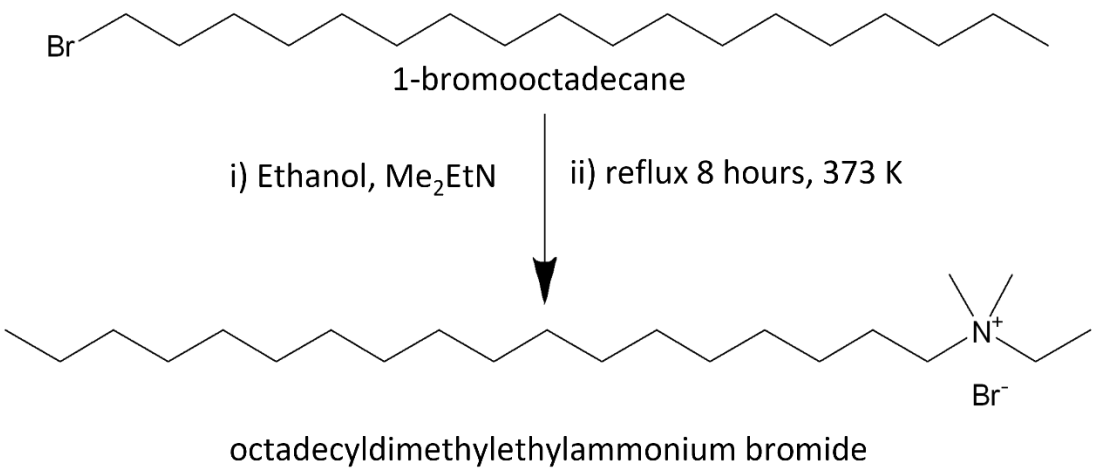

Scheme 4.1 reaction of 1-bromooctadecane with N,N-dimethylethylamine to form octadecyldimethylethylammonium bromide surfactant, C_{18}DMEAB. This general method was modified for the preparation of the C_{18}DEMAB, C_{18}TEAB, C_{20}DMEAB, C_{20}DEMAB, C_{20}TEAB, C_{22}DMEAB, C_{22}DEMAB and C_{22}TEAB surfactants.

C_{18}DMEAB. ^{1}H NMR ($CDCl_3$): δ/ppm 0.81 (t, CH_3, [3H]), 1.17-1.39 (br s, CH_2 and CH_3, [33H]), 1.61-1.71 (m, CH_2, [2H]), 3.32 (s, CH_3, [6H]), 3.42-3.50 (m, CH_2, [2H]), 3.66 (q, CH_2, [2H]). $^{13}C\{^{1}H\}$ NMR ($CDCl_3$): δ/ppm 8.57, 14.05, 22.61, 22.72, 26.24, 29.18, 29.28, 29.34, 29.41, 29.53, 29.58, 29.61, 29.63, 31.85, 32.78, 34.02, 50.64, 59.35, 63.46, 76.85, 77.17, 77.49. MS (ESI^+ in CH_3OH): found *m/z* = 326.6; required for $\{C_{22}H_{48}N^+\}$: m/z = 326.

C_{18}DEMAB. ^{1}H NMR ($CDCl_3$): δ/ppm 0.81 (t, CH_3, [3H]), 1.02-1.46 (br s, CH_2 and CH_3, [36H]), 1.61-1.75 (m, CH_2, [2H]), 2.96 (s, CH_3, [3H]), 3.14-3.25 (m, CH_2, [2H]), 3.3 (q, CH_2, [4H]). $^{13}C\{^{1}H\}$ NMR ($CDCl_3$): δ/ppm 8.81, 14.09, 22.39, 22.66, 26.40, 28.15, 29.33, 29.39, 29.42, 29.45, 29.48, 29.52, 29.58, 29.63, 31.90, 32.83, 34.04, 56.62, 60.62, 76.76, 77.08, 77.40. MS (ESI^+ in CH_3OH): found *m/z* = 340.6; required for $\{C_{23}H_{50}N^+\}$: m/z = 340.

C_{18}TEAB. ^{1}H NMR ($CDCl_3$): δ/ppm 0.81 (t, CH_3, [3H]), 1.11-1.46 (br s, CH_2 and CH_3, [36H]), 1.29-1.41 (m, CH_3, [3H]), 1.78 (m, CH_2, [2H]), 3.28 – 3.48 (m, CH_2, [8H]). $^{13}C\{^{1}H\}$ NMR ($CDCl_3$): δ/ppm 8.15, 14.11, 22.13, 22.69, 26.55, 28.19, 28.77, 29.17, 29.36, 29.41, 29.44, 29.55, 29.59, 29.62, 29.66, 29.69, 31.93, 32.86, 34.02, 53.64, 57.65, 76.72, 77.03, 77.35. MS (ESI^+ in CH_3OH): found *m/z* = 354.6; required for $\{C_{24}H_{52}N^+\}$: m/z = 354.

C_{20}DMEAB. ^{1}H NMR ($CDCl_3$): δ/ppm 0.81 (t, CH_3, [3H]), 1.12-1.42 (br s, CH_2 and CH_3, [37H]), 1.65 (m, CH_2, [2H]), 3.32 (s, CH_3, [6H]), 3.40-3.50 (m, CH_2, [2H]), 3.66 (q, CH_2, [2H]). $^{13}C\{^{1}H\}$ NMR ($CDCl_3$): δ/ppm 8.58, 14.07, 22.64, 22.70, 22.74, 26.27, 29.21, 29.31, 29.36, 29.44, 29.56, 29.61, 29.66, 29.77, 31.88, 32.81, 50.68, 59.33, 63.45, 69.19, 71.92, 76.80, 77.12, 77.44. MS (ESI^+ in CH_3OH): found *m/z* = 354.6; required for $\{C_{24}H_{52}N^+\}$: m/z = 354.

C_{20}DEMAB. ^{1}H NMR ($CDCl_3$): δ/ppm 0.81 (t, CH_3, [3H]), 1.13-1.26 (br s, CH_2 and CH_3, [37H]), 1.34 (t, CH_3, [3H]),1.58-1.69 (m, CH_2, [2H]) 3.20 (s, CH_3, [3H]), 3.32 (m, CH_2, [2H]), 3.55 (q, CH_2, [4H]). $^{13}C\{^{1}H\}$ NMR ($CDCl_3$): δ/ppm 8.30, 14.07, 22.36, 22.64, 25.77, 26.37, 29.18, 29.31, 29.39, 29.44, 29.49, 29.57, 29.61, 29.65, 29.66, 31.88, 32.81, 34.04, 38.62, 50.25, 56.65, 60.53, 76.80, 77.11, 77.44. MS (ESI^+ in CH_3OH): found *m/z* = 368.6; required for $\{C_{25}H_{54}N^+\}$: m/z = 368

C_{20}TEAB. ^{1}H NMR ($CDCl_3$): δ/ppm 0.81 (t, CH_3, [3H]), 1.08-1.41 (br s, CH_2 and CH_3, [43H]), 1.78 (m, CH_2, [2H]), 3.16 – 3.45 (m, CH_2, [8H]). $^{13}C\{^{1}H\}$ NMR ($CDCl_3$): δ/ppm 8.15, 14.11, 18.32, 22.13, 22.69, 26.51, 28.19, 28.77, 29.17, 29.20, 29.36, 29.41, 29.44, 29.55, 29.59, 29.62, 29.66, 29.69, 31.93, 32.86, 34.02, 53.64, 57.67, 76.72, 77.03, 77.35. MS (ESI^+ in CH_3OH): found *m/z* = 382.7; required for $\{C_{26}H_{56}N^+\}$: m/z = 382.

C_{22}DMEAB. ^{1}H NMR ($CDCl_3$): δ/ppm 0.81 (t, CH_3, [3H]), 1.13-1.25 (br s, CH_2 and CH_3, [38H]), 1.34 (t, CH_3, [3H]), 1.60-1.69 (m, CH_2, [2H]), 3.32 (s, CH_3, [6H]), 3.40-3.47 (m, CH_2, [2H]), 3.65 (q, CH_2, [2H]). $^{13}C\{^{1}H\}$ NMR ($CDCl_3$): δ/ppm 8.03, 13.48, 13.81, 14.07, 22.04, 22.37, 22.47, 22.64, 22.74, 25.67, 26.27, 29.07, 29.21, 29.40, 29.52, 29.67, 31.28, 31.88, 50.43, 50.71, 59.06, 76.20, 76.53, 76.84, 77.11, 77.44. MS (ESI^+ in CH_3OH): found *m/z* = 382.6; required for $\{C_{26}H_{56}N^+\}$: m/z = 382.

C_{22}DEMAB. ^{1}H NMR ($CDCl_3$): δ/ppm 0.81 (t, CH_3, [3H]), 1.13-1.25 (br s, CH_2 and CH_3, [41H]), 1.28-1.37 (t, CH_3, [3H]), 1.59-1.68 (m, CH_2, [2H]), 3.21 (s, CH_3, [3H]), 3.29-3.37 (m, CH_2, [2H]), 3.56 (q, CH_2, [4H]). $^{13}C\{^{1}H\}$ NMR ($CDCl_3$): δ/ppm 8.31, 9.25, 14.08, 22.37, 22.44, 22.64, 25.77, 26.38, 28.14, 28.73, 29.19, 29.31, 29.39, 29.45, 29.49, 29.57, 29.62, 29.67, 31.88, 32.80, 47.87, 50.26, 56.63, 60.53, 76.80, 77.11, 77.44. MS (ESI^+ in CH_3OH): found *m/z* = 396.7; required for $\{C_{27}H_{58}N^+\}$: m/z = 396

C_{22}TEAB. ^{1}H NMR ($CDCl_3$): δ/ppm 0.81 (t, CH_3, [3H]), 1.13-1.27 (br s, CH_2, [44H]), 1.29-1.39 (t, CH_3, [3H]), 1.57-1.68 (m, CH_2, [2H]), 3.17 – 3.49 (m, CH_2, [8H]). $^{13}C\{^{1}H\}$ NMR ($CDCl_3$): δ/ppm 8.13, 8.74, 14.10, 22.10, 22.66, 26.48, 28.16, 28.75, 29.16, 29.33, 29.40, 29.41, 29.45, 29.52, 29.58, 29.63, 29.67, 29.69, 31.90, 32.83, 34.04, 46.19, 55.59, 57.57, 58.46, 76.76, 77.08, 77.39. MS (ESI^+ in CH_3OH): found *m/z* = 410.7; required for $\{C_{28}H_{60}N^+\}$: m/z = 410.

4.3.2 Growth of mesoporous silica on indium-tin oxide electrodes

(i) **C_{18}DMEAB and C_{20}DMEAB**

The silica films were prepared on an indium-tin oxide (ITO) transparent electrode using the EASA method previously reported by Goux et al.[13] and employed for the work in Chapter 3. The sol electrolyte was prepared by adding 0.1 mol dm^{-3} $NaNO_3$ (0.1700 g, 2.00 mmol, ＞97 %, Timstar Laboratory Suppliers Ltd) in 20 cm^3 water and 20 cm^3 ethanol, and TEOS, 98 %, Sigma Aldrich, 905 μL), then C_{18}TAB (0.4801 g, 1.22 mmol) was added to the sol electrolyte.

For the C_{18}DMEAB (0.4801 g, 1.18 mmol) and C_{20}DMEAB (0.3000 g, 0.69 mmol) systems, the ethanol component was replaced with 20 cm^3 isopropyl alcohol to dissolve the surfactant at room temperature and all other reagents were kept constant when preparing the deposition electrolyte. The sol pH was adjusted to pH 3 by the slow addition of 0.2 mol dm^{-3} HCl in water. The sol was then hydrolysed for 2.5 h with stirring at 25 ℃.

(ii) **C_{18}DEMAB, C_{18}TEAB, C_{20}DEMAB, C_{20}TEAB, C_{22}DMEAB, C_{22}DEMAB and C_{22}TEAB**

The sol electrolyte synthesis was modified from the standard procedure when using C_{18}DEMAB (0.4801 g), C_{18}TEAB (0.4801 g), C_{20}DEMAB (0.3000 g), C_{20}TEAB (0.3000 g), C_{22}DMEAB (0.3000 g), C_{22}DEMAB (0.3000 g) and C_{22}TEAB (0.3000 g). The films were prepared by adding 0.1 mol dm^{-3} $NaNO_3$ in water (20 cm^3) with isopropyl alcohol (20 cm^3), adding TEOS (905 μL) and creating an acidic sol medium by adjusting the pH close to 3 using 0.2 mol dm^{-3} HCl. The sol was then stirred for 90 minutes, then the surfactants were added and allowed to stir for a further 30 minutes. Due to the increased hydrophobicity of surfactants, C_{18}DEMAB, C_{18}TEAB, C_{20}DEMAB, C_{20}TEAB, C_{22}DMEAB C_{22}DEMAB and C_{22}TEAB, the temperature was increased to 40 ℃ to ensure complete dissolution. The sol electrolyte was hydrolysed for 2.5 hours.

4.3.3 The electro-assisted deposition of mesoporous silica on ITO electrodes

The electrochemical cell setup consisted of a Teflon cell with a 15 mm × 20 mm ITO-coated glass (surface resistivity = 14-16 Ω^{-1}, Ossila) working electrode, stainless steel cone counter electrode and a silver rod pseudo reference electrode. A constant potential of -1.25 V was applied for a duration of 20 seconds using a Biologic SP150 potentiostat. The silica films were quickly washed with water and ethanol after each deposition, then placed in a drying oven at 130 ℃ for 16 hours. The surfactants were removed by submerging the film in a solution of 0.2 mol dm^{-3} HCl/ethanol for 15 minutes under gentle stirring. The films were then examined by GISAXS and CV to provide evidence of surfactant removal.

4.4 Results and Discussion

4.4.1 Pore structure and characterisation of EASA films

The surfactant chain length was kept constant at 18 carbons as the hydrophilic head was substituted with ethyl groups, thus steadily increasing the surfactant head size as shown in schematic 4.1. The increase in head size also increased its hydrophobicity and changed its solubility in the sol, therefore the sol composition was modified. This was achieved by adjusting the surfactant and TEOS concentrations to approximately 30 mmol dm^{-3} and 101 mmol dm^{-3} with a surfactant: silica ratio of about 0.30:1 for each surfactant. The water: ethanol ratio was changed to attempt silica deposition on ITO whereby the *P*6*mm* pore symmetry and vertical orientation was maintained. For C_{18}DMEAB, the water: ethanol ratio was 50: 50, 75: 25 and 15: 85 however, mesostructured films were difficult to obtain. Therefore, the water: ethanol combination was replaced with water: isopropyl alcohol with a ratio of 50:50 to obtain EASA films with the desired hexagonal pore structure. For C_{18}DEMAB and C_{18}TEAB, the water: isopropyl alcohol ratio was kept constant at 50:50 and the sol temperature raised to 40 ℃ to achieve complete surfactant dissolution and hence EASA films with the preferred structure and orientation. Depositions were carried out at an applied potential of -1.25 V for 20 seconds. Longer deposition times resulted in a build-up of silica spheres on the ITO surface due to condensation reactions in the bulk sol.[10,13,6] The sol electrolyte was maintained at approximately 40 ℃ during depositions for the surfactants with ethyl rich head groups, and the resulting films were then cleared of silica by-products using deionised water and ethanol on the surface and dried. Surfactant was removed from the pores by soaking in a solution containing ethanol acidified with a little HCl.

The in-plane GISAXS pattern shown in Fig. 4.23, was used to ascertain pore ordering and orientation of the resulting film with C_{18}DMEAB. There was no visual sign of problems associated with film adhesion or any irregularities. The 1D in-plane scattering pattern for the silica film with C_{18}DMEAB revealed features corresponding to the 10 (2.02°) 11 (3.50°) and 20 (4.18°) lattice planes. The modification of the surfactant head saw a drop-off in peak intensity, suggesting micelle disorganisation starting to occur within the silica film. A further shift of the GISAXS feature corresponding to the 10 lattice plane to smaller angle was seen, this pointed towards an increase in the d spacing and pore spacing a_0, values to 4.4 nm and 5.10 nm compared to the C_{18}TAB produced film at 4.15 nm and 4.79 nm respectively. Campos et al.[14] reported similar XRD features for the aqueous dispersions of mesoporous hybrid silicas using cetyldimethylethylammonium bromide. On the contrary, Christiansen et al.[15] examined the synthesis of layered mesoporous silicate materials using cetyldimethylethylammonium bromide. It was understood that a disorganised lamellar structure was identified for the silica material with hydrothermal treatment

lasting a day. However, after 3 days of heat treatment the silica-lamellar mesoporous material was highly organised.

In Fig. 4.23ii (inset), the 2D diffraction image for the silica film produced by C_{18}DMEAB reveals distinct spots, which is associated with the 10 reflection. For C_{18}TAB, the diffraction spots are more concentrated than those found in C_{18}DMEAB, indicating an increase in pore disorder, which draws a parallel with 1D GISAXS data. Nevertheless, the spots are direct evidence that the pores are oriented vertically to the surface. A diffraction ring is noticed for the film with C_{18}DMEAB, albeit at low intensity, and is indicative of surface aggregates to the point where they are detectable by in-plane GISAXS, as explained in the Chapter 3.

Figure 4.23 presents 1D and 2D (inset) GISAXS patterns of a silica film using C_{18}DEMAB respectively. The alkylammonium bromide surfactant was modified further to incorporate two ethyl substituents and one methyl to the hydrophilic head. The starting sol electrolyte was adjusted by replacing the ethanol solvent with isopropyl alcohol to bring the C_{18}DEMAB surfactant into dissolution. These changes were necessary to deposit porous silica onto the ITO surface successfully and to answer questions on whether the hexagonal pore arrangement would increase or lessen further relative to films with C_{18}TAB and C_{18}DMEAB. This resulted in reduced intensity and broadening of the 10 diffraction peak, suggesting a further reduction in hexagonal ordering for the silica film with C_{18}DEMAB (as shown in Fig. 4.23).

The synthesis of porous silica films by the EASA method tends to produce mesopores that orient vertical to the substrate's surface. 2D GISAXS (shown in Fig. 4.23iii inset) was used to confirm the pore structure and orientation of the film after removing the surfactant from the pores. Bragg spots can be clearly observed along the horizontal direction, which can be indexed to the 10 reflection, fitting the Laue group of *P6mm* with vertically oriented pores. A diffraction ring can be seen in the image, which is higher in intensity than observed for C_{18}DMEAB.

In contrast, the silica film produced with C_{18}TEAB gave rise to a disordered film, as indicated by the 1D GISAXS pattern shown in Fig. 4.23. A sizeable reduction in peak intensity of the 10 peak and the absence of 11, 20 and 21 peaks were spotted, suggesting a significant loss in the ordering of pores. Ryoo et al.[2] studied the mesostructural phases of MCM-41 materials with cationic surfactants of increasing head size. The findings summarise that docosyltrimethylammonium bromide is likely to result in lamellar mesophases, whereas, switching to a bulkier head group such as triethylammonium bromide would favour a hexagonally ordered mesophase. This is contrary to what is obtained for EASA-derived silica films using the same surfactants.

According to the 2D GISAXS image of C_{18}TEAB silica film (shown in Fig. 4.23 iv inset), weaker spots were observed for the 10 plane compared to the other C_{18} modified surfactants, however, because the spots are visible it clearly identifies the pore position as vertical with the system remaining highly disorganised. As can be seen (Fig 4.23), the GISAXS plots of the EASA films with C_{18} modified head groups show a significant reduction in the 10 peak and the gradual disappearance in the 11, 20 and 21 diffraction peaks compared to those of C_{18}TAB. Nevertheless, the most promising sample is the C_{18}DMEAB templated silica film, as the distortion of the hexagonal pattern is minimal and the GISAXS 10 peak moves to larger pore spacing values compared to C_{18}TAB as revealed previously.

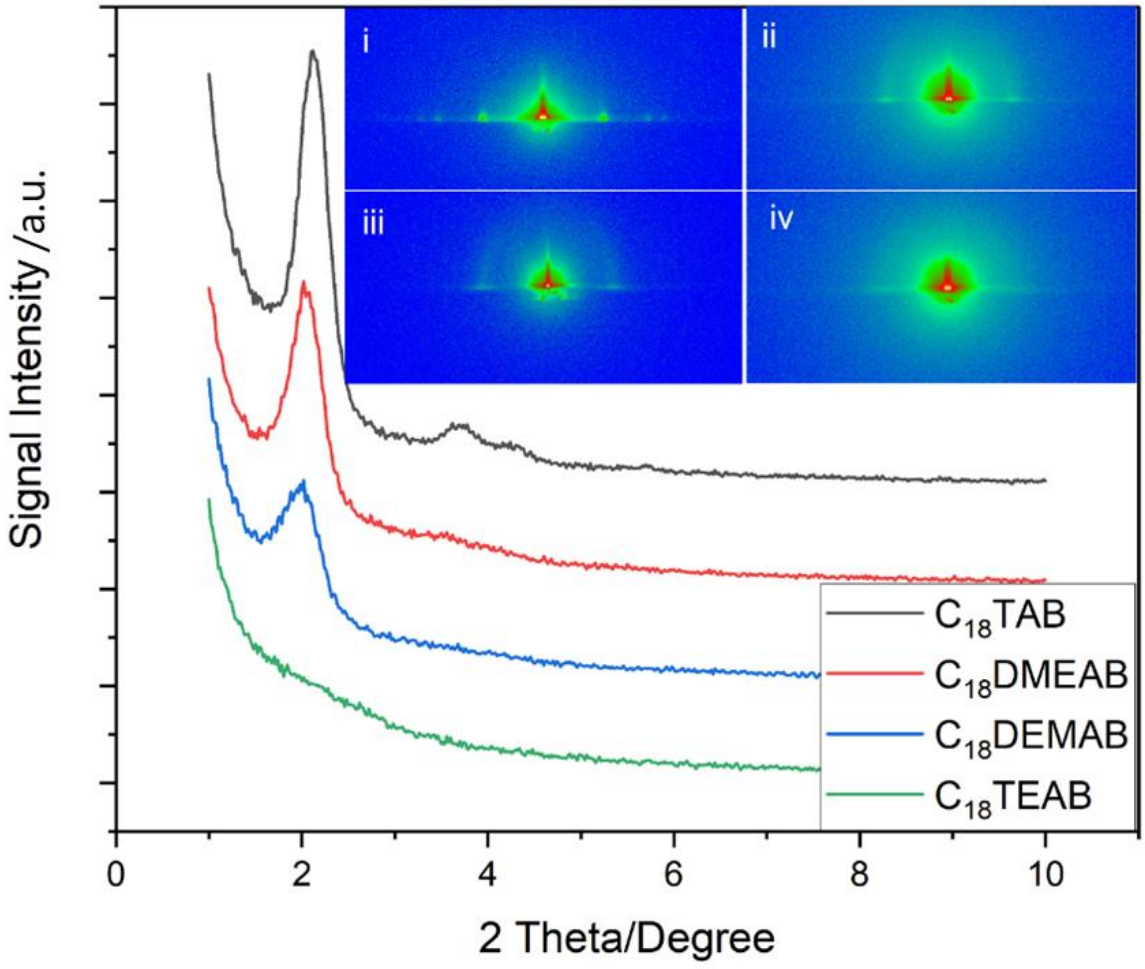

Figure 4.23 1D in-plane GISAXS scattering patterns of mesoporous silica films templated by C_{18}TAB, C_{18}DMEAB, C_{18}DEMAB and C_{18}TEAB deposited at a potential of -1.25 V (vs. Ag/Ag^+) for 20 s on ITO electrodes (top left; inset: 2D GISAXS images of silica films templated by (i) C_{18}TAB, (ii) C_{18}DMEAB, (iii) C_{18}DEMAB and (iv) C_{18}TEAB.

There are two established ways to remove the surfactant template, either by washing in acidic alcoholic bath or by calcination. The former method was applied and the EASA films with C_{18}TAB, C_{18}DMEAB, C_{18}DEMAB and C_{18}TEAB were characterised by SEM (shown in Fig. 4.24). The top view SEM images of each film shows good surface coverage with no signs of microcracks or poor adhesion. The estimated film thickness for the EASA film with C_{18}TAB was 125 nm and was found to be in similar regions to the other EASA film thicknesses. It should be noted that silica aggregates were found on the surface for films with C_{18}TAB, C_{18}DMEAB and C_{18}DEMAB, consequently, silica continues to condense even after the passing of current, giving rise to a thin silica layer formed over the underlying film. The formation of silica spheres is largely associated with the Stöber process, where the silica oligomers form around the micelles in the bulk solution. This causes the silica spheres to stick to the forming gel film.[4]

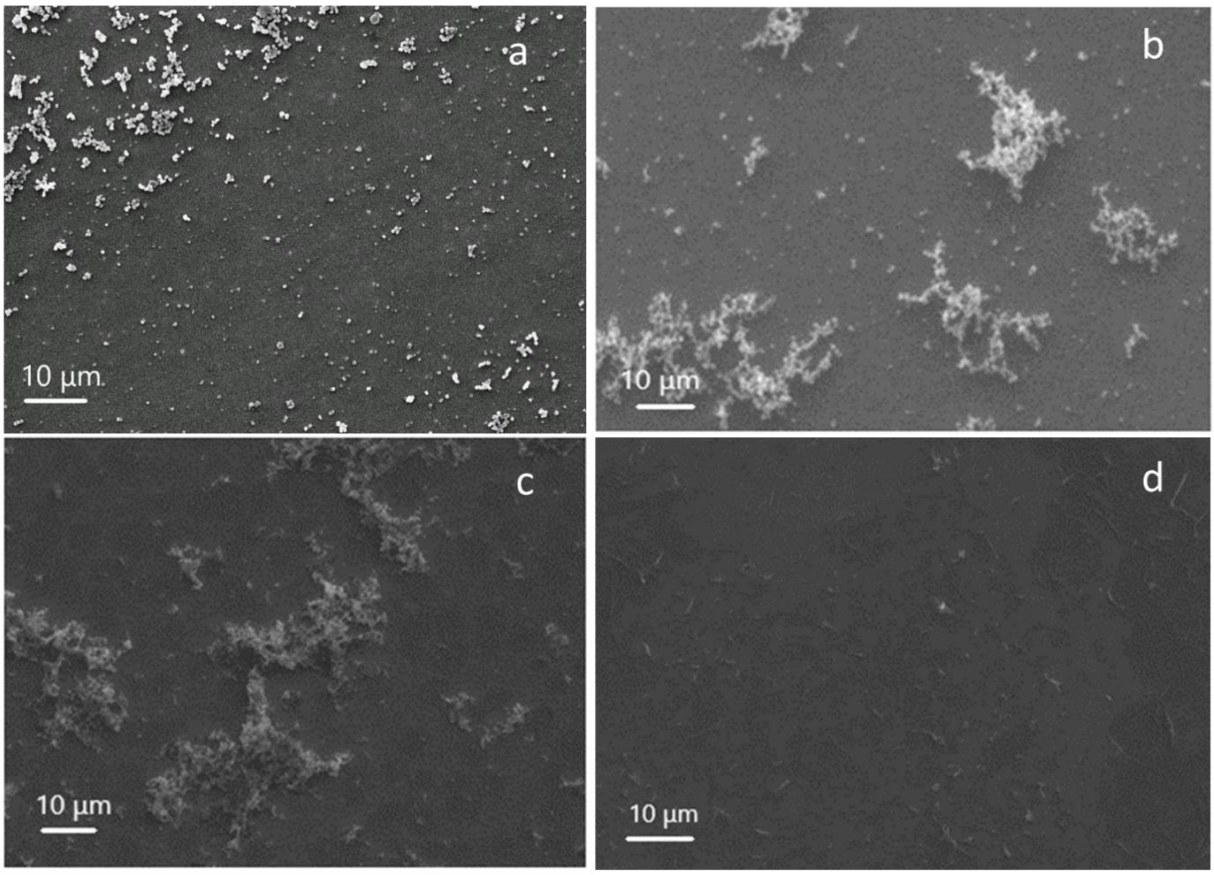

Figure 4.24 Top view SEM images of EASA films with (a) C_{18}TAB, (b) C_{18}DMEAB, (c) C_{18}DEMAB and (d) C_{18}TEAB deposited at an applied potential of -1.25 V (Ag/Ag^+) for 20 s on ITO electrodes.

Mesoporous silica films produced by the EASA method were characterised based on their ordered or disordered arrangement of pores. The structural properties of these materials such as large pore volume, ordered mesopores, variable pore sizes and uniform pore architecture can be modified by the variation of surfactant head sizes.[2] TEM provides information on the morphological features of the EASA-derived silica films and are shown below as follows.

TEM imaging was carried out on the EASA films generated with C_{18}TAB, C_{18}DMEAB, C_{18}DEMAB and C_{18}TEAB by Yisong Han using a JEOL ARM200f double-corrected TEM operated at 200 kV. The images were taken by stripping small sections of film from the ITO surface with a scalpel to investigate the mesoporous structure. Previously, the GISAXS data (shown in Fig. 4.23) suggested a gradual loss of hexagonal micelle organisation as the hydrophilic head increased with methyl groups sequentially replaced with ethyl substituents. The TEM images in Fig. 4.25 show the C_{18}TAB produced film to have a highly organised hexagonal structure of mesopores. As the surfactant head size increases, this initiates a slight distortion of the hexagonally ordered film with C_{18}DMEAB, and with C_{18}DEMAB and C_{18}TEAB further loss in pore ordering is observed, which correlates with the GISAXS data (shown in Fig. 4.23). It should be stated, that the GISAXS data confirm that all films possess vertically oriented pores, it is only the hexagonal ordering that is lost in comparison to the film with C_{18}TAB. Loss of order with increasing cationic surfactant head size has been linked to repulsions between the larger surfactant head groups causing steric hinderance to occur, slowing down the process of micellization as a result of fewer bromide counterions condensing in the vicinity of the micelle.[1,16] Film formation occurs below the critical micellar concentration (CMC), which is stated to be around 30 mmol dm^{-3} for CTAB in a sol electrolyte with 50:50 water:ethanol.[13,17] This provides evidence that the surfactant template does not self-assemble in the desired hexagonal arrangement in the sol, it is the electric field which drives the interaction between positively charged surfactant molecule and the negatively charged ITO electrode. In turn, this favours the formation of hemimicelles (in its hexagonal shape) and induces silica condensation and hence SiO_2 film formation with vertical pores. The hexagonal pore structure occurs when working below the CMC and so, knowledge of the CMC is less critical here than it would be in a “standard” sol-gel study.

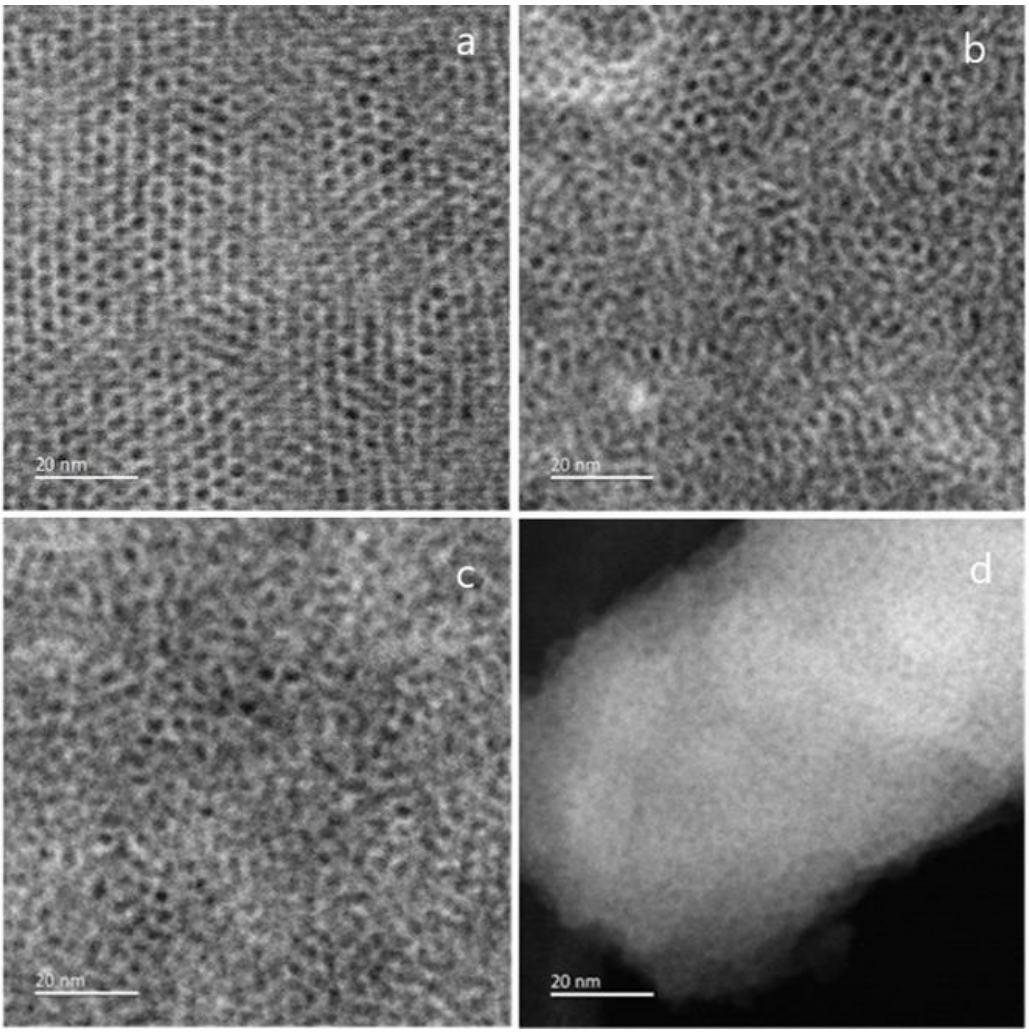

Figure 4.25 TEM images of mesoporous silica films generated by (a) C_{18}TAB, (b) C_{18}DMEAB, (c) C_{18}DEMAB and (d) C_{18}TEAB deposited at -1.25 V (vs. Ag/Ag^{+}) for 20 s on ITO electrodes.

4.4.2 Pore transit measurements of redox molecules through EASA films on ITO electrodes

Pore transit measurements were carried out for a range of EASA films using an anionic probe molecule. These investigations were undertaken to determine whether the effect of increasing the surfactant head size would influence the ability of ions to move through the pores, which would be evident from deviations in the voltametric profiles. The electrochemical reduction and oxidation of ferricyanide is shown in Eq. 1. The porosity was determined using 0.5 mmol dm^{-3} $[Fe(CN)_6]^{3-/4-}$ in a solution containing 0.1 mol dm^{-3} $NaNO_3$ as the background electrolyte (as shown in Fig. 4.26).

$$[Fe(CN)_6]^{3-} + e^{-} \underset{\text{Oxidation}}{\overset{\text{Reduction}}{\rightleftharpoons}} [Fe(CN)_6]^{4-} \qquad \text{Eq 1}$$

Upon extracting the surfactant from the pores, a drop in peak current and a large peak to peak separation is observed, most likely due to electrostatic repulsions between the anionic molecule and silanol groups attached to the silica pore walls, which could be associated with the Donnan exclusion effect[18] (as shown in Table 4.1). The voltametric peak profiles for the films with C_{18}TAB to C_{18}TEAB, were seen to decrease in current intensity, comparative to that of bare ITO (shown in Fig 4.26 inset). As mentioned previously, this suggests the possibility that steric hindrance from the larger surfactant head size plays a pivotal role in the organisation of pores, in turn affecting the ion diffusion rates through the silica film. Interestingly, the films with C_{18}DEMAB and C_{18}TEAB reveal no faradaic current, with the voltammograms similar in shape to functionalised carbon electrodes run in supercapacitor studies exhibiting excellent capacitive behaviour,[19] as well as mirroring that of blocked pores before the surfactant has been removed from the film.[20,21] Nevertheless, this can be ascribed to a significant decline in the film's hexagonal ordered pore structure due to the bulkier surfactant heads, leading to a curtailment in mass transport properties.

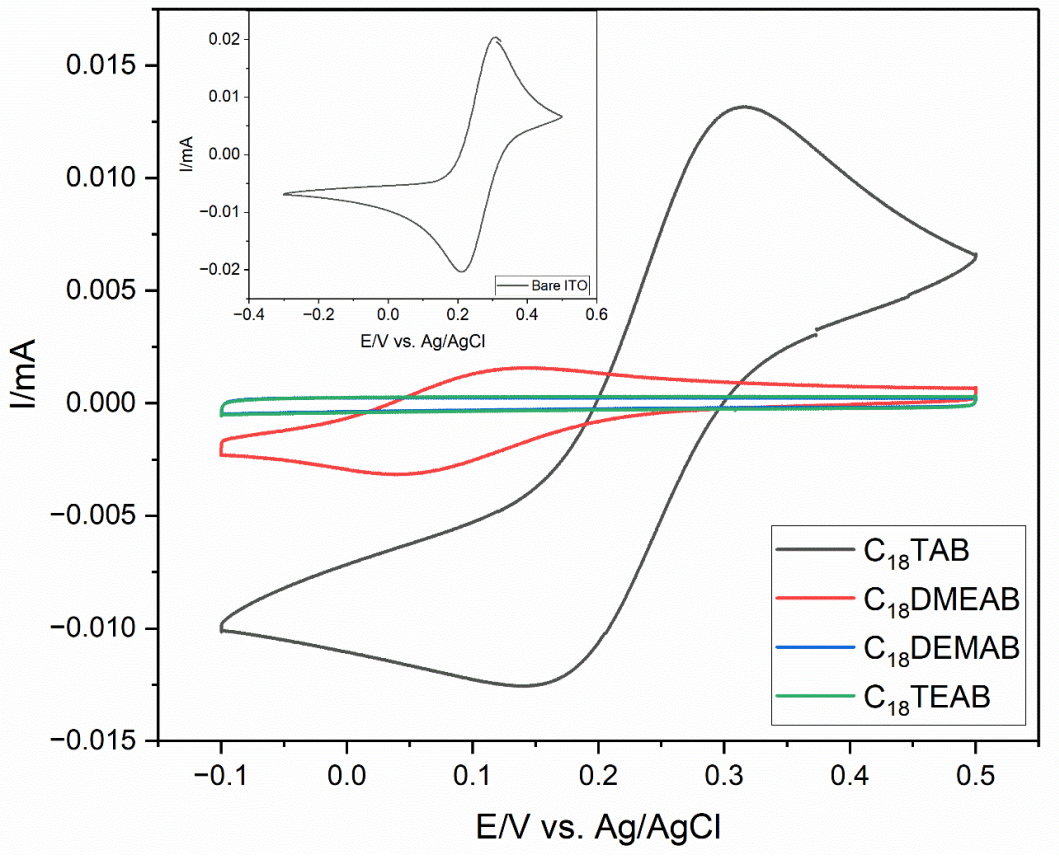

Figure 4.26 Cyclic Voltammograms (right) (20 mV s^{-1} sweep rate) of 0.5 mmol dm^{-3} $[Fe(CN)_6]^{3-/4-}$ in 0.1 mol dm^{-3} $NaNO_{3(aq)}$ on bare ITO electrode (inset). The generated mesoporous silica films using C_{18}TAB (black line), C_{18}DMEAB (red line), C_{18}DEMAB (blue line) and C_{18}TEAB (green line) as the surfactants were deposited at -1.25 V (vs. Ag/Ag^{+}) for 20 s on ITO electrodes.

Table 4.1. The electrochemical data of a range of mesoporous silica films collected from CVs.

Surfactants/Electrode	Redox Probe	I_{pa} / mA	I_{pc} / mA	ΔE_p / mV
Bare ITO	$[Fe(CN)_6]^{3-/4-}$	2.02×10^{-2}	-2.03×10^{-2}	90
C_{18}TAB	$[Fe(CN)_6]^{3-/4-}$	1.35×10^{-2}	-1.26×10^{-2}	148
C_{18}DMEAB	$[Fe(CN)_6]^{3-/4-}$	1.58×10^{-3}	-3.01×10^{-3}	104
C_{18}DEMAB	$[Fe(CN)_6]^{3-/4-}$	N/A	N/A	N/A
C_{18}TEAB	$[Fe(CN)_6]^{3-/4-}$	N/A	N/A	N/A

EIS was employed to further characterise the EASA films produced with the various head groups (Fig 4.27 a and 4.27 b). The Nyquist plots were carried out in the same redox probe molecule solution as the pore transit measurements described above. The EIS plots can be simulated using a simple Randles equivalent circuit where R_s, R_{ct} and C_{dl} are the electrolyte resistance, charge transfer resistance and double layer capacitance, respectively. The Nyquist plots of C_{18}TAB and C_{18}DMEAB derived silica films are composed of a semicircle in the high frequency range and a 45° straight line due to the Warburg impedance (Z_w). Previous works have shown that mass transport of redox-active molecules through porous silica films is governed by diffusion processes.[7,10,13] Therefore, the charge transfer resistance is highly dependent on the number of open pores available for ion transport and ionic charge from redox active molecules. Fitting to the Randles circuit, it was found that the R_{ct} of bare ITO was 144.0 Ω, which was lower than the R_{ct} of 416.6 Ω and 830.2 Ω obtained in films produced by C_{18}TAB and C_{18}DMEAB, showing higher conductivity for the transparent electrode. The incorporation of two or three ethyl groups attached to the surfactant's hydrophobic tail resulted in much larger and imperfect semicircles (Fig. 4.27b), suggesting poorer pore accessibility of the redox active ion, $[Fe(CN)_6]^{3-/4-}$ transporting through the silica films than that seen with the C_{18}TAB and C_{18}DMEAB films. Moreover, despite the increased pore spacing and possible pore expansion found in C_{18}DMEAB produced film, the R_{ct} value is higher than for C_{18}TAB due to pore disorder and the limited number of available pores present, which hinder the diffusion of redox molecules within the silica pore channels. The EIS data agree with those from the CVs, presenting further evidence that the reduction in pore order with increasing head size is accompanied by loss of access to the electrode surface.

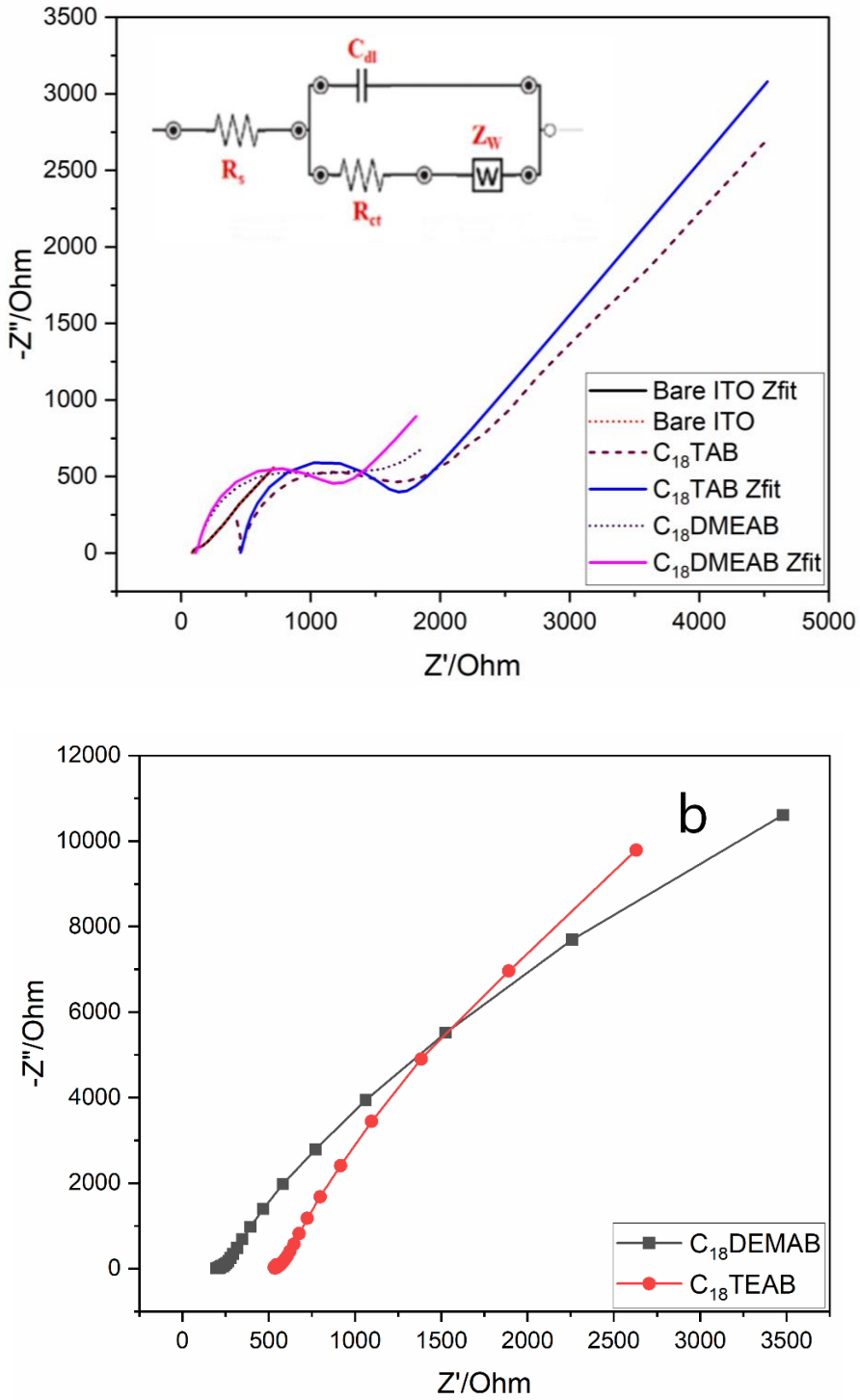

Figure 4.27 Nyquist plots (a) of bare ITO, mesoporous silica films on ITO electrodes with C_{18}TAB and C_{18}DMEAB as the surfactant templates and Randle's equivalent circuit (chapter two, ref. 18) (inset), and (b) of mesoporous silica films on ITO electrodes with C_{18}DEMAB and C_{18}TEAB as the surfactant templates. The data was recorded in 0.5 mmol dm^{-3} $[Fe(CN)_6]^{3-/4-}$ containing 0.1 mol dm^{-3} $NaNO_{3(aq)}$ as the supporting electrolyte. The generated mesoporous silica films using C_{18}TAB, C_{18}DMEAB, C_{18}DEMAB and C_{18}TEAB as the surfactants were deposited at -1.25 V (vs. Ag/Ag^+) for 20 s on ITO electrodes. All experiments were carried out after surfactant removal.

4.4.3 Ellipsometric porosimetry measurements of EASA films on ITO electrodes

EP was used to establish the pore size growth of EASA films using surfactants with a constant carbon chain length of 18 carbons and modified head groups. In the EP measurements, an isotherm of a mixture of type I (b) and type IV (b) is observed for the silica film with C_{18}DMEAB (as shown in Fig 4.28).[22] It is noticeable that there is an initial increase in the relative partial pressure in the mid-range between 0.05 and 0.12 P/P_0, which is caused by toluene filling the pores. For the adsorption-desorption branches, no hysteresis loop is present indicating that the process is not associated with capillary condensation. For the C_{18}DMEAB produced film, the PSD plot displays a peak pore size of 3.42 nm determined from the desorption branch (shown in Fig. 4.29) which is larger than the peak pore size observed for the silica film with C_{18}TAB at 3.24 nm acquired from the desorption isotherm.[10] The isotherm curves represent wide micropores and small mesopores, with similar literature found for toluene isotherms of silica films produced by C_nTAB.[10,23]

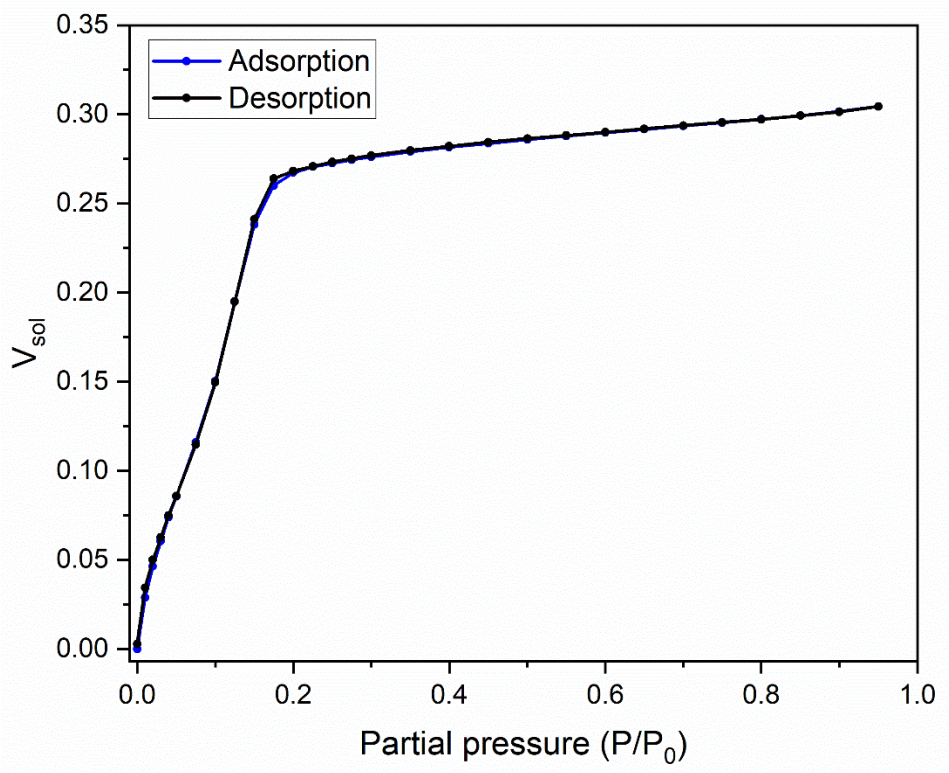

Figure 4.28 The adsorption/desorption isotherm of the EASA film produced by C_{18}DMEAB on an ITO substrate using toluene as the adsorptive.

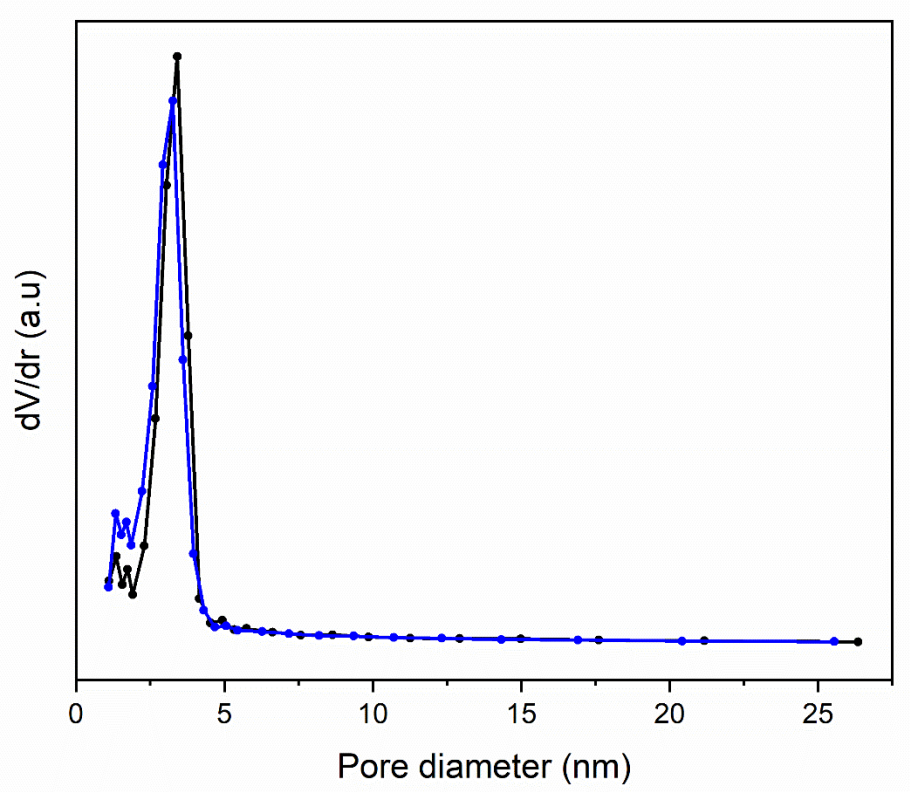

Figure 4.29 The pore size distribution curves determined from adsorption (blue) and desorption (black) isotherms of a mesoporous silica film produced using C_{18}DMEAB on an ITO substrate.

The porosity measurement for the film with C_{18}DEMAB was carried out after surfactant removal by placing the film in an acidic ethanol solution and then dried at 130 ℃ to evaporate ethanol from the pores. The following isotherm for the film templated by C_{18}DEMAB is shown in Fig. 4.30. The isotherm mirrors that of type I (b) and type II and from the desorption branch, a drop in the solvent volume is noticed at around 0.23 P/P_0 which is accompanied by a large hysteresis loop (type H4),[22] indicating the commencement of capillary condensation in the mesoporous material. The disordered sol-gel film could lead to problems related to pore blockage and cavitation which is determined by the type H4 hysteresis and is highly dependent on pore permeability, pore geometry and pore size.[24] The large peak in the PSD plot obtained from the desorption branch displayed an artificial peak pore size of 3.90 nm (as shown in Fig. 4.31) due to the disordered nature of the film allowing toluene desorption to occur at a rapid rate.[25]

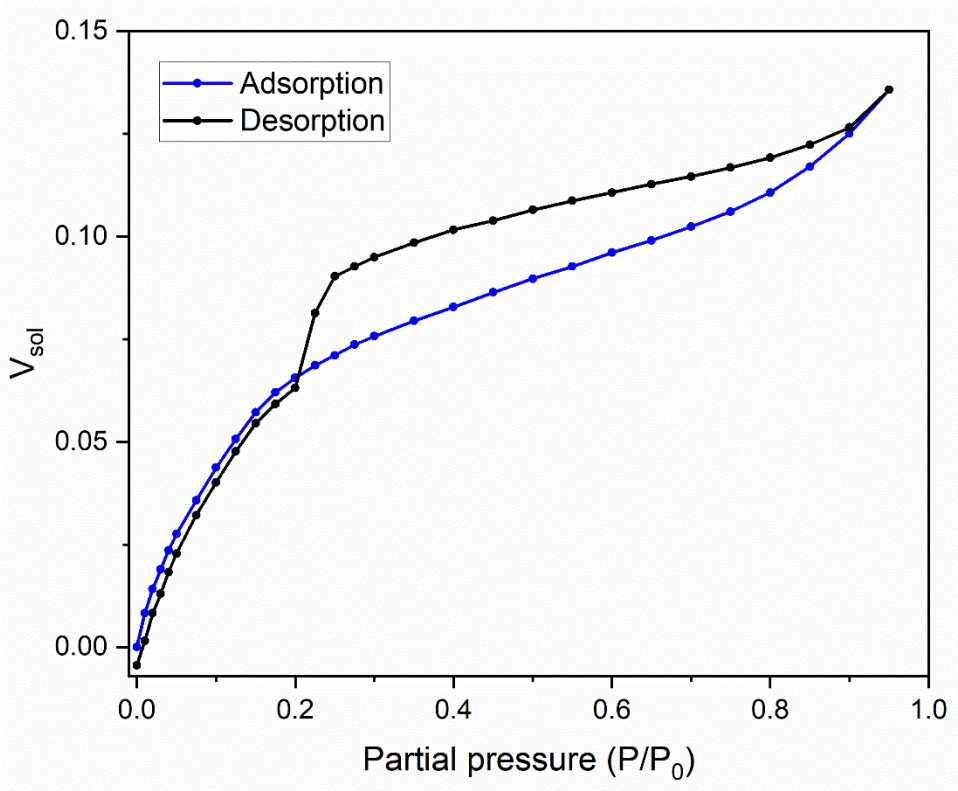

Figure 4.30 The adsorption/desorption isotherm of the EASA film produced by C_{18}DEMAB on an ITO substrate using toluene as the adsorptive.

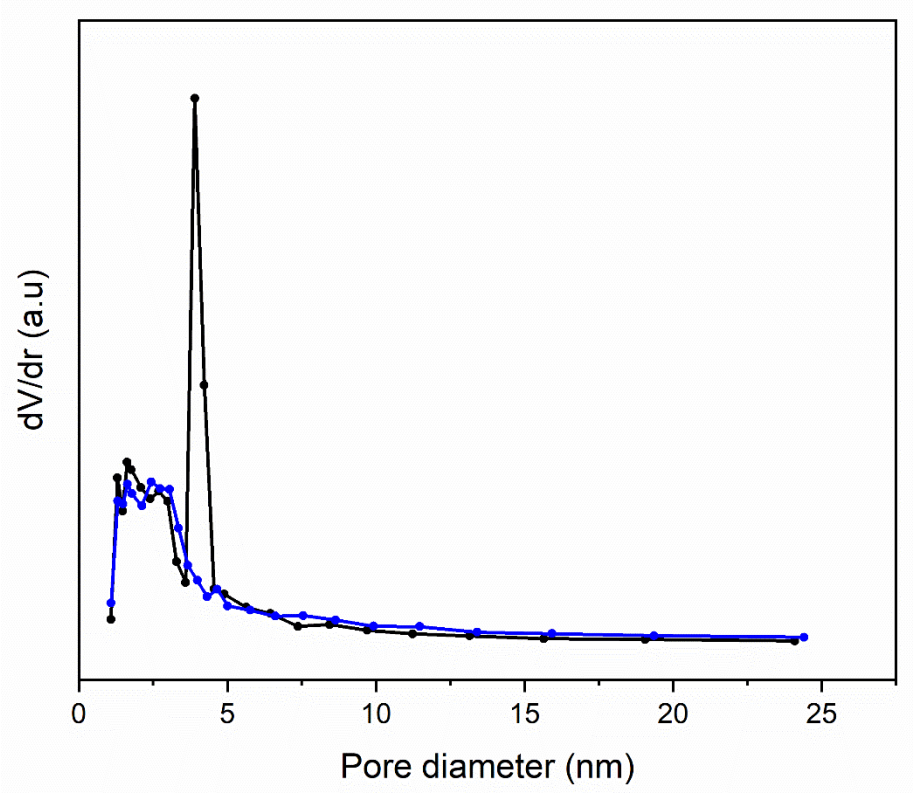

Figure 4.31 The pore size distribution curves determined from adsorption (blue) and desorption (black) isotherms of a mesoporous silica film produced by C_{18}DEMAB on an ITO substrate.

The surfactant head size was modified further by the addition of three ethyl moieties to the cationic head, with EP measurements undertaken at room temperature to determine the porosity characteristics of the C_{18}TEAB templated silica film. As shown in Fig. 4.32, the adsorption isotherm shows a dramatic increase at higher partial pressures which is indicative of higher rates of pore filling from the adsorptive in relation to lower pressure regions. The adsorption branch of the isotherm mostly imitates that of type II, by the clarity of separation between monolayer coverage, multilayer adsorption, and the filling of mesopores. From the adsorption branch, the reduction in the solvent volume (V_{sol}) followed by a hysteresis loop at around 0.14 relative pressures is observed. This behaviour is similar to argon-based isotherms for SBA-16 silica materials using non-ionic surfactants reported by Kim et al.,[26] and for the C_{18}DEMAB film whereby the reduction in V_{sol} was the cause of the fabricated pore diameter obtained from the desorption isotherm. The artificial peak pore size for the C_{18}TEAB film was determined at 3.76 nm (Fig. 4.33). Nevertheless, the peak pore size at 3.53 nm witnessed from the minor peaks in the adsorption branch which most likely represents an accurate measure of the mesopore size.

The hysteresis found in the desorption isotherm matches the type H3 as opposed to the H4 hysteresis type found in C_{18}DEMAB. The rationale behind this is the depletion of toluene uptake at lower partial pressure, due to a limited amount of micropores present within the silica material. From the GISAXS and electron microscopy observations, it was understood that the hexagonal pore structure became distorted with increasing surfactant head size, however, the PSD plots for C_{18}DEMAB and C_{18}TEAB reveal accurate peak pore sizes despite the significant increase in pore disorder of the systems. The isotherm curves are reminiscent of materials where pore blockage/cavitation takes precedence and is most often seen for ordered and disordered porous materials such as SiO_2-templated materials, sandstones, clays, and Zeolites.[24]

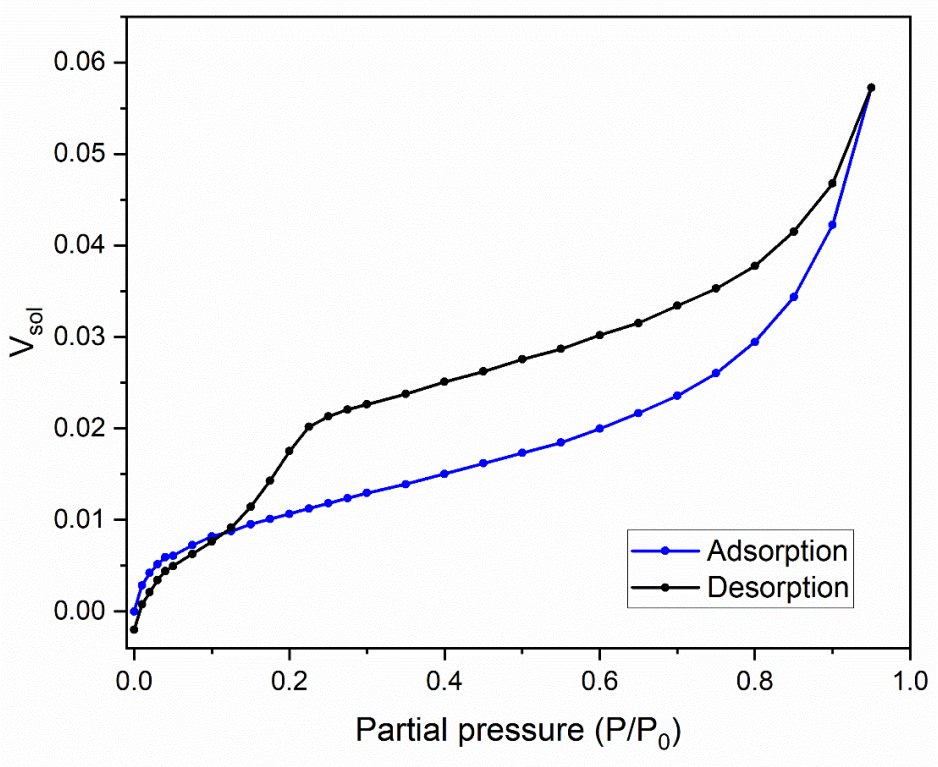

Figure 4.32 The adsorption/desorption isotherms of the EASA films produced by C_{18}TEAB on an ITO substrate using toluene as the adsorptive.

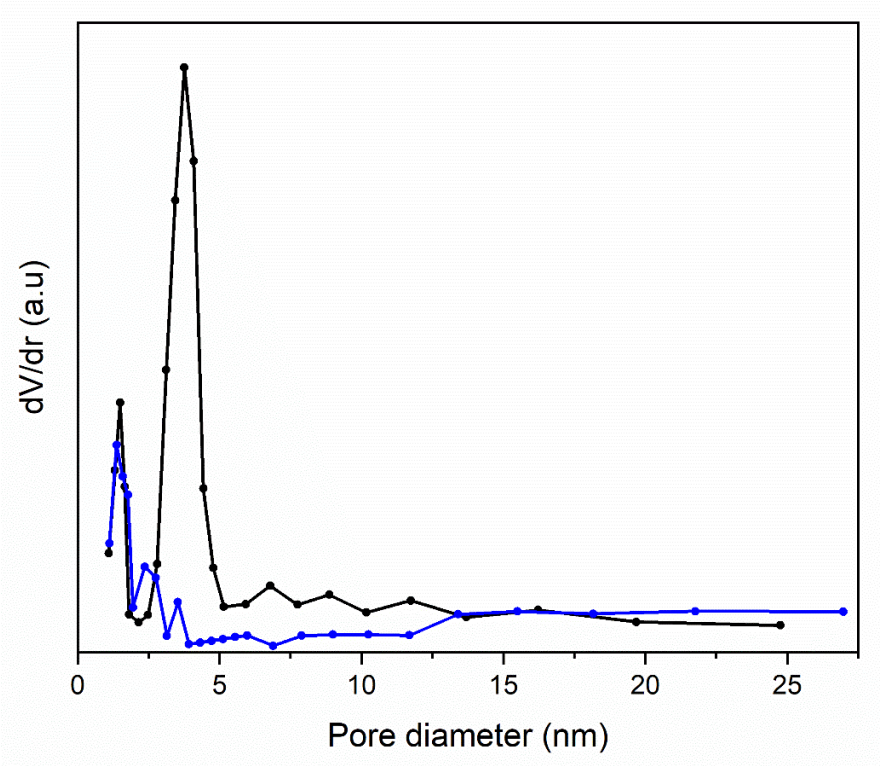

Figure 4.33 The pore size distribution curves determined from adsorption (blue) and desorption (black) isotherms of a mesoporous silica film produced by C_{18}TEAB on an ITO substrate.

4.4.4 Grazing incidence small angle X-ray scattering analysis of EASA films using C_{20} and C_{22} surfactants of increasing head sizes

The carbon chain length was increased to 20 carbon atoms to investigate the effect of head group modification of surfactants on the production of EASA films. Figure 4.34 shows the GISAXS plots of EASA Films templated by C_{20}TAB, C_{20}DMEAB, C_{20}DEMAB and C_{20}TEAB after surfactant extraction. The silica sample showed a broadening of the diffraction peak for the C_{20}DMEAB produced film at 2 θ = (2.12 °), which can be attributed to the 10 lattice plane. Interestingly, the drop in 10 peak intensity along with the shift to higher angle, which associates to smaller d-spacing (d_{10}) and pore spacing (a_0) values of 4.20 nm and 4.81 nm, is clearly evident. Values for C_{20}TAB were d_{10} = 4.48 nm and a_0 = 5.18 nm. It is to be noted that the shape of micelles can be elucidated from the surfactant packing, which is reliant on the surfactant geometry. The equation for the surfactant packing (g) is as follows; $g = V/(a_0L)$, where V is the volume of the extended surfactant chain, a_0 is the area of the bulky head group and L is the length of surfactant chain which is important to determine the surfactant organisation of mesostructured materials. The surfactant properties such as the carbon chain length, counter ion charge and bulk of the head group are very important in the analysis of the mesostructure in its ultimate form.[27] For instance, the SBA-3 silica material using CTAB favours the formation of hexagonal mesophases whereas SBA-1 with a larger surfactant head size C_{16}TEAB tends to produce cubic mesophases under fixed temperatures of 273 K, indicating the influence of different surfactant heads on the mesophase.[27,28]

An interesting phenomenon was observed for films with C_{20} modified head groups, where the 10 peak moves to higher angle despite the increase in surfactant (C_{20}DMEAB) size. An opposite trend was noticed for films with C_{22} modified head groups, which saw the 10 peak move to lower angle. Typically, as the surfactant size increases, the diffraction peaks shift to lower 2 θ values, in turn revealing higher d-spacings. This trend is seen for C_{18} and C_{22} films but that with C_{20}, it was inconsistent.

In the case of C_{20}DMEAB, the loss in ordering and smaller d-spacing is possibly due to the hydrophilic head interacting with the C_{20} chain, causing the alkyl chain length to shrink in size, which disturbs the micellisation process and most likely initiates changes to micelle size and hence the mesopores of porous silicas. The system requires further investigation to fully resolve what is happening. Similar behaviours were reported by Lin et al.[1] for MCM-41 materials produced by cetylbenzyldimethylammonium bromide, $C_{25}H_{46}BrN$. They established that interaction between the surfactant head and tail causes the extended tail to shrink, leading to MCM-41 materials with smaller pore diameters. They also stated that steric hinderance of the surfactant head was the cause for the poor hexagonal arrangement observed in the XRD pattern.

Huo et al.[29,15] discovered that the ratio between the volume and length of the surfactant chain for the alkyltrimethylammonium bromide surfactants (C_nMe_3Br, where C_n ranges from 8-18), does not change with increases to the hydrophobic tail. However, as C_n extends beyond 20 carbon atoms, the surfactant tail starts to curl, which causes a decrease in the length l, without significant changes to the volume. This phenomenon increases the value of g which results in micelles formed with reduced arch shape for surfactants such as $C_{20}Me_3Br$ and $C_{22}Me_3Br$, leading to porous silicas with lamellar mesophases. On the contrary, surfactant tail lengths between C_8-C_{18} tends to favour hexagonal MCM-41.

For the film with C_{20}DEMAB, a further loss in hexagonal pore order is observed (as shown in Fig. 4.34). However, despite the lowered intensity of the 10 diffraction peak at 2θ = 1.96 °, it is clear that it moves to higher d-spacing than that shown with C_{20}TAB and C_{20}DMEAB, suggesting an increase in the a_0 value and the possibility of pore growth. The GISAXS pattern for the film with C_{20}TEAB shows an even further lowering of 10 peak intensity at 2θ = (1.90 °), compared to C_{20}DEMAB, the disappearance in 11, 20 and 21 reflections are seen similarly to other films with modified head groups. Interestingly, the 10 peak shifts to a larger d-spacing and is more intense, indicating an improvement in the hexagonal order than that with C_{18}TEAB.

In order to confirm the mesoporous structure of the silica films with C_{20} surfactants of increasing head sizes as well as providing evidence of vertical pore orientation, 2-dimensional GISAXS was used for the characterisation process. Figure 4.34 inset shows the 2D GISAXS images of the films templated by C_{20}TAB, C_{20}DMEAB, C_{20}DEMAB and C_{20}TEAB. All films exhibit in-plane Bragg spots on the horizontal plane however, the long-range order Bragg spots related to the 11, 20 and 21 lattice planes disappear as the hydrophilic head size increases, which complements the 1D scattering patterns (shown in Fig 4.34). Diffraction rings of relatively high intensity are visible for C_{20}TAB but drop in intensity as the surfactant head size grows, implying that surface aggregates can be mitigated or reduced by the presence of larger surfactants in the sol medium. The general trend is that the Bragg spot intensity reduces as the head size increases but an outlier to this development is the C_{20}TEAB film, where the spots are more concentrated than that shown with C_{18}TEAB.

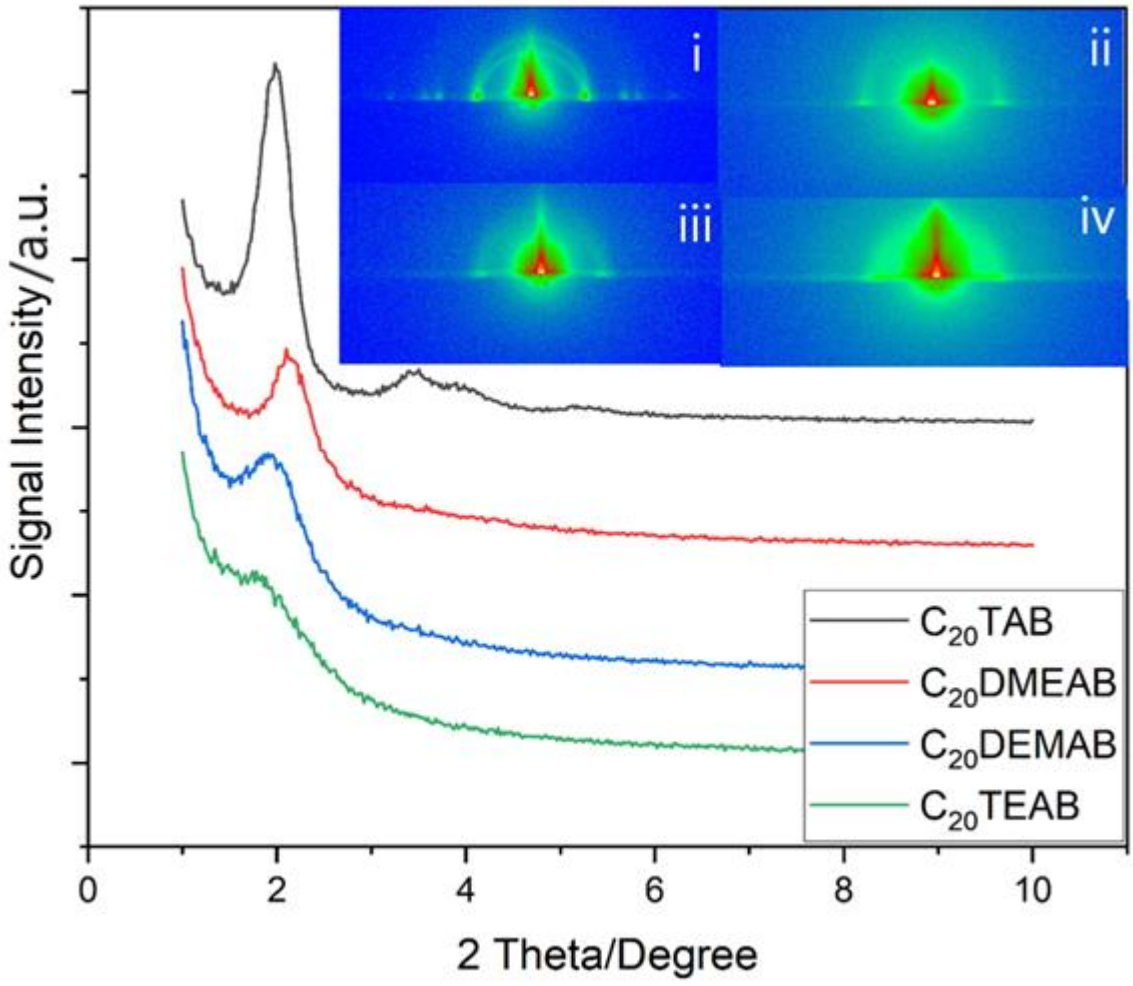

Figure 4.34 1D in-plane GISAXS scattering patterns of mesoporous silica films templated by C_{20}TAB, C_{20}DMEAB, C_{20}DEMAB and C_{20}TEAB deposited at a potential of -1.25 V (vs. Ag/Ag^{+}) for 20 s on ITO electrodes (top left; inset: 2D GISAXS images of silica films templated by (i) C_{20}TAB, (ii) C_{20}DMEAB, (iii) C_{20}DEMAB and (iv) C_{20}TEAB.

The sol recipe was altered for the C_{22}DMEAB templated film as it became apparent that the effects of surfactant on the solubility and dissolution in the sol electrolyte needed to be explored. The surfactant/silica ratio was 0.17 to ease the dissolution process, the sol appearance was cloudy due to the undissolved surfactant, this was resolved by raising the sol temperature to 40 ℃ to liquify the surfactant and the electro-assisted deposition of silica was performed at around 40 ℃. This was not the case for films with C_{18}DMEAB and C_{20}DMEAB as heat treatment was not necessary.

Figure 4.35 displays the 1D in-plane scattering patterns obtained for films with C_{22}TAB, C_{22}DMEAB, C_{22}DEMAB and C_{22}TEAB. As can be seen, the diffraction feature relating to the 10 plane decreases in intensity, suggesting the gradual degradation in hexagonal ordering as each methyl moieties interchanged with ethyl in the cationic head group. For the film grown by C_{22}DMEAB, the 10 peak at 2θ = (2.00°) moves to lower angle which is a common theme for the alkyltrimethylammonium

bromide surfactants discussed in the previous chapter and contrary to the film with C_{20}DMEAB, indicating surfactant stability during the micellar process. The GISAXS pattern for the film with C_{22}DEMAB reveals significant peak expansion for the feature at 2θ = (1.98 °), relating to the 10 reflection, signifying a further loss of hexagonal ordering compared to C_{22}TAB and C_{22}DMEAB templated films. The 10 peak observed at 2θ = (1.88 °), for the film with C_{22}TEAB is greater in intensity than for C_{18}TEAB and C_{20}TEAB, suggesting that increasing the alkyl chain length whilst retaining the triethylammonium bromide (TEAB) head group not only increases the lattice parameters but also minimises hexagonal pore disorder.

The 2D GISAXS patterns pertaining to EASA films with C_{22}TAB, C_{22}DMEAB, C_{22}DEMAB and C_{22}TEAB are shown in the inset of Figure 4.35. It is readily apparent the presence of Bragg spots on the parallel plane for all EASA films are noticed. Additionally, the film with C_{22}DMEAB retains the 11 and 20 lattice planes, which is not the case for C_{18}DMEAB and C_{20}DMEAB, demonstrating an improvement in the pore order. Another scattering feature saw in-plane rings around the spots which are most intense for C_{22}DMEAB. These features are minimal for the C_{18} modified surfactant head groups but are seen frequently for films with C_{20} and C_{22} modified head groups. Moreover, the 10 Bragg spots for films produced by C_{22}TEAB is significantly more focussed than for C_{18}TEAB and C_{20}TEAB, corresponding well to the 1D scattering patterns observed in the previous sections.

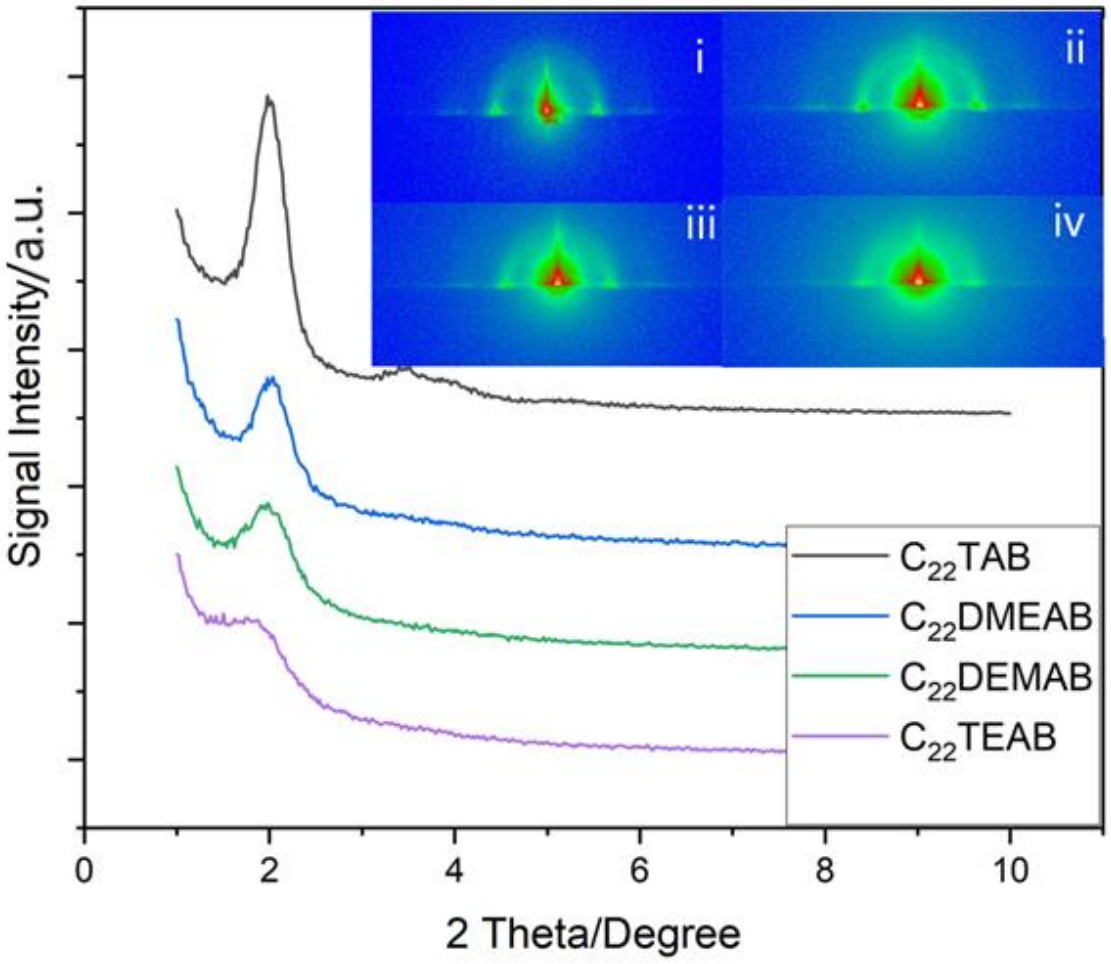

Figure 4.35 1D in-plane GISAXS scattering patterns of mesoporous silica films templated by C_{22}TAB, C_{22}DMEAB, C_{22}DEMAB and C_{22}TEAB deposited at a potential of -1.25 V (vs. Ag/Ag^+) for 20 s on ITO electrodes (top left; inset: 2D GISAXS images of silica films templated by (i) C_{22}TAB, (ii) C_{22}DMEAB, (iii) C_{22}DEMAB and (iv) C_{22}TEAB.

4.4.5 Conclusions

Surfactants modified with larger head groups and TEOS were used to synthesise EASA-derived silica films. A gradual deterioration in the pore order was observed as the surfactant head size grew. In silica films produced with C_{18}DMEAB the GISAXS revealed a significant increase in the lattice spacing without a significant reduction in hexagonal pore ordering relative to the silica film with C_{18}TAB. The film with C_{20}DMEAB revealed smaller pore spacings than observed for C_{20}TAB due to surfactant instability during the micellization process. An increase in the hexagonal order was confirmed when increasing the alkyl chain length from C_{18} to C_{22} with a fixed triethylammonium bromide head group. The electrochemical signals showed no faradaic current for films with C_{18}DEMAB and C_{18}TEAB, suggesting films with surfactant-blocked pores. The structural pore order greatly influences the rate of charge transfer resistance $[Fe(CN)_6]^{3-/4-}$ through the pores, which was reflected in the impedance data. Ellipsometric porosimetry confirmed that

the pore diameter of the silica films increased with increasing head group size, although the accessible pore volume also decreased.

The use of EASA films with surfactants of increasing head sizes provides an alternative route to the enhancement in pore spacing and hence pore size, and as such, these developments may be beneficial for future work on templated electrodeposition and as reliable sensors.

4.4.6 References

1 H. Lin and S. Cheng, Effect of delayed neutralization on the synthesis of mesoporous MCM-4 1 molecular sieves, *Microporous Mater.*, 1997, **10**, 111–121.

2 R. Ryoo, C. H. Ko and I. Park, Synthesis of highly ordered MCM-41 by micelle-packing control with mixed surfactants, *Chem. Commun.*, 1999, 1413–1414.

3 D. Zhao, P. Yang, D. I. Margolese, F. Chmelka and G. D. Stucky, Synthesis of continuous mesoporous silica thin films with three-dimensional accessible pore structures, *Chem. Commun.*, 1998, **1**, 2499–2500.

4 Z. Teng, G. Zheng, Y. Dou, W. Li, C. Y. Mou, X. Zhang, A. M. Asiri and D. Zhao, Highly ordered mesoporous silica films with perpendicular mesochannels by a simple stöber-solution growth approach, *Angew. Chemie - Int. Ed.*, 2012, **51**, 2173–2177.

5 K. Kao, C. Lin, T. Chen, Y. Liu and C. Mou, A General Method for Growing Large Area Mesoporous Silica Thin Films on Flat Substrates with Perpendicular Nanochannels, *J. Am. Chem. Soc.*, 2015, 3–6.

6 A. Walcarius, E. Sibottier, M. Etienne and J. Ghanbaja, Electrochemically assisted self-assembly of mesoporous silica thin films, *Nat. Mater.*, 2007, **6**, 602–608.

7 A. Walcarius, Mesoporous materials and electrochemistry, *Chem. Soc. Rev.*, 2013, **42**, 4098–4140.

8 C. Robertson, R. Beanland, S. A. Boden, A. L. Hector, R. J. Kashtiban, J. Sloan, D. C. Smith and A. Walcarius, Ordered mesoporous silica films with pores oriented perpendicular to a titanium nitride substrate, *Phys. Chem. Chem. Phys.*, 2015, **17**, 4763–4770.

9 D. F. Rohlfing, J. Rathouský, Y. Rohlfing, O. Bartels and M. Wark, Functionalized mesoporous silica films as a matrix for anchoring electrochemically active guests, *Langmuir*, 2005, **21**, 11320–11329.

10 N. A. N. Mohamed, Y. Han, A. L. Hector, A. R. Houghton, E. Hunter-Sellars, G. Reid, D. R. Williams and W. Zhang, Increasing the Diameter of Vertically Aligned, Hexagonally Ordered Pores in Mesoporous Silica Thin Films, *Langmuir*, 2022, **38**, 2257–2266.

11 Y. Guillemin, J. Ghanbaja, E. Aubert, M. Etienne and A. Walcarius, Electro-assisted self-assembly of cetyltrimethylammonium-templated silica films in aqueous media: Critical effect of counteranions on the morphology and mesostructure type, *Chem. Mater.*, 2014, **26**, 1848–1858.

12 H. A. Scheraga and J. K. Backus, Flow Birefringence in Solutions of n-Hexadecyltrimethylammonium Bromide, *J. Am. Chem. Soc.*, 1951, **73**, 5108–5112.

13 A. Goux, M. Etienne, E. Aubert, C. Lecomte, J. Ghanbaja and A. Walcarius, Oriented mesoporous silica films obtained by electro-assisted self-assembly (EASA), *Chem. Mater.*, 2009, **21**, 731–741.

14 A. F. P. De Campos, A. R. O. Ferreira, L. Lorena, P. Paulo, M. Neto and D. Cardoso, Synthesis and properties of hybrid silicas containing alkylammonium surfactants, *Catal. Today*, 2020, **344**, 41–51.

15 S. C. Christiansen, D. Zhao, M. T. Janicke, C. C. Landry, G. D. Stucky and B. F. Chmelka, Molecularly ordered inorganic frameworks in layered silicate surfactant mesophases, *J. Am. Chem. Soc.*, 2001, **123**, 4519–4529.

16 N. V Sastry, N. M. Vaghela and V. K. Aswal, Fluid Phase Equilibria Effect of alkyl chain length and head group on surface active and aggregation behavior of ionic liquids in water, *Fluid Phase Equilib.*, 2012, **327**, 22–29.

17 S. Besson, C. Ricolleau, T. Gacoin, C. Jacquiod and J. P. Boilot, Highly ordered orthorhombic mesoporous silica films, *Microporous Mesoporous Mater.*, 2003, **60**, 43–49.

18 C. Karman, N. Vilà and A. Walcarius, Amplified Charge Transfer for Anionic Redox Probes through Oriented Mesoporous Silica Thin Films, *ChemElectroChem*, 2016, **3**, 2130–2137.

19 K. Seok, L. Ye, J. Seo and H. Taek, Capacitive behavior of functionalized activated carbon - based all - solid - state supercapacitor, *Carbon Lett.*, 2021, **31**, 1041–1049.

20 T. Sikolenko, C. Despas, N. Vilà and A. Walcarius, Thickness control in electrogenerated mesoporous silica films by wet etching and electrochemical monitoring of the process, *Electrochem. commun.*, 2019, **100**, 11–15.

21 G. Giménez and G. Ybarra, Preparation of mesoporous silica thin fi lms at low temperature : a comparison of mild structure consolidation and template extraction procedures, *J. Sol-Gel Sci. Technol.*, 2020, 287–296.

22 M. Thommes, K. Kaneko, A. V. Neimark, J. P. Olivier, F. Rodriguez-Reinoso, J. Rouquerol and K. S. W. Sing, Physisorption of gases, with special reference to the evaluation of surface area and pore size distribution (IUPAC Technical Report), *Pure Appl. Chem.*, 2015, **87**, 1051–1069.

23 C. Robertson, A. W. Lodge, P. Basa, M. Carravetta, A. L. Hector, R. J. Kashtiban, J. Sloan, D. C. Smith, J. Spencer and A. Walcarius, Surface modification and porosimetry of vertically aligned hexagonal mesoporous silica films, *RSC Adv.*, 2016, **6**, 113432–113441.

24 M. Thommes, Characterization of Nanoporous Materials, *Chemie Ing. Tech.*, 2010, **82**, 1059–1073.

25 C. Schlumberger and M. Thommes, Characterization of Hierarchically Ordered Porous Materials by Physisorption and Mercury Porosimetry — A Tutorial Review, *Adv. Mater. Interfaces*, 2021, **8**, 1–25.

26 T. Kim, R. Ryoo, M. Kruk, K. P. Gierszal and M. Jaroniec, Tailoring the Pore Structure of SBA-16 Silica Molecular Sieve through the Use of Copolymer Blends and Control of Synthesis Temperature and Time, *J. Phys. Chem. B*, 2004, **108**, 11480–11489.

27 H. Kao, Y. Liao and C. Ting, Synthesis of cubic mesoporous silica SBA-1 with bulky headgroup surfactant cetyltripropylammonium bromide, 2007, **98**, 80–88.

28 and G. D. S. Qisheng Huo, David I. Margolese, Ulrike Ciesla, Dirk G. Demuth, Pingyun Feng, Thurman E. Gier, Peter Sieger, Ali Firouzi, x Bradley F. Chmelka, Ferdi Schuth, Organization of Organic Molecules with Inorganic Molecular Species into Nanocomposite Biphase Arrays, *Chem. Mater.*, 1994, **6**, 1176–1191.

29 Q. Huo, D. I. Margolese and G. D. Stucky, Surfactant Control of Phases in the Synthesis of Mesoporous Silica-Based Materials, 1996, **4756**, 1147–1160.

Chapter 5 The electrodeposition of porous nickel films from an EASA derived route

This chapter examines the synthesis of porous nickel films as electrode materials for supercapacitor applications, in order to investigate whether the electrodeposition of templated nickel would potentially lead to the development of pores within the electrode material.

Nickel was deposited on ITO using a CTAB surfactant and boric acid in an acidified aqueous solution. The presence of nickel was confirmed by EDX but films were shown to be amorphous by XRD and no ordered porosity was suggested by GISAXS. Electron microscopy was used to identify the porosity of CTAB-templated film along with the difference in structural morphology when compared with the non-templated film. The electrochemical accessible surface area for CTAB-templated nickel was estimated to be greater than for non-templated nickel. Finally, the specific capacitance determined from CV studies of CTAB-templated nickel was almost two times greater than observed for non-templated nickel at 5 mV s^{-1}.

5.1 Acknowledgement

I would like to thank Nikolay Zhelev for analysing the surface topology and elemental composition for both non-templated and CTAB-templated nickel films by SEM and EDX measurements.

5.2 Introduction

Nickel is widely used as an electrode material in many electrochemical applications, such as alkaline water electrolysers[1,2], fuel cells[3], supercapacitors[4] and electrochemical hydrogenation of organomolecules.[5] Nickel based electrodes are also effective as battery materials[6] with examples in cadmium-nickel oxide, zinc-nickel oxide and hydrogen-nickel oxide. High surface area nickel electrodes are often important in electrochemical technologies as reactions occur directly on the electrode surface. Therefore, increasing the surface area of nickel is imperative for the improvement in the nickel electrode's electrochemical performance. Previous attempts to increase the surface area of nickel stem from the production of sintered microporous nickel[7] and porous Raney nickel, whereby Ni alloys with aluminium and zinc are etched in solution before deposition onto the substrate.[8] These processes involve heat treatment or alkaline leaching from concentrated solutions.[7] This results in disorganised porous nickel systems. Therefore, despite the high surface area, the movement of liquids or gases through the porous network is challenging. On the contrary, nickel materials with ordered porosity accompanied by high surface areas would facilitate faster diffusion of liquids and gases through the medium , potentially providing superior electrochemical performance for the electrode material.[7]

The production of mesoporous nickel through the liquid crystal templating electrodeposition method was first reported by Nelson et al.[7] who produced hexagonal lyotropic crystalline phases consisting of Brij 56 and Brij 78 surfactants dissolved in an aqueous solution containing nickel(II) acetate as the precursor, to generate porous nickel films with 2D hexagonal pores. The nickel films were highly ordered with pore spacings between 5 and 8 nm. The electroactive surface area was 100 times greater than pure nickel (without surfactant template in the electrolyte mixture), indicating promise for supercapacitor technology, pulse powered devices and current collectors. Ganesh and Lakshminarayanan[9] synthesised mesoporous nickel films from a prepared hexagonal liquid crystalline phase of a non-ionic surfactant 2-[4-(2,4,4-trimethylpentan-2-yl)phenoxy]ethanol (Triton X-100) in a water/poly(acrylic acid) medium in 2004. The films delivered a large specific capacitance, suggesting possible utility in supercapacitors. In addition, the material also showed a high accessible surface area, which could find use as a hydrogen evolving cathode. Bartlett et al.[10] reported the electrodeposition of Ni/Co alloy from a hexagonal LLC phase using CTAB as the surfactant. They discovered that LLC with CTAB has higher conductivity than LLC electrolytes with non-ionic surfactants. Furthermore, the former process was also favoured due to the ease of electrodeposition from an LLC and CTAB solution. Nasirpouri et al.[11] electrodeposited nickel films from an LLC phase of CTAB at different concentrations to synthesise mesoporous nickel electrodes for applications related to electrochemical energy storage and conversion. TEM

confirmed the nickel film with 30 wt % CTAB produced hexagonally-arranged pores. The same films were later used to demonstrate good magnetic properties.

Motivated by this work, CTAB-templated nickel films on ITO electrodes were synthesised from an EASA-derived approach using a solution containing a nickel precursor ($NiCl_2$. $6H_2O$) and CTAB as the cationic surfactant. The structure and electrochemical performance of the films were determined by a range of analytical techniques.

5.3 Experimental summary

The nickel films were electrodeposited on ITO electrodes. The electrolytes were prepared by adding 0.1 mol dm^{-3} nickel(II) chloride hexahydrate ($NiCl_2.6H_2O$, 2.3800 g, 99 %, Sigma Aldrich), 0.1 mol dm^{-3} boric acid (H_3BO_3, 0.6200 g, ≥ 99 %, Sigma Aldrich) and CTAB (0.4801 g, ≥ 98 %, Sigma Aldrich) in water.[7] The same conditions were applied for the non-templated nickel film, but without CTAB. The electrolyte pH was adjusted to pH 3 by slowly adding 0.2 mol dm^{-3} HCl in water. The surfactant solubility was problematic as CTAB did not dissolve in the electrolyte mixture, so the mixture was heated to 40 ℃ for 15 minutes to fully dissolve the surfactant.

Before the deposition of nickel, ITO coated glass plates with measurements of 15 mm × 20 mm (ITO; surface resistivity 14-16 Ω, Ossila) were cleaned with isopropyl alcohol, ethanol, and ultrapure water to remove unwanted contamination. The electrochemical set-up involved a transparent ITO working electrode, platinum gauze counter electrode and the reference electrode was Ag/AgCl in 4 mol dm^{-3} KCl solution.

A constant potential of -1.25 V was applied to the working electrode using chronoamperometry to electrodeposit nickel on the ITO surface, for a duration of 30 seconds using a biologic SP150 potentiostat. The nickel films were quickly rinsed with ultrapure water and ethanol after each attempted deposition, then allowed to dry in air. The CTAB surfactant was removed by submerging the nickel electrode in a beaker containing ethanol over a 24-hour period under gentle stirring.[12]

5.4 Results and Discussion

5.4.1 Electrodeposition of solid and CTAB-templated nickel films on ITO electrodes

The deposition of nickel using a cationic surfactant CTAB was investigated with the goal of producing a network of vertical pores for use as an electrode in supercapacitors. An EASA-derived method[13] was used and involves the direct replacement of silica with nickel, while the sodium nitrate was substituted with boric acid, which was important for the suppression of nickel hydroxide formation in solution.[11] The addition of CTAB in the nickel electrolyte resulted in poor dissolution so the electrolyte was heated to 40 ℃ to dissolve the surfactant fully.[11,7] A stable potential of -1.25 V was applied to deposit nickel onto ITO for a duration of 30 seconds, as initial deposition at -1.0 V produced films that were visually inhomogeneous. The resulting non-templated nickel film was visually crack-free, uniform, and shiny black in colour. On the contrary, the nickel film templated by CTAB was translucent in colour however, on closer viewing a rainbow-coloured tint was evident on the ITO surface. The nickel films with surfactant were deposited at 40 ℃ and once deposition came to an end, the films with or free of surfactants were washed with deionised water and ethanol to remove any residues on the film surface.

Cyclic voltammetry (CV) measurements were used to determine the effect of CTAB during the nickel electrodeposition process. CV plots of the background electrolytes with boric acid and containing nickel in the presence and absence of CTAB were recorded at a sweep rate of 20 mV s^{-1} on ITO electrodes, as depicted in Fig. 5.1.

In Fig. 5.1 a, the electrolyte solution containing $NiCl_2.6H_2O$ without the presence of CTAB gave rise to a reduction peak starting to appear at -0.55 V (vs. Ag/AgCl) which constitutes to the onset reduction potential, indicating the starting point of the electrochemical reduction of Ni^{2+} to metallic Ni^0. As the potential moves towards the negative direction, a cathodic reduction peak is observed at -1.0 V (vs. Ag/AgCl) attributed to the reduction of Ni^{2+} to Ni^0. Moreover, on the reverse scan the onset oxidation potential appears at -0.38 V (vs. Ag/AgCl), which leads to an anodic oxidation peak appearing at -0.06 V (vs. Ag/AgCl) that can be associated with the stripping of nickel from the ITO surface. The reduction potential of nickel ions was similar for acidic chloride solutions containing SO_2^{4-} ions for the co-deposition of nickel-tin alloys previously reported by Rudnik et al.[14] At more negative potentials nickel reduction is accompanied by hydrogen evolution reaction, as hydrogen reduction most commonly appears with nickel electrodeposition in solutions containing chloride ions (Eq. 5.1).[11] A well-defined hysteresis loop can be seen at -0.3 V which is associated with nucleation, and therefore to the driving force for nickel reduction.

$$Ni + H_2O + e^- \rightarrow NiH + OH^-$$

$$NiH + H_2O + e^- \leftrightarrow Ni + H_2 + OH^- \qquad \text{Eq. 5.1}$$

$$2NiH \leftrightarrow 2Ni + H_2$$

Fig. 5.1 b shows the CV of the background electrolyte containing $NiCl_2.6H_2O$ and CTAB deposited on the electrode surface. From the CV, the electrochemical behaviour of nickel is affected by the incorporation of CTAB in the electrolyte mixture. Two cathodic peaks were observed at -0.74 V and -0.92 V (vs. Ag/AgCl) which could be attributed to the reduction of Ni^{2+} to Ni^{1+} and Ni^{2+} to Ni^0 from nickel(II) bromo or chloro species respectively. An explanation for the formation of $NiBr_2$ is most likely due to the interaction between the surfactant counterion (Br-) and the nickel precursor in solution, which would be consistent with the two redox peaks observed on the cathodic scan. Sengottuvelan et al.[15] reported the synthesis of nickel(II) halide complexes with pyridine ligands. After cycling the nickel bromide complex, a reduction potential was noticed at -0.77 V, which was similar to the potential observed for the nickel electrolyte containing CTAB. Furthermore, hysteresis loops are clearly visible at around -0.8 V, -0.6 V and -0.3 V (vs. Ag/AgCl). Additionally, on the backward scan an anodic peak comes into view at -0.07 V (vs. Ag/AgCl) which is due to oxidation of Ni^0 to Ni^{2+}. It is to be noted that the CV corresponding to the background electrolyte shows a higher current intensity for the anodic peak (3 mA) compared with that of Ni electrolyte with CTAB, indicating that stripping appears complete and therefore, making the process reversible. Whereas the current intensity for the anodic oxidation peak relating to Ni electrolyte with CTAB is significantly reduced (0.03 mA), suggesting that deposition appears predominately irreversible. Nevertheless, the reduced stripping of nickel in presence of CTAB is possibly due to nickel reacting in solution making the surface less reactive i.e., solution decomposition.

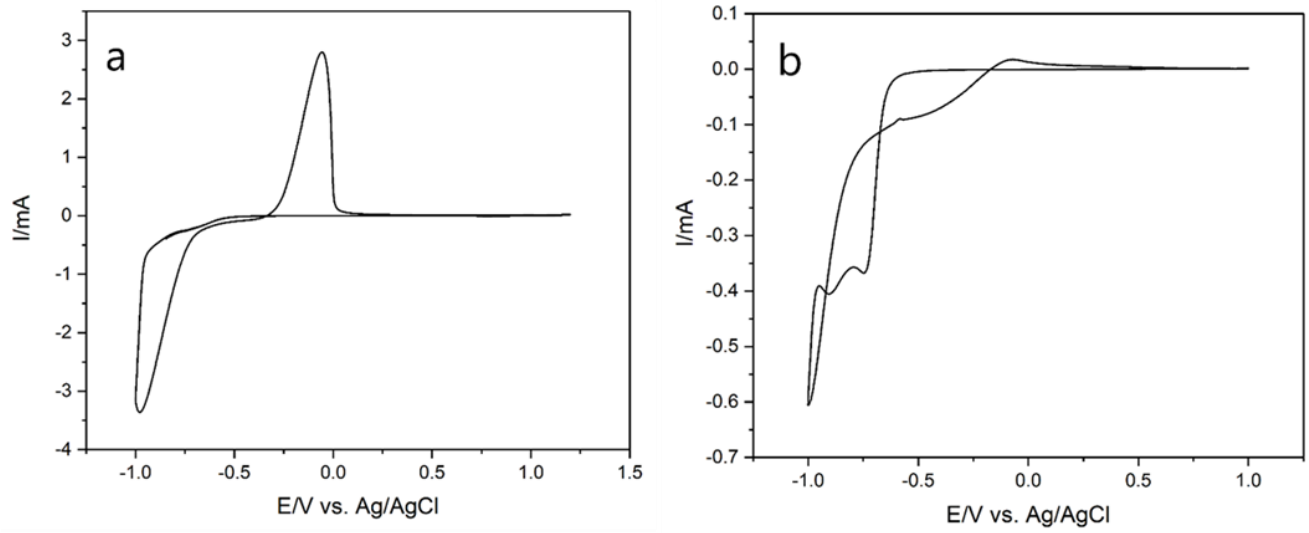

Figure 5.1 CV of background electrolytes obtained from (a) $NiCl_2.6H_2O$-H_3BO_3 and (b) $NiCl_2.6H_2O$-H_3BO_3-CTAB using an ITO electrode. The potential window of the electrolytes was 1 to -1 V (vs. Ag/AgCl) then back to 1 V at 20 mV s^{-1} scan rate.

In order to investigate the effect of surfactant on the nickel growth process, chronoamperometry was carried out, and the result is displayed in Fig. 5.2. The current-time curves acquired for the deposition of non-templated nickel using ITO is shown in Fig 5.2 a. The electrodeposition process results in nucleation and growth of nuclei scattered across the electrode surface. The appearance of the I-t curve begins with an initial increase in current which is ascribed to the double layer charging together with the deposition of the first nuclei on the ITO surface. This is followed by a dramatic increase in current, which is due to the growth of nuclei caused by the increasing surface area of the electrode. The current starts to drop off at a steady rate due to the growth in the diffusion layer at the electrode surface.

The current transient for the nickel film with CTAB on ITO at -1.25 V (vs. Ag/AgCl) in Fig. 5.2 b shows an initial characteristic response where the peak forms and decays, which is due to electrode charging and double layer formation, then a brief constant current is observed suggesting a period of initiation and as nickel nucleation and growth proceeds, the current increases gradually with time and so contributing to the third region.[16] Interestingly, at 3 seconds the current increases until approximately 15 seconds where the current starts to level off. This could be due to a combination between the rate-determining growth of nickel formed around the CTAB micelles, the changing surface area and high-water concentration leading to fast diffusion of hydroxide ions in solution.

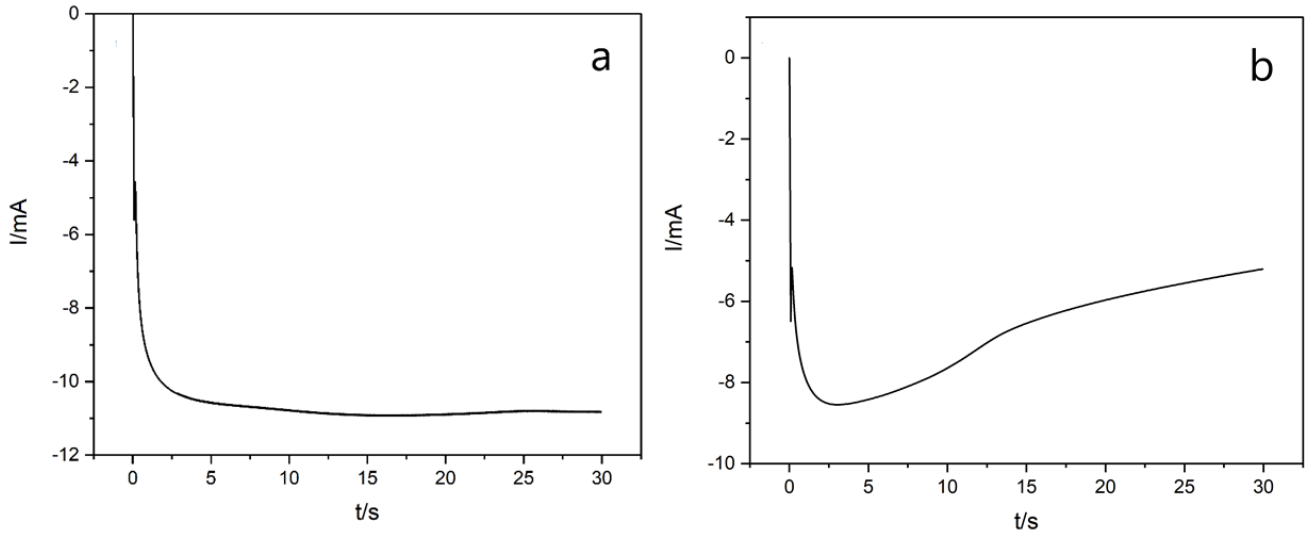

Figure 5.2 Current-time transients for the electrodeposition of non-templated (a) and CTAB-templated (b) nickel films on ITO electrodes deposited at -1.25 V (vs. Ag/AgCl) for 30 seconds.

5.4.2 Structure and characterisation of the nickel films on ITO electrodes

Figures 5.3 and 5.4 show the recorded diffraction patterns for non-templated and CTAB-templated nickel films deposited on ITO substrates. For XRD analysis, the nickel films were deposited for 60 seconds rather than 30 seconds to differentiate between the ITO and nickel peaks. The typical face centred cubic peaks for nickel (JCPDS card No. 01-087-0712)[17] at 111, 200, 220, 311 and 222 correspond to the Bragg angles (2θ) of 44.66 °, 52.02 °, 76.46 °, 93.24 ° and 98.60 °, suggesting the existence of crystalline nickel (JCPDS card No. 01-087-0712).[17] This proves that the film deposited from this electrolyte without CTAB is indeed metallic nickel.

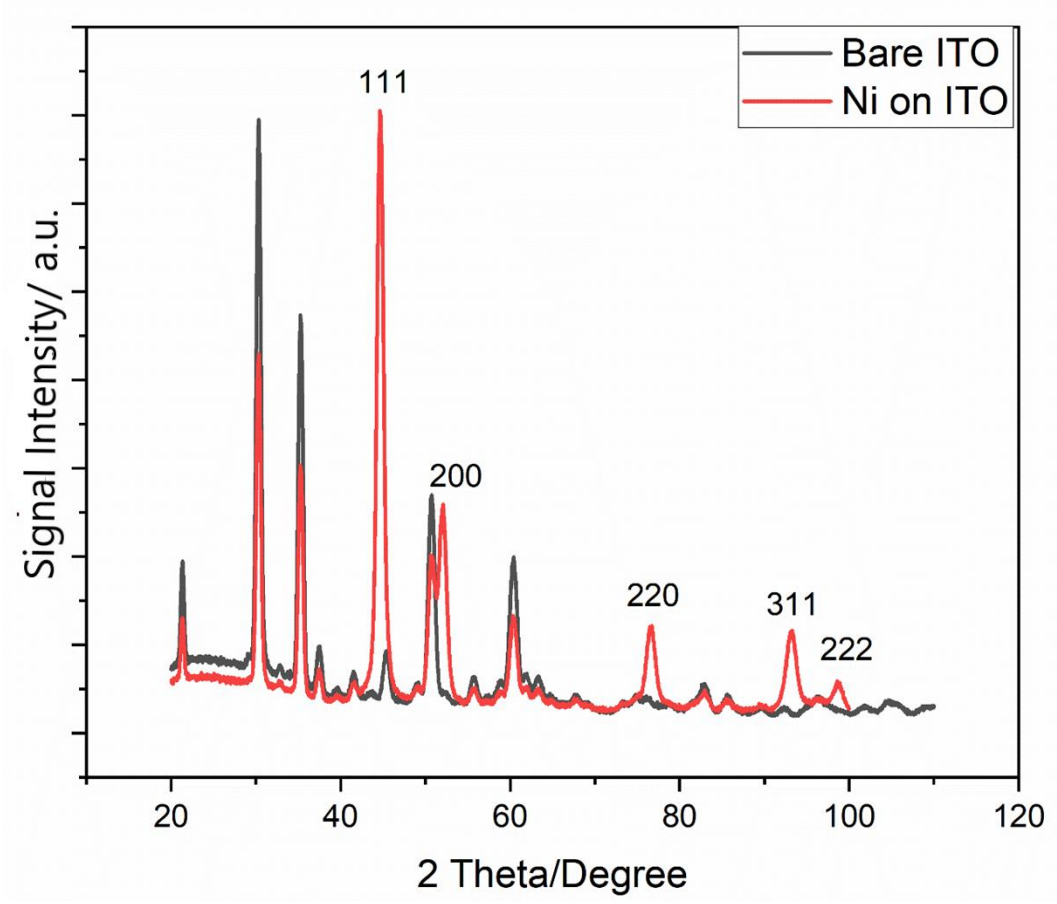

Figure 5.3 XRD patterns of bare ITO (black) and nickel film without CTAB (red) deposited on an ITO electrode at -1.25 V (vs. Ag/AgCl) for 60 seconds.

For the CTAB-templated nickel film, the surfactant was removed from the nickel sample by immersing the film in a solution containing ethanol for a 24-hour period at 25 °C, before undergoing XRD analysis. Fig. 5.4 depicts XRD patterns of ITO and CTAB-templated nickel. It is apparent that the peak positions concerning ITO appear at 2θ values = 21.34°, 30.36°, 35.28°, 50.76° and 60.4°, which correspond to the polycrystalline cubic phases of 211, 222, 400, 441 and 622 respectively. It is evident that no diffraction peaks relating to crystalline nickel are present in the XRD data. Interestingly, mesoporous nickel films electrodeposited by lyotropic liquid crystal templating using CTAB as the surfactant template were reported by Nasirpouri et al.[11] No Bragg diffraction peaks corresponding to crystalline nickel were observed, which was explained by the disordered nature of the nickel particles formed around the surrounding micelles. Therefore, further investigations were undertaken on the films produced in this study to attempt to confirm whether elemental nickel was present in the CTAB templated film.

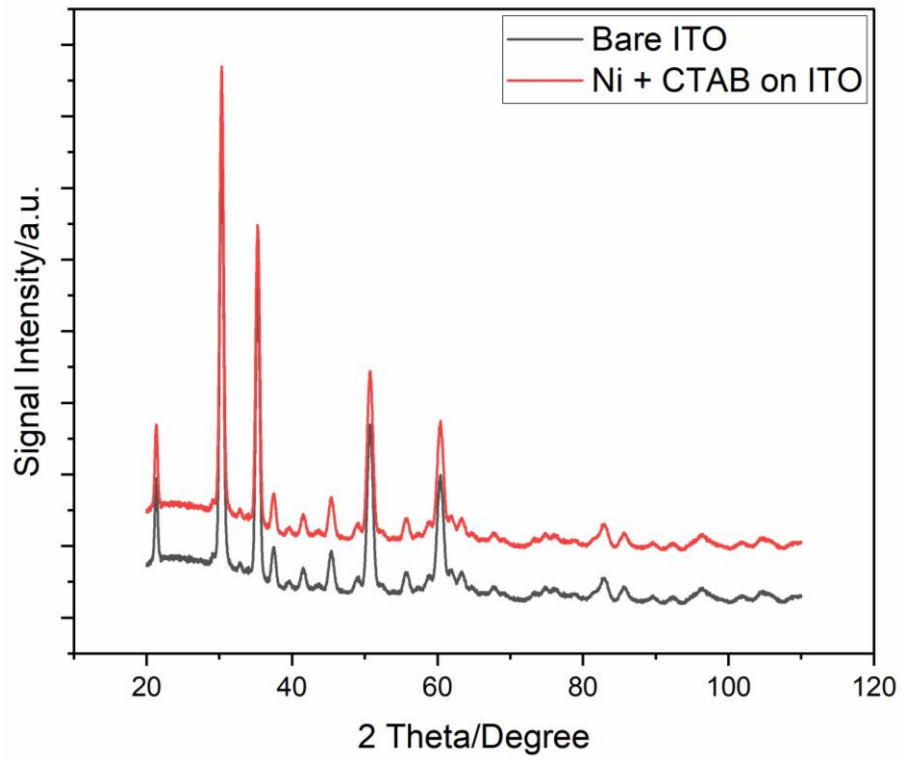

Figure 5.4 XRD patterns of bare ITO (black) and CTAB-templated nickel film (red) deposited on an ITO electrode at -1.25 V (vs. Ag/AgCl) for 60 seconds. XRD analysis was carried out after template removal.

The 1D in-plane GISAXS pattern of a CTAB-templated nickel film after the removal of the surfactant is displayed in Fig. 5.5. The incident beam angle which produced the most intense features was 0.4 °, at which well-defined peaks corresponding to the 21, 22, 40, 44 and 62 cubic phases of the ITO electrode underneath. The results indicate that the CTAB-templated nickel film is amorphous, and that no significant volume of crystallinity is present.

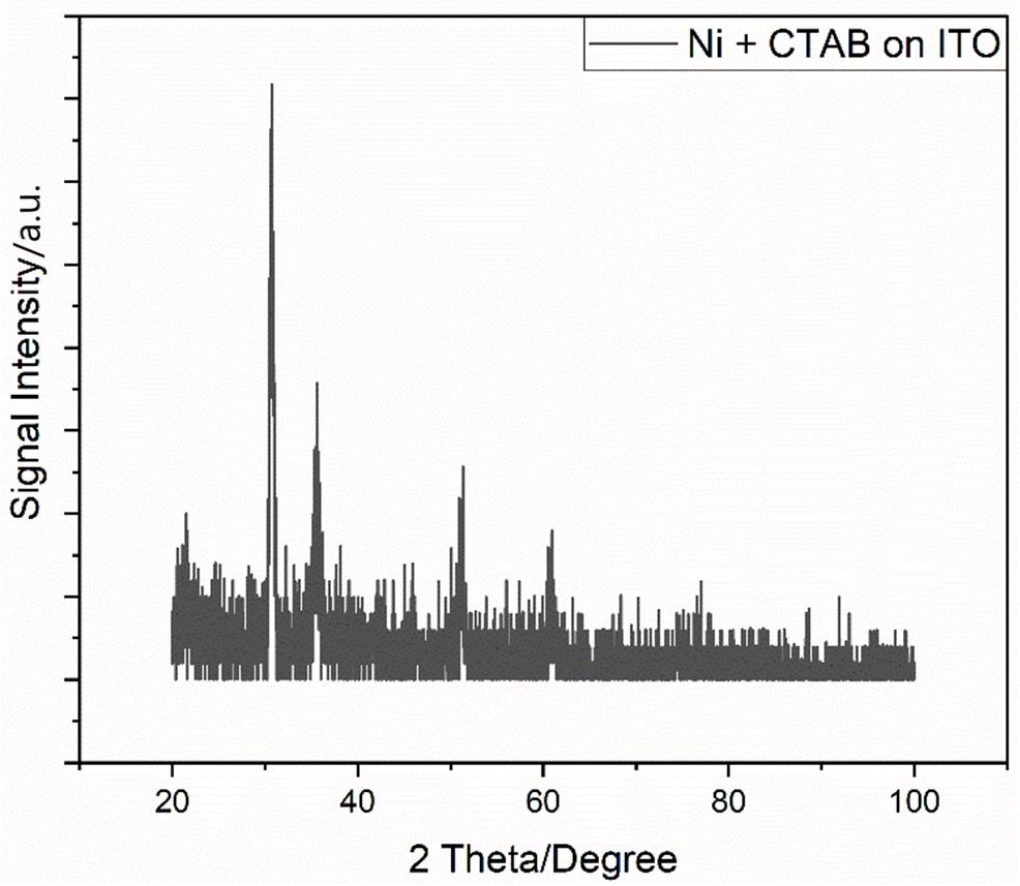

Figure 5.5 1D in-plane GISAXS pattern of a nickel film templated with CTAB deposited at a potential of -1.25 V (vs. Ag/AgCl) for 60 s on an ITO electrode. Experimental analysis was carried out post surfactant removal.

The FEG-SEM images of non-templated and CTAB-templated nickel films are shown in Fig. 5.6. From the images, the surface morphology is different between the films, the non-templated film showing a uniform, smooth, and crack-free appearance (Fig. 5.6 a). On the other hand, the CTAB generated film appears to be rougher in texture with lumps or nodules on the surface (Fig. 5.6 b) resembling the overgrowth of silica deposits as described in previous chapters. Nevertheless, the images also revealed a microcrack-free and homogeneous surface. Therefore, it is clear that the presence of CTAB greatly affects the nucleation and growth process during deposition, causing a significant change in the surface structure, which correlates well with the current transients discussed in Fig 5.2. The film thicknesses of the non-templated and CTAB-templated nickel films were calculated[18] from Eq. 5.2 where Q is the charge on oxidation process of nickel (non-templated film = 1.173 C and CTAB-templated film = 0.624 C) , M_w is the molecular mass of metallic nickel, Z is the number of electrons, F is the faraday constant, A is the electrode area and ρ is the volumetric mass density of nickel (8.90 g cm^{-3}), giving estimated values of 80 nm and 43 nm, respectively.

$$d = \frac{QMw}{zFA\rho} \qquad \text{Eq. 5.2}$$

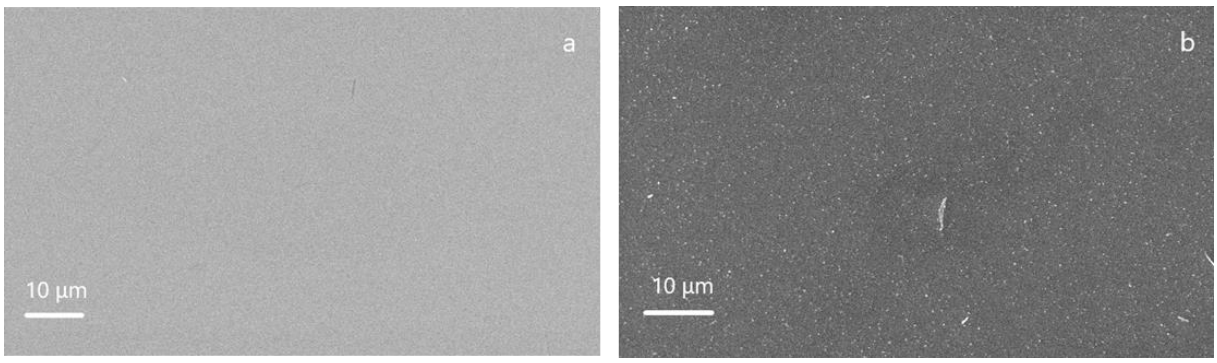

Figure 5.6 Top view SEM image of non-templated (a) and CTAB-templated (b) nickel films on ITO electrodes deposited at -1.25 V (vs. Ag/AgCl) for 30 seconds. Image (b) was obtained after template removal.

The EDX spectrum (Fig. 5.7) was used to determine the composition of the deposit in the CTAB templated film, and specifically to determine whether elemental nickel was present. The data confirms the presence of carbon, oxygen, nickel, indium, and tin, with atomic percentages of 6.06 %, 65.83 %, 11.31 %, 14.93 % and 0.75 %, respectively. An extra peak at around 0.05 keV is most likely due to nitrogen. The existence of carbon and nitrogen in the EDX spectrum may indicate small amounts of residual CTAB surfactant remaining in the pores. The peak at 0.85 keV confirms that nickel is present in the film templated by CTAB. The oxygen peak at 0.5 keV is due to the underlying ITO electrode and possible exposure to the atmosphere.

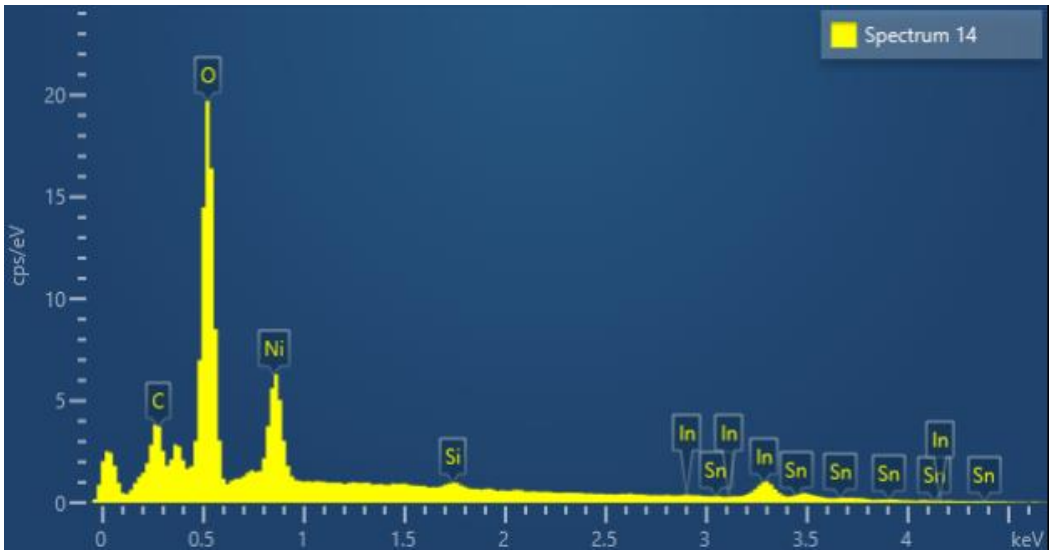

Figure 5.7 EDX spectrum of a CTAB-templated nickel film deposited onto an ITO electrode at a potential of -1.25 V (vs. Ag/AgCl) for 30 seconds. The EDX analysis was recorded post-template removal.

The magnification of the SEM micrograph was increased to examine the surface morphology further for the non-templated and CTAB-templated nickel films, as shown in Fig. 5.8. The top view

SEM image in Fig. 5.8 a indicates that the non-templated film shows a dense framework with little to no porosity present. Furthermore, Fig. 5.8 b clearly shows the presence of interconnected pores within the nickel film templated by CTAB, indicating the porous nature of the film, albeit highly disorganised. This is consistent with CTAB acting as a 'scaffold' and once removed, porous nickel is produced. Yin et al.[19] synthesised porous nickel films using an anodic aluminium oxide template by electron beam evaporation. They discovered that the rate of evaporation was important for controlling the thickness of the porous nickel, which was less than 30 nm at a rate of 5 A s^{-1} after template removal, as well as showing a highly ordered porous structure, as determined by SEM imaging. Moreover, the film thickness of non-templated nickel is higher than CTAB-templated nickel, possibly owing to its porosity, making it less dense than the non-templated nickel and could explain to some degree why only the ITO diffraction peaks are observed in the XRD pattern of CTAB-templated nickel.

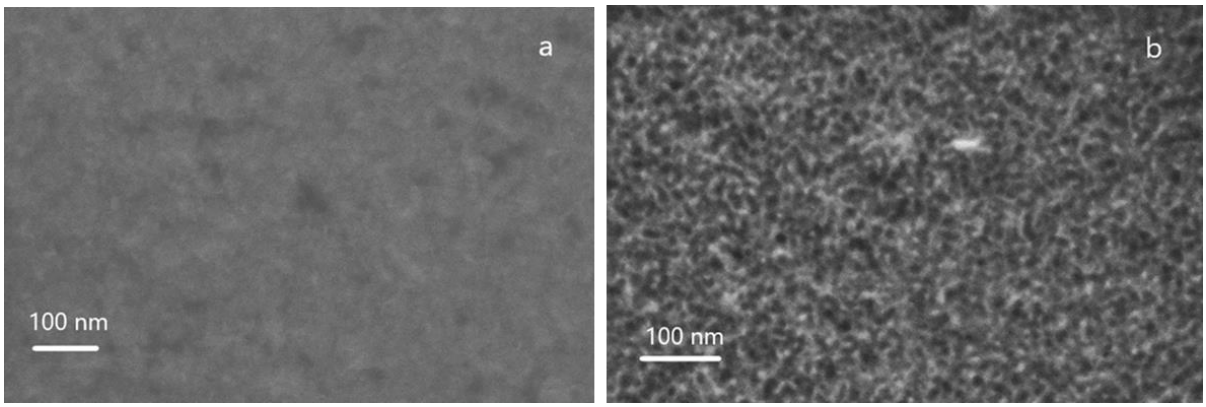

Figure 5.8 Top view SEM images of non-templated (a) and CTAB-templated (b) nickel films on ITO electrodes deposited at -1.25 V (vs. Ag/AgCl) for 30 seconds. SEM analysis was recorded post-template removal.

5.4.3 Electrochemical performance of non-templated and CTAB-templated nickel films

The electrochemically active surface area (ECSA) for non-templated and CTAB-templated nickel films were determined using CV (Fig 5.9 a and 5.10 a) to ascertain the double layer capacitance in a potential region of - 0.2 to - 0.4 V (vs. Ag/AgCl) and - 0.1 to - 0.4 V (vs. Ag/AgCl) where no faradaic processes were observed at a range of scan rates of 20, 50, 70, 100, 200 and 300 mV s^{-1} (as shown in Figs. 5.9 and 5.10). It is thought that the capacitive current measured in this non-faradaic region is associated with double layer capacitance. Therefore, the charging current ($i_{c)}$ is proportional to the scan rate (v) and double layer capacitance (C_{DL}) as demonstrated by Eq. 5.3. The current was then plotted against scan rate (Figs. 5.9 b and 5.10 b), which produced a straight line where the gradient equals C_{DL} (Figs. 5.9 b and 5.10 b). The electrochemical double layer

capacitance for the non-templated and CTAB-templated nickel films were 4.10×10^{-2} mF and 6.33×10^{-2} mF, respectively.

$$I_c = \nu C_{DL} \qquad \text{Eq. 5.3}$$

$$ECSA = C_{DL}/C_s \qquad \text{Eq. 5.4}$$

Considering that the specific capacitance (C_s) value for Ni based electrodes is 103.9 mF cm^{-2}, the ECSA can be obtained from the gradient (C_{DL}) in agreement with Eq. 5.4.[20,21] Therefore, the estimation of the surface areas of both non-templated and CTAB-templated nickel films were 3.9×10^{-4} cm^2 and 6.0×10^{-4} cm^2, respectively, which indicates that CTAB-templated nickel has a surface area that is greater than non-templated nickel under similar conditions. The larger ECSA correlates well with images from top view SEM, which clearly indicates the array of pores across the surface for the CTAB templated film.

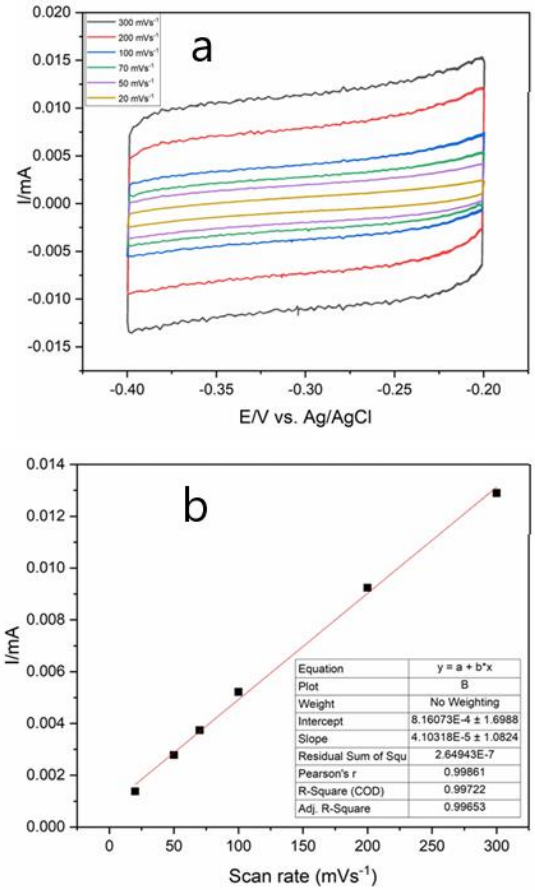

Figure 5.9 The electrochemical surface area measurements of the non-templated nickel film deposited at -1.25 V (vs. Ag/AgCl) for 30 seconds in 1 mol dm^{-3} KOH aqueous solution. CVs (a) were plotted in the potential region where faradaic reactions were absent at multiple scan rates of 20, 50, 70, 100, 200 and 300 mV s^{-1}. A constant potential of - 0.3 V was used to measure the current. The double layer capacitance was estimated by plotting the charging current as a function of scan rate (b) for the non-templated nickel film.

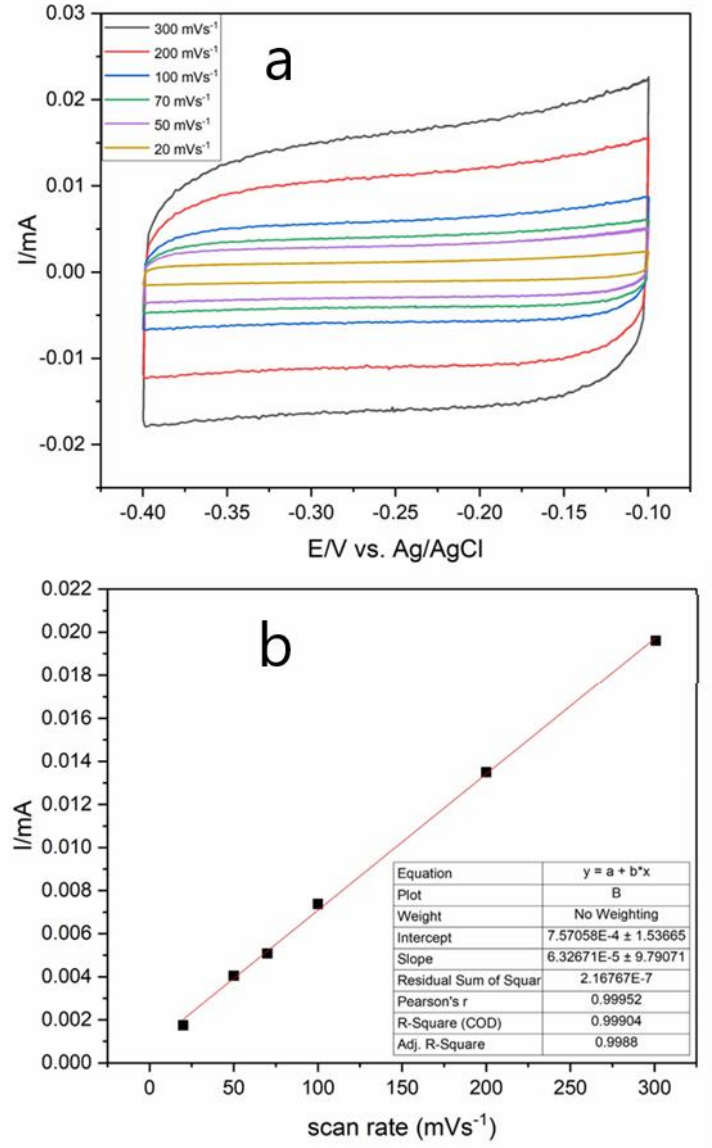

Figure 5.10 The electrochemical surface area measurements of the CTAB-templated nickel film deposited at -1.25 V (vs. Ag/AgCl) for 30 seconds in 1 mol dm^{-3} KOH aqueous solution. CVs (a) were plotted in the potential region where faradaic reactions were absent at scan rates of 20, 50, 70, 100, 200 and 300 mV s^{-1}. A constant potential of - 0.25 V was used to measure the current. The double layer capacitance was estimated by plotting the charging current as a function of scan rate (b) for the CTAB-templated nickel film.

It is reported in the literature that nickel electrodes in alkaline aqueous potassium hydroxide solutions, a chemical reaction occurs forming $Ni(OH_2)$ and NiOOH as seen in Eq. 5.5, with water forming on the electrode surface as hydroxide ions readily interact with neighbouring protons from the bulk solution to counterbalance the charge from the anionic species.[22,7]

$$\mathbf{Ni(OH)_2 + OH^- \leftrightarrow NiOOH + H_2O + e^-} \qquad \textbf{Eq. 5.5}$$

The comparative voltametric profiles of non-templated (red curve) and CTAB-templated (black curve) nickel films in 1 mol dm^{-3} KOH at 20 mV s^{-1} are presented in Fig. 5.11. It is assumed that

changes in peak-to-peak separation, 40 mV (red curve) and 180 mV (black curve), could be associated with electrolyte resistance for the film deposited with CTAB. However, the addition of $NiCl_2.6H_2O$ and CTAB to the electrolyte induced a cathodic current at 0.37 V (vs. Ag/AgCl), which represents the reduction onset potential and indicates the beginning of Ni^{3+} reduction to Ni^{2+}. In the reverse scan, the anodic onset potential at 0.36 V (vs. Ag/AgCl) suggests the start of oxidation of Ni^{2+} to Ni^{3+}. The non-templated film produced similar onset potentials to the film with CTAB, indicating the likelihood that changes in peak separation could be associated with variations in capacitance.

As shown in Fig. 5.11, a single pair of redox peaks is observed in the CV (red curve), the anodic and cathodic peaks observed at 0.41 V (vs. Ag/AgCl) and 0.33 V (vs. Ag/AgCl) represent the reduction of Ni(III) to Ni(II) through the formation of $Ni(OH)_2$ from NiOOH. In contrast, the CV plot (black curve) displays oxidation 0.54 V (vs. Ag/AgCl) and reduction 0.18 V (vs. Ag/AgCl) which is due to the formation of NiOOH and later reduction to $Ni(OH)_2$. Interestingly, the CV curve area is significantly larger for the templated film compared to the non-templated film and the large peak current and improved electrochemical performance of the templated film is most likely due to the high surface area offered by the porous nickel structure. In a general sense, the area under the CV is measured to determine the capacitance of the electrode material over the same potential window.[23] In this case, the CTAB-templated nickel film shows larger peak currents comparative to the non-templated film, indicating a much-improved capacitive behaviour.

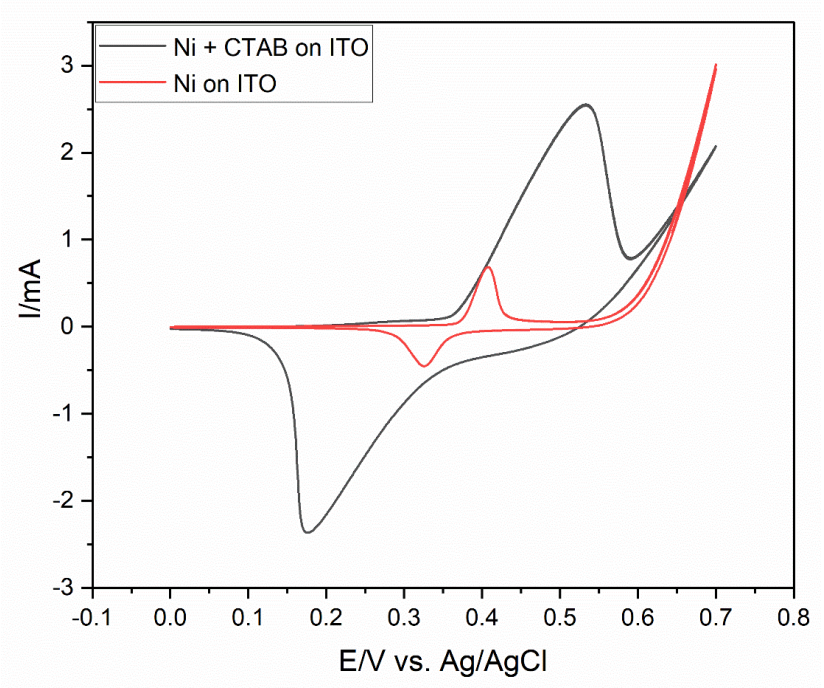

Figure 5.11 CVs of non-templated (red curve) and CTAB-templated (black curve) nickel films deposited at -1.25 V (vs. Ag/AgCl) for 30 seconds in 1 mol dm^{-3} KOH aqueous solution with each CV running for a maximum of 10 cycles at a scan rate of 20 mV s^{-1}.

EIS was used to analyse the non-templated and CTAB templated nickel films by way of Nyquist plots as shown in Fig. 5.12. The EIS data were fitted using the Randles equivalent circuit where R_s, R_{ct} and C_{dl} be situated the solution resistance, electron transfer resistance and double layer capacitance, respectively. Each plot consisted of a semicircle and a straight line with the high frequency region providing information on the electrode resistance. The charge transfer kinetics can be obtained from the diameter of the semicircle, which in turn is linked to film-solution interface and electrode design.[24] The 45 ° straight line in the low frequency region is connected to the diffusion behaviour, often referred to as Warburg impedance, Z_w. In the EIS plot, the R_{ct} values obtained for the non-templated and CTAB-templated nickel films were 3.13 and 1.47 Ω, respectively. The CTAB-templated nickel electrode has a lower electron transfer resistance compared to the non-templated nickel, suggesting that CTAB-templated nickel improves the electron transfer resistance due to the large surface area as well as better electrolyte accessibility in the vicinity of the electrode. Interestingly, the 45° straight line is significantly more curved for the non-templated film compared to the CTAB-templated film, which suggests a better capacitive behaviour for CTAB-templated nickel. This implies that porous nickel has potential as an electrode material in supercapacitor applications.[23]

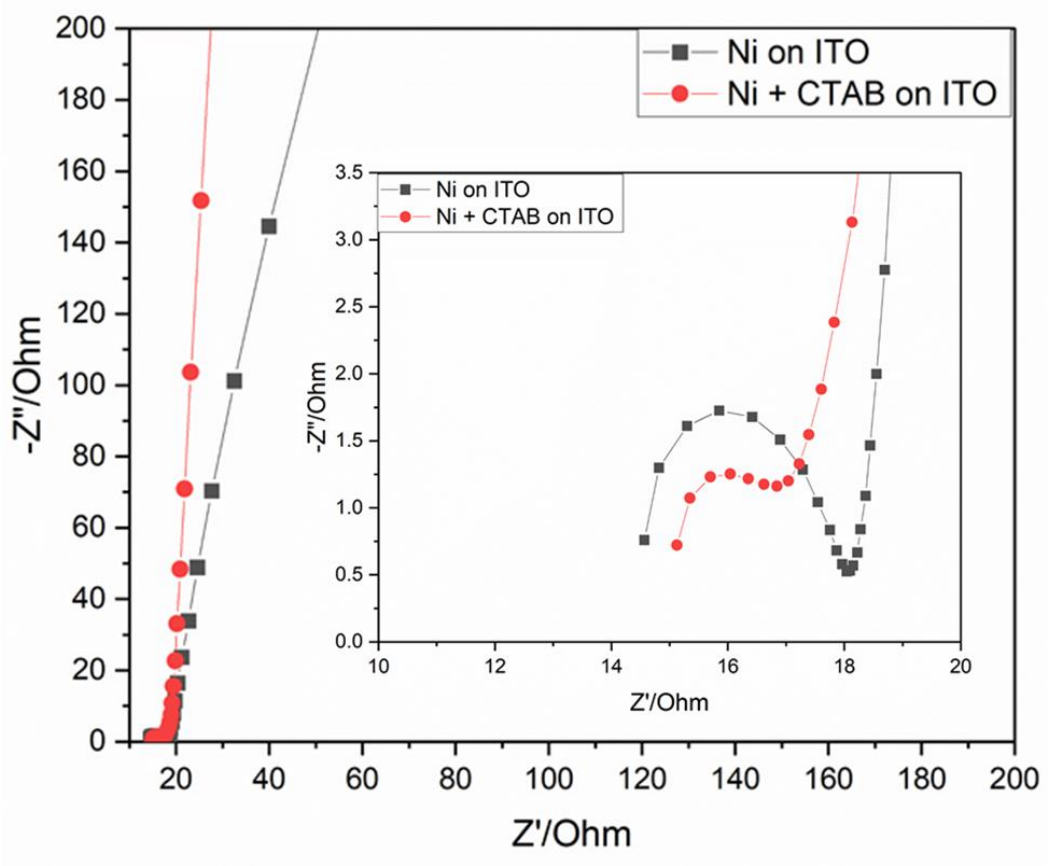

Figure 5.12 Nyquist plots of impedance spectra collected from a frequency range of 250KHz to 100 MHz: a perturbation amplitude of 10 mV for non-templated and CTAB-templated nickel films deposited at -1.25 V (vs. Ag/AgCl) for 30 seconds in 1 mol dm^{-3} KOH aqueous solution.

The capacitive behaviour of non-templated and CTAB-templated nickel films was determined using CV through a conventional three electrode set-up. The CVs were performed at multiple scan rates ranging from 5 to 200 mV s^{-1} inside the potential window of -0.1 to 0.8 V vs. Ag/Ag/Cl (Fig. 5.13). The redox peaks are representative of the capacitive characteristics of the nickel films. For instance, the well-defined oxidation and reduction peaks (Figs. 5.13 a) at 50 mV s^{-1} at approximately 0.41 V (vs. Ag/AgCl) and 0.30 V (vs. Ag/AgCl) can be attributed to the faradaic reactions of the $Ni(OH)_2$/NiOOH redox couple on the electrode surface. The variation in peak potential separation between the non-templated and CTAB-templated films (Table 5.1) is most likely caused by morphological changes to the nanostructured surfaces.[23] As previously stated, the SEM image of CTAB-templated nickel seems to indicate a porous network scattered across the film. It is to be noted that increasing the scan rate does not affect the well-defined redox peaks, indicating that porous nickel is highly capable of sustaining fast redox processes.

$$C_S = \frac{\int idv}{2 \times S \times M \times V} \qquad \text{Eq. 5.6}$$

The same CV plots were also utilized to calculate the specific capacitance (C_s) of non-templated and CTAB-templated nickel films as a function of scan rate (as shown in Fig. 5.13 c) using Eq. 5.6. Where C_s is the specific capacitance (F g^{-1}), $\int idv$ is the integrated area under the CV curve, S is the sweep rate (mV s^{-1}), M is the electrode's active mass (g), and V is the applied voltage window (V). The value of the electrode active mass which was determined by calculating the difference between the ITO electrode and the nickel coated ITO films in the presence and absence of CTAB, along with the applied voltage range is shown in Table 5.2. The specific capacitance of CTAB-templated nickel (red line) was calculated at 1565 F g^{-1} at 5 mV s^{-1}, which is significantly higher than the specific capacitance of 822 F g^{-1} for non-templated nickel (black line) at the same scan rate. It is also apparent that at 200 mV s^{-1}, the specific capacitance of CTAB-templated nickel is almost twice that of non-templated nickel, at 415 F g^{-1} vs. 242 F g^{-1}. This is accredited to increases in surface area and pore volume that make it possible to maintain good capacitive behaviour of the porous electrode at faster scan rates. In the case of the porous nickel, at faster scan rates the capacitance decreases. This is mostly caused by ion diffusion being restricted to the surface. whereas at slower scan rates, the electrolyte accesses both the surface and inside the pore channels, leading to a higher capacitance.[23]

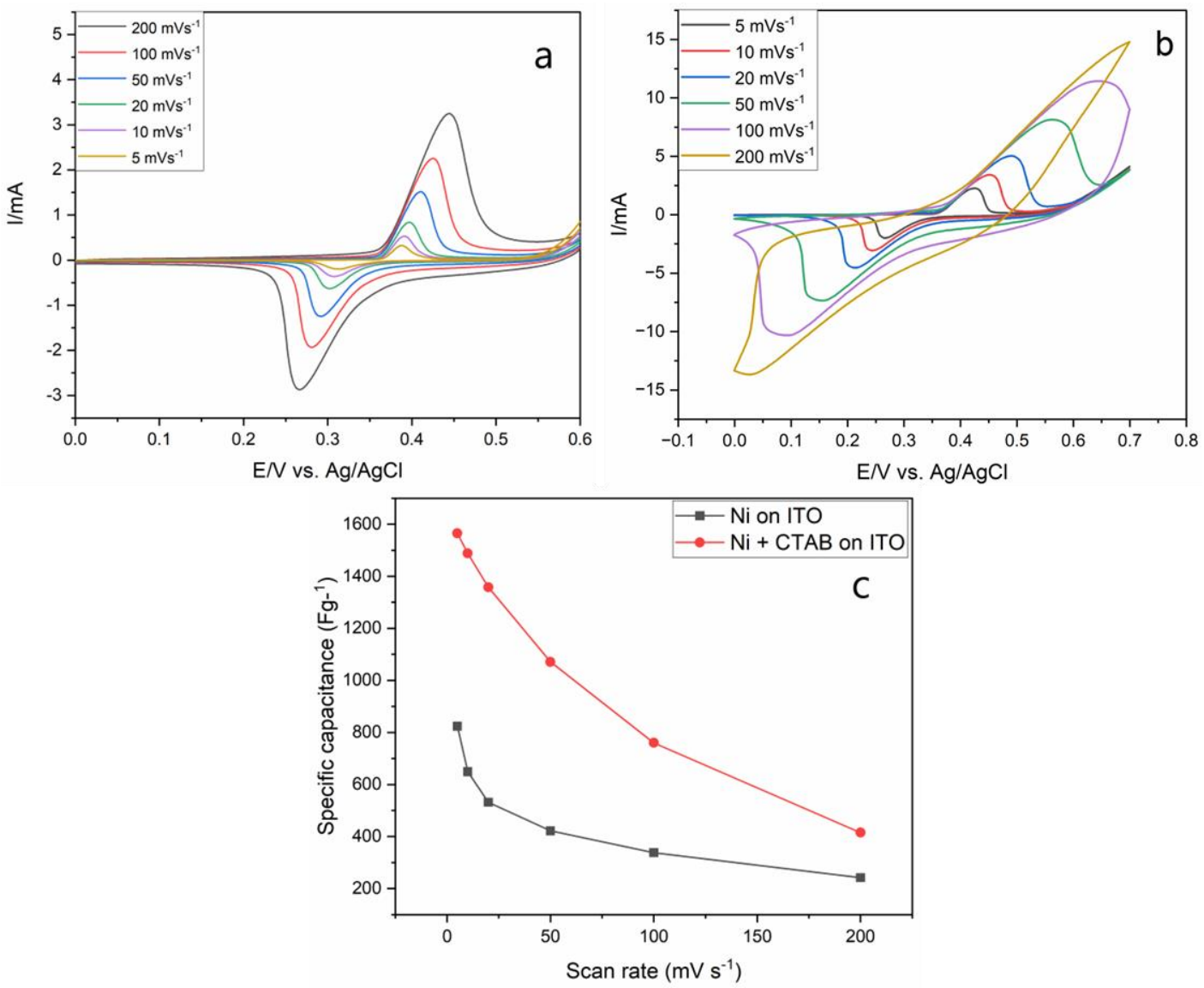

Figure 5.13 CVs of non-templated (a) and CTAB-templated (b) nickel films deposited at -1.25 V (vs. Ag/AgCl) on ITO electrodes at multiple rates of 5, 10, 20, 50, 100 and 200 mV s^{-1}. Variation of specific capacitance vs. scan rate (c) for non-templated (black line) and CTAB-templated (red line) nickel films.

Table 5.1 Extrapolated data obtained from CVs for non-templated nickel film on ITO.

Scan rate / mV s^{-1}	*Peak to peak potential separation, Δ_{EP} / mV calculated for non-templated nickel*	*Peak to peak potential separation, Δ_{EP} / mV calculated for CTAB-templated nickel*
5	*78*	*158*
10	*84*	*209*
20	*94*	*275*
50	*116*	*400*
100	*143*	*546*
200	*175*	*660*

Table 5.2 The mass and the potential range used to determine the specific capacitance of non-templated and CTAB – templated nickel films.

Scan rate / mV s^{-1}	*Mass /g of non-templated nickel film*	*Mass /g of CTAB-templated nickel film*	*Potential range /E of non-templated nickel film*	*Potential range /E of CTAB-templated nickel film*
5	*0.0090*	*0.0072*	*0.5 V – 0 V*	*0.7 V – 0 V*
10	*0.0086*	*0.0073*	*0.5 V – 0 V*	*0.7 V – 0 V*
20	*0.0086*	*0.0071*	*0.5 V – 0 V*	*0.7 V – 0 V*
50	*0.0089*	*0.0072*	*0.5 V – 0 V*	*0.7 V – 0 V*
100	*0.0086*	*0.0072*	*0.5 V – 0 V*	*0.7 V – 0 V*
200	*0.0087*	*0.0071*	*0.5 V – 0 V*	*0.7 V – 0 V*

5.4.4 Conclusions

Mesoporous nickel films have been successfully electrodeposited by the EASA derived method using an inexpensive surfactant, CTAB. Crystalline nickel was observed with wide-angle XRD for non-templated nickel but that with CTAB-templated nickel was amorphous. The surface area was greater for CTAB-templated nickel compared to non-templated nickel. The capacitive behaviour for CTAB-templated nickel was found to be highly affected by the porosity. The specific capacitance of non-templated nickel was found to be 822 F g^{-1}, which was almost two times lower than the specific capacitance of CTAB-templated nickel at 1565 F g^{-1} at 5 mV s^{-1}. The preparation of porous nickel films via an EASA-derived approach presents promise for electrode materials for durable supercapacitors in KOH electrolytes.

5.4.5 References

1 M. Schalenbach, O. Kasian and K. J. J. Mayrhofer, An alkaline water electrolyzer with nickel electrodes enables efficient high current density operation, *Int. J. Hydrogen Energy*, 2018, **43**, 11932–11938.

2 C. Karacan, F. P. Lohmann-Richters, M. Shviro, G. P. Keeley, M. Müller, M. Carmo and D. Stolten, Fabrication of High Performing and Durable Nickel-Based Catalyst Coated Diaphragms for Alkaline Water Electrolyzers, *J. Electrochem. Soc.*, 2022, **169**, 054502.

3 Y. Kiros and S. Schwartz, Long-term hydrogen oxidation catalysts in alkaline fuel cells, *J. Power Sources*, 2000, **87**, 101–105.

4 S. Kim, J. Kang, S. Kim and J. Jang, A new approach to high-performance flexible supercapacitors : Mesoporous three-demensional Ni-electrodes, *Nano Energy Elsevier*, 2017, **39**, 639–646.

5 V. Anantharaman and P. N. Pintauro, The Electrocatalytic Hydrogenation of Glucose: I . Kinetics of Hydrogen Evolution and Glucose Hydrogenation on Raney Nickel Powder, *J. Electrochem. Soc.*, 1994, **141**, 2729–2741.

6 B. Vincent, C. A.; Scrosati, *Modern Batteries- An Introduction to Electrochemical Power Sources*, London, 2nd edn., 1997.

7 P. A. Nelson, J. M. Elliott, G. S. Attard and J. R. Owen, Mesoporous nickel/nickel oxide - A nanoarchitectured electrode, *Chem. Mater.*, 2002, **14**, 524–529.

8 T. Kenjo, Chromium-Doped Raney Nickel Catalyst for Hydrogen Electrodes in Alkaline Fuel Cells, *J. Electrochem. Soc.*, 1985, **132**, 383–386.

9 V. Ganesh and V. Lakshminarayanan, Preparation of high surface area nickel electrodeposit using a liquid crystal template technique, *Electrochim. Acta*, 2004, **49**, 3561–3572.

10 P. N. Bartlett, D. Pletcher, T. F. Esterle and C. T. John Low, The deposition of mesoporous Ni/Co alloy using cetyltrimethylammonium bromide as the surfactant in the lyotropic liquid crystalline phase bath, *J. Electroanal. Chem.*, 2013, **688**, 232–236.

11. A. Lasia and A. Rami, Kinetics of hydrogen evolution on nickel electrodes, *J. Electroanal. Chem.*, 1990, **294**, 123–141.

12 C. Li, B. Jiang, N. Miyamoto, J. H. Kim, V. Malgras and Y. Yamauchi, Surfactant-Directed Synthesis of Mesoporous Pd Films with Perpendicular Mesochannels as Efficient Electrocatalysts, *J. Am. Chem. Soc.*, 2015, **137**, 11558–11561.

13 A. Walcarius, E. Sibottier, M. Etienne and J. Ghanbaja, Electrochemically assisted self-assembly of mesoporous silica thin films, *Nat. Mater.*, 2007, **6**, 602–608.

14 E. Rudnik, A. Czernecka and C. Solution, The Influence Of Potential-Current Conditions On The Electrodeposition Of Ni-Sn Alloys From Acidic Chloride-Sulphate Solution, *Arch. Metall. Mater.*, 2014, **59**, 195–198.

15 N. Sengottuvelan, S. K. Kang and Y. Kim, Coordination Mode of 2-Dimethylaminomethyl-3-hydroxypyridine with Nickel (II) Halides : Structural and Electrochemical Properties, *Bull. Korean Chem. Soc.*, 2008, **29**, 1784–1786.

16 B. H. R. Suryanto, C. A. Gunawan, X. Lu and C. Zhao, Tuning the electrodeposition parameters of silver to yield micro/nano structures from room temperature protic ionic liquids, *Electrochim. Acta*, 2012, **81**, 98–105.

17 S. Pilban Jahromi, N. M. Huang, A. Kamalianfar, H. N. Lim, M. R. Muhamad and R. Yousefi, Facile synthesis of porous-structured nickel oxide thin film by pulsed laser deposition, *J. Nanomater.*, 2012, **2012**, 1–4.

18 K. Bieńkowski, M. Strawski and M. Szklarczyk, The determination of the thickness of electrodeposited polymeric films by AFM and electrochemical techniques, *J. Electroanal. Chem.*, 2011, **662**, 196–203.

19 A. Yin, J. H. Kim and J. Xu, Fabrication of nanostructured thin films using porous alumina templates, *Mater. Res. Soc. Symp. Proc.*, 2006, **951**, 75–82.

20 U. K. Chime, A. C. Nkele, S. Ezugwu, A. C. Nwanya, N. M. Shinde, M. Kebede, P. M. Ejikeme, M. Maaza and F. I. Ezema, Recent progress in nickel oxide-based electrodes for high-performance supercapacitors, *Curr. Opin. Electrochem.*, 2020, **21**, 175–181.

21 X. Liu, J. Wang and G. Yang, Amorphous nickel oxide and crystalline manganese oxide nanocomposite electrode for transparent and flexible supercapacitor, *Chem. Eng. J.*, 2018, **347**, 101–110.

22 M. Amjad, D. Pletcher and C. Smith, The Oxidation of Alcohols at a Nickel Anode in Alkaline t - Butanol / Water Mixtures, *J. Electrochem. Soc.*, 1977, **124**, 203–206.

23 Z. Hu, L. Zu, Y. Jiang, H. Lian, Y. Liu, Z. Li, F. Chen, X. Wang and X. Cui, High Specific Capacitance of Polyaniline / Mesoporous Manganese Dioxide Composite Using KI-H 2 SO 4 Electrolyte, *Polym. MDPI*, 2015, **7**, 1939–1953.

24 B. Saravanakumar, X. Wang, W. Zhang, L. Xing and W. Li, Holey two dimensional manganese cobalt oxide nanosheets as a high-performance electrode for supercapattery, *Chem. Eng. J.*, 2019, **373**, 547–555.

Chapter 6 Conclusions and Perspectives

6.1 Conclusions

The potentially controlled deposition of vertically oriented mesoporous silica films using the electrochemically assisted surfactant assembly method (EASA) has been demonstrated. Surfactants were modified by extending the single straight alkyl chain along with increasing the head sizes to achieve films with larger pore diameters. Another aspect of this thesis focussed on the electrodeposition of nickel films on conductive electrodes using cetyltrimethylammonium bromide (CTAB) as the surfactant. The templated nickel films were used as potential electrodes for supercapacitors.

Mesoporous silica films with larger pore diameters together with vertical hexagonal *P*6*mm* mesopores using EASA has been successfully achieved. This was possible by modifying the surfactant resulting in faster ion transport through the films and so, providing a platform as feasible templates for generating metal and semiconducting nanowire arrays in the preferred vertical orientation. The EASA method can be broadened to other mesoporous metal oxides of zirconia and titania films.

The silica films were characterised by GISAXS, electron microscopy, cyclic voltammetry and ellipsometric porosimetry (EP). The gradual extension of the linear chained surfactants was limited to 24 carbons, as the C_{24}TAB templated silica film showed poor hexagonal order and similar pore spacings to that of C_{20} and C_{22} films, although the vertical position of pores was present. A modified Randles-Sevcik equation was used to calculate ion diffusion rates within mesoporous silica films using redox probe molecules. The diffusion coefficients increased with two carbons added consecutively to the surfactant chain, indicating an enhancement in pore size. Furthermore, the pore spacings implied the possibility of pore expansion, with EP confirming the steady increase in peak pore sizes for C_{16}, C_{18}, C_{20} and C_{22} films determined from the desorption branch of the isotherm. The peak pore sizes fell between 2 and 5 nm, an extension that has not been achieved using the EASA method. The ability to modify the electrode surface of porous silicas by pushing the pore diameter beyond the 2 nm mark without compromising pore order, provides new opportunities to improve the sensitivity and selectivity of larger organomolecules to produce electrochemical sensors or in our case, the increase in pore diameter would offer a platform for the successful deposition of metallic and semiconducting nanowires inside the pore channels with improved stability. In such cases, this would make for a promising template for producing thermoelectric materials. Moreover, our efforts also focused on increasing the pore diameter of mesoporous silica films using modified surfactants of increasing head sizes as this was

seldom reported in the literature with regards to EASA. The cationic surfactants were synthesised in a similar fashion to the straight chained surfactants discussed above however, there was a significant increase in head size whilst simultaneously increasing the aliphatic tail from C_{18} to C_{22}. GISAXS analysis of the silica films showed the continual loss of hexagonal pore arrangement with increasing surfactant head size. The pore spacings for the C_{18} and C_{22} films were found to increase with larger surfactants but an anomaly to this trend was eicosyldimethylethylammonium bromide, C_{20}DMEAB, which could be due to the hindrance of the micellisation process caused by surfactant instability, further works are needed to disclose this phenomenon. It was revealed that the hexagonal pore structure could be improved by increasing the surfactant chain length from C_{18} to C_{22} with a triethylammonium bromide, TEAB head group. No faradaic current was observed for films templated by surfactants with two or three ethyl groups, and pore order was also reduced. However, vertical pores were retained. Impedance measurements indicated resistance to transit of redox active molecules did increase with surfactants of increasing head sizes. EP substantiated the increase in pore diameter for the silica films despite a decrease in pore volume.

Besides SiO_2, another promising material was developed by electrodeposition in this research endeavor. Like the silica films, porous metals can be obtained with the aid of a surfactant template, in this case porous nickel films were synthesised using CTAB as the surfactant. Wide-angle XRD depicted the presence of crystalline nickel for the non-templated film. On the contrary, only the underlying ITO surface was verified for the templated film. The porosity and presence of metallic nickel for the templated film was clarified by SEM coupled with an EDX detector. Electrochemical evaluations suggested that the templated film could exhibit better supercapacitor performance in KOH electrolyte, owing to its higher surface area compared to the non-templated film at 6.0×10^{-4} cm^2 and 3.9×10^{-4} cm^2. This rise in surface area led to the templated film showing a much higher specific capacitance in relation to the non-templated film, determined to be 1565 F g^{-1} and 822 F g^{-1} at 5 mV s^{-1}.

6.2 Perspectives

Considering the interest for these silica films in electrochemistry, broader applications on the use of such films would be found in sensing devices, as functional catalysts or in electronics. Further research needs to be conducted in order to produce porous electrode materials for many technological advancements in particular, electrochemical sensors, thermoelectric materials and supercapacitors. In the following section some ideas for future research are provided in detail.

In this thesis, mesoporous silica films were successfully prepared by an electro-assisted deposition technique using a range of cationic surfactants. Further studies would entail the synthesis of

larger and more functionalised surfactants for the preparation of ordered mesoporous silicas with pore sizes above 5 nm using EASA. A possible route would involve attaching an aromatic ring to the end of the alkyl chain of a quaternary ammonium surfactant using multi-step reaction schemes namely carbon-carbon coupling reactions involving a Grignard reagent followed by nucleophilic S_N2 type reactions to quaternise the surfactant system.

Furthermore, the expansion of pores in mesoporous silica films were produced by surfactants with modified head groups using EASA. Further works could focus on understanding factors that could affect the micellisation process for the C_{20}DMEAB surfactant which produced smaller d-spacings than C_{20}TAB, as determined by 1D GISAXS data. For instance, the parameters of pH, surfactant concentration, sol temperature, and silica/surfactant ratio could be experimentally examined to gauge whether d-spacings and hence pore sizes increase.

Lastly, the effect of CTAB surfactant on the electrodeposition of nickel has been demonstrated. The tuning of pore diameter using larger surfactants for example C_{20}TAB and C_{22}TAB, could lead to better electrochemical performance of these templated nickel electrode materials by further increasing the active surface area in turn enhancing the capacitive behaviour and specific capacitance of the active material for supercapacitor applications. Another key component would be to carry out further experimentation on the nickel composition using XPS and/or Raman spectroscopy to further clarify the presence of metallic nickel for the templated film. Moreover, once porous nickel has been established using larger surfactants, the electrodeposition of other d-block metals namely platinum, cobalt, palladium, and copper using straight chained surfactants of C_{16}, C_{18}, C_{20} and C_{22} would make for useful nanostructured materials that could be used for catalysis, fuel cells, batteries, and electrochemical capacitors.